Title	Development of Novel Metal Ion Beam Systems with Liquid-Metal Ion Sources(Dissertation_)
Author(s)	Gotoh, Yasuhito
Citation	Kyoto University ( )
Issue Date	2002-03-25
URL	https://doi.org/10.14989/doctor.r10927
Right	
Type	Thesis or Dissertation
Textversion	author

Development of Novel Metal Ion Beam Systems

with Liquid-Metal Ion Sources

Yasuhito Gotoh

November, 2001

Development of Novel Metal Ion Beam Systems

with Liquid-Metal Ion Sources

Yasuhito Gotoh

November, 2001

Abstract

The present dissertation dealt with the issues related to the development of novel ion beam systems based on liquid-metal ion sources (LMIS). Unlike the conventional application of LMIS, which is represented by the focused ion beam (FIB) technology, argument made here was how to use a large portion of the ions extracted from the source. An LMIS has unique features. Among these features, ultra high vacuum (UHV) compatibility with no use of a harmful source material is one of the most attractive advantages. Use of pure metal causes no pollution of environments, which will be important for the manufacturing in the new century. In Chapter 1, Introduction, the author emphasized the current status and problems in the application and technology of LMIS's, pointing out three major problems. The author dealt with these issues in the following three parts: part I: undetermined ionization mechanism at a high current regime, part II: difficulties in converging a strongly divergent beam, and part III: insufficient ion current with the conventional type LMIS's.

Part I dealt with the fundamentals of the ion beam characteristics. In Chapter 2, fundamental characteristics of the ion beam extracted from some element metal ion sources, which were experimentally obtained, were given. The author showed that the electric field at the ionization point decreases with an increase in the source current. Paying an attention to this phenomenon, the author pointed out that at the high current regime, the conventional theoretical model does not work. Introducing an assumption to one of the fundamental equations which dominate the liquid cone formation, the author successfully explained the behavior of the decrease in the electric field at the high current regime. In Chapter 3, the author proposed a high temperature field evaporation (HTFE) model of which formulation is similar to that of the conventional theory but allows extremely high temperature at the apex, extending the theory to molecular ions. So far, high temperature was suggested but nobody could show an evidence for this HTFE. The author explained the atom flux ratio of doubly charged ions to singly charged ions (R_{21}), and that of molecular ions (R_{dm}). In Chapter 4, the author investigated the characteristics of alloy ion sources and extended the HTFE model to the alloy ion source. As a result, the author could show that HTFE model also holds for alloy ion sources, especially for the behavior of R_{21}.

Part II dealt with the development of novel ion beam systems to demonstrate successful transport of the ion beams extracted from an LMIS. Chapter 5 dealt with the issue related to focusing of the divergent beam extracted from the LMIS. The author designed a novel electrostatic lens system suitable for use in focusing the divergent beam. The property of this lens was evaluated both by computer simulation and by experiments. Next, the author designed and constructed an ion implantation system. A unique implantation, molecular

ion implantation, was demonstrated with the gold-antimony ion source. Doubly charged heterogeneous molecular ions were implanted to a silicon substrate. In Chapter 6, the author applied the lens system to the novel thin film formation process of metal ion beam self-sputter deposition. Copper thin films were deposited by this unique deposition. It was found that the films show a low electrical resistivity.

Since the feasibility of the metal ion beams was shown, the author finally developed high current metal ion sources in Part III, Chapter 7. Arranging the ion emission points up to approximately 40 in a linear array, a metal ion beam of 9.1 mA was obtained. The details of the solutions to the problems in heating the system and in holding system were given. Analyzing the ion beam profiles, the author showed a distortion of beam profile from axial symmetry. This means presence of self-convergent effect due to the shielding effect by the neighboring cusps. Based on the above experimental results and the system developed in Chapter 5, the author designed the lens for the linear array source, and demonstrated the formation of a metal sheet beam.

In Chapter 8, the author concluded the present dissertation. Three major problems that prevent an LMIS from playing an important role in materials science has now been solved, thus application of LMIS systems will become active in the materials science in near future.

Acknowledgments

Contents

II   Development of systems for single point source   119

List of Symbols

Table: List of symbols

Symbol	Meaning
A	constant in relation between intensity ratio of doubly charged ions to singly charged ions and electric field for post-ionization theory
B	coefficient for the field dependent term in relation between intensity ratio of doubly charged ions to singly charged ions and electric field for post-ionization theory
B_r	brightness
B_{rn}	normalized brightness
C	constant in empirical relation between current and electric field; superscript at the left shoulder either IH or PI means that the value is for the image hump model or for the post-ionization theory
D	coefficient for the filed dependent term in empirical relation between current and electric field; superscript at the left shoulder either IH or PI means that the value is for the image hump model or for the post-ionization theory
E	energy (general)
E_0	incident energy of ion
E_1	primary ion energy
E_b	binding energy
ΔE	energy spead
F	electric field (general)
F_{ev}	evaporation field; superscript 1 or 2 at the right shoulder means F_{ev} for singly charged or doubly charged ion
F_L	Laplace field
F_P	Poisson field
G	ionic core potential
H	sublimation energy
H_m	sublimation energy for molecules with m atoms
$I(r)$	ion current as a function of radial position r
I_a	current accepted towards the given solid angle
I_{ang}	angular intensity
I_i	ion current
I_{int}	integrated current
I_{ms}	mass separated current
I_s	source current

Table: (*continued*)

Symbol	Meaning
I_{tr}	transported ion current
I_Ω	angular current; subscript of 1, 2, mon, dim, and tri means that the value is for the singly charged monatomic ions, doubly charged monatomic ions, singly charged monatomic ions, singly charged dimer ions, and singly charged triatomic ions
J	current density (general)
J_i	current density for $i-$times ionized atom
J_i	current density at image position
J_o	current density at object position
K	kinetic energy of liquid per volume
L	length of drift space
M	magnification of lens system
$\mathbf{M}$	transfer matrix
N	atomic density (general)
N_0	coefficient related to sputtering yield
N_s	surface atomic density
N_v	atomic density per unit volume
P	hydrodynamic pressure
Q	potential barrier (general)
Q_i	potential barrier for $i-$times ionized ions at surface; subscript either IH or PI may be placed just before the subscript i, which means that the potential barrier is for the image hump model or for the post-ionization theory
Q_{21}	difference of potential barrier: $Q_2 - Q_1$
R	radius of curvature for sector magnet
R_0	coefficient of R_{21}
R_{21}	atomic intensity ratio of M^{2+}/M^+
R_{dm}	current ratio of M_2^+/M^+
R_{tm}	current ratio of M_3^+/M^+
R_p	projected range
S	area (general)
S_F	electric field stress
$S_{F(L)}$	virtual stress due to Laplace field
S_{SC}	virtual stress due to space charge
S_T	surface tension stress
S_e	electronic stopping power
S_n	nuclear stopping power
T	temperature (general)
T_a	local temperature of the apex

Table: (*continued*)

Symbol Meaning

T_{cr}	critical temperature necessary to satisfy HTFE model
T_{m}	melting point
T_{s}	source temperature
U	potential (general)
U_{a}	atomic potential
U_{i}	ionic potential
V	voltage (general)
V_{acc}	acceleration voltage
V_{ext}	extraction voltage
V_{i}	beam voltage at the image space
V_{o}	beam voltage at the object space
V_{post}	voltage of post-stage lens
V_{pre}	voltage of pre-stage lens
V_{sup}	suppressor voltage
V_i	ionization potential for $i-$times ionization
W	input power
X	$-2(1 + S_{\mathrm{T}}/4K)/(1 + S_{\mathrm{T}}/K)$
ΔX	deviation from the critical relation between F_{P} and r_{a}
Y_I	power of the relation between F_{P} and I_{Ω}
Y_J	power of the relation between F_{P} and J
Z	atomic number
a_i	coefficient of series expansion of J with respect to F
a_0	Bohr radius
a_{U}	Universal screening length
b_i	coefficient of series expansion of J with respect to r_{a}
c	velocity of light
c_3	$(4/3)\sqrt{m_{\mathrm{I}}/e}$
c_{M}	atomic composition of constituent M at the ionization point
d	emitter-extractor gap
d_{g}	grain size of the crystallites in thin film
d_{sep}	separation of two cylinder lenses
e	elemental charge
f	focal length; subscript either i or o means the value is for the image space or for the object space
f_{eff}	effective atom evaporation rate
g	acceleration coefficient of gravity
h	height
i, j	variables for summation

Table: (*continued*)

Symbol Meaning

Symbol	Meaning
k	charge number
$\bar{k}$	average charge number
k_{B}	Boltzman's constant
ℓ	length of jet-like protrusion
ℓ_0	mean free path of electron in solid
m, n	number of atoms in molecules
m_{ij}	component of matrix $\boldsymbol{M}$
m_{I}	mass of ion
n_{o}	reflective index in object space
n_{i}	reflective index in image space
$\boldsymbol{p}(p_x, p_y)$	position vector of ion with the component (p_x, p_y)
q	liquid flow
q_{t}	total atom flow
q_{e}	atom flow escaping from surface due to evaporation
r	radial length
r_{a}	apex radius
r_{i}	beam radius at the image space
r_{o}	beam radius at the object sapce
r_0	initial apex radius of the liquid
s_1	coefficent of field in the rate of ionization
s_1'	$s_1 \times k_{\mathrm{B}}T$
s_{21}	coefficient of filed in intensity ratio of doubly charged ions to singly charged ions
s_{21}'	$s_{21} \times k_{\mathrm{B}}T$
s_i	coefficient of field in current density for i times charged ion
u_{c}	focal length; subscript i or o means that the value is for the image space or the object space
v	velocity (general)
v_{i}	velocity at image side
v_{o}	velocity at object side
$\boldsymbol{x}$	x direction vector consists of the position and tangent; subscript either in, or out means that the vector is for the entrance, and the exit of an ion optical element, and also subscript exit means for the exit of the pre-stage lens
x	position in x direction; subscript either in or out means that the value is for that at the entrance or exit of the optical element
Δx	tangent of beamlet in x direction; subscript either in or out means that the value is for that at the entrance or exit of the optical element
$\boldsymbol{y}$	y direction vector with the same meaning and subscript with x direction

Table: (*continued*)

Symbol   Meaning

---

y	position in y direction with same subscript meaning as x direction
Δy	tangent of beamlet in y direction with same subscript meaning as x direction
z	position in z direction (axial direction)
z_a	atomic radius
z_c	critical point for ionization in charge exchange model
z_{es}	position of electric surface
z_{in}	position where lens effect occurs (object side)
z_m	midfocal length; subscript either i or o means that the value is for the image space or for the object space
z_{out}	position where lens effect ceases (image side)
z_p	distance from principal plane to plane of reference
z_r	position of the reservoir end .
z_s	suddle point
Γ	reflection coefficint of electrons at grain boundary
Λ	energy conversion factor
Ω	solid angle (general)
Ω_{eff}	effective emission solid angle
Ω_N	solid angle of ion collector normal to the ion incidence
Φ_M	atom flux rate of metal M
Ψ	rotation angle of sector magnet
α	coefficient for electrical resistivity
α_i	converging half angle
α_o	acceptance angle
β	geometrycal factor
γ	surface tension
γ_{ie}	secondary electron emission coefficient
δ_{cr}	parameter of critical relation of electric field and temperature
ε_0	permittivity of vacuum
ζ_i	power of relation between I and I_Ω
θ	emission angle
θ_r	tip cone half angle
θ_t	half angle of liquid jet
η	suppression factor of evaporation rate
κ	thermal conductivity
ν	vibration frequency
ν'	ratio of vibration frequency of dimer to that of monomer

Table: (*continued*)

Symbol Meaning

Symbol	Meaning
ν_{ejec}	ejection frequency of surface atoms
ξ_{ana}	rate of decrease of R_{21}, analytical variant
ξ_{s}	rate of decrease of R_{21}, experimental vaule for I_{s}
ξ_{Ω}	rate of decrease of R_{21}, experimental value for I_{Ω}
π	circular constant
ρ	electrical resistivity
ρ_0	electrical resistivity of bulk copper
ρ_{g}	electrical resistivity of grain scattering
ρ_{m}	weight density
σ	cross section
ϕ	work function
ψ	angle
ψ_{eje}	ejection angle of sputtered particle

Constants of materials

Table: Constants of materials

Constants	Units	Ib			IIIb			Ref.
		Cu	Ag	Au	Al	Ga	In	
Z		29	47	79	13	31	49	
m_I	a.m.u.	63.55	107.9	197.0	26.982	69.72	114.8	[1]
z_a	Å	1.35	1.52	–	1.26	1.26	1.44	[2]
ρ_m	10^3 kg m^{-3}	8.933	10.492	19.3	2.70	5.93	7.28	[1]
N_v	10^{28} m^{-3}	8.43	5.85	5.89	6.02	5.08	3.79	[1]
T_m	°C	1083	962	1063	660	29.8	157	[1]
γ	N m^{-1}	1.3	0.9	1.1	0.9	0.7	0.6	[3]
κ	W K m^{-1}	401	428	318	235	85	87	[1]
ϕ	eV	4.6	4.6	4.3	4.1	4.1	4	[4]
H	eV	3.50	2.96	3.78	3.34	2.78	2.6	[4]
E_b	eV	1.99	1.65	2.25	1.95	1.52	0.95	[5]
V_1	eV	7.726	7.576	9.225	5.986	5.999	5.786	[4]
V_2	eV	20.292	21.49	20.5	18.828	20.51	18.869	[4]
F_{ev}^1	10^{10} V m^{-1}	3.0	2.4	5.3	1.9	1.5	1.3	[4]
F_{ev}^2	10^{10} V m^{-1}	4.3	4.5	5.4	3.5	3.9	3.2	[4]

to be continued

Table: (*Continued*)

Constants	Units	IVb				Vb	Ref.
		Si	Ge	Sn	Pb	Sb	
Z		14	32	50	82	51	
m_I	a.m.u.	28.09	72.59	118.7	207.2	121.8	[1]
z_a	Å	1.17	1.22	1.40	–	1.36	[2]
ρ_m	kg m^{-3}	2.42	5.46	7.30	21.0	6.62	[1]
N_v	10^{28} m^{-3}	5.00	4.50	3.68[a]	3.30	3.25	[1]
T_m	°C	1415	937	232	323	630	[1]
γ	N m^{-1}	0.7	0.6	0.5	0.4	0.3	[3]
κ	W K m^{-1}	170	67	67	35	26	[1]
ϕ	eV	4.8	4.8	4.4	4.1	4.6	[4,6]
H	eV	4.90	3.97	3.12	2.04	2.7	[4,6]
E_b	eV	3.21	2.76	1.99	0.99	3.06	[5]
V_1	eV	8.15	7.88	7.344	7.416	8.641	[4,6]
V_2	eV	16.35	16.12	14.632	15.032	16.53	[4,6]
F_{ev}^1	10^{10} V m^{-1}	4.7	3.5	2.6	2.0	3.2	[4,6]
F_{ev}^2	10^{10} V m^{-1}	3.4	2.9	2.3	2.3	3.0	[4,6]

[a]white tin (β phase)

References

[1]   S. Chikazumi, K. Kigoshi and S. Tanuma: *Kaitei Saishin Genso Chishiki (The Latest Element Information, Revised)* (Tokyo Shoseki, Tokyo, 1985) [in Japanese].

[2]   C. Kittel: *Introduction to Solid State Physics, 5th edition* (John Wiley and Sons, New York, 1976).

[3]   R. C. Weast ed., *Handbook of Chemistry and Physics*, 55th Edition, (CRC Press, Cleveland, 1974) F-23.

[4]   T. T. Tsong: Surf. Sci. **70** (1978) 211.

[5]   Vályi: *Atom and Ion Sources* (John Wiley and Sons, London, 1977).

[6]   D. G. Brandon: Surf. Sci. **3** (1964) 1.

Chapter 1
Introduction

This chapter gives the introduction of the present research program. First, the author briefly reviews some features of liquid-metal ion sources (LMIS's) and the application and technology related to each feature of an LMIS. The author emphasizes the potential of an LMIS, especially from the viewpoint of metal ion source which is suitable in use for highly efficient materials processing, less harmful to environment. After pointing out the advantages in use of LMIS's, the author shows some difficulties, which become significant in applying an LMIS of the current models to this novel materials processing. The arguments are classified into three major parts: modeling of the LMIS, focusing of divergent beam, and intensification of the source. The author illustrates the solutions to these difficulties. Finally, the author shows the flow of the present research.

1.1   Liquid-metal ion sources

1.1.1   Structure and principle

When a high electric field is applied to a surface of a liquid on a rigid base, the liquid surface is pulled by this electric stress to be deformed. If the electrostatic stress S_F, excesses the surface tension stress S_T, the liquid is pulled to form a cone as illustrated in Fig. 1.1. The entire figure of this cone is called the "Taylor cone", because Sir Taylor [1] was the first who investigated the field stabilized shape of the cone. He analytically derived that the apex half angle is 49.3°. It has been confirmed [2] that the approximate shape of the cone is almost the "Taylor cone", although a jet-like protrusion is formed at the apex [3]. In the case of a negative field, positive ions are produced at the apex [4]. This phenomenon is called "field emission" and the ion source based on this phenomenon is called "liquid-metal ion source" (LMIS). Here it should be noted that although the term "field emission" is commonly used, the ion emission mechanism is now believed to be field evaporation [5] which is not based on quantum mechanical electron tunneling.

In order to apply a strong electric field, the liquid-metal is mounted on a thin wire of which apex has been electrochemically etched (needle-type) [6], or the liquid-metal is sustained by a narrow capillary (capillary-type) [4,7]. Sometimes a needle is inserted into a capillary to fix the ion emission point [8], or a porous refractory metal is used to control

Electric field stress S_F Ion emission

Raduis: r_0

Liquid–metal   Surface tension stress S_T Infinitesimal radius

Taylor cone

$S_F > S_T$

(a)   (b)
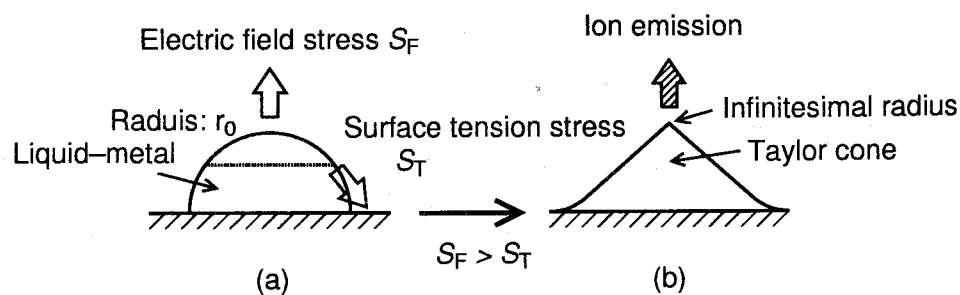
Figure 1.1: Schematic drawing of operational principle of liquid-metal ion source: (a) before applying high field, and (b) after applying high field.

porous region

liquid–metal   needle   liquid–metal

capillary

needle

(a)   (b)   (c)   (d)
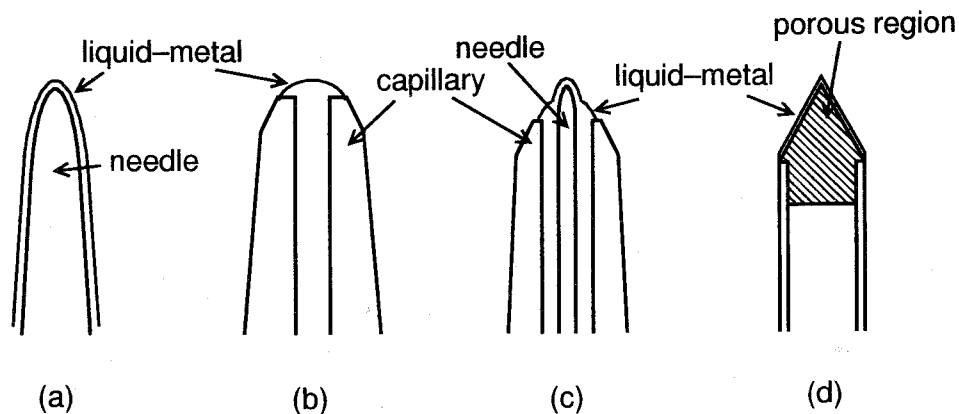
Figure 1.2: Schematic drawings of typical liquid-metal ion sources. (a) needle-type, (b) capillary-type, (c) capillary-needle-type, and (d) impregnated-electrode-type. Generally the ion source is installed upside down for easiness of ion extraction.

the liquid flow (impregnated-electrode-type) [9]. Schematic drawings of these types of ion sources are illustrated in Figs. 1.2(a)–1.2(d). Figures 1.2(a)–1.2(d) indicate the needle-type, capillary-type, capillary-needle-type, and impregnated-electrode-type, respectively. In any of these ion sources, liquid-metal is supplied from the behind of the ionization point. The flow of liquid-metal is driven by a negative electro hydrodynamic stress [10], so this ion source is also called as "electro hydrodynamic ion source" [11]. Also "molten metal field ion source" is used [12]. In the present dissertation, the term "liquid-metal ion source (LMIS)", which is most commonly used, is adopted.

The materials available in LMIS's are not restricted to metals, but to semiconductors and semimetals. The word "metal" used in the present dissertation includes wide range of elements that maintain solid or liquid phase at room temperature.

1.1.2 Feature of liquid-metal ion sources

An LMIS is now well known as an ion source for the focused ion beam (FIB) technology [26, 27]. Since the late 1970's, developments of FIB machines and microfabrication technology has been pursued by many researchers. LMIS's were used in the FIB technology because they are point sources with high brightness. Besides the FIB technologies, the LMIS's have been studied in the other fields such as space propulsion [11]. From the ion source-engineering point of view, they have very unique features as a metal ion source. In this dissertation, the author reviews the application and technology of LMIS's from this point of view. The author must stress here that the standpoint of the present dissertation is different from that of FIB technology. Here, the author lists up the features of LMIS's and corresponding application fields made so far. Each feature is listed in contrast with common metal ion sources of plasma-type or sputter-type.

a) Point source

One of the most important feature of an LMIS is probably such that it is a point source, as described above. Krohn and Ringo showed that the brightness of LMIS is quite high [7], which resulted in enthusiastic competition of the development of the FIB machines [13–17]. These developments have their origin at the paper by Seliger and co-workers [13]. The normalized brightness reached $5 \times 10^{15} \mathrm{Am}^{-1}\mathrm{sr}^{-1}$ [13], and this value is almost three orders of magnitude higher than those of the other ion sources [18]. The source size is approximately several nanometers [19]. Originally, the FIB technologies have been expected for microfabrication of semiconductor devices with the dimension of less than 1 μm, but is currently used for mask repairing or sample preparation for an electron microscope [20]. Figure 1.3 shows various kinds of FIB machines developed so far [13,17]. Also, the FIB has been used to fabricate micromachines or vacuum microelectronics devices [21–25]. A

(a)

HEATER
RESERVOIR
LIQUID GALLIUM
TUNGSTEN NEEDLE
EMITTING TIP
EXTRACTION
ELECTRODE
V_{HTR}
V_{EXT}

OBJECT
APERTURE
$2\alpha_0$
32 MM
ACCELERATING
LENS
ELECTRODES
V_{LENS}

ELECTROSTATIC
DEFLECTION
ELECTRODE
50 MM

CHANNEL
ELECTRON
MULTIPLIER
$2\alpha_i$

TARGET

(b)

ION SOURCE
CONDENSER LENS
MASS-SEPARATOR
OBJECTIVE LENS
BEAM DEFLECTOR
TARGET WAFER
STAGE
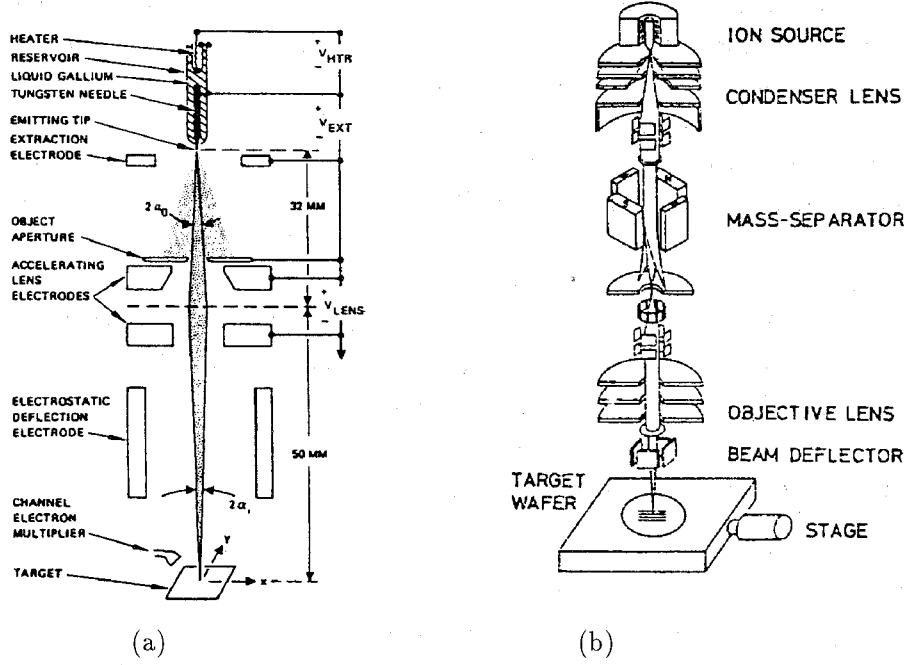
Figure 1.3: Various kinds of focused ion beam systems. (a) The first FIB machine developed by Seliger et al.[13] and (b) one of the FIB machines which are equipped with a Wien filter[17].

good review [26] and a list of LMIS's [27] are already published, and it is not necessary to duplicate the successful developments of FIB systems here in this dissertation. In these systems, only a small portion of the extracted beam, approximately $10^{-5} - 10^{-3}$ is used.

Although the virtual source size is slightly larger than the actual source size due to extraction optics [19], it is small enough as compared with the plasma-type or the sputter-type sources that have an extraction aperture of 0.5 to 2 mm. Unlike these sources, the source material is fed to the ionization point in a liquid state. The density of the source material is thus larger than these ion sources by approximately eight orders of magnitude, if we assume that typical gas pressure in the discharge chamber is ~1 Pa. The point source means also having small emittance, which is very attractive for the accelerators in which ion beam is transported from several meters to several kilometers. Indeed, some researchers attempted to mount LMIS to an accelerator [28,29].

Filling orifice

Cs emerges here

Emitter channel
(sputtered deposits
maintain slit width,
· l = 1μm)

Slit lips
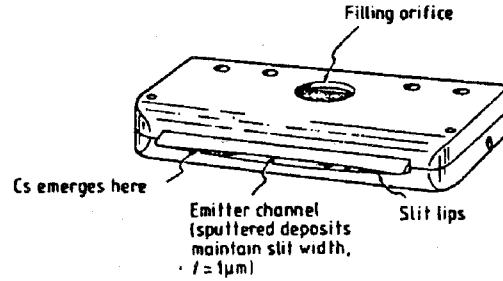
Figure 1.4: Schematic drawing of liquid-metal ion thrusters of slit capillary configuration[32]. In this figure, only ion-emitter is illustrated. An extraction electrode is necessary to generate an ion beam.

Table 1.1: Comparison of metal ion sources. ν means necessary, and (ν) means necessary in some cases.

System component	Plasma-type	Sputter-type	LMIS
Vaporizer (high temp.)	ν		
Heater (low temp.)			ν
Discharge P.S. (dc, rf, mw, etc)	ν	ν	
Filament (cathode)	(ν)	(ν)	
Extraction P.S.	ν	ν	ν
Magnetic field	(ν)	(ν)	
Target bias P.S.		ν	
Gas feeding system	(ν)	ν	

b) Simple structure

Another significant feature of this ion source is its simplicity. Only a pair of an ion emitter and an extraction electrode is required. The ion emitter generally consists of a hair-pin filament and an etched needle which is spot-welded to the filament [6]. Even though the capillary-type, a thin cylinder and counter electrode is necessary. It is surprising that metal ions can be obtained only by applying a high voltage between an ion-emitter and a counter electrode, with small heating power, as compared with the other metal ion sources that require a complicated heater assembly on the arc chamber. In the early stage of LMIS developments, researchers found superiority of this ion source as an ion thruster [30–35], an ion engine for space propulsion. Figure 1.4 shows a schematic drawing of the slit capillary type LMIS for space propulsion [34]. As compared with a chemical thrust, an electric propulsion is highly efficient, because we can give a high momentum to the ionized atoms by applying a high voltage between the source and extractor. The most plausible candidate for an ion engine is a Kaufman type ion source [36], which is classified into a plasma source. For the ion thruster, the material to be ionized is mercury(Hg) or cesium(Cs), which does not require intentional heating. In plasma-type metal ion sources [36,37], if it has low vapor pressure at room temperature, a furnace is necessary to vaporize the source material. And as described above, it is also necessary to maintain the arc chamber at a high temperature. Thus, generally, the structure of a metal ion source is complicated. Table 1.1 denotes the comparison of various kinds of metal ion sources, from the structural point of view. In this table, elements required for each ion source are shown by a check (ν). The check in parentheses shows that it is not always necessary for some types of ion sources. This table clearly shows the simplicity of the LMIS.

c) Low power consumption

As well as the simple structure, one of the major advantages of an LMIS is low power consumption. The power required for the operation of the LMIS is only some tens watts [9], which is necessary to melt the source material. This is also attractive for an ion thruster and an injector of accelerator. In the plasma-type metal ion source, power consumption of heater assembly is generally high. The sputter-type ion source requires no heating [38], but use of sputtering causes a finite efficiency so the total power consumption should be large.

d) No gas flow and ultrahigh vacuum compatibility

In addition to above, since an LMIS requires no gas flow, and it can be operated at a relatively low temperature, it requires a vacuum system with a small pump. For a stable operation, ultrahigh vacuum (UHV) is preferred rather than high vacuum [39]. This implies
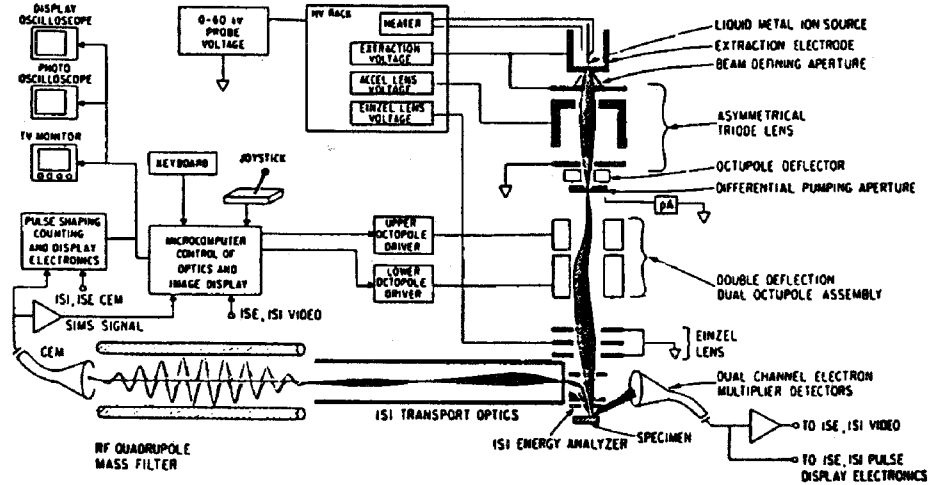
Figure 1.5: An example of secondary ion mass spectroscopy with LMIS[41].

that the LMIS is compatible to UHV systems. As for the plasma-type metal sources, it is difficult to suppress gas flow from the discharge chamber, and thus the pumping system should be large to maintain high vacuum. This UHV-compatibility matches the requirements in microanalysis machines such as scanning ion microprobe [40–45]. Scanning ion microprobe is a microbeam secondary ion mass spectrometry, and deals with the surface phenomena, sensitive to the ambient. Figure 1.5 shows a schematic diagram of the SIMS system equipped with a LMIS [41]. Also an ion irradiator with a LMIS for *in situ* scanning tunneling microscope observation of ion-irradiated semiconductor surface has been also developed [46].

The UHV compatibility is preferred not only from the surface analysis point of view, but also from the materials processing point of view. Especially for crystal growth, incorporation of residual gas atoms is a serious problem. Even for the sputtering apparatus, background pressure is reduced to UHV region. The equipment that uses gaseous material should have gas inlet. To achieve UHV, tremendously large amount of effort is required to eliminate gases from gas feeding pipes.

e) Generation of pure metal ion beam

If we can handle the source with an element metal, the extracted ion beam consists of ions of a single element. For a sputter-type ion source, it is inevitable to extract discharge gas
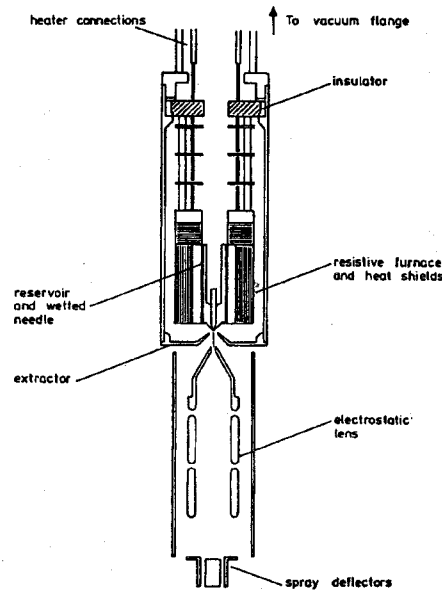
Figure 1.6: Configuration of field emission deposition system[48].

ions together with the metal ions, except for a negative ion source. To select the ions one wants to have, mass-separation is necessary. Taking this advantage, applications of LMIS to film deposition [47, 48] were performed. Figure 1.6 shows the field emission deposition system [48]. The component of the machine necessary for this deposition is only an ion emitter and a counter electrode settled with a substrate. In Fig. 1.6, the system which is equipped with an additional lens system is illustrated. The ion source was operated at a very high current from a single point, resulting in a large amount of droplet emission [49]. Since final texture of the coating involves large droplets, it would not be appropriate for electronic device fabrication as it was.

For a plasma-type ion source, volatile molecules such as hydride or chloride are also ionized, and this results in addition of hydrogen or chlorine ions within the plasma. Although the control of the ion species in plasma has been being possible [38, 50], they still contains small amount of impurity ions. Formation of pure metal ion beam by a LMIS is based on use of pure metal material, and control of the impurities is easily achieved.

f) No toxic source material and no exhaustion of toxic material

If the material with a high vapor pressure such as metal hydride, fluoride, or chloride is used in a plasma-type ion source, these materials give serious damage to the ion source itself

and also to the vacuum systems, due to its high reactivity. Furthermore, these materials are generally toxic [51]. An expensive eliminator should be placed before exhaustion of the pumping system. In the LMIS, materials used is in an element form or in an alloy form [52–62], and we can choose materials that are not toxic, thus use of an LMIS matches the requirements of materials processing of new century: "gentle" (less harmful) to the environments.

g) Generation of unique ions

It should be also recognized that LMIS provides various kinds of ion species: singly charged atomic ions, doubly charged atomic ions, singly charged molecular ions, and doubly charged molecular ions. Generally, formation of multiply charged ions is difficult in the plasma-type sources and the relative current of the doubly charged ions are typically 10 to 20 % of that of the singly charged ions [63–65], except the ion sources specially designed for production of multiply charged ions such as Electron Cyclotron Resonance (ECR) ion sources [66] or Electron Beam Ion Sources (EBIS's) [67]. As for the sputter-type source, we can expect little doubly charged ions [38]. Recent development of MEtal Vapor Arc (MEVVA) ion sources made it possible to produce highly charged metal ions [68] in pulsed mode. But such a source that could be operated in dc mode is restricted to the LMIS. Because the doubly charged ions have a high potential energy, some researchers pay their attention to the interaction between solid and these ions.

On the other hand, the LMIS has once attracted much interest as an ion source for small metal cluster formation [69]. The interest was mostly concerned with the stability of metal clusters and there was little action for deposition with these ions, except the formation of isolated clusters on substrates to know the nature of these clusters [70]. The effect of the molecules in depositing thin films or implantation is not fully understood, but some experiments showed that the film property is superior to that deposited with atomic ions [71,72]. So far, molecular ion beam deposition or implantation have not been performed. But due to the high impact to surface, it will become interesting technique.

These characteristics reflect a unique feature of the surface effect ionization.

1.1.3 Expected role of LMIS in materials science

The features of LMIS and expected application fields are schematically drawn in Fig. 1.7. In the figure, the conventional applications are located at the upper left hand side, which took advantages of the point source. The application areas where LMIS's will play a significant role in the future are drawn at the right hand side. Since an LMIS possesses a potential to establish novel ion beam processing's which are highly efficient, in ultrahigh vacuum, and less harmful to environment, which is required for the processing in the new

Conventional applications   ┌──── Novel applications ────┐

┌─────────────────────────────┐   ┌──────────────────────────────┐
│ FIB   │   │   Novel processing   │
│   Microfabrication   │   │   Novel deposition   │
│   SIMS   │   │   Novel implantation   │
│   SEM/TEM samples   │   │   UHV systems   │
│   │   │   │
│   ┌──────────────────┐   │   │   ┌──────────────┐   │
│   │ Point source   │   │   │   │ Unique ions │   │
│   └──────────────────┘   │   │   └──────────────┘   │
│ ┌──────────────────┐   │   │   ┌──────────────┐   │
│ │ Simple structure │   │   │   │ No gas flow │   │
│ └──────────────────┘   ╱ │   │   └──────────────┘   │
│   (LMIS)   │
│   ╲   ┌──────────────────┐   │
│   │ Pure metal ions │   │
│   └──────────────────┘   │
│ ┌────────────────────────┐ ┌──────────────────┐   │
│ │ Low power consumption │ │ No toxic materials │   │
│ └────────────────────────┘ └──────────────────┘   │
│ Large current application   │
│   Ion thruster (ion engine)   Field emission deposition   │
│   │
│   "Pure Processing": gentle to environment   │
└──┘

Figure 1.7: Features of LMIS and expected application fields

century. The author calls this new process "pure processing". Especially for a high current, large area processing, no attempts have been made so far. The author expects LMIS to serve as an ion source for this "pure processing". Processing with pure metal ions and/or atoms does not require eliminator in the vacuum system due to no exhaustion of harmful gases or liquids. Since all the ions will act in the process, thus the power efficiency is extremely high unlike the other processes such as plasma processing's. The source can be made compactly which means the machine occupies only small portion of a factory. With all these advantages, ion implantation, thin film coating, surface modification, or etching will be performed effectively in UHV, with minimum pollution of environment.

1.2 Subjects to be solved for use of LMIS in pure processing

1.2.1 Three key factors of ion beam processing system

Although LMIS's have the above advantages, applications to materials science have been limited to a quite small field. One of the major reasons for this would be a low output and difficulty in handling. Cease of enthusiastic developments in FIB technology clearly indicates the present problem. Since the large scale integrated circuit requires a large number of the same patterns on a silicon wafer, which requires a long processing time. Only the technology that survived is a cutting tool for an electron microscope, which does not need large-scale manufacturing. Considering this, development of the systems which have high output, and are easy to handle is necessary. In the ion beam system development, the following three key factors [73] are generally important: a) production of the ions which one wants to use, b) control of the ions with electric or magnetic field and transport them to the place where the process takes place, and c) control of the final energy and quantity of the ions. When we see the LMIS and its system, they have incompleteness in all of the above key factors. For example, on the ion source design, there is no guide to select source materials when one wants to have a certain ion species. This is entirely due to the fact that the ionization mechanism of the LMIS is not fully understood. Although the ionization mechanism is believed to be field evaporation [5], the arguments have been restricted to the very small current regime. As for the high current regime, we do not have any concrete model. Only a little amount of data is available at high current regime, because the researches who focused on the high current application have their basis on military application, and thus the disclosed information is not so much. So we should first collect the ion emission data in a wide current range. To transport the ions extracted from the LMIS to a distant place, convergence of the different beam is necessary. Since the ion beam extracted from the LMIS has a large divergence with a half angle of up to 40° [74], a conventional lens system does not work well for effective focusing of the ion beam. Even though the ion beam is effectively transported, the absolute value of the ion current is approximately several hundreds of microamps from a single point source and is still insufficient. For use in various kinds of applications, for example thin film formation, intensification of the ion source is necessary. In the following, the author further discusses these subjects and shows the way to solve the problems.

1.2.2   Establishment of model for ion source operation

In contrast to the interest in application of LMIS's, less intensive studies were performed to establish the theoretical model including ionization mechanism. So far, experimental results were compared with the field evaporation theory [75–77] developed for an atom probe. At present, the model of the ionization and related issues proposed by Swanson and Kingham [78] may be a probable candidate for the understainding of the LMIS. Figure 1.8 shows the schematic diagram of the ionization mechanisms around the tip apex [5,78]. The entire shape is approximated by the "Taylor-cone" [1]. They insist that the jet-like protrusion, which has been observed by transmission electron microscope [3,79,80] is formed on the Taylor cone owing to the balance between surface tension stress S_T and electric field stress S_F. The major ionization process is considered to be field evaporation [81] and subsequent process is field ionization [82,83], which is owing to the production of thermally evaporated atoms from the liquid shank. However, there is no quantitative description on this field evaporation. Doubly charged ions are considered to be formed by post-ionization [84,85]. The post-ionization theory gives the electric field at the apex from the charge state distribution, however, we do not know the current density because the theory does not give the current density. In their model, singly charged dimer ions are generated mostly by field ionization. In order to achieve the ion current of one-tenth of the field evaporated ions, the pressure required around the liquid apex should be so large that this model is not plausible. Detailed quantitative arguments will be made in Chapter 3. In Table 1.2, the author summarized the ionization mechanism for some ion species and discrepancies of these mechanisms.

In order to further understand the singularity of the LMIS, the author compares the LMIS with the plasma-type ion sources from the ion source engineering point of view. Generally, the ion source itself can be divided into three major parts due to its function: 1) feeding of material to be ionized, 2) ionization, and 3) extraction and beam formation [86]. These three functions are closely related each other, but we can primarily argue each segment separately in the usual cases. For example, the material to be ionized is fed as vapor from a furnace and we can control the quantity of the vapor by adjusting heating power. This control is independent of the ionization process, which is dominated by the arc voltage and current. Also for an ion extraction, we must be careful of the design of the extractor so as to match the generated plasma with an appropriate ion optics, but we can determine extraction field in accordance with the plasma density and electron temperature [87].

In the case of the LMIS, however, these three functions are concentrated on the liquid apex [18]. It is an inherent character due to the simplicity of the LMIS. Figure 1.9 shows the schematic drawing of the parameters related to the ionization mechanism and parameters that we can observe in the LMIS. Many parameters such as the apex radius r_a, the electric

field ionization of neutrals
produces M⁺ and singly
charged clusters

polarization forces
attract some
neutrals

some neutrals
escape

possible post-ionization to
M²⁺, M³⁺ and doubly
charged clusters

field evaporation
mainly M⁺
some clusters M₂⁺, M₃⁺ etc.

thermal evaporation
of neutral atoms
and clusters

~10 Å
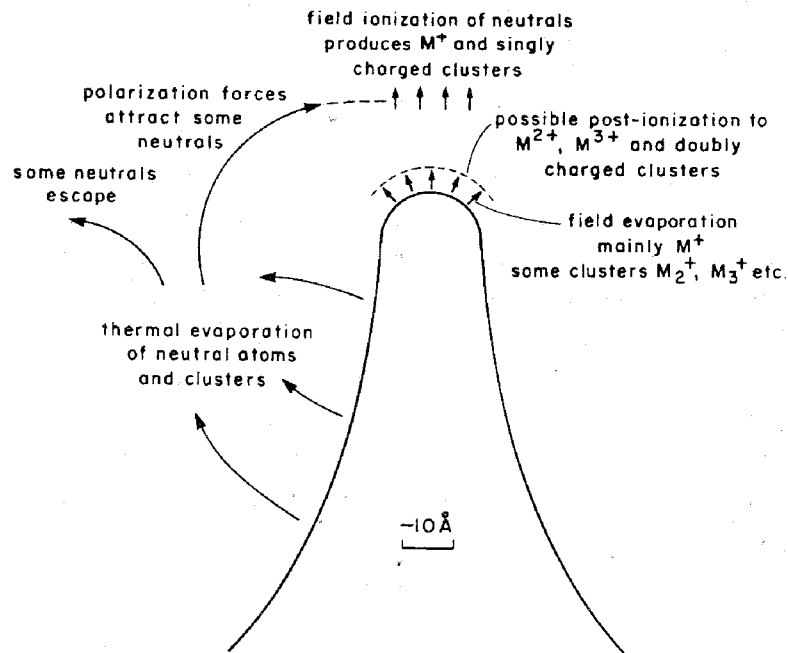
Figure 1.8: Proposed ionization mechanisms of LMIS (after Swanson and Bell) [5].

Table 1.2: Ionization mechanism for different ion species proposed by Swanson and Bell[5].

Ion species	Ionization mechanism	Question
Singly charged atomic ions	Field evaporation	Rate of ionization ?
Doubly charged atomic ions	Post-ionization	
Singly charged dimer ions	Mostly field ionization	Absolute current?

field strength F, the jet length ℓ, the temperature at the apex T_a, and the current density J are automatically adjusted under a given voltage V and a given electrode configuration. We must solve the following equation with the ion current I_i,

$$I_i = V(r_a, J, F, \ell, T_a). \tag{1.1}$$

It may be easy to solve the equation if we had several relations of current-voltage characteristics. But the equation could be solved only when the formulation is defined. In the present case, however, the relations among these parameters are complicated, thus it is difficult to determine the formulation. Ishitani *et al.* claimed that the material of which composition is dominated by that with higher surface tension γ achieves the higher electric field [88]. However, it is difficult to say this because an element with higher γ value generally has also a high evaporation field F_{ev} as shown in Fig. 1.10. The abscissa and ordinate of Fig. 1.10 are γ and F_{ev}, respectively. These two parameters are almost in proportion each other. The Ishitani *et al.*'s claim can be interpreted also as the material with higher F_{ev} achieves higher operating field.

If we want to know the relation between J and F, we usually express the relation using series expansion,

$$J = \sum_{i=-\infty}^{\infty} a_i F^i. \tag{1.2}$$

Accumulation of data of J and F, in this case, will define the formulation of J and F. One of the difficulties in determining these coefficients, a_i, is such that we can not obtain the direct relation between J and F for the case of LMIS. We must start with a simple relation between V and I_i. In the present dissertation, the author derives the empirical relation between J and F from the relative intensity of the doubly charged ions and singly charged ions. A unique phenomenon, reduction of J with an increase in I_i was observed in the present study. The author examines the conditions that produce such a relation.

1.2.3 Transport of divergent ion beam

Although the LMIS is a point source, but full use of the ion beam is not easy. As reported by many researchers, an ion beam extracted from LMIS's has a large divergence together with a wide energy spread, thus effective focusing of such a beam is an essential subject in transporting the beam. Generally, a point source, which means a source with a negligible emittance, is preferred for focusing, as is seen in the development of FIB machines. However, when we want to use all the ions including the marginal beam, focusing becomes difficult due to spherical aberration. The spherical aberration is caused by the difference of the focal length for the beamlets with different initial angles, as shown in Fig. 1.11(a). Since the spherical aberration is proportional to the third power of the emission angle [89],
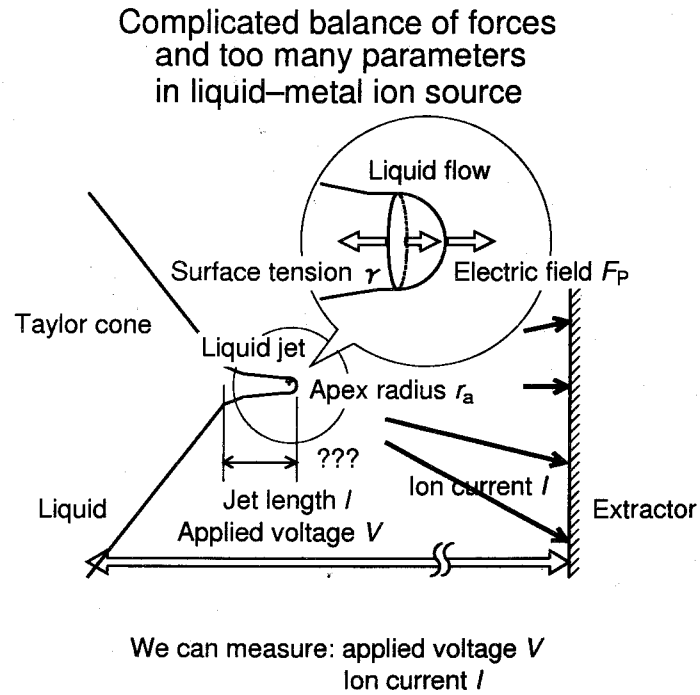
Figure 1.9: Schematic drawing of parameters and parameters that we can observe.
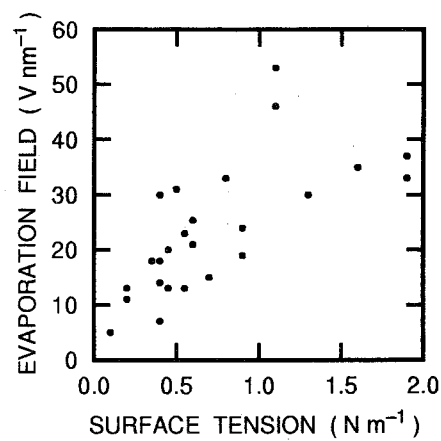
Figure 1.10: Relation between surface tension and evaporation field.
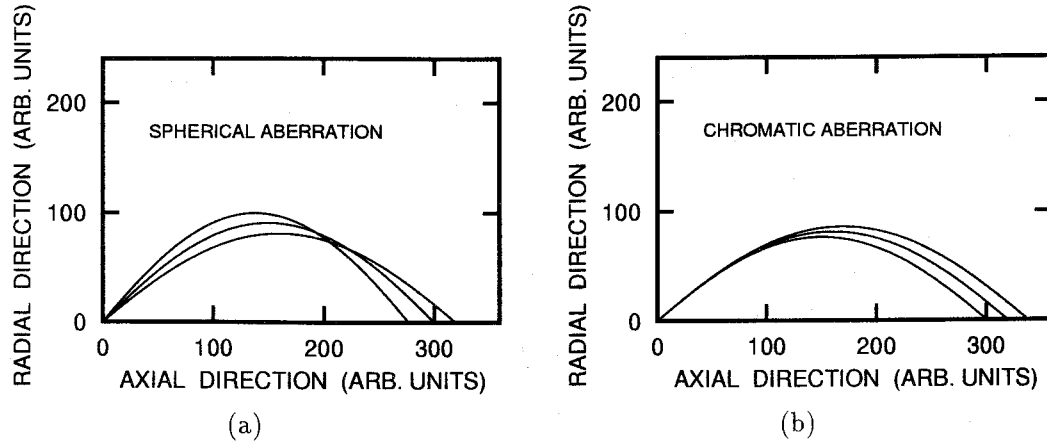
Figure 1.11: Schematic drawing of the effect of two major aberrations in LMIS. (a) Spherical aberration and (b) chromatic aberration.

the effective focusing of a strongly divergent beam becomes difficult. Furthermore, LMIS's have a fairly wide energy spread at a high current regime, this causes a deterioration of focusing property due to chromatic aberration, of which concept is illustrated in Fig. 1.11(b). To achieve a highly efficient metal ion beam facility, it is necessary to demonstrate that almost all ions are to be transported to the target. In the facilities made with LMIS's so far, effective focusing of divergent beam was not intended; it is not necessary to take care of ejected ions except charge neutralization in ion thruster, and some deposition experiments were done with a conventional cylinder lens system.

To converge a strongly divergent beam, it is necessary to focus it at the very early stage of its divergence, otherwise the beam diameter will become too large to be transported. To change the direction of the ion motion, one of the effective ways is to apply the electric field to these ions where the velocity of is very slow. The author designed the lens system in which ions are first decelerated just after extraction, and then accelerated inward the lens. It is also necessary to demonstrate the effective transport with mass separation.

1.2.4   Intensification of ion source

Seeing the feasibility of the LMIS with a single emission point, it is necessary to intensify the ion source itself. Further intensification with a single emission point is not possible, due to instability of liquid cone. Ion emission from multiple points should be realized, as has already done for the ion thruster [30]. However, as seen in Fig. 1.12, the available materials are restricted to mercury and cesium, or organic solutions [90], which can not be
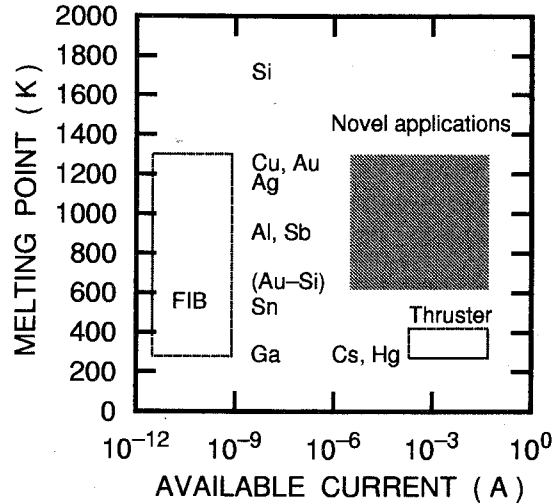
Figure 1.12: The range of available current and materials which is expected as novel applications. The materials of which melting point is included in the hatched region will be available.

used in the electronic device fabrication. While the FIB technology did not develop any high current LMIS, although it developed wide variety of ions. From this point of view, such a high current LMIS in which the metal with a high melting point is available, should be developed.

Considering an ion beam system, formation of a sheet beam is expected because of mass separation. Thus, ion emission points should be arranged in a line. To obtain 10 mA class ion source, which is comparable to the conventional metal ion sources [37], several tens emission points are required, as demonstrated later. There are some difficulties to develop such an ion source: (1) heating of the ion source, and (2) uniform field formation at each apex, and so on. As well as the development of the intense metal ion source, the lens system for arrayed, divergent beam is necessary. To develop such a lens system, detailed measurement of the ion beam characteristics extracted from array sources is required because no report on this issue is found in the literature.

If these problems are solved, LMIS will play an important role in the materials science, as well as in the other application fields.
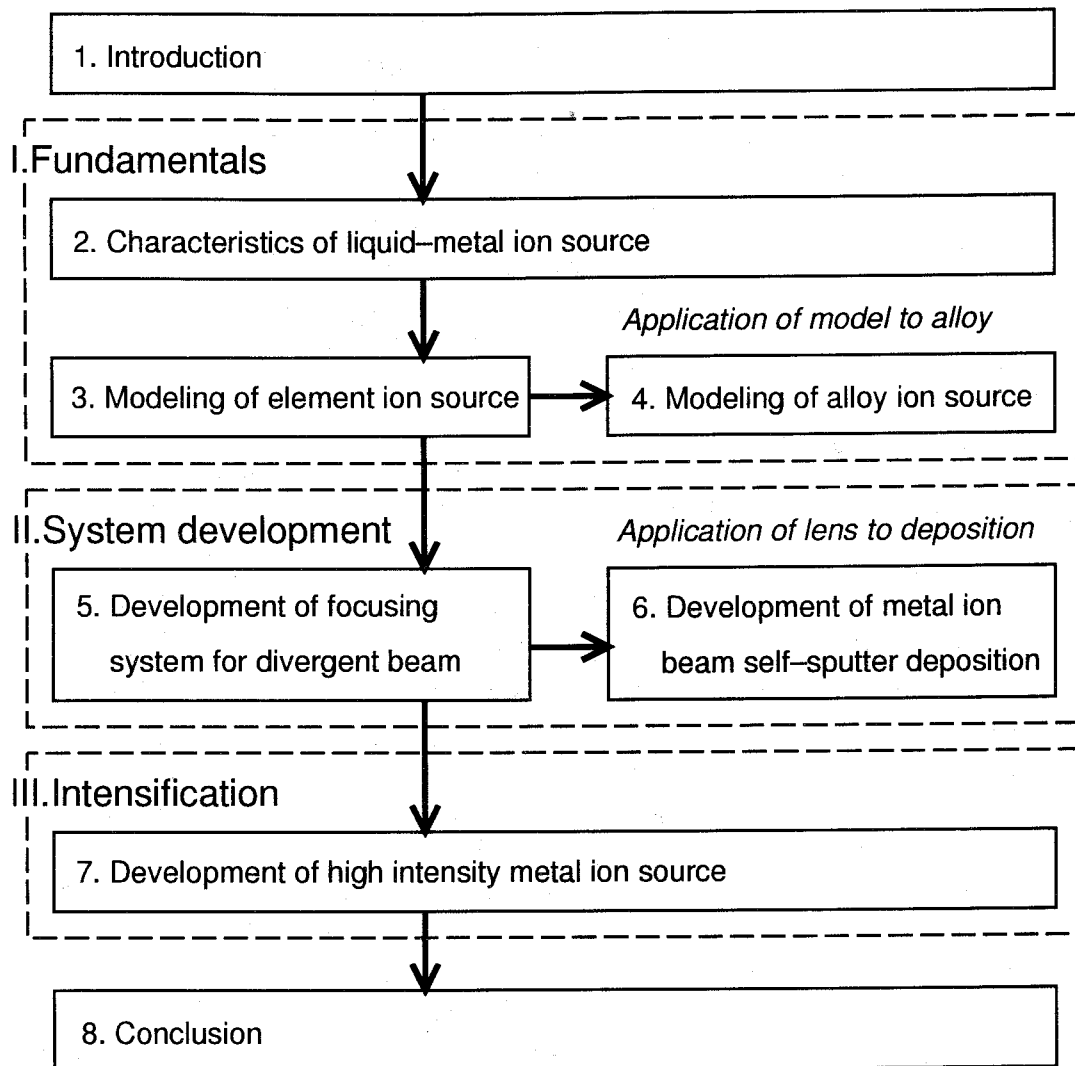
Figure 1.13: Flow chart of the present research.

1.3   Research flow of the present dissertation

The present dissertation aims the development of high current ion beam processing systems that can provide novel applications with the LMIS's. Consequently, these systems are novel ion beam systems that have never been developed. Figure 1.13 shows the flow chart of the present research. The present dissertation is divided into three major parts: (a) fundamentals of the LMIS, (b) development of the systems for a single point source, and (c) intensification of the LMIS by multipoint emission. In the first two parts, the author describes primarily on the LMIS with a single emission point. Characterization and modeling of the LMIS is given in the first part. In the second part, and the author shows the way to converging the divergent ion beam and its application. The last part is given as a consequence of the second part, the author constructs high current LMIS's with multiple emission points. Details of each part are described below.

First, in Chapter 2, the author characterizes the nature of the ion beam extracted from LMIS's with element metals. It is shown that the ratio of the ion current of the doubly charged ions with respect to that of singly charged ions, decreased with an increase in the source current. The author derives the empirical formulation of its charge state in the same chapter [91]. Some argument on the ionization mechanism [92-94] is given in Chapter 3 on the basis of the results obtained in Chapter 2. The author starts with the equations of the space charge limited current and the fluid dynamic equation at the liquid apex, and derives a criterion for the decrease of the F at the apex. It is shown that weaker dependence of J on F as compared with the conventional theory is necessary. The author concludes that the ionization at a high current regime is primarily due to the field evaporation but with an extremely high local temperature. Also the author gives an analysis of the operation of alloy sources in Chapter 4 [59, 95, 96]. Incorporation of heterogeneous element gives us a useful information on the ionization mechanism, and shows that the hypotheses made in Chapters 2 and 3 also holds for the alloy sources. And the same time, the author gives a guide to select source material for a given element.

After obtaining the information of the source, the author develops the lens system [95, 97] which converges the divergent beam extracted from the LMIS, as will be described in Chapter 5. Physically asymmetric lens system is designed and the performance of the lens is evaluated with a computer simulation and experiments. An ion implantation system is designed on the basis of the designed lens system. A unique implantation experiment of "molecular ion implantation" is also demonstrated. In Chapter 6, the author demonstrates a novel ion beam processing of metal ion beam self-sputter deposition (MIBSSD) [98] using the lens system developed in Chapter 5. Replacing the conventional gas type ion source by a LMIS, ion beam sputtering becomes fully UHV compatible, and pure metal film formation will be possible. This MIBSSD is one of the processes that produce a large amount of

atoms which has a kinetic energy appropriate for thin film formation. This is one of the solutions for the huge space charge problem in transporting the particles with the kinetic energy of 10 – 20 eV. In the present case, Cu was used.

In Chapter 7, the author develops high current ion sources with multiple tip-and-reservoirs (TAR's) [99–103]. Some technological difficulties are first argued and the solutions for these problems are given with some different versions of the preliminary test ion sources. The author examines some different problems due to the multipoint emission high current sources. The source materials chosen are Au, Ge, Cu and In. The author finally designs and construct a high current ion sources with multiple TAR's with series load. The In ion current of 9.1 mA was obtained from the 39-point source. The lens system suitable to this high current source is also developed and the formation of a sheet beam is demonstrated. Finally in Chapter 8, the author concludes the present dissertation and will give a future prospect of the LMIS technologies.

References in Chapter 1

[1] G. Taylor: Proc. Roy. Soc. (London) A **280** (1964) 383.

[2] A. E. Bell and L. W. Swanson: Appl. Phys. A **41** (1986) 335.

[3] H. Gaubi, P. Sudraud, M. Tencé and Van de Walle: *Proc. of 29th Field Emission Symposium*, Göteberg, Sweden, eds. H. O. Audren and H. Norden (Stockholm, Almqvist and Wiksell, 1982) p.357.

[4] V. E. Krohn: Prog. Astronaut. Rocketry **5** (1961) 73, through R. Clampitt and D. K. Jefferies: Nucl. Instrum. Meth. **149** (1978) 739.

[5] L. W. Swanson and A. E. Bell: *Liquid Metal Ion Sources*, in *The Physics and Technology of Ion Sources*, ed. I. G. Brown (John Wiley and Sons, New York, 1989) Chapter 15, p.313.

[6] A. Wagner and T. M. Hall: J. Vac. Sci. Technol. **16** (1979) 1871.

[7] V. E. Krohn and G. R. Ringo: Appl. Phys. Lett. **27** (1975) 479.

[8] T. Noda, T. Okuwaki and H. Tamura: Oyo Butsuri (Applied Physics) **54** (1985) 935 [in Japanese].

[9] J. Ishikawa and T. Takagi: J. Appl. Phys. **56** (1984) 3050.

[10] A. Wagner: Appl. Phys. Lett. **40** (1982) 440.

[11] J. F. Mahoney, A. Y. Yahiku, H. L. Daley, R. D. Moore and J. Perel: J. Appl. Phys. **40** (1969) 5101.

[12] R. Clampitt and D. K. Jefferies: *Molten metal field ion sources, Inst. Phys. Conf. Ser.* No.38 (IOP, Bristol, 1978) Chapter 1, p. 12.

[13] R. L. Seliger, J. W. Ward, V. Wang and R. L. Kubena: Appl. Phys. Lett. **34** (1979) 310.

[14] R. L. Kubena, F. P. Stratton, J. W. Ward, G. M. Atkinson and R. J. Joce: J. Vac. Sci. Technol. B **7** (1989) 1798.

[15] T. Ishitani, H. Tamura and H. Todokoro: J. Vac. Sci. Technol. **20** (1982) 80.

[16] T. Ishitani, K. Umemura and H. Tamura: Nucl. Instrum. Meth. **218** (1983) 363.

[17] E. Miyauchi, H. Arimoto, H. Hashimoto, T. Furuya and T. Utsumi: Jpn. J. Appl. Phys. **22** (1983) L287.

[18] Y. Gotoh: *Analysis of Liquid-Metal Ion Sources and Transport of Intense Ion Beam*, M. E. Thesis, Kyoto University 1987 [in Japanese].

[19] N. K. Kang and L. W. Swanson: Appl. Phys. A **30** (1983) 95.

[20] Seiko Instruments, Commercial catalog SMI9200, 1999.

[21] Y. Gotoh, K. Inoue, T. Ohtake, H. Ueda, Y. Hishida, H. Tsuji and J. Ishikawa: Jpn. J. Appl. Phys. **33** (1994) L63.

[22] Y. Gotoh, T. Ohtake, N. Fujita, K. Inoue, H. Tsuji and J. Ishikawa: J. Vac. Sci. Technol. B **13** (1995) 456.

[23] J. Ishikawa, T. Ohtake, Y. Gotoh, H. Tsuji, N. Fukayama, K. Inoue, S. Nagamachi, Y. Yamakage, M. Ueda, H. Maruno and M. Asari: J. Vac. Sci. Technol. B **13** (1995) 452.

[24] Y. Gotoh, N. Fujita, H. Tsuji, J. Ishikawa, S. Nagamachi and M.Ueda: J. Micromech. and Microeng. **9** (1999) 364.

[25] M. Takai, T. Kishimoto, H. Morimoto, Y. K. Park, S. Lipp, C. Lehrer, L. Frey, H. Ryssel, A. Hosono and S. Kawabuchi: Microelectron. Eng. **41/42** (1998) 453.

[26] J. Orloff: Rev. Sci. Instrum. **64** (1993) 1105.

[27] P. D. Prewett and G. L. R. Mair: *Focused Ion Beams from Liquid Metal Ion Sources* (John Wiley and Sons, New York, 1991).

[28] P. M. Read, J. T. Maskrey and G. D. Alton: Rev. Sci. Instrum. **61** (1990) 502.

[29] O. Sakamoto, E. Iwamoto, J. Ishikawa and T. Takagi: Nucl. Instrum. Meth. B **54** (1991) 75.

[30] R. Clampitt and D. K. Jefferies: *Proc. of Electric Propulsion and Its Space Applications*, Toulouse, June 21-23, 1972 (1972) p.145.

[31] R. Clampitt: Nucl. Instrum. Meth. **189** (1981) 111.

[32] P. J. Billquist and J. L. Yntema: Nucl. Instrum. Meth. **178** (1980) 9.

[33] K. Brand: Nucl. Instrum. Meth. **154** (1978) 595.

[34] C. Bartoli, H. von Rohden, S. P. Thompson and J. Blommers: J. Phys. D. **17** (1984) 2473.

[35] J. Mitterauer: IEEE Trans. on Plasma Science **PS-15** (1987) 593.

[36] H. R. Kaufman: NASA Tech. Note D-585 (1961).

[37] D. Aitken: *Freeman Ion Sources*, in *The Physics and Technology of Ion Sources*, ed. by I. G. Brown (Wiley and International, New York, 1989) Chapter 9, p.187.

[38] M. Yamashita: J. Vac. Sci. Technol. A **7** (1989) 151.

[39] P. D. Prewett: *Proc. 10th Symposium on Ion Sources and Ion Assisted Technology ISIAT'85*, June, Tokyo, 1985 (The Research Group of Ion Engineering, Kyoto, 1985) p.585.

[40] C. A. Evans, Jr. and C. D. Hendrickes: Rev. Sci. Instrum. **43** (1972) 1527.

[41] R. Levi-Setti and T. R. Fox: Nucl. Instrum. Meth. **168** (1980) 139.

[42] A. Wagner: Nucl. Instrum. Meth. **218** (1983) 355.

[43] R. Levi-Setti, P. LaMarche, K. Lan, T. H. Shields and Y.-L. Wang: Nucl. Instrum. Meth. **218** (1983) 368.

[44] A. R. Bayly, A. R. Waugh and K. Anderson: Nucl. Instrum. Meth. **218** (1983) 375.

[45] R. E. Thurstans and J. Wolstenholme: Vacuum **37** (1987) 289.

[46] J. Ishikawa, H. Tsuji, K. Kameyama, S. Shimada and Y. Gotoh: Appl. Surf. Sci. **100/101** (1996) 370.

[47] R. Clampitt: Thin Solid Films **64** (1979) 471.

[48] P. D. Prewett, L. Gowland, K. L. Aitken and C. M. O. Mahony: Thin Solid Films **80** (1981) 117.

[49] A. Wagner, T. Vankatesan, P. M. Petroff and D. Barr: J. Vac. Sci. Technol. **19** (1981) 1186.

[50] S. Sakai, M. Takahashi and M. Tanjyo: Rev. Sci. Instrum. **71** (2000) 960.

[51] S. Goto, M. Ikeda and I. Hara Ed.: *Sangyo Chudoku Binran, Zoho-ban (Handbook of Industrial Toxication, First Supplement)* (Ishiyaku Shuppan, Tokyo, 1981) [in Japanese].

[52] V. Wang, J. W. Ward and R. L. Seliger: J. Vac. Sci. Technol. **19** (1981) 1158.

[53] K. Gamo, T. Ukegawa, Y. Inomoto, Y. Ochiai and S. Namba: J. Vac. Sci. Technol. **19** (1981) 1182.

[54] E. Miyauchi, H. Hashimoto and T. Utsumi: Jpn. J. Appl. Phys. **22** (1983) L225.

[55] T. Ishitani, K. Umemura and H. Tamura: Jpn. J. Appl. Phys. **23** (1984) L330.

[56] T. Ishitani, K. Umemura, S. Hosoki, S. Takayama and H. Tamura: J. Vac. Sci. Technol. A **2** (1984) 1365.

[57] H. Arimoto, A. Takamori, E. Miyauchi and H. Hashimoto: Jpn. J. Appl. Phys. **23** (1984) L165.

[58] G.-M. Chen, Y. Gotoh, H. Tsuji, J. Ishikawa and T. Takagi: *Proc. 9th Symp. on Ion Sources and Ion-Assisted Technology ISIAT'85*, Tokyo, June 3-5, 1985 (The Research Group of Ion Engineering, Kyoto, 1985) p.81.

[59] Y. Gotoh, H. Tsuji and J. Ishikawa: Jpn. J. Appl. Phys. **35** (1996) 3670.

[60] H. Arimoto, E. Miyauchi and H. Hashimoto: Jpn. J. Appl. Phys. **26** (1987) L253.

[61] W. M. Clark, Jr., R. L. Seliger, M. W. Utlaut, A. E. Bell, L. W. Swanson, G. A. Schwind and J. B. Jergenson: J. Vac. Sci. Technol. B **5** (1987) 197.

[62] H. Arimoto, E. Miyauchi and H. Hashimoto: Jpn. J. Appl. Phys. **26** (1987) L253.

[63] R. G. Wilson: *Ion Mass Spectra* (John Wiley and Sons, New York, 1974).

[64] Y. Gotoh, H. Kubo, H. Tsuji and J. Ishikawa: Rev. Sci. Instrum. **71** (2000) 1160.

[65] J. Ishikawa, Y. Takeiri and T. Takagi: Rev. Sci. Instrum. **55** (1984) 449.

[66] Y. Jongen and C. M. Lyneis: *Electron Cyclotron Resonance Ion Sources*, in I. G. Brown ed. it The Physics and Technology of Ion Sources (John Wiley and Sons, New York, 1989) Chapter 10, p.207.

[67] E. D. Donets: *Electron Beam Ion Sources*, in I. G. Brown ed. *The Physics and Technology of Ion Sources* (John Wiley and Sons, New York, 1989) Chapter 12, p.245.

[68] I. G. Brown: *The Metal Vapor Vacuum Arc Ion Source*, in I. G. Brown ed. *The Physics and Technology of Ion Sources* (John Wiley and Sons, New York, 1989) Chapter 16, p.331.

[69] K. Sakaguchi, K. Mihama and Y. Saito: J. Appl. Phys. **70** (1991) 5049.

[70] C. W. Hu, A. Kasaya, A. Wawro, N. Horiguchi, R. Czajka, Y. Nishina, Y. Saito and H. Fujita: Mater. Sci. Eng. A **A217/218** (1996) 103.

[71] J. Ishikawa, Y. Takeiri, K. Ogawa and T. Takagi: J. Appl. Phys. **61** (1987) 2509.

[72] T. Takagi: *Ionized Cluster Beam Deposition and Epitaxy* (Noyes Publications, Park Ridge, 1988).

[73] Y. Gotoh: *Ion Biimu Gijutsu, (Ion Beam Technology)*, Chapter 2, Section 5, in *Zukai Hakumaku Gijutsu (Illustrated Thin Film Technology)*, eds. M. Mashita, T. Hata and I. Kojima (Baifukan, Tokyo, 1999) p.45 [in Japanese].

[74] P. D. Prewett, D. K. Jefferies and T. D. Cockhill: Rev. Sci. Instrum. **52** (1981) 562.

[75] D. G. Brandon: Surf. Sci. **3** (1964) 1.

[76] T. T. Tsong: Surf. Sci. **70** (1978) 211.

[77] T. T. Tsong: *Atom-Probe Field Ion Microscopy* (Cambridge University Press, Cambridge, 1990).

[78] L. W. Swanson and D. R. Kingham: Appl. Phys. A **41** (1986) 223.

[79] G. Benassayag, P. Sudraud and B. Jouffrey: Ultramicroscopy **16** (1985) 1.

[80] B. Praprotnic, W. Dreisel, Ch. Dietzsch and H. Niedrig: Surf. Sci. **314** (1994) 353.

[81] R. G. Forbes: Vacuum **48** (1997) 85.

[82] R. Gomer: Appl. Phys. **19** (1979) 365.

[83] D. R. Kingham and L. W. Swanson: Appl. Phys. A **41** (1986) 157.

[84] N. Ernst and Th. Jentsch: Phys. Rev. B **24** (1981) 6234.

[85] D. G. Kingham: Surf. Sci. **116** (1982) 273.

[86] J. Ishikawa: *Iongen Kogaku (Ion Source Engineering)* (Aionikusu, Tokyo, 1985) [in Japanese].

[87] R. G. Wilson and G. R. Brewer: *Ion Beams with Application to Ion Implantation* (John Wiley and Sons, New York, 1973).

[88] T. Ishitani, K. Umemura and Y. Kawanami: J. Appl. Phys. **61** (1987) 748.

[89] Nihon Gakujutu Shinkokai Ed.: *Denshi Ion Biim Handobukku Dai 2-Han (Electron and Ion Beam Handbook, 2nd Edition* (Nikkan Kogyo Shinbun, Tokyo, 1986) [in Japanese].

[90] P. D. Kidd: J. Spacecraft **5** (1968) 1034.

[91] Y. Gotoh, T. Kashiwagi, H. Tsuji and J. Ishikawa: Appl. Phys. A **64** (1997) 527.

[92] Y. Gotoh, H. Tsuji and J. Ishikawa: Appl. Surf. Sci. **146** (1999) 377.

[93] Y. Gotoh, H. Tsuji and J. Ishikawa: Rev. Sci. Instrum. **71** (2000) 725.

[94] Y. Gotoh, H. Tsuji and J. Ishikawa: Ultramicroscopy **89** (2001) 69.

[95] J. Ishikawa, Y. Gotoh, H. Tsuji and T. Takagi: Nucl. Instrum. Meth. B **21** (1987) 186.

[96] Y. Gotoh, H. Tsuji and J. Ishikawa: Ultramicroscopy **73** (1998) 83.

[97] Y. Gotoh, H. Tsuji and J. Ishikawa: Rev. Sci. Instrum. **71** (2000) 780.

[98] Y. Gotoh, T. Amioka, H. Tsuji and J. Ishikawa: Rev. Sci. Instrum. **67** (1996) 1996.

[99] J. Ishikawa, H. Tsuji and Y. Gotoh: Nucl. Instrum. Meth. B **55** (1991) 343.

[100] Y. Gotoh, N. Fukayama, H. Tsuji and J. Ishikawa: Rev. Sci. Instrum. **63** (1992) 2438.

[101] J. Ishikawa, Y. Gotoh, N. Fukayama, Y. Ogata, K. Yoshida and H. Tsuji: Vacuum **44** (1993) 357.

[102] Y. Gotoh, J. Ishikawa, H. Tsuji, N. Fukayama and Y. Ogata: Nucl. Instrum. Meth. B **74** (1993) 35.

[103] Y. Gotoh, K. Yoshida, T. Kawai, N. Fukayama, Y. Ogata, H. Tsuji and J. Ishikawa: Rev. Sci. Instrum. **65** (1994) 1351.

Part I

Fundamentals of
liquid-metal ion sources

Chapter 2
Characteristics of liquid-metal ion sources

In this chapter, the author shows the experimental results on the analysis of ion beams extracted from single emission-point sources with some element source materials. In order to design the ion beam systems, information on ion current density, radial ion distribution, energy spread, and mass spectrum should be investigated. Besides for the above purpose, the mass spectra give us useful information that reflects the physical phenomena occurring at the ionization point. One of the interesting finding is that the ion flux ratio of doubly charged ions to singly charged ions decreases with an increase in the source current, that is, extraction voltage. The author estimates the electric field at the ionization point on a basis of the conventional field evaporation theory. After emphasizing the discrepancy between the experiments and the theory, the author introduces an assumption with which the theory agrees well with the experiments.

2.1 Configuration of the liquid-metal ion source

Liquid-metal ion sources used in the present chapter and throughout the study were an impregnated-electrode-type (IELMIS) [1]. The reason why this type of ion source was employed, is its capability of providing high current and also use of wide variety of ions [1]. In this chapter together with Chapter 4 and 5, an ion emission tip with a single point was used. The ion emitter is composed of a cylindrical reservoir made of tungsten (W), and porous region, which is machined to have a conical tip for ion emission, as shown in Fig. 2.1(a). The outer diameter of the reservoir was approximately 2 mm and the diameter was reduced toward the tip. The tip was rather thick as compared with the conventional needle-type ion source that has a diameter of typically 0.3 – 0.6 mm. Figure 2.1(b) has a rectangular reservoir and this tip will be used for the high current ion source. The author will describe the latter source later in Chapter 7.

The schematic figure of the entire ion source is shown in Fig. 2.2. The tip-and-reservoir (TAR) is fixed with knife-edged electrodes at two points. The knife-edged electrodes introduce heating current with an advantage that the point contact allows a large current flow but does not allow transfer of heat [2]. At the upper site, the reservoir was fixed with four knife-edged electrodes and at the lower site, with two knife-edged electrodes. In order to
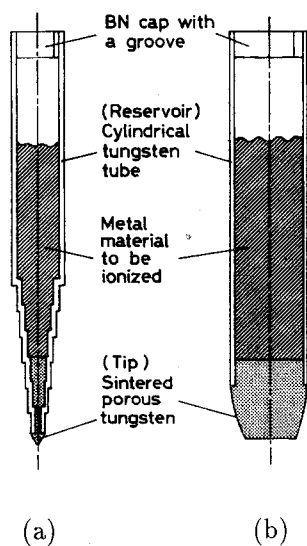
Figure 2.1: Schematic diagram of the tip-and-reservoir used in the present study. (a) single point source with cylindrical reservoir, and (b) multi-point source with rectangular reservoir.
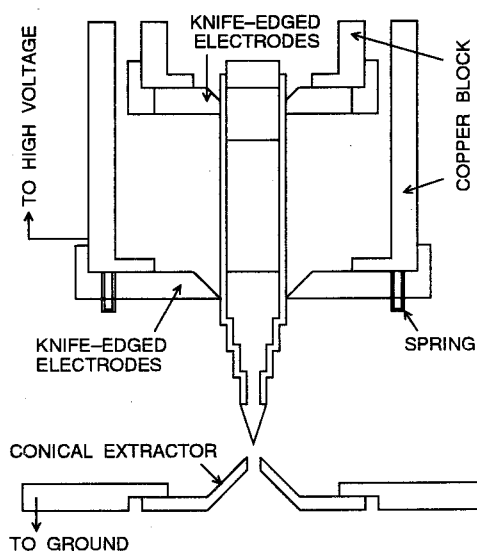
Figure 2.2: Schematic diagram of the impregnated-electrode-type liquid-metal ion source.

release the stress due to the expansion of reservoir at the temperature higher than 1000°C, springs made of thin stainless steel were inserted [3].

All the experiments were done in the vacuum vessels that were evacuated by an oil diffusion pump with a liquid nitrogen trap. The residual gas pressure was approximately 10^{-4} Pa. The extraction region can be observed through a view port to confirm the source temperature or the extraction gap. The investigations were made for the purpose of the collection of beam characteristics at relatively higher current as compared with FIB technologies. The range was almost 1 to 200 μA of the source current. The detailed observation enabled us to perform analysis on the ion emission site.

2.2   Current-voltage characteristics

The ion current was measured with a Faraday cup just below the ion source. For a single emission point source, negative bias of 90 V was applied to the suppressor to eliminate the secondary electrons from escaping out the collector. Ion current I_i is defined by the collector current. The source current I_s is defined by the current that flows from the ion emitter. I_s involves the current of the secondary electrons which are produced at the extractor and get back toward the emitter. Although I_s is not the exact ion current, I_s represents the total emission current. Most of the current-voltage ($I_i - V_{ext}$) characteristics of the present chapter is measured with a conical extractor with an aperture of 2 mm. The source temperature T_s was monitored by a pyrometer. T_s was defined by the temperature of the reservoir just below the lower knife-edged electrode.

Figure 2.3(a) shows the $I_i - V_{ext}$ characteristics of the In ion source. The ion emission started at the threshold voltage V_{th} of 7.4 kV. As the V_{ext} increased, I_i increased. Reducing V_{ext} below V_{th}, it was possible to observe ion emission. This threshold V_{th} is determined by the break in the balance between S_T and S_F [4]. The source could provide up to 400 μA. At I_i of 400 μA, I_s was almost 3 mA. Similar characteristics were obtained for the impregnated-electrode-type Ag ion source [1], and currents more than 300 μA were observed for the impregnated-electrode-type Ga, Au, and Cu ion sources in the present study. This current is larger than most of the needle-type sources, whose upper limit of I_s is generally several tens microamps [4]. Realization of this large current is due to the control of the liquid flow at the porous region [1]. If the liquid is transported along the surface of the needle, flow impedance is fairly large, only small current would be obtained [5]. The capability of this large ion current is important in arguing the ion emission mechanism later in Chapter 3. The change in the slope of $I_i - V_{ext}$ curve at 10 – 11 kV is attributed to the increase in T_s due to the significant heating by electron bombardment of the emitter, and subsequent reduction of viscosity of the liquid. The raise in the temperature could be
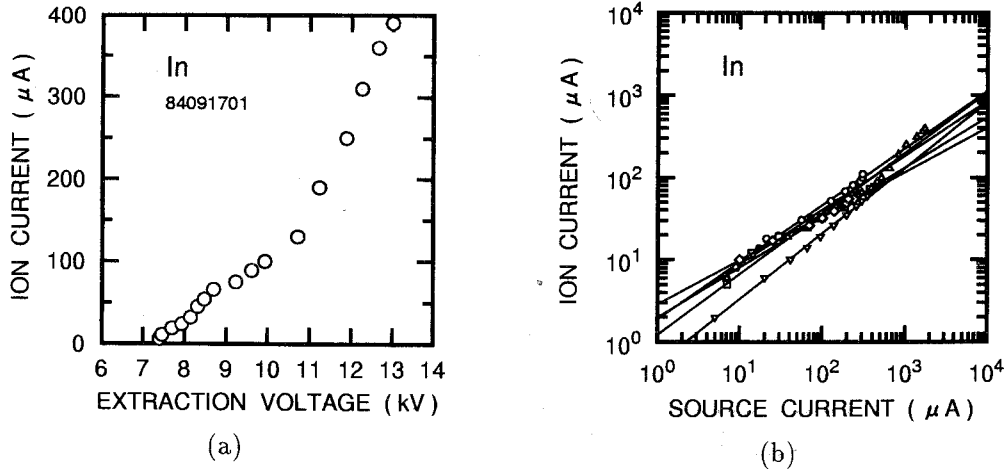
Figure 2.3: Current-voltage characteristics of the In ion source. (a) $I - V$ curve and (b) relation between I_i and I_s.

visually observed, and found to be 700°C. It should be noted that an excess increase of I_s allow increase of the reservoir temperature. However, at the lower current, heating was not significant.

The relationships between I_i and I_s for several runs are shown in Fig. 2.3(b). I_i/I_s determines the efficiency of the power supply. Although the extraction configurations differ among these data, many runs exhibited that the relation between I_s and I_i is given by

$$I_i \propto I_s^{0.6 \sim 0.7}. \tag{2.1}$$

This implies that operation at a higher current reduces the efficiency of this ion source. It should also be noted that I_i is almost the same value with I_s at 1 - 10 μA.

2.3 Beam profile

2.3.1 Spatial distribution of ion current

It is necessary to investigate the beam profile, current distribution along the radial direction, for designing the lens system, because LMIS's generally have a large divergence [6,7]. Beam profiles were measured by a movable Faraday cup that has a beam limiter with an aperture of 4 mm in diameter. The Faraday cup could move along two directions, each perpendicular to the other. In this experiment, the beam profile at the 31.5 mm below the ion emission point was measured along one direction.
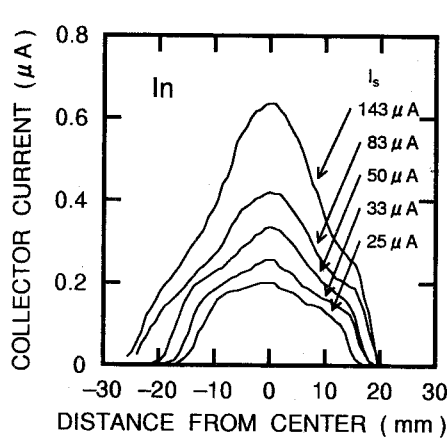
Figure 2.4: Beam profile of various source currents.
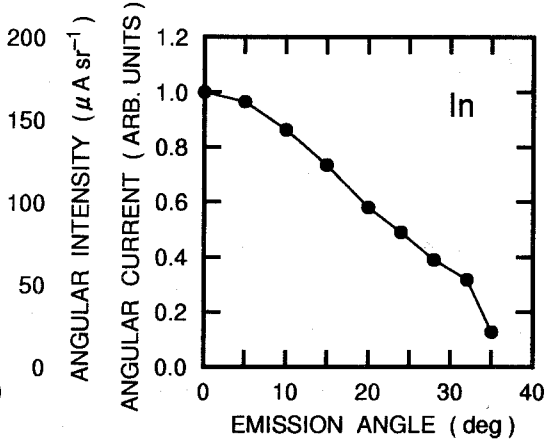
Figure 2.5: Angular current of In ion beam.

Figure 2.4 shows the beam profiles at various I_s values. The abscissa is the distance from the center and the ordinate is the ion current detected by the ion collector $I(r)$. As I_s increased, the beam profile became wider. Rapid fall down at the edge in the right-hand side is due to the shielding effect of the extractor. The width of the beam divergent half angle exceeded 30°. This value is comparable with the results reported so far [7].

Since the information which is required for the design of ion beam systems would be a radial distribution rather than a spatial distribution in Cartesian coordinates, here we convert the obtained data to the angular distribution. Generally, angular intensity which is defined by the ion current emitted in a unit solid angle is used for electron microscopes especially for such a case that the source radius or current density cannot be defined. If we neglect the optics at the extraction region, the radial current distribution in the form of angular current $I_\Omega(\theta)$ is expressed by

$$I_\Omega(\theta) = I(r)/\Omega_0 \cos\theta, \qquad (2.2)$$

where Ω_0 shows the solid angle of the ion collector used for the beam profile measurement from its normal direction. Figure 2.5 shows the angular distribution of the current of the In beam. As compared with the needle-type, the ion current is concentrated to the center. This is due to the fact that the porous cone of IELMIS forms a convergent field and ion trajectory is bent toward the axis.

2.3.2 Angular intensity along the axis

As described in eq.(2.2), it is convenient to use the ion current emitted toward a solid angle. Generally, this value is normalized by a unit solid angle, and the normalized value
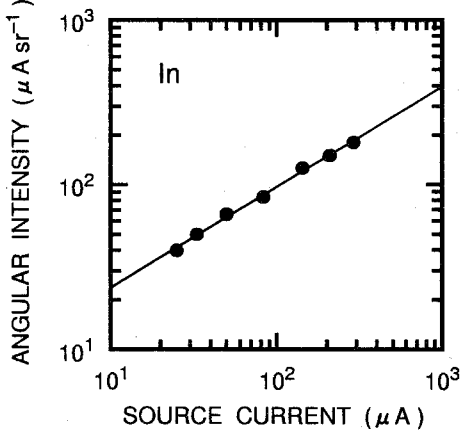
Figure 2.6: Angular intensity of In beam.   Figure 2.7: Equivalent emission area.
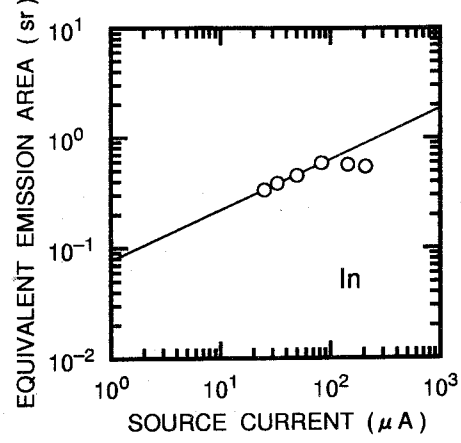
is called the angular intensity. Figure 2.6 shows the angular intensity I_{ang} of the ion beams extracted from an In ion source. The angular intensity I_{ang} depended on I_s.

$$I_{ang} \propto I_s^{0.6}.$$ (2.3)

For Ga, In, and Au, the relation between I_{ang} and I_s is approximately expressed by the above equation [8]. This relation means that the solid angle Ω of the ion emission has the following relation,

$$\Omega \propto I_s^{0.4}.$$ (2.4)

Figure 2.7 shows the effective emission solid angle Ω_{eff} as a function of I_s. Here Ω_{eff} is defined by the following formula.

$$\Omega_{eff} = \frac{1}{I_\Omega(0)} \int_0^{r_{max}} I(r) \times 2\pi dr = \frac{I_{int}(r_{max})}{I_\Omega(0)},$$ (2.5)

where r is the radial position of the ion collector, r_{max} is the maximum radial position where ion current could be observed, and $I_{int}(r_{max})$ is the total ion current. The slope of the plots is 0.46, and this value is in good agreement with the above discussion. The saturation seen at the higher current regime is due to limitation of the beam bay the extractor. The interpolation of Ω_{equ} to 1 μA gives 0.08 sr and the extrapolation of Ω_{equ} to 1 mA gives 2 sr, which correspond to the emission angle of 9.2° and 47°, respectively.

Since the extracted beam is axially symmetric, the current at the margin occupies the large portion of the total ion current. This is easily supposed from eq.(2.5). Figure 2.8 shows the integrated current along the radial position. Here the integrated current $I_{int}(r)$ is defined by

$$I_{int}(r) = \int_0^r I(r) \times 2\pi dr.$$ (2.6)
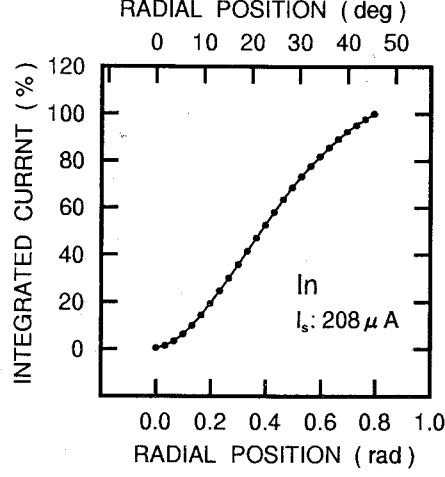
Figure 2.8: Integrated current along the radial position.

As is clearly shown, use of the ion beam within the divergent angle of 20°, only 40 % of the beam is available. Thus, to achieve effective transport of the ion beam, focusing of this divergent beam is necessary.

It should be noted that one cannot judge whether the current density increased with an increase in I_s, although I_{ang} increased with an increase in I_s. I_{ang} toward a limited solid angle Ω_N is expressed by the following formula, when the detailed extraction optics is neglected.

$$I_{ang} = Jr_a^2\Omega_N, \tag{2.7}$$

where Ω_N is the solid angle for the ion collector, r_a is the apex radius, and J is the current density. The experimental results give us only I_{ang} but not individual parameters of J and r_a. For designing the ion beam systems, it may be adequate to know I_{ang}. But the present dissertation aims also modeling of the ionization point. We should make much more precise measurement on the ionization point. The author will mention such a measurement later in Section 2.6.

2.4 Energy distribution

The energy spread of the beam is an important characteristic because it determines the focusing property of the lens system. The energy distribution (ED) was measured by the retarding potential method. The ion beam was extracted by V_{ext} of several kV. In this measurement, the ion source potential was set at the ground potential and the extraction
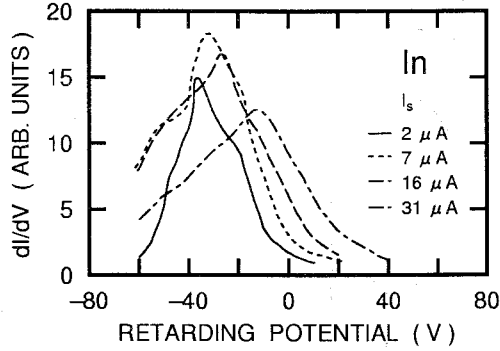
Figure 2.9: Energy distribution curve of
In ion source.
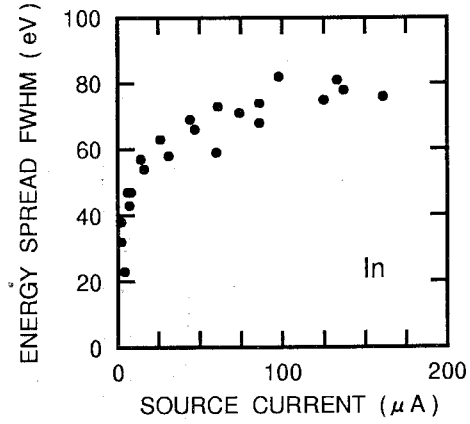
Figure 2.10: Energy spread of In ion
source as a function of I_s.

electrode was negatively biased. The retarding potential was given around the ground
potential. Figure 2.9 shows the ED curves at various I_s for the In ion source. The origin
of the abscissa is equivalent to the potential of the ion source. The zero-kinetic energy is
$-V_{ext}$. The negative value means that the ions have energy deficit with respect to the ion
emitter potential. The field evaporated ion has energy deficit because the ions are ejected
into vacuum due to the lowering of the surface barrier, owing to the strong electric field [10].
The ED became broader with an increase in I_s. Also it was seen that the peak position
of the distribution shifted toward higher energy. The energy spread (ES) was calculated
from the distribution with the full width at half maximum and plotted in Fig. 2.10. The
ES increased rapidly with an increase in I_s, and reached wider than 80 eV at the higher
current regime. This large ES causes large chromatic aberration in an electrostatic lens
system. The reason for the increase of ES is believed to be attributed to the strong space
charge interaction between the ions (Börsch effect) [11].

2.5 Emittance and brightness

In an ion beam system, emittance or brightness is primarily important, because the emit-
tance directly reflects the easiness of transport of the produced ions. Emittance represents
a lateral dispersion of the ions in the beam, in contrast with the ES that is the velocity dis-
persion along the ion motion. The emittance of an LMIS is rather small [3], so the common
technique [12] to measure the emittance is not available, except for the case that measure-
ment is done with very precise machine [13]. With an FIB machine, we can measure the

brightness instead. The brightness B_r is expressed by [14]

$$B_r = \frac{I_i}{(\pi r_i^2)(\pi \alpha_i^2)} = \frac{J_i}{\pi \alpha_i^2},$$ (2.8)

where r_i is the radius of the focused spot, α_i is the converging half angle, and J_i is the current density at the focused spot. If the magnification M of the lens system is known, the current density at the source J_o is, in principle, known. The normalized brightness B_{rn} can be calculated from the following equation,

$$B_{rn} = \frac{c^2}{v^2} B_r,$$ (2.9)

where c is the velocity of light and v is the velocity of the ion beam. The conservation of the normalized brightness holds throughout the ion beam path, thus we obtain

$$J_o = \left(\frac{v_o}{v_i}\right)^2 \left(\frac{\alpha_o}{\alpha_i}\right)^2 J_i = \frac{V_o}{V_i} \left(\frac{\alpha_o}{\alpha_i}\right)^2 J_i,$$ (2.10)

where α_o is the acceptance angle, and V_o and V_i are the voltages corresponding to the ion energy at the object and image space (beam voltage). There is a following relation between α_i and α_o.

$$\alpha_i = \frac{V_o}{V_i} M \alpha_o,$$ (2.11)

where M is the magnification of the lens system. So, finally we can estimate J_o by

$$J_o = \frac{V_i}{V_o} \frac{1}{M^2} J_i.$$ (2.12)

The author measured the brightness of the Ga ion beam in a limited acceptance angle by an FIB system developed by themselves [15,16] and showed the value is as small as that of conventional needle-type [16]. The smallest beam diameter was 0.4 μm and J_i reached 160 mAcm^{-2} = 1.6×10^3 A m^{-2}. The maximum B_{rn} was consequently 2.6×10^{15} Am^{-2}sr^{-1}, when I_s was 5 μA and α_o of 1.5 mrad. The detailed optical property of the lens system used in the FIB machine had been calculated by Orloff and Swanson [17], $M = 1.4$ for the deceleration mode with the beam voltage ratio of $V_i/V_o = 4$. The calculated J_o becomes 0.32 A cm^{-2} = 3.2×10^3 A m^{-2}. If the relation described above is valid, r_a will become 0.14 μm. This value is large as compared with the practical source size. This is because the beam diameter was dominated by the chromatic aberration [18]. This was confirmed by the calculation with an assumption of ΔE of 20 eV [19]. Although the brightness B_{rn} does not reflect J_o but gives the lowest limit of J_o.

2.6 Mass spectrum

2.6.1 Mass spectrum of element ion sources

Measurement of the mass spectrum is of great importance not only because we can obtain the fraction of the desired ion species, but also because we can get some information that is useful for analysis of the ion emission point. The mass spectra were measured with a magnetic sector of which the radius of the curvature was 600 mm, and the deflection angle was 60°. For Ga and In, mass spectra measurements were performed with the resolution slit with a width of 2–3 mm. For Cu, Au, Sn, and Ge, the entrance aperture and the resolution slit were modified. As is shown later, these ion sources emit a large amount of doubly charged ions, and the accurate estimate of the atomic flux ratio of doubly charged ions to singly charged ions, R_{21} is of great importance for the analysis of the ionization point. In order to obtain the accurate R_{21}, the incident aperture and the resolution aperture were set as 2 mm in diameter and 17 mm in diameter, respectively. The large value of the resolution aperture allowed collecting all the ions with relatively large energy spread as described above. If the entrance of the magnet is approximated by a point and the exit aperture is large enough, all the ions of same species could be gathered within the energy distribution of approximately 400 eV for 7 keV beam, neglecting the fluctuation of the power supplies. Collection of all ions was confirmed by the presence of a plateau at the mass peak.

Figure 2.11(a)-2.11(d) show the mass spectra for some element metal ion sources: (a) In, (b) Cu, (c) Au, and (d) Sn. As shown in Fig. 2.11(a), The In ion source yielded the singly charged atomic ions with a small amount of molecular ions. The Ga ion source yielded a quite similar mass spectrum. For the Cu ion source, we can observe a small amount of doubly charged atomic ions. For the Au ion source, the intensity of the doubly charged atomic ions were comparable (almost half) with that of the singly charged ions. A minor amount of molecular ions were also observed. For the Sn ion source, the dominant ion species were doubly charged atomic ions. The current of the molecular ions were higher than the ion sources above described. The Ge ion source yielded a quite similar mass spectrum. These differences in the atom flux ratio of the doubly charged ions to the singly charged ions are explained qualitatively in terms with field evaporation theory [20, 21], except the presence of the molecular ions. Generally, molecular ions are not observed in atom probe except for group IV elements [10]. The major reason for the difference among the mass spectra is attributed to the difference in $V_2 - \phi$ value. The author will discuss the difference of these mass spectra among the different metals in detail later in the section 2.7.
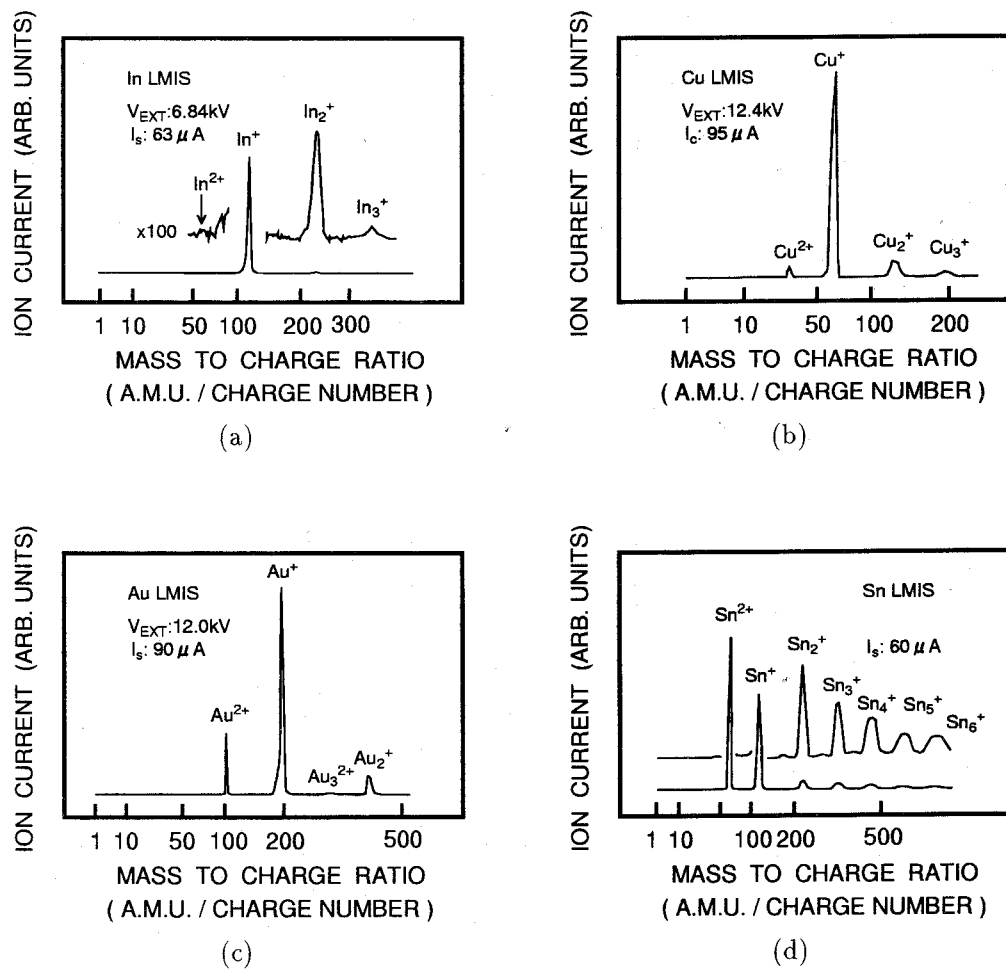
Figure 2.11: Mass spectra of element metal ion sources. (a) In, (b) Cu, (c) Au, and (d) Sn.
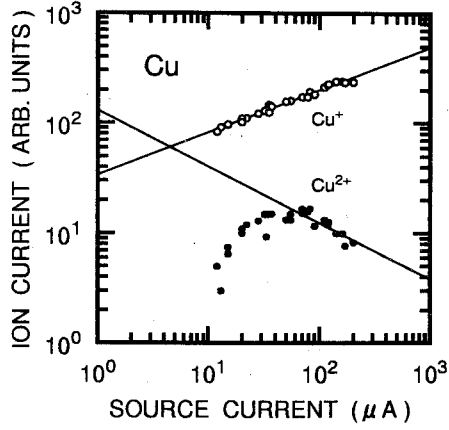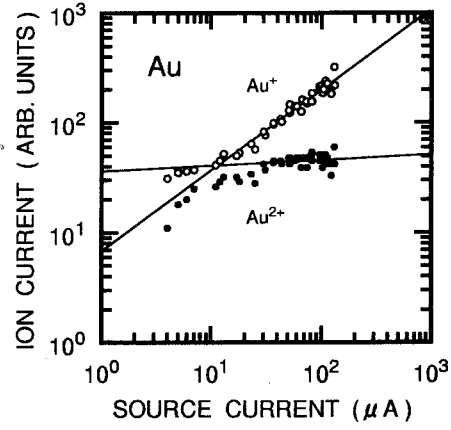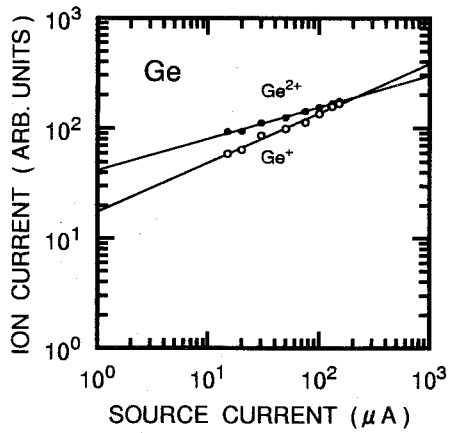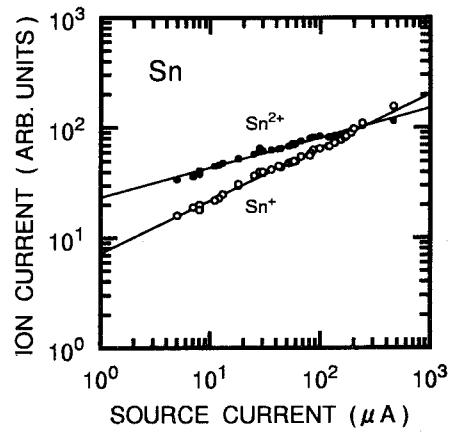
Figure 2.12: Ion currents of M^{2+} and M^+ extracted from LMIS's as a function of I_s. (a) Cu, (b) Au, (c) Ge, and (d) Sn ion sources. Solid circles show the currents of M^{2+}, and open circles show those of M^+.
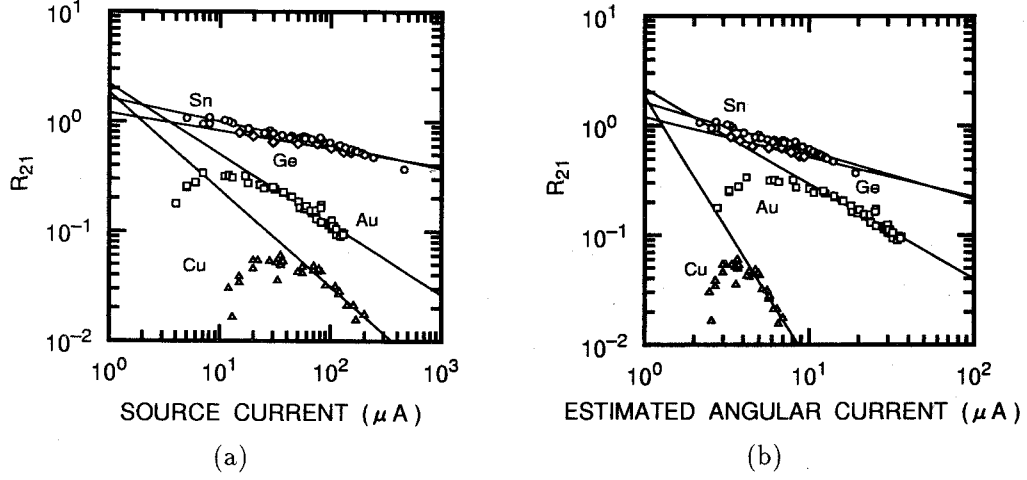
Figure 2.13: Relation between R_{21} and emission current. (a) as a function of I_s, and (b) as a function of I_Ω.

2.6.2 Angular currents of doubly charged and singly charged ions

Figures 2.12(a)–2.12(d) show the mass analyzed ion currents of M^+ and those of M^{2+} from the Cu, Au, Ge, and Sn ion sources, respectively. Solid circles indicate the intensities of M^{2+} and open circles indicate those of M^+. As for Cu, Cu^+ increased monotonically, while Cu^{2+} once increased and then decreased at I_s higher than 30 μA. As for Au, Au^+ increased, but Au^{2+} saturated at the higher I_s regime. Furthermore, at the very low current regime, slope of Au^+ and Au^{2+} changed: at low current regime, the increase of doubly charged ions was larger than that of singly charged ions. On the contrary to these, Ge and Sn ions showed almost monotonical increase with I_s. It is seen that irrespective of the material, slope of the current of M^+, ζ_1 was steeper than that of M^{2+}, ζ_2. For all cases, ζ_1 and ζ_2 were less than unity, which had been also reported by some researchers [1,9]. This is due to the enlargement of the emission angle with the increase in the emission current as described earlier.

Here the author focuses on the ion flux ratio of M^{2+} and M^+, R_{21}. R_{21} is defined by

$$R_{21} = \frac{I_{\Omega_2}/2}{I_{\Omega_1}}, \tag{2.13}$$

where I_{Ω_2} and I_{Ω_1} are the mass analyzed ion currents of M^{2+} and M^+, respectively. These currents were ion quantities toward a fixed solid angle, and represent a certain kinds of ion currents without the effect of enlargement of ion emission area. Figures 2.13(a) and 2.13(b) indicate the flux ratio R_{21}'s as a function of I_s and I_Ω. The author defines the angular

Table 2.1: Dependence of ζ_1 and ζ_2 on the angular current I_Ω.

Elements	Temperature (K)	Slope of I_Ω		Max R_{21}	Min R_{21}
		ζ_1	ζ_2		
Cu	1400	0.37	-0.23^a	0.060	0.018
Au	1400	0.74^b	0.048^b	0.34	0.090
Ge	1400	0.45	0.28	0.79	0.53
Sn	1000	0.48	0.27	1.08	0.37

[a]fitting performed at $I_s > 50\mu$A.

[b]fitting performed at $I_s > 20\mu$A.

current I_Ω by the ion current toward a solid angle, especially for the singly charged ions, if not specified. That is,

$$I_\Omega = \left[\frac{I_s}{1\mu\text{A}}\right]^{\zeta_1} \times 1\mu\text{A}. \tag{2.14}$$

These figures show that the R_{21} values decreased as I_s or I_Ω increased, at the higher current regime. For Cu and Au, R_{21} had a maximum at I_s of 10 – 30 μA. Similar tendency was seen for Cu based alloy ion sources [22] and also reported for Al ion sources [23,24]. It should be noted that the rate of decrease differs largely among the metal materials: those have higher R_{21} values show a slower decrease. The author will argue the difference in this rate of decrease of R_{21} later in Section 2.7. Also it should be noted that the intercept of the fitted power function approximately coincided at the reduced current of 1. The results were summarized in Table 2.1.

2.6.3 Emission of molecular ions

As shown in Fig. 2.11, molecular ions were observed in the mass spectrum. Despite the study on the formation mechanism of atomic ions, only a few arguments on the molecular ion formation can be seen in the literature. Some researchers claim that the evaporated molecule is field ionized [25,26] or that the charged droplet is torn into smaller clusters
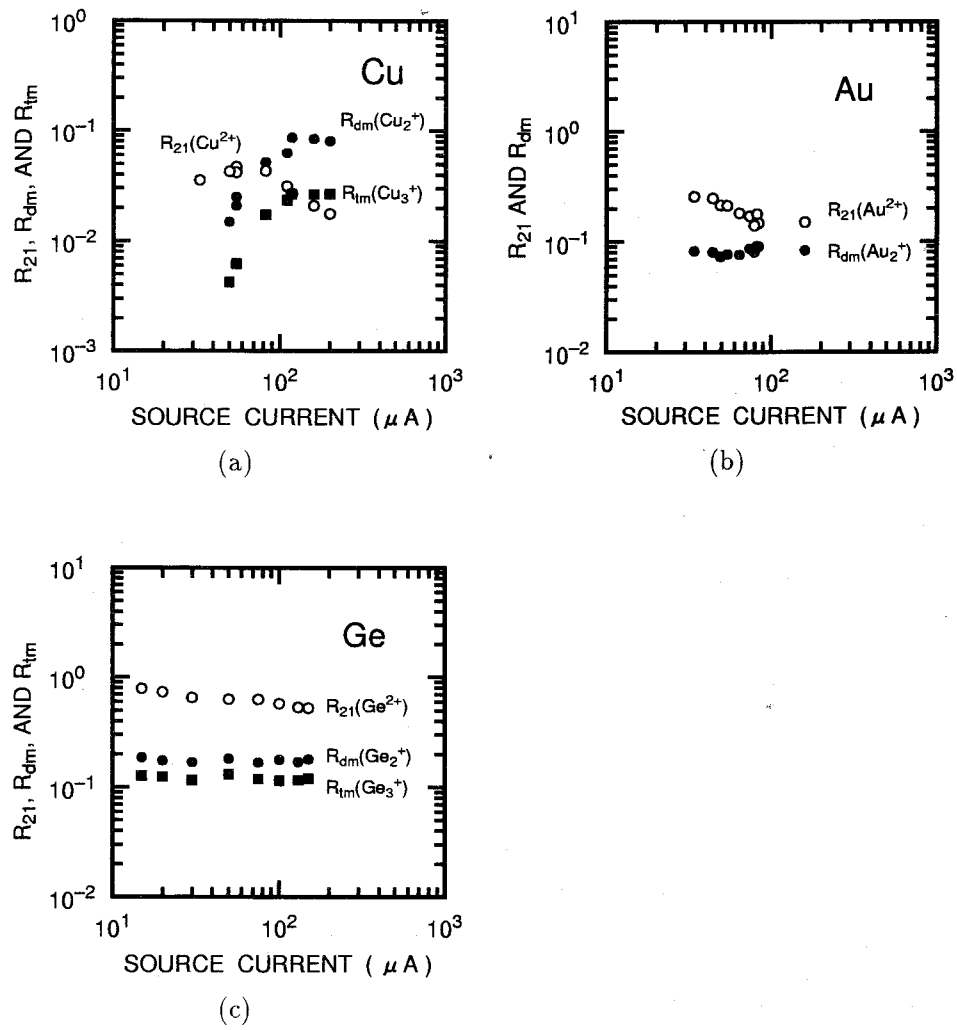
Figure 2.14: Relative currents of molecular ions as a function of I_s. (a) Cu, (b) Au, and (c) Ge ion sources.

Table 2.2: Values of R_{21} and R_{dm} for some element metal ion sources.

Metal	Doubly charged ions		Dimer ions	
	Currents R_{21} (μA)		Currents R_{dm} (μA)	
Au	4 – 131	0.09 – 0.34	34 – 158	0.076 – 0.083
Cu	12 – 200	0.017 – 0.06	12 – 200	0 – 0.083
Ge	15 – 150	0.55 – 0.79	15 – 150	0.17 – 0.18
Sn	5 – 460	0.37 – 1.08	60	0.097

[27, 28]. Figure 2.14(a)–2.14(c) show typical examples of the molecular ion intensity as a function of I_s for Cu, Au and Ge ion sources, respectively. Here the author defines R_{dm} as the current ratio of dimer ions $I_{\Omega dim}$ to that of atomic ions $I_{\Omega atm}$,

$$R_{dm} = \frac{I_{\Omega dim}}{I_{\Omega atm}}. \tag{2.15}$$

Quite similarly, we can define R_{tm} as the current ratio of trimer ions $I_{\Omega tri}$ to that of atomic ions,

$$R_{tm} = \frac{I_{\Omega tri}}{I_{\Omega atm}}. \tag{2.16}$$

R_{dm} and R_{tm} of Cu rapidly increased with an increase in I_s, and at the higher current regime, they tended to saturate. While R_{dm} for the Au and Ge ion sources did not change significantly. Less significant change in R_{dm} for the Au ion source would be because the above current range is higher than the current which gives maximum of R_{21}. The R_{dm} together with R_{21} is summarized in Table 2.2.

2.7 Estimation of electric field as a function of source current

2.7.1 Field evaporation models

Since some experimental data have been acquired, it is now possible to argue whether the results could be explained by the conventional field evaporation theory or not. Here in this dissertation, the author assumes that the ionization mechanism for singly charged ions is primarily field evaporation. This is because the other ionization mechanisms such as field ionization does not explain the absolute value of the extractable current observed for LMIS's. The author also assumes that the charge state distribution observed in the previous section reflects that at the ionization point. Although intense interaction between ions and neutrals including charge exchange process and Coulomb interaction are expected just in front of the ion emission site, as is supposed from the presence of the plasma ball [29], the effect of neutralization would be less significant as compared with the original yield of singly charged ions and doubly charged ions. Detailed argument on the modification of the charge state distribution due to the dense space charge and the neutral atom density near the ionization region will be pursued in Appendix A. In the following, the author briefly explains some ion formation mechanisms. As the author showed in Chapter 1, since the field evaporation process is thermally activated process, the expression of barrier height Q becomes the major issue of the field evaporation theory. There are some models for the determination of Q: image hump model and charge exchange model.

Image-hump model

The image hump (IH) model [20,21,30] assumes that the metal atom is already ionized at the surface, and overcomes the potential barrier lowered by the image force, namely, the Schottky effect. The potential diagram for this model is given in Fig. 2.15. The lowest thick curve which has a local maximum at $z = z_s$, is the potential curve for the ionized atoms. This curve can be obtained by synthesizing the external electric field and the image force. The lowest level of the neutral atoms is assumed to be atomic sublimation energy. In this model, ionization point can not be clearly defined, and thus it is difficult to define the potential curve. However, the barrier is expressed by the potential difference between the sublimation energy and the maximum of the hump. The current density for a $k-$times ionized ion is expressed as follows.

$$\begin{cases} J_k = keN_s\nu \exp\left(-\dfrac{-Q_{\text{IH},k}(F)}{k_B T}\right), \\ Q_{\text{IH},k}(F) = H + \Sigma_i V_i - k\phi - \left(\dfrac{k^3 e^3}{4\pi\varepsilon_0}\right)^{1/2} F^{1/2}, \end{cases} \qquad (2.17)$$
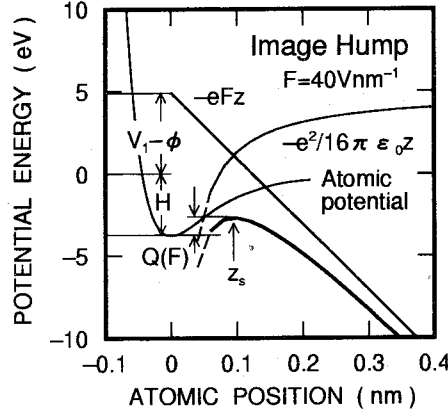
Figure 2.15: Potential diagram of IH model.

where N_s is the surface atomic density, ν is the vibration frequency of the surface atom, F is the electric field, k_B is Boltzman's constant, T is the temperature, H is the sublimation energy, V_i is the ionization potential for an i−times charged ion, ϕ is the work function, ε_0 is the permittivity of vacuum, and e is the electronic charge. The above equation does not include the effect of polarization for simplicity.

This model includes the potential difference between an atom in the liquid and an ion in vacuum by assuming the Born-Harber energy cycle [10]. The values of $Q_{IH,k}(F)$ for Au and Cu are shown in Fig. 2.16(a) and 2.16(b), respectively. As described previously, we cannot know the current density at the emission site. And thus, most of the cases, F is discussed under the assumption that Q is almost zero. If we agree this, the field F_{ev} which realizes the zero-energy barrier is uniquely given by

$$F_{ev} = (H + \Sigma_i V_i - k\phi)^2 \left(\frac{4\pi\epsilon_0}{k^3 e^3} \right). \tag{2.18}$$

This F_{ev} is called the "evaporation field." We can obtain F_{ev} value for singly charged ions as well as that for doubly charged ions, by putting physical parameters of the liquid to eq.(2.18). The values of F_{ev}'s for most elements range between 10 and 60 V nm^{-1}. For some elements, F_{ev} of doubly charged ions is lower than that of singly charged ions. If we assume the field corresponds to the lower F_{ev} value between the doubly and the singly charged ions, is applied to the apex, we can uniquely determine the operating field. The determined field gives R_{21} value, but generally this value does not agree with the experimentally obtained R_{21}. If we do not adopt the above assumption, we have two independent parameters of F
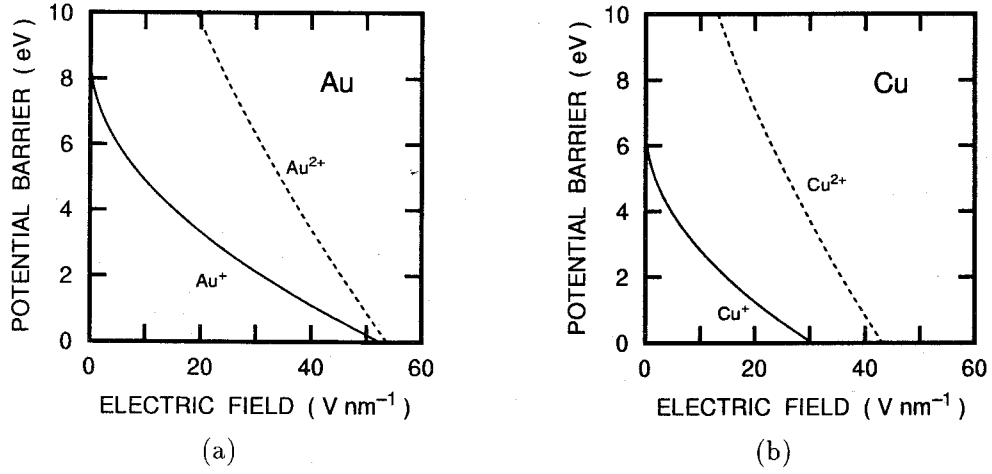
Figure 2.16: Values of $Q_{\text{IH},k}$ for (a) Au and (b) Cu.

and $k_{\text{B}}T$. R_{21} can be written as

$$R_{21} = \frac{J_2/2}{J_1} = \exp\left(-\frac{V_2 - \phi}{k_{\text{B}}T}\right)\exp\left(-\frac{2\sqrt{2} - 1}{k_{\text{B}}T}F^{1/2}\right). \tag{2.19}$$

If we put $R_0 = \exp\left(-\dfrac{V_2 - \phi}{k_{\text{B}}T}\right)$, then F can be calculated by

$$F = \frac{4\pi\varepsilon_0}{(2\sqrt{2} - 1)^2 e^3}\left[k_{\text{B}}T\ln\left(\frac{R_{21}}{R_0}\right)\right]^2. \tag{2.20}$$

From these equations, F is dependent on T. Substituting the reservoir temperature, we can calculate F values.

Charge-exchange model

The charge exchange (CE) model [31] is now considered to be the most realistic model for field evaporation. The potential diagram for this model is given in Figs. 2.17(a)—2.17(c). Figures 2.17(a), 2.17(b), and 2.17(c) show the potential diagrams for a neutral atom, the potential diagram for an ion, and difference between these potentials with the presence of the external electric field, respectively. This model takes the interatomic potential near the surface atom into consideration. We can consider both an atomic potential and an ionic potential, and the latter would be higher than the former by approximately $V_1 - \phi$. If a strong filed is applied to the surface, the ionic potential would be bent and finally crosses the atomic potential curve at the point $z = z_c$, as shown in Fig. 2.17(c). Due to
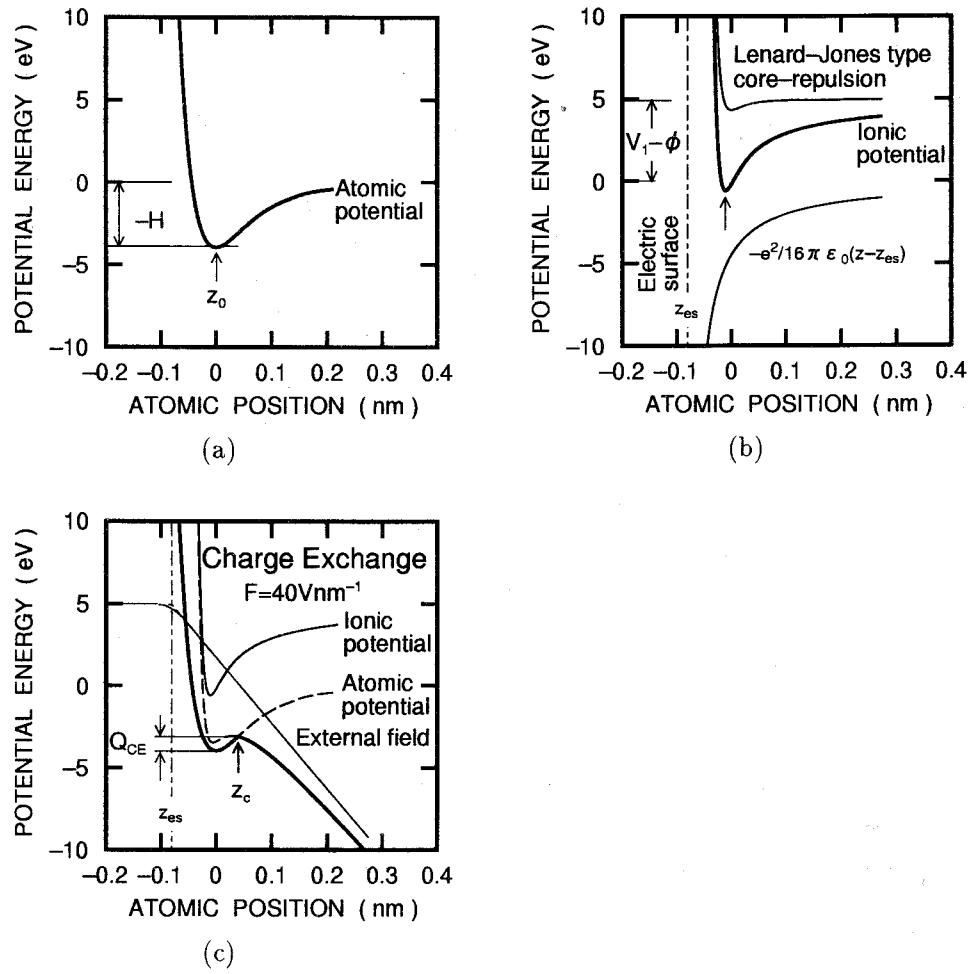
Figure 2.17: Potential diagrams of CE model. (a) a neutral atom, (b) an ion, and (c) differences between these two states and the position where the charge-exchange occurs.

the difficulties in formulating the interatomic potentials both for atoms and ions, there is little quantitative argument for this model. Nevertheless, the rate of ion formation can be written as [10]

$$\begin{cases} J_1 = eN_s\nu \exp\left(-\frac{Q_{CE,1}(F)}{k_B T}\right), \\[2mm] Q_{CE,1}(F) = U_i(z_c, F) - U_a(z_0, F), \\[2mm] U_a(z_0, F) = -H, \\[2mm] U_i(z_c, F) = V_1 - \phi - eF(z_c - z_{es}) - \dfrac{e^2}{16\pi\varepsilon_0(z_c - z_{es})} + G(z_c), \end{cases} \qquad (2.21)$$

where $Q_{CE,1}(F)$ is the activation energy for singly charged ions, $U_a(z_0, F)$ is the atomic potential (sublimation energy), $U_i(z, F)$ is the ionic potential with the image force and the external field, z_{es} is the virtual electric surface with respect to the physical surface, and $G(z)$ is the ionic core repulsion term. For detailed discussion, the effect of the polarization should be taken into consideration. In the above formulation, the electric surface was taken differently from the physical surface because of penetration of the external field into the interior of the metal. The electric surface is expressed by z_{es}, and the image potential and the potential due to the external field should be modified. Figure 2.17(b) and 2.17(c), the dot-dashed line represents the electric surface.

The barrier $Q_{CE,2}$ may be written similarly, but the formulation may become more complicated than $Q_{CE,1}$. The difficulties is entirely due to the fact that the interatomic potential between the atom and the ion. z_0 denotes the lattice position of an atom and z_c denotes the position where an atom is ionized (cross point of ionic potential and atomic potential).

So far, Lenard-Jones potential was used for $G(z)$. Recent progress of many body potential such as embedded atom method [32–34] made the behavior of surface atoms of fcc metals descriptive. Miskovsky and Tsong [35] applied this interatomic potential to the calculation of field evaporation. However, it is still difficult to make a sketch for doubly charged ions.

If we assume that the shape of the interatomic potential curve for an ion does not differ significantly from that of an atom, except for the absolute value of $V_1 - \phi$, F_{ev} can be estimated. Tsong derived the equation [10]

$$F_{ev} = \frac{1}{kz_a}\left[H + \sum V_i - k\phi - \frac{k^2 e}{16\pi\varepsilon_0 z_a}\right], \qquad (2.22)$$

where z_a is an atomic radius. As a matter of fact, the calculated results of F_{ev} with the CE model is approximately the same with those obtained with the IH model, thus the author will not make an argument with CE model for the present rough sketch.
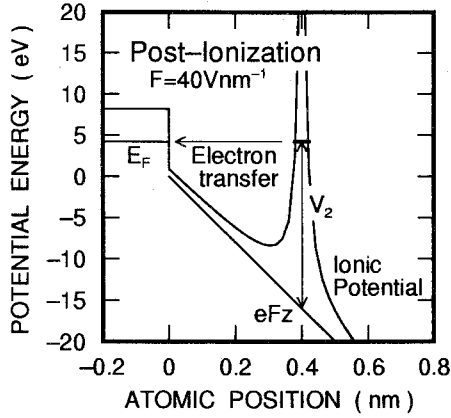
Figure 2.18: Potential diagram of PI model.
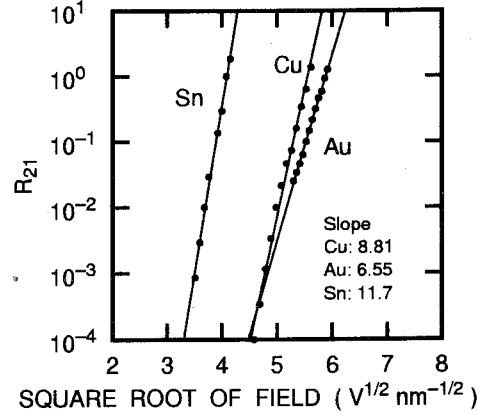
Figure 2.19: Charge state distribution for Au, Cu and Sn predicted by post-ionization theory.

2.7.2 Post-ionization model

The post-ionization model [36,37] is developed to correct the charge state distribution of the field evaporated ions for the atom probe. The theory assumes that the doubly charged ions are formed by electron tunneling from the field evaporated singly charged ions to the solid surface. It does not request the first stage field evaporation rate. The potential diagram of this PI model is shown in Fig. 2.18. If the ion which desorbed the surface is located at the position $z = z_c$, where the potential energy of the electrons of the outer shell is the same as the Fermi level of the surface, an electron may transfer back to the surface due to tunneling effect. Calculated results of charge state distribution is available in the Kingham's paper [37]. The data are redrawn for Au, Cu and Sn in Fig. 2.19. The author has fitted the curve by

$$\ln R_{21} = A + B \ln \sqrt{F}, \tag{2.23}$$

where A and B are fitting parameters. Once A and B are determined and R_{21} is measured, we can easily derive F at the ionization point from the above equation. The values of A and B are listed in Table 2.3.

Using the image hump (IH) model and the post-ionization (PI) theory, the author calculated the relationship between F and I_s.

Table 2.3: Coefficients of A and B obtained from Kingham's paper.

Element	A	B
Cu	-4.90×10^1	8.81
Au	-3.86×10^1	6.55
Sn	-4.80×10^1	11.7

2.7.3   Electric field as a function of source current

Image hump model

The operating F's were calculated for the four kinds of metals using the experimentally obtained R_{21} values. Figures 2.20(a) – 2.20(d) show the calculated F's as a function of I_s. The physical parameters necessary to calculate F were taken from Tsong's table [21] except for Ge for which the parameters were taken from Brandon's table [20]. In these figures, dashed line and dot-dashed line show F_{ev}'s for singly charged ions (F_{ev}^1) and that for doubly charged ions (F_{ev}^2), respectively. In order to calculate F, the source temperature T_s is necessary. In Figs. 2.20(a)–2.20(d), T_s is shown in each figures. Solid lines are the curve fitted by a power function. As for Cu and Au, the calculated values of F exceed these F_{ev}'s, which means these values are less meaningful. For Ge and Sn, we obtain reasonable values. The calculated fields are between 26.6 and 26.8 V nm^{-1} for Ge and 21.5 and 21.9 V nm^{-1} for Sn. The dependence of I_s on F is so strong that only a little change in F can be seen.

F at the high current regime is approximated by the logarithmic function.

$$\ln F = {}^{IH}C + {}^{IH}D_s \ln(I_s) = {}^{IH}C + {}^{IH}D_\Omega \ln(I_\Omega). \tag{2.24}$$

C and D are coefficients. The superscript IH means that these values are for the IH model. I_Ω was defined by the angular current of the singly charged ions, as described earlier. We may also write,

$$\begin{cases} I_s = \exp\left(-\dfrac{{}^{IH}C}{{}^{IH}D_s}\right) F^{1/{}^{IH}D_s}, \\[2mm] I_\Omega = \exp\left(-\dfrac{{}^{IH}C}{{}^{IH}D_\Omega}\right) F^{1/{}^{IH}D_\Omega}. \end{cases} \tag{2.25}$$

Table 2.4: Coefficients of ^{IH}C, $^{IH}D_s$, and $^{IH}D_\Omega$ obtained from the experimental results.

Metal	^{IH}C	$^{IH}D_s$	$1/^{IH}D_s$	$^{IH}D_\Omega$	$1/^{IH}D_\Omega$
Ge	3.28	-3.5×10^{-3}	-285	7.8×10^{-3}	-129
Sn	3.08	-3.6×10^{-3}	-278	7.4×10^{-3}	-134

Table 2.5: Coefficients of ^{PI}C, $^{PI}D_s$, and $^{PI}D_\Omega$ obtained from the experimental results.

Element	^{PI}C	$^{PI}D_s$	$1/^{PI}D_s$	$^{PI}D_\Omega$	$1/^{PI}D_\Omega$
Cu	3.46	-3.89×10^{-2}	-25.7	-1.06×10^{-1}	-9.43
Au	3.58	-3.27×10^{-2}	-30.6	-4.46×10^{-2}	-22.4
Sn	2.84	-8.87×10^{-3}	-113	-1.85×10^{-2}	-54.1

In Table 2.4, values of ^{IH}C, $^{IH}D_s$, $1/^{IH}D_s$, $^{IH}D_\Omega$, and $1/^{IH}D_\Omega$ are listed. I_s is almost proportional to F^{-280}, which is extremely strong dependence of I_s on F.

Post-ionization theory

Figures 2.21(a) and 2.21(b) show the relations between F and I_s, and between F and I_Ω, respectively. We have assumed that F can be expressed as

$$\ln F =^{PI}C +^{PI}D_s \ln I_s =^{PI}C +^{PI}D_\Omega \ln I_\Omega, \qquad (2.26)$$
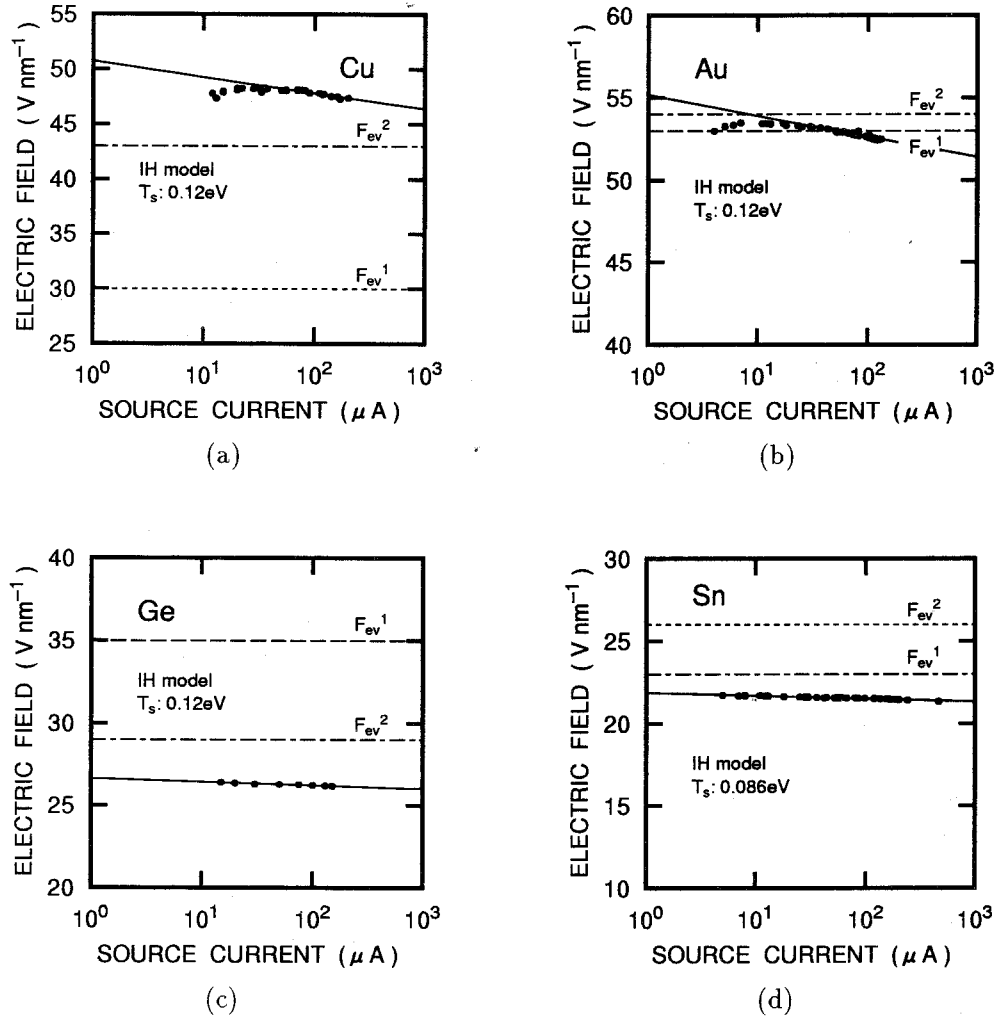
Figure 2.20: Relation between I_s and F_P calculated by the image hump model. (a) Cu, (b) Au, (c) Ge, and (d) Sn.

(a)   (b)
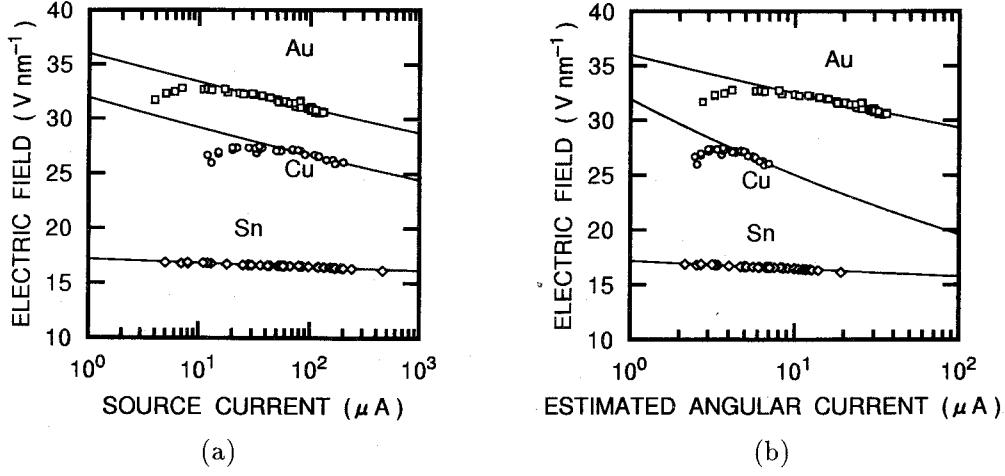
Figure 2.21:   Relation between I_s or I_Ω and F calculated by post-ionization theory.

where $^{\mathrm{PI}}C$, $^{\mathrm{PI}}D_s$, and $^{\mathrm{PI}}D_\Omega$ are fitting parameters.

$$\begin{cases} I_s & = & \exp\left(-\dfrac{^{\mathrm{PI}}C}{^{\mathrm{PI}}D_s}\right) F^{1/^{\mathrm{PI}}D_s}, \\[3mm] I_\Omega & = & \exp\left(-\dfrac{^{\mathrm{PI}}C}{^{\mathrm{PI}}D_\Omega}\right) F^{1/^{\mathrm{PI}}D_\Omega}. \end{cases} \qquad (2.27)$$

The obtained values of C and D are denoted in Table 2.5. From this table, it is noted that the current is proportional to F^{-10} to F^{-50}. This dependence of F on I_Ω is less significant as compared with the IH model.

Table 2.6 summarizes the calculated parameters. The author will try to reproduce these relations in the following section.

2.8   Relation between electric field and source current

2.8.1   Essential equations

In order to analyze the obtained results, here we formulate the relation between F and I_s or I_Ω. Generally, Poisson's equation and relation between J and F determines the field. In the present case, however, fluid dynamic equation should be taken into consideration, due to deformation of liquid structure. Consequently, these three essential relations should be satisfied by the apex radius r_a, the electric field at the apex F_P, the current density J, and the applied voltage V. Here subscript P of F implies that the field at the apex is shielded by the space charge effect, thus the field is obtained from the solution of Poisson's

Table 2.6: Observed angular current of individual ions I_{Ω_i} and R_{21} values with their dependence on I_s or on I_{Ω_1}. Estimated field at the apex with the image hump model F_{IH} and that with the post-ionization theory F_{PI} are calculated.

Elements	Temperature	Slope of I_Ω		Max R_{21}	F_{IH}	F_{PI}	Slope of R_{21}	
	(K)	ζ_1	ζ_2	Min R_{21}	(V nm^{-1})	(V nm^{-1})	ξ_s	ξ_Ω
Cu	1400	0.37	-0.23^a	0.060	$-^c$	26.3	0.89^a	2.4
				0.018	$-^c$	25.4		
Au	1400	0.74^b	0.048^b	0.34	$-^c$	33.2	0.64^b	0.81
				0.090	$-^c$	30.0		
Ge	1400	0.45	0.28	0.79	26.8	$-$	0.16	0.36
				0.53	26.6	$-$		
Sn	1000	0.48	0.27	1.08	21.9	16.9	0.21	0.44
				0.37	21.5	15.6		

[a] fitting performed at $I_s > 50\mu A$.

[b] fitting performed at $I_s > 20\mu A$.

[c] no appropriate value found.

equation. Some researchers claim that one of the possible reason for the decrease of R_{21} is shielding effect due to space charge [38]. But this shielding effect does not explain the experimental results, as will be shown below.

Rate of ionization for field evaporation

Based on the field evaporation theory [20,21], the relation between the current density of k—times charged ions J_k and F_P can be written in the form

$$J_k = J_{k0}\exp[s_k F_P^{1/2}],\qquad(2.28)$$

where J_{k0} is the current density preexponential, and s_k is the temperature-dependent co-efficient for k—times charged ions. J is obtained summing J_1 and J_2. For the case of the image hump model,

$$s_k = \frac{(ke)^{3/2}}{(4\pi\varepsilon_0)^{1/2}k_B T}.\qquad(2.29)$$

Fluid dynamic equation

The formula which represents the fluid dynamic (FD) equation without viscosity is the Bernoulli's equation,

$$P + \frac{1}{2}\rho_m v^2 + \rho_m g h = 0,\qquad(2.30)$$

where P is the pressure, ρ_m is the weight density, v is the liquid velocity, g is the acceleration coefficient of the gravity, and h is the height. Generally, the effect of the gravity is neglected for the LMIS. The application of this equation to the apex of the liquid was shown by Kingham and Swanson [39]:

$$-\frac{1}{2}\varepsilon_0 F_P^2 + \frac{2\gamma}{r_a} + \frac{1}{2}\rho\left(\frac{J}{eN_v}\right)^2 = 0,\qquad(2.31)$$

where γ is the surface tension, and N_v is the atomic density per unit volume. The first two term represent the pressures at the top of the liquid-jet, showing the electric field stress S_F, and the surface tension stress S_T, respectively. The third term represents the kinetic energy of the liquid flow per unit volume K. The above equation can be rewritten as:

$$\frac{1}{2}\varepsilon_0 F_P^2 = \frac{1}{2}\rho_m\left(\frac{J}{eN_v}\right)^2 + \frac{2\gamma}{r_a}.\qquad(2.32)$$

This equation shows the massive flow of the liquid is promoted by the pressure difference between S_F and S_T. In their article, Kingham and Swanson calculated the values in the above equation, and concluded that K dominates the right-hand side [39] at the high current regime. This model is thought to be a "dynamic" model because the current is driven by S_F. While Forbes [40] stands at the opposite side, a "static" model based on the fact that S_F is almost in balance with S_T, and slight difference causes the flow of the liquid.

Poisson's equation

Since the space charge at the apex is significant, thus the entire potential calculation should be made to solve Poisson's equation. It is not easy to solve the Poisson's equation for the liquid jet structure, thus here we assume a simpler model of a pair spheres for the ion emitter and the extractor geometry. As shown by Gomer [41] and Miskovsky and Cutler [42], Poisson's equation with regard to the potential U in a spherical coordinate is written as

$$\frac{\mathrm{d}^2 U}{\mathrm{d}r} = \frac{I_\Omega}{2\pi\varepsilon_0} \left(\frac{m_\mathrm{I}}{2e}\right)^{1/2} \left[U + \frac{k_\mathrm{B}T}{2e}\right]^{-1/2} r^{-2} - 2\frac{\mathrm{d}U}{\mathrm{d}r}r^{-1}, \qquad (2.33)$$

We can solve the above equation numerically with a digital computer under the boundary condition of $\mathrm{d}U/\mathrm{d}r = -F_\mathrm{P}$ and $U = 0$ at $r = r_\mathrm{a}$. The solved value of U at $r = d$ gives the extraction voltage V_ext.

Relationship between source current and physical parameters

Substituting eqs.(2.32) and (2.28) into eq.(2.33), we can solve the equation numerically. In order to simulate the operation of LMIS, the calculation was performed in the following procedure. First, the voltage which corresponds to the threshold voltage V_th was given. This is because LMIS has V_th where the liquid is pulled by the electric stress to form a cone, as described earlier. Reducing r_a, the solution of the above equations with space charge is calculated. Once the parameters were determined, then V was increased and also the parameters were optimized to satisfy the essential equations. Repetition of this process provides the relation among the parameters. The temperature was assumed to be 0.12 eV which corresponds to 1400 K. The other parameters chosen are for Au. Figures 2.22(a) and 2.22(b) show the relations between I_Ω and F_P, and I_Ω and r_a, respectively. Because of rapid increase of J of the low temperature field evaporation, increment of F_P is small, but the F_P never decreased. r_a was enlarged with an increase in I_Ω.

2.8.2 Discrepancy of calculated results with experimental results

Kingham and Swanson [39] showed the increase of r_a with an increase in I_Ω, from eq.(2.32) and Forbes [40] also derived the similar result from the same equation but assuming different balancing condition. The enlargement of r_a is thus generally accepted. However, F_P increased with an increase in I_Ω, and this result does not agree with the experimental results. The present results clearly demonstrated that the decrease of R_{21} can not be explained in terms with the space charge shielding. The validity of this numerical simulation will be confirmed in Chapter 3.

One of the reasons for this discrepancy would be attributed to the fact that the present solution gives large S_F value as compared with S_T. The IH model requires a relatively
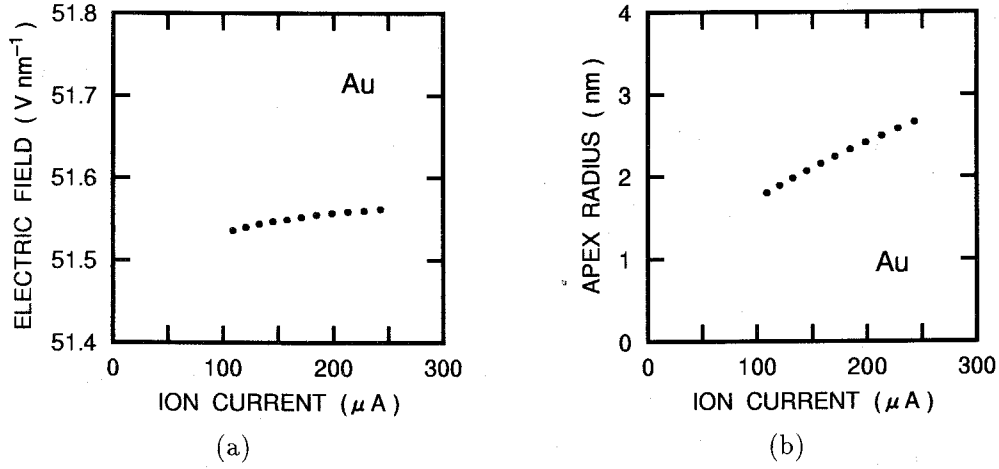
Figure 2.22: Relation between (a) I_Ω and F and (b) I_Ω and r_a as a solution of the eqs.(2.28) -(2.33).

large field value for Au, for example. K is proportional to r_a^{-4}, and S_T is proportional to r_a^{-1}. In order to give a large value to the sum of the right hand side of eq.(2.32), significant reduction in r_a is necessary, thus K becomes larger than S_T. This agrees with the description seen in the Kingham and Swanson's paper [39], which the author already mentioned in the previous subsection. Figure 2.23 clearly indicates the present situation. This figure gives the relation among the magnitude of each term in fluid dynamic equation as a function of r_a. In the figure, K's which correspond to 1μA, 10μA, and 100μA and S_T are drawn. S_F is not dependent on r_a apparently, but it corresponds to sum of the above two terms, thus S_F can be known automatically. In the ordinate at the right-hand side, F_P converted from S_F is given. The operating point is shown by the solid circles. For the case of Kingham and Swanson, the magnitude of K is larger than that of S_T [39]. The present result reproduces their result.

Here the author points out the problem of the theory of Kingham and Swanson. In their theory, since Q is almost zero, and consequently

$$J = eN_s\nu \qquad \text{or} \qquad I = eN_s\nu\pi r_a^2. \tag{2.34}$$

The ion current of 100 μA corresponds to 6×10^{14} ions s^{-1}. Here, we assume the emission area 7×10^{-14} cm^{-2}, where about 100 atoms are arranged (r_a=1.5 nm). In such a situation, the emission frequency of 6×10^{12} Hz for each atomic site is required. This is almost the vibration frequency of the surface atoms. This requires all the atoms at the surface desorb into vacuum. This is a consequence of the assumption of $Q = 0$. This also means the
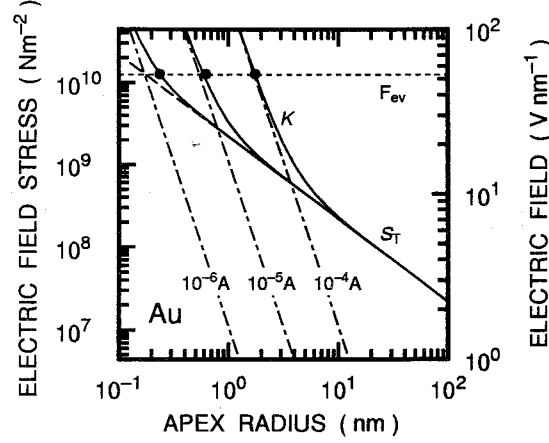
Figure 2.23: Working points for the model of Kingham and Swanson in the diagram apex radius vs electric field stress. Solid circles show the working points.

liquid flow is continuous and no boundary between liquid and vacuum is found. In this case, ionization mechanism can not be argued because all the atoms leave the surface immediately as an ion. Although Kingham and Swanson assumed clear surface at the apex, it is not a consistent model. While Forbes' static model seems to be more consistent from this point of view. But his static model does not explain the emitted current.

2.9 Proposal of new model at the apex

2.9.1 Analytical expression of electric field as a function of emission current

Here in this section, the author attempts to show the relation among I_s, r_a, and F_P from the fluid dynamic equation. The major point that the author would like to point out is the magnitude of each term in the right-hand side of eq.(2.32). As described above, it is doubtful that S_T is negligible against S_F. It is because with such an assumption, the surface atoms should be ejected into vacuum immediately after the atoms are incident on the surface, and also because liquid would not form a stable cone without presence of surface tension. Taking the above facts into consideration, it may be natural to consider the liquid jet is terminated at the point where the kinetic energy exceeds the surface tension stress. Whether the Poisson's equation holds or not is here out of the question.
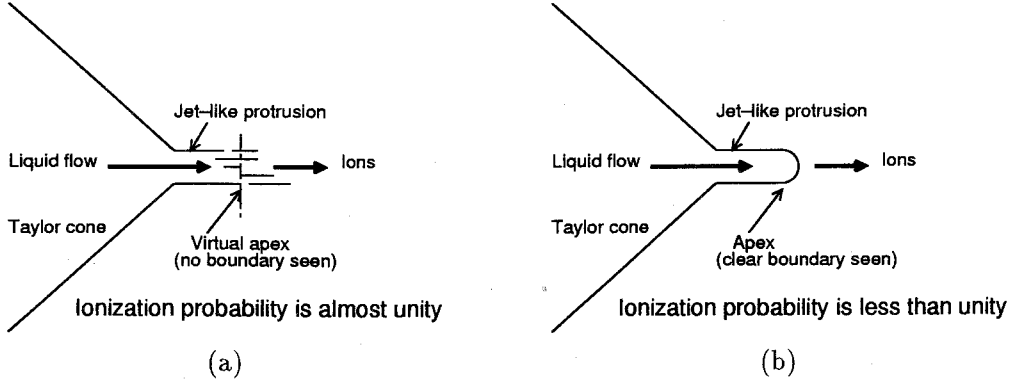
Figure 2.24: Schematic drawings of the liquid with the model of (a) Kingham and Swanson, and (b) Forbes.

We assume S_T is comparable with S_F. Then we may write

$$\frac{1}{2}\varepsilon_0 F_P^2 \sim \frac{2\gamma}{r_a}. \tag{2.35}$$

Also we assume that K is comparable with S_T. This is because if K is larger than S_T, stabilization of the cone by the presence S_T becomes less effective.

$$\frac{1}{2}\rho_m v^2 = \frac{2\gamma}{r_a}. \tag{2.36}$$

Under these conditions, we can calculate F_P by equating S_T with the above assumption,

$$\frac{1}{2}\varepsilon_0 F_P^2 = \frac{4\gamma}{r_a}. \tag{2.37}$$

Eq.(2.36) can be written as

$$\frac{1}{2}\rho_m \left[\frac{I_i}{\overline{k}eN_v r_a^2}\right]^2 = \frac{2\gamma}{r_a}, \tag{2.38}$$

where $\overline{k}$ is the mean charge of the emitted ions. From eq.(2.38), relation between I_Ω and r_a can be derived as

$$r_a = \left[\left(\frac{1}{\overline{k}eN_v}\right)^2 \frac{\rho_m}{4\gamma}\right]^{1/3} I_i^{2/3}. \tag{2.39}$$

Substituting eq.(2.39) to eq.(2.37), we obtain

$$F_P = \sqrt{\frac{8\gamma}{\varepsilon_0}} \left[(\overline{k}eN_v)^2 \frac{4\gamma}{\rho_m}\right]^{1/6} I_i^{-1/3}. \tag{2.40}$$

This is the relation between F_P and I_i, showing that F_P decreases in accordance with a minus one-third power of I_i. This equation holds only when the dependence of J on F_P is less sensitive than the conventional field evaporation theory. The results are different from those obtained by Kingham and Swanson [39]: $r_a \propto I_i^{1/2}$ and F_P =const.

2.9.2 R_{21} as a function of angular current

Based on the formulation in eq.(2.28), R_{21} can be written as

$$R_{21} = R_0 \exp\left[s_{21} F_P^{1/2}\right], \qquad (2.41)$$

where s_{21} is the temperature-dependent coefficient. In the case of the IH model,

$$s_{21} = (2\sqrt{2} - 1)\left(\frac{e^3}{4\pi\varepsilon_0}\right)^{1/2}\frac{1}{k_B T}. \qquad (2.42)$$

By differentiating both sides, we obtain

$$\frac{dR_{21}}{R_{21}} = \frac{s_{21}}{2}\frac{dF_P}{F_P^{1/2}}. \qquad (2.43)$$

Substituting eq.(2.40) and its differential into eq.(2.43) gives

$$\frac{dR_{21}}{R_{21}} = -\frac{s_{21}}{3}\left[(\overline{k}eN_v)^2\frac{\gamma^4}{2\varepsilon_0^3\rho_m}\right]^{1/12}I_i^{-7/6}dI_i. \qquad (2.44)$$

Here we put ξ_{ana} as

$$\xi_{ana} = \frac{s_{21}}{3}\left[(\overline{k}eN_v)^2\frac{\gamma^4}{2\varepsilon_0^3\rho_m}\right]^{1/12}, \qquad (2.45)$$

and assuming $I_i^{7/6}$ is almost equivalent to I_i, we obtain

$$\frac{dR_{21}}{R_{21}} = -\xi_{ana}\frac{dI_i}{I_i}. \qquad (2.46)$$

Integrating both sides gives

$$R_{21} = R_0 I_i^{-\xi_{ana}}. \qquad (2.47)$$

Equation (2.47) shows that the R_{21} can be written by a power function of I_i.

2.9.3 Comparison between theoretically and empirically obtained rates of decrease in electric field

We can calculate ξ_{ana} for each metal by putting physical parameters into eq.(2.45). Table 2.7 shows the calculated ξ_{ana}. Cu and Au have higher ξ_{ana} values than Ge and Sn, which agrees with the experimental values. Only the discrepancy is that ξ_{ana} for Sn is smaller than that of Ge, and this may be because the Sn ion source was operated at the lower temperature. From the analytically obtained ξ_{ana} and the experimentally obtained ξ_Ω or ξ_s, the value of s_{21} can be estimated. These values are also listed in Table 2.7. s_{21} ranged between 0.7 to 5.2×10^{-4}m$^{1/2}\cdot$V$^{-1/2}$ which is in good agreement with the theoretical s_{21} value of 3.2×10^{-4} m$^{1/2}\cdot$V$^{-1/2}$ at 1400 K. To estimate I_i exactly is difficult thus use of

Table 2.7: Physical parameters and ξ values for examined metals.

	Cu	Au	Ge	Sn
$N_v(10^{28}\text{atoms m}^{-3})$	8.43	5.89	4.40	3.68
γ (Nm^{-1})	1.3	1.1	0.6	0.5
$\overline{k}$	1.06	1.25	1.44	1.52
ξ_{ana} (10^3)	$4.6s_{21}$	$3.9s_{21}$	$3.5s_{21}$	$3.1s_{21}$
ξ_{s}	0.89	0.64	0.16	0.21
ξ_{Ω}	2.4	0.81	0.36	0.44
s_{21} for ξ_{s} (10^{-4}m$^{1/2}$·V$^{-1/2}$)	1.9	1.6	0.45	0.68
s_{21} for ξ_{Ω} (10^{-4}m$^{1/2}$·V$^{-1/2}$)	5.2	2.1	1.0	1.4
T_{a} estimated from ξ_{s} (eV)	0.36	0.42	1.5	1.0
T_{a} estimated from ξ_{Ω} (eV)	0.13	0.33	0.69	0.50

either ξ_s or ξ_Ω may include some errors. If we neglect the change in the secondary electron yield, ξ_s would be more realistic. Lower values of s_{21} than the conventional theory means that the dependence of J on F_P is weaker or the local temperature T_a at the ionization point may be higher than T_s. We can estimate T_a from the obtained s_{21} and found that T_a's for most of the materials were higher than T_s. From the present estimation, T_a becomes 0.1 to 1 eV, which corresponds to 1000°C to 10,000°C. The calculated value scattered among the materials, but are almost around 1 eV. The author can not determine the reason for the scattered T_a at this stage of discussion, but the scatter may be related to the difference in the thermal conductivity. Otherwise dependence of Q on F_P is less than the conventional field evaporation theory. Anyway, the author has derived a possible model of the LMIS operation.

2.10   Conclusion

This chapter dealt with the experimental results of the characterization of the ion beams extracted from the LMIS's. The obtained results are:

- Ion beam characteristics such as current-voltage characteristics, beam profile, energy distribution, brightness, and mass spectrum which are necessary to design the lens system were measured.

- The mass spectra were measured and the atom flux ratio of doubly charged atomic ions to singly charged atomic ions, R_{21} and that of molecular ions to atomic ions R_{dm} were obtained as a function of I_s.

- In order to explain the experimental results, numerical simulation was performed, but only a discrepancy was seen. Introducing restriction of the magnitude to the kinetic energy of liquid, a good agreement between experiments and theory was seen.

The first issue is of importance for design of ion beam systems, and the latter two issues are of importance for analysis of the ionization point. Although the assumption made in the present chapter explained the experimental tendency, at this stage of argument, it is not still confirmed that the model is self-consistent. Thus, in the next chapter, the author will discuss the ion formation mechanism of LMIS further in detail.

References in Chapter 2

[1] J. Ishikawa and T. Takagi: J. Appl. Phys. **56** (1984) 3050.

[2] T. Kishi: *Electron Impact Vaporization Ion Source with Trapping Effect of Electron Beam*, Dissertation, Kyoto University, 1982 [in Japanese].

[3] T. Takamori: *Impregnated-Electrode Type Liquid Metal Ion Source*, M. E. thesis, Kyoto University, 1984 [in Japanese].

[4] A. Wagner and T. M. Hall: J. Vac. Sci. Technol. **16** (1979) 1871.

[5] A. Wagner: Appl. Phys. Lett. **40** (1982) 440.

[6] L. W. Swanson, G. A. Schwind, A. E. Bell and J. E. Brady: J. Vac. Sci. Technol. **16** (1979) 1864.

[7] P. D. Prewett, D. K. Jefferies, and T. D. Cockhill: Rev. Sci. Instrum. **52** (1981) 562.

[8] Y. Gotoh: *Ion Beam Characteristics of Impregnated-Electrode-Type Liquid-Metal Ion Source*, B. E. Thesis, Kyoto University, 1985 [in Japanese].

[9] A. E. Bell and L. W. Swanson: Appl. Phys. A **41** (1986) 335.

[10] T. T. Tsong: *Atom-Probe Field Ion Microscopy* (Cambridge University Press, Cambridge, 1991).

[11] H. Börsch: Z. Phys. **139** (1954) 115 [in German].

[12] R. G. Wilson and G. R. Brewer: *Ion Beams with Application to Ion Implantation* (John Wiley and Sons, New York, 1973).

[13] G. D. Alton and P. M. Read: J. Phys. D **22** (1989) 1029.

[14] J. Ishikawa, Y. Gotoh and T. Takagi: *Proc. of 9th Symposium on Ion Sources and Ion-Assisted Technology, ISIAT'85*, Tokyo, June, 1985 (The Research Group of Ion Engineering, Kyoto, 1987) p.87.

[15] J. Ishikawa, Y. Gotoh, H. Tsuji and T. Takgai: Nucl. Instrum. Meth. **B21** (1987) 186.

[16] Y. Gotoh, *Analysis of Liquid-Metal Ion Sources and Transport of Intense Ion Beam* M. E. Thesis, Kyoto University, 1987 [in Japanese].

[17] J. Orloff and L. W. Swanson: J. Appl. Phys. **50** (1979) 2494.

[18] T. Kashiwagi, Y. Gotoh, H. Tsuji, J. Ishikawa and T. Takagi: *Proc. of 11th Symposium on Ion Sources and Ion-Assisted Technology, ISIAT'87*, Tokyo, June, 1987 (The Research Group of Ion Engineering, Kyoto, 1987) p.207.

[19] T. Kashiwagi: *Intensification of Impregnated-Electrode-Type Liquid-Metal Ion Sources*, M. E. Thesis, Kyoto University, 1988 [in Japanese].

[20] D. G. Brandon: Surf. Sci. **3** (1964) 1.

[21] T. T. Tsong: Surf. Sci. **70** (1978) 211.

[22] T. Ishitani, K. Umemura and Y. Kawanami: J. Appl. Phys. **61** (1987) 748.

[23] A. E. Bell, G. A. Schwind and L. W. Swanson: J. Appl. Phys. **53** (1982) 4602.

[24] H. Yamada and H. Torii: Rev. Sci. Instrum. **57** (1986) 1282.

[25] R. J. Culbertson, G. H. Robertson and T. Sakurai: J. Vac. Sci. Technol. **16** (1979) 1868.

[26] L. W. Swanson: Nucl. Instrum. Meth. **218** (1983) 3417.

[27] R. Hornsey and T. Ishitani: Jpn. J. Appl. Phys. **29** (1990) L1107.

[28] R. Hornsey and T. Ishitani: Jpn. J. Appl. Phys. **29** (1990) 2116.

[29] A. Wagner, T. Vankatesan, P. M. Petroff and D. Barr: J. Vac. Sci. Technol. **19** (1981) 1186.

[30] E. W. Müller: Phys. Rev. **102** (1956) 618.

[31] R. Gomer and L. W. Swanson: J. Chem. Phys. **38** (1963) 1613

[32] M. S. Daw and M. I. Baskes: Phys. Rev. Lett. **50** (1983) 1285.

[33] M. S. Daw and M. I. Baskes: Phys. Rev. B **29** (1983) 6443.

[34] S. M. Foiles, M. I. Baskes and M. S. Daw: Phys. Rev. B **33** (1986) 7983.

[35] N. M. Miskovsky and T. T. Tsong: Phys. Rev. B **46** (1992) 2640.

[36] N. Ernst and Th. Jentsch: Phys. Rev. B **24** (1981) 6234.

[37] D. G. Kingham: Surf. Sci. **116** (1982) 273.

[38] Referee's comment of the paper: Y. Gotoh, H. Tsuji and J. Ishikawa: Ultramicroscopy **89** (2001) 69.

[39] D. R. Kingham and L. W. Swanson: Appl. Phys. A **34** (1984) 123.

[40] R. G. Forbes: Appl. Surf. Sci. **67** (1993) 9.

[41] R. Gomer: Appl. Phys. **19** (1979) 365.

[42] N. M. Miskovsky and P. H. Cutler: Appl. Phys. A **28** (1982) 73.

Chapter 3
Modeling of element metal ion sources

In the previous chapter, the author pointed out that the experimental results could not be explained by the conventional field evaporation theory. On the contrary, with an assumption of a high temperature, it is possible to explain the behavior of the atom flux ratio of the doubly charged ions to that of the singly charged ions. In the present chapter, the author proposes the high temperature field evaporation (HTFE) model and discusses its consistency. First, the author defines the formulation of HTFE model. Next, the author discusses the necessary condition for explaining the experimental results. Then the author gives a practical temperature required for the HTFE model. Good agreement between the theoretically derived temperature and the experimentally observed temperature. Finally, the author gives one possible model of LMIS operation.

3.1   Proposal of a model of liquid apex

3.1.1   High temperature field evaporation model

The modeling of the LMIS has been attempted so far, including consideration of the liquid jet structure [1-7], but all these treatments assumed the conventional field evaporation model: constant F predicted by the low temperature field evaporation (LTFE) theory. Here the author defines LTFE as a conventional model, which is based on the fact that T_a is the same with T_s. The field is as high as 10 – 60 V nm^{-1} for most of the elements. However, as shown in the previous chapter, this high F does not allow balance of S_T with S_F. Furthermore, so far as we assume LTFE, decrease of R_{21} can not be explained.

In the previous chapter, the author pointed out that restriction of the magnitude of the term in the fluid dynamic equation leads an agreement with the experimental results [8]. In this model, J should be weakly dependent on F_P than that of conventional LTFE. Here the author examines the high temperature field evaporation (HTFE) model for the LMIS at the relatively high current regime. Since with the HTFE model, the dependence of J on F_P is weak, requirements in Chapter 2 are satisfied. This model is based on the same formula with the conventional field evaporation [9] but allows an extremely high temperature at the apex. Since the apex of the jet-like structure is non-equilibrium state, the temperature in excess of boiling point, for example, 1 eV (10,000°C) may be plausible. Kingham and

Swanson already mentioned this non-equilibrium condition [10], but no concrete model with an experimental evidence has been reported. The analysis of the apex temperatures has been mostly concerned with the examination of the possibility of field ionization process.

In the present model, the author generalizes the HTFE model and applying the same ion formation process for molecular ions. Although some researchers have claimed the various kinds of formation mechanisms of molecular ions [11–14], no argument was made assuming the same ionization mechanism with atomic ions. Currently, the ionization mechanism of molecular ions is considered to be mainly field ionization [12], but the explanations made everywhere is based on the Culbertson *et al.*'s experimental evidence of energy deficit [11]. The absolute value of the energy deficit is greatly affected by the Börsch effect [15], and it is difficult to determine the major ionization mechanism as field ionization. Since the Müller's consideration of field evaporation model (IH model) [16] is based on the Born-Haber energy cycle [17], it is possible to apply the same concept to molecular ions. The Born-Haber energy cycle was proposed by Born and also by Haber independently to obtain the cohesive energy for an ionic crystal from vapor phase [18]. Extension of this idea to molecular in vacuum will not include serious difficulties. Allowing the molecular ion formation mechanism, we have obtained another relation between F_P and I_s.

3.1.2   Formulation of high temperature field evaporation model

The formulation of the present HTFE model is written as:

$$\begin{cases} J_{k,m} = keN_s\nu_m \exp\left[-\dfrac{Q_{k,m}(F)}{k_B T_a}\right], \\ Q_{k,m}(F) = mH - (m-1)E_b + \displaystyle\sum_{i=1}^{k} V_i - k\phi, - \left(\dfrac{k^3 e^3}{4\pi\varepsilon_0}\right)^{1/2} F_P^{1/2} \end{cases} \tag{3.1}$$

where k and m is the charge number and number of atoms included in the ion, and E_b is the binding energy between atoms. ν_m is the surface vibration frequency. If we consider the dimer ion formation, ν_2 can not be the same with that of an atom, ν_1. Dimers would have fewer chances to be ionized because two atoms should be ejected towards the vacuum at the same time. For this reason, we should consider here ν_2 is smaller than ν_1. If we know the sublimation energy of the molecules, H_m, $mH - (m-1)E_b$ should be replaced by H_m. The HTFE model assumes a local high temperature, T_a, thus F_P will be lower than that of the conventional LTFE. This means that post-ionization [19] hardly occurs, thus R_{21} will be uniquely defined by the present model. The difference of the present model from the conventional model is denoted in Table 3.1.

Quite similarly, we can formulate the HTFE model with CE model. But as mentioned before, it is difficult to describe the field dependence of the barrier height in this model. If

Table 3.1: Comparison of the conventional and the present models..

Terms		Conventional model	Present model
Ionization model for	M^+	FE^a and FI(small portion)^b	HTFE^c
	M^{2+}	Post-ionization	HTFE
	M_2^+	unknown process and	HTFE
		FI of neutral from shank	
Temperature at apex		Source temperature	Extremely high
Electric field		High and constant	Lower and variable

^{a}FE   Field evaporation

^{b}FI   Field ionization

^{c}HTFE   High temperature field evaporation as a main ionization process
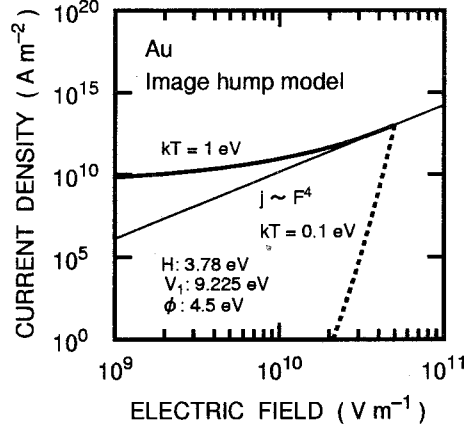
Figure 3.1: Relation between J and F calculated with the IH model.

the core-repulsion for an atom and an ion is the same, we may write

$$Q_{\mathrm{CE}} = H + \sum V_i - k\phi - \frac{k^2 e^2}{16\pi\varepsilon_0 z_{\mathrm{a}}} - keF z_{\mathrm{a}}. \tag{3.2}$$

Since z_{a} is generally $0.1 \sim 0.14$ nm [20], so the coefficient of F is approximately 0.1 nm. Differentiating the above equation, we obtain

$$\mathrm{d}Q_{\mathrm{CE}} = -kez_{\mathrm{a}}\mathrm{d}F, \tag{3.3}$$

while by the IH model,

$$\mathrm{d}Q_{\mathrm{IH}} = -\left(\frac{k^3 e^3}{4\pi\varepsilon_0}\right)^{1/2}\frac{1}{2F^{1/2}}\mathrm{d}F. \tag{3.4}$$

If we adopt the unit V m^{-1}, the coefficient of Q_{CE} is $1 \sim 1.4 \times 10^{-10}$ eV m V^{-1}, and that of Q_{IH} is less than 1.9×10^{-10} eV m V^{-1}. Thus, the field dependence is similar for both models. Based on the above consideration, the author uses the formulation of IH model for HTFE formulation.

Figure 3.1 shows the relation between J and F_P by HTFE and LTFE theories. The thick solid line and the thick dashed line are dependence of J on F owing to HTFE and LTFE models, respectively. It is shown that the dependence of J on F is lowered for HTFE from this figure. Thin solid line shows the slope for HTFE curve at 40 V nm^{-1}. This slope indicates that $J \propto F^4$.

3.1.3 Possible heating mechanism

Some reasons can be considered as the cause of heating of liquid cone: Joule heating and electron bombardment. Prewett *et al.* [21] and Mair and Aitken [22] calculated T_a for Taylor cone and cone with liquid jet structures. The formulation of the temperature at the apex T_a when the liquid jet has sufficient length ℓ is:

$$T_a = T_s + \frac{\ell}{\pi \kappa r_a^2 (1 + \theta_t \ell / r_a)} \left[W + \frac{\rho I_i^2 \ell}{2\pi r_a^2 (1 + \theta_t \ell / r_a)}, \right] \tag{3.5}$$

where T_s is the temperature at the shank, ℓ is the jet length, κ is the thermal conductivity, θ_t is the cone half angle, W is the input power to the liquid apex, I_i is the ion current excluding secondary electrons, and ρ is the electrical resistivity. The first term in the right hand side is external heating due to, for example, backstreaming electrons, and the second term is Joule heating. In this equation, T_a is sensitive to θ_t. According to the observation of emission tip in operation by transmission electron microscope, liquid jet is sharp enough [23, 24]: it is almost cylinder with the length of ℓ and radius of r_a. At the current higher than several tens μA, the jet is sharp enough, and at the current up to 30 μA, jet length is almost zero. For external heating due to electron bombardment, it is necessary that these electrons should be produced within an area of some micrometers [25]. Otherwise, the origin of the secondary electrons should be just on the axis. It is because the trajectory of the charged particle is most significantly affected by the field where its velocity is small.

Later, the author will argue the temperature increase at very low current regime, where the jet length is very small. In this case, the eq.(3.5) will be reduced to [21]

$$T_a = T_s + \frac{W}{2.2\kappa r_a}, \tag{3.6}$$

where W is the input power at the apex. Electron backstreaming of about 1 μA of 5 keV, $W = 5$ mW. The temperature increase would be 1200 K for r_a of 5 nm, for the case of Cu of which κ is 400 W K^{-1} cm^{-1}. For the case of Sn of which κ is 67 W K^{-1} cm^{-1}, the temperature increase would be 6800 K. It should be noted that the temperature increase is strongly dependent on κ. So good thermal conductor of Cu or Au, and Ge and Sn would behave differently. As the input power is proportional to the current of backstreaming electrons, which would be proportional to the emission current, it is expected that T_a increases with an increase in I_s or I_Ω.

3.1.4 Simplification of the model

In order to simplify the arguments, the author treats the present issue in the spherical coordinates. As described above, the jet-like structure should be taken into consideration,

but the purpose of the present attempt is to give a rough sketch of the model of the LMIS and not to give the precise parameters. The author first neglects the jet-like structure. Even if the jet like structure is taken into consideration, F at the apex does not differ significantly.

3.2 Estimation of temperature and electric field with experimental data

3.2.1 Validity of molecular ion formation mechanism

Before discussing the HTFE model, it is necessary to check the molecular ion formation mechanism, which has not been argued elsewhere. It is because the author will use the results of observation of molecular ions as an evidence of HTFE. The experimental results obtained in the previous chapter is given again in Table 3.2. In the table, F_{ev}'s for the singly charged atomic ions, doubly charged atomic ions, and singly charged dimer ions are also listed. F_{ev} was calculated by assuming the height of the surface hump is equal to zero. The values of E_b's were taken from Ref. [26]. For Au, F_{ev} for dimer is higher as compared with those of atomic ions, while for Cu, F_{ev} for dimer is close to that of doubly charged ions. The experimental results for Cu and Au ion sources are explained in terms with the above values: the currents of the molecular ions and doubly charged atomic ions were comparable. The In ion source yielded negligible amount of doubly charged ions but relatively large mount of dimer ions. From Table 3.2, it is seen that F_{ev} for dimer ions is lower than that for doubly charged ions. The relative ion currents of molecular ions with respect to the atomic ions are qualitatively explained as well as the doubly charged atomic ions with respect to the singly charged atomic ions.

3.2.2 Estimation of temperature and field

As for the Cu ion source, we have the detailed relation between the currents of singly charged atomic ions, doubly charged atomic ions, and singly charged dimer ions, and I_s as described in Chapter 2. In the model assumed above, we can roughly estimate the temperature from eq.(3.1). R_{dm} can be written as

$$R_{dm} = \nu' \exp\left(-\frac{H - E_b}{k_B T_a}\right),$$
(3.7)

where ν' is the ratio of the vibration frequency of a dimer to that of an atom. Since R_{dm} is not a function of F_P, the temperature $k_B T_a$ can be exclusively estimated by

$$k_B T_a = \frac{H - E_b}{-\ln(R_{dm}/\nu')}.$$
(3.8)

Table 3.2: Relative ion currents of molecular ions and evaporation fields.

Metal	Relative ion currents		Evaporation fields ($V \cdot nm^{-1}$)		
	R_{21}	R_{dm}	M^+	M^{2+}	M_2^+
Au	0.09 – 0.34	0.076 – 0.083	53	54	73
Cu	0.017 – 0.06	0 – 0.083	30	43	46
In	–	0.01	13	32	25
Sn	0.37 – 1.08	0.097	26	23	36
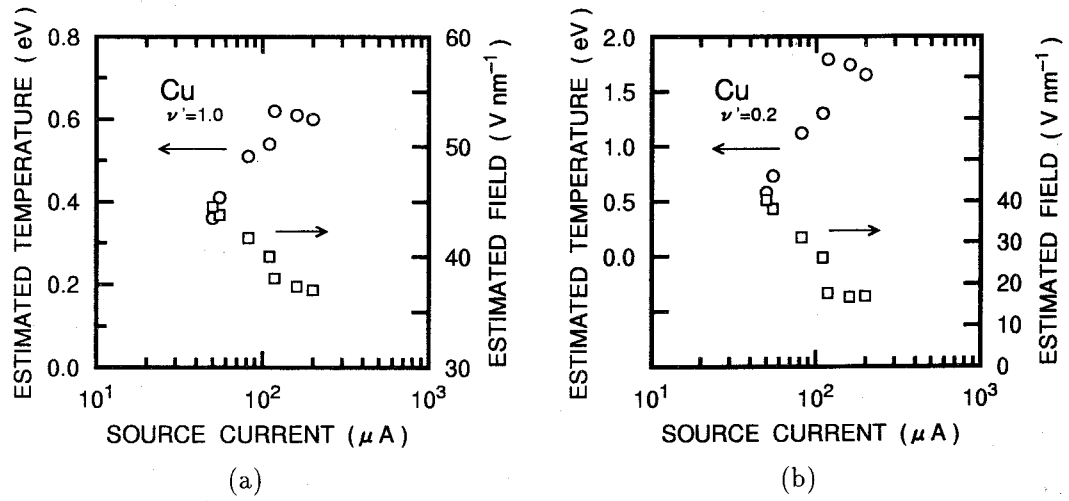
Figure 3.2: Estimated temperature and field for Cu ion source. (a) $\nu' = 1.0$ and (b) $\nu' = 0.2$.

Once the temperature is determined, we can calculate F_P from

$$F_P = \left[\frac{4\pi\varepsilon_0}{(2\sqrt{2}-1)^2 e^3}\right][k_B T_a \ln(R_{21}) + V_2 - \phi]^2. \tag{3.9}$$

Figures 3.2(a) and 3.2(b) show the examples of the results of above estimation with ν' of 0.2 and 1, respectively. The experimental data shown in Fig. 2.14 were used, and in this region R_{21} has already began to decrease. $k_B T_a$ is first estimated from eq.(3.8) with the data shown in Fig. 2.14. Then F_P is estimated from eq.(3.9) with the above estimated values. Determination of an appropriate value of ν' is difficult, but the estimated T_a was approximately 0.5 – 2 eV. In the current regime of 50 to 200 μA, T_a increased and F_P decreased monotonically.

3.2.3   Effects of change in temperature and field on R_{21}

In the following, the author will try to establish a model of LMIS with the experimental results on R_{21}. Here it is necessary to summarize the effects of the change in T_a and also that in F_P on R_{21}. R_{21} can be written as

$$R_{21} = \exp\left[-\frac{V_2 - \phi - s'_{21}F_P^{1/2}}{k_B T_a}\right] = \exp\left[-\frac{Q_{21}(F_P)}{k_B T_a}\right], \tag{3.10}$$

where Q_{21} is the numerator in block parenthesis. Here the author excludes the effect of $k_B T_a$ from s_{21}, thus the author writes newly s'_{21} as $s_{21} \times k_B T_a$. Differentiating eq.(3.10), we obtain,

$$\frac{dR_{21}}{R_{21}} = \frac{s'_{21}}{2k_B T_a}\frac{dF_P}{F_P^{1/2}} + \frac{Q_{21}(F_P)}{k_B T_a}\frac{d(k_B T_a)}{(k_B T_a)}. \tag{3.11}$$

Whether R_{21} increases or decreases is defined by the above equation. The temperature dependence is different between the materials with higher and lower F_{ev} for doubly charged ions. In the case of the material with a higher F_{ev} for the doubly charged ions, $Q_{21}(F_P)$ is positive, either increase of F_P or $k_B T_a$ causes an increase in R_{21}. Condition for the decrease of R_{21} at the higher current is

$$\frac{s'_{21}}{2k_B T_a}\frac{dF_P}{F_P^{1/2}} + \frac{Q_{21}(F_P)}{k_B T_a}\frac{d(k_B T_a)}{(k_B T_a)} < 0. \tag{3.12}$$

From the above equation, decrease of either T_a or F_P is necessary. Increase of F_P or decrease of T_a are not plausible from the present heating mechanism. In fact, the mass spectroscopic investigation showed saturated temperature at the region where R_{21} decreased. Thus, at a higher current regime, decrease in F_P is necessary. At the low current regime, R_{21} increased. For this, it is not necessary to increase F_P. An increase in $k_B T$ will increase R_{21}, if F_P does not change significantly. In the following sections, the author will argue these increase and decrease of F_P and T_a much more in detail.

3.3 Criterion for decrease of electric field

3.3.1 Relationship among the physical parameters

Although it is possible to explain the variation of mass spectrum including molecular ions with the HTFE model, we must check whether the three essential equations holds or not. Here the three essential equations mean the equation of rate of ion formation, the FD equation, and the Poisson's equation: eqs.(2.28), (2.31), and (2.33), as described in the previous chapter. The author begins with the derivation of the critical relation for the decrease of F_P, because it is generally difficult to be accepted. Here in this section, T_a is assumed to be constant for simplicity. The author uses the equation of space charge limited current (SCLC) with small charge approximation [2,27] instead of the Poisson's equation for analytical investigation. The equation of SCLC with small charge approximation can be written as

$$F_L^2 - F_P^2 = \frac{c_3}{\varepsilon_0} J \sqrt{V}, \tag{3.13}$$

where F_L is the Laplace field (the potential without space charge), F_P is the Poisson field (the potential with space charge), $c_3 = (4/3)\sqrt{2M_I/e}$, and V is the applied voltage. The meaning of this equation is such that the space charge almost shields the Laplace field. The Laplace field F_L can be written as,

$$F_L = \frac{V}{\beta r_a} \tag{3.14}$$

where β is the coefficient weakly dependent on r_a. For hyperboloid, $\beta = \{\ln(4d/r_a)\}/2$, where d is the distance between the tip and the counter electrode [28]. Putting eq.(3.14) into eq.(3.13) and differentiating both sides, we obtain

$$2\left[\left(\frac{V}{\beta r_a}\right)^2 - \frac{c_3}{4\varepsilon_0} J \sqrt{V}\right] \frac{dV}{V} = 2\left(\frac{V}{\beta r_a}\right)^2 \frac{dr_a}{r_a} + \frac{c_3}{\varepsilon_0} J \sqrt{V} \frac{dJ}{J}. \tag{3.15}$$

Here the change of F_P was assumed to be small. Taking $(V/\beta r_a)^2 \sim (c_3/\varepsilon_0) J \sqrt{V}$ into consideration, eq.(3.15) can be reduced to

$$\frac{3}{2}\frac{dV}{V} = 2\frac{dr_a}{r_a} + \frac{dJ}{J}. \tag{3.16}$$

This is the same equation that can be derived from Langmuir-Child equation in spherical coordinates [29], and the author checked the Poisson field can be neglected even in the present case with a large value of F_P [30]. As shown experimentally, F_P decreased with an increase in V. It can be also said that J decreased with an increase in V. To allow this, the right-hand side of eq.(3.16) should be positive, even though the second term is

negative. This means that r_a rapidly increases with an increase in V. As described earlier, the increase of r_a with an increase in I_s is generally accepted [1,31]. The dependence of J on r_a should satisfy

$$2\frac{\mathrm{d}r_a}{r_a} > -\frac{\mathrm{d}J}{J}, \tag{3.17}$$

through F_P or the other parameters. This can be written as

$$J \propto \frac{1}{r_a^n}, \quad n < 2 \qquad \text{or} \qquad J = \sum_{i=-\infty}^{2} \frac{b_i}{r_a^i}, \tag{3.18}$$

where b_i is the coefficient of the series expansion of J. This is a general equation of the criterion for the decrease of the electric field with an increase in the voltage. To apply this equation to LMIS, the FD equation at the apex should be included in the present consideration.

3.3.2 Required relation between electric field and current density for decrease of R_{21}

As already described, the FD equation at the apex [1] can be written as

$$S_F = \frac{1}{2}\varepsilon_0 F_P^2 = \frac{1}{2}\rho_m v^2 + \frac{2\gamma}{r_a} = \frac{1}{2}\rho_m \left(\frac{J}{eN_v}\right)^2 + \frac{2\gamma}{r_a} = K + S_T. \tag{3.19}$$

The authors have treated this equation without massive flow and shown the possibility of the formation of a space charge stabilized liquid cone for liquid-metal electron sources [32]. Differentiating both sides of eq.(3.19), we obtain the following equation after some arithmetical manipulation.

$$\frac{\mathrm{d}J}{J} = \frac{\frac{1}{2}\varepsilon_0 F_P^2}{\frac{1}{2}\rho_m(J/eN_v)^2}\frac{\mathrm{d}F_P}{F_P} + \frac{1}{2}\frac{2\gamma/r_a}{\frac{1}{2}\rho_m(J/eN_v)^2}\frac{\mathrm{d}r_a}{r_a} = \frac{S_F}{K}\frac{\mathrm{d}F_P}{F_P} + \frac{1}{2}\frac{S_T}{K}\frac{\mathrm{d}r_a}{r_a}. \tag{3.20}$$

Substituting eq.(3.20) to eq.(3.16),

$$\frac{3}{2}\frac{\mathrm{d}V}{V} = 2\left[1 + \frac{1}{4}\frac{S_T}{K}\right]\frac{\mathrm{d}r_a}{r_a} + \frac{S_F}{K}\frac{\mathrm{d}F_P}{F_P}. \tag{3.21}$$

From this equation, it is possible that both r_a and F_P increase with an increase in V, but also it is possible that either of r_a or F_P increases and the other decreases. Whether the case is the former or the latter can be known by setting the right hand side is equal to zero,

$$2\left[1 + \frac{1}{4}\frac{S_T}{K}\right]\frac{\mathrm{d}r_a}{r_a} + \frac{S_F}{K}\frac{\mathrm{d}F_P}{F_P} = 0. \tag{3.22}$$

From eq.(3.22),

$$F_{\mathrm{P}} \propto r_{\mathrm{a}}^{-2\frac{1+S_{\mathrm{T}}/4K}{S_{\mathrm{F}}/K}} = r_{\mathrm{a}}^{-2\frac{1+S_{\mathrm{T}}/4K}{1+S_{\mathrm{T}}/K}} = r_{\mathrm{a}}^{X}. \tag{3.23}$$

The relative magnitudes of S_{T}, K, and S_{F} are not known and some researchers assumed differently, as described earlier. For example, Kingham and Swanson [1] treated the equation with no restriction of magnitudes of these terms, Forbes [31] treated that S_{T} is in balance with S_{F}. The author [8] has assumed in Chapter 2, the liquid cone is terminated where $K \sim S_{\mathrm{T}}$. These different treatments, the author here defines: the case I: Kingham and Swanson, the case II: Gotoh *et al.*, and the case III: Forbes. For each of them, the critical relation becomes,

$$\left\{ \begin{array}{lll} \text{Case I} & S_{\mathrm{T}}/K \to 0, & F_{\mathrm{P}} \propto r_{\mathrm{a}}^{-2}, \\ \text{Case II} & S_{\mathrm{T}}/K \to 1, & F_{\mathrm{P}} \propto r_{\mathrm{a}}^{-5/4}, \\ \text{Case III} & S_{\mathrm{T}}/K \to \infty, & F_{\mathrm{P}} \propto r_{\mathrm{a}}^{-1/2}, \end{array} \right. \tag{3.24}$$

For the current density,

$$\frac{\mathrm{d}J}{J} = \left[1 + \frac{3S_{\mathrm{T}}/K}{4 + S_{\mathrm{T}}/K}\right] \frac{\mathrm{d}F_{\mathrm{P}}}{F_{\mathrm{P}}} = Y_J \frac{\mathrm{d}F_{\mathrm{P}}}{F_{\mathrm{P}}}. \tag{3.25}$$

In a similar way with eq.(3.24), the critical relation between J and F_{P} is

$$\left\{ \begin{array}{lll} \text{Case I} & S_{\mathrm{T}}/K \to 0, & J \propto F_{\mathrm{P}} \\ \text{Case II} & S_{\mathrm{T}}/K \to 1, & J \propto F_{\mathrm{P}}^{8/5} \\ \text{Case III} & S_{\mathrm{T}}/K \to \infty, & J \propto F_{\mathrm{P}}^{4} \end{array} \right. \tag{3.26}$$

From this equation, to decrease F_{P} as I_{s} increases, in other words, V increases, the relation between F_{P} and J should be as weak as $J \propto F_{\mathrm{P}}^{4}$.

3.3.3 Dependence of source current and current density on electric field

Since we have given the relation between I_{Ω} and F_{P} in the previous chapter, we can know whether the decrease of F_{P} is possible or not for the given ionization model. Here considering the angular current I_{Ω},

$$\frac{\mathrm{d}I_{\Omega}}{I_{\Omega}} = 2\frac{\mathrm{d}r_{\mathrm{a}}}{r_{\mathrm{a}}} + \frac{\mathrm{d}J}{J}. \tag{3.27}$$

If the relation between r_{a} and F_{P} is slightly deviated from the critical relation, we may write

$$F_{\mathrm{P}} \propto r_{\mathrm{a}}^{X+\Delta X}, \tag{3.28}$$

eq.(3.25) will be

$$\frac{\mathrm{d}J}{J} = \left[1 + \left(1 + \frac{1}{2(X + \Delta X)}\right)\frac{S_{\mathrm{T}}}{K}\right] \frac{\mathrm{d}F_{\mathrm{P}}}{F_{\mathrm{P}}} = Y_J \frac{\mathrm{d}F_{\mathrm{P}}}{F_{\mathrm{P}}}. \tag{3.29}$$
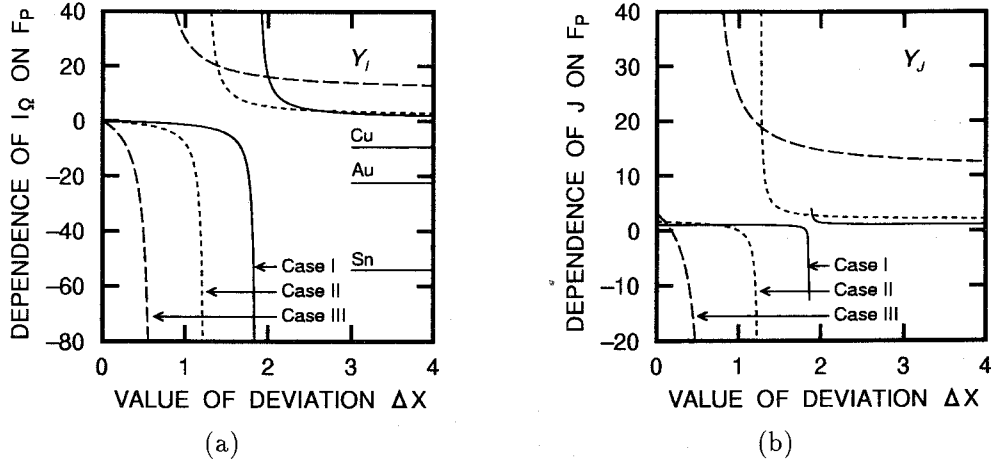
Figure 3.3: Relation between (a) I_s and F_P, and (b) J and F_P.

This equation is reduced to eq.(3.25) when $\Delta X = 0$. And eq.(3.27) will be

$$\frac{dI_\Omega}{I_\Omega} = \frac{\Delta X(1 + S_T/K)}{X + \Delta X}\frac{dF_P}{F_P} = Y_I\frac{dF_P}{F_P}. \tag{3.30}$$

Figures 3.3(a) and 3.3(b) show the dependence of I_Ω on F_P and J on F_P, that is, Y_I and Y_J as a function of ΔX. Solid, dashed, and broken lines represent the characteristics for the cases I, II, and III, respectively. Here it should be noted that $K = 0$ gives divergence of the relation, so S_T/K was taken as 0.1 and 10 for the cases I and III, respectively. In Fig.3.3(a), relation for Cu, Au, and Sn ion sources calculated with the PI theory in Chapter 2 is indicated. Assuming the case I, if $\Delta X < 2$, then $dI_\Omega > 0$ with $dF_P < 0$, which qualitatively agrees with the experimental result. However, taking the fact into consideration that dependence of $F_P \propto I_\Omega^{-10}$, X should be close to 2. For the case III, $\Delta X < 1/2$ is necessary and also ΔX should be close to 1/2. Under such a situation, dependence of J on F_P becomes very weak. Again here considering the case I. For Cu, $Y_I = -9.43$ is realized at $\Delta X = 1.67$, and for Au, $Y_I = -22.4$ is realized at $\Delta X = 1.78$. Obtained indices of relation Y_J's are 0.84 and 0.5, respectively. These values are surprisingly small for field evaporation. This discrepancy may be attributed to the first assumption: the field dependence of PI theory is still strong. And if the dependence of I_Ω on F_P is weaker, the dependence of J on F_P becomes stronger, and vice versa.

If we assume the conventional LTFE, the dependence of J on F_P is more strong, and it is clearly seen that the dependence of I_Ω on F_P is also strong. For example, the dependence of J on F_P is almost the thirty-first power. This corresponds to $\Delta X = 1.862$ in Fig. 3.3(b), and the resultant value of Y_J in Fig. 3.3(a) is almost 1200. For the cases II and III,
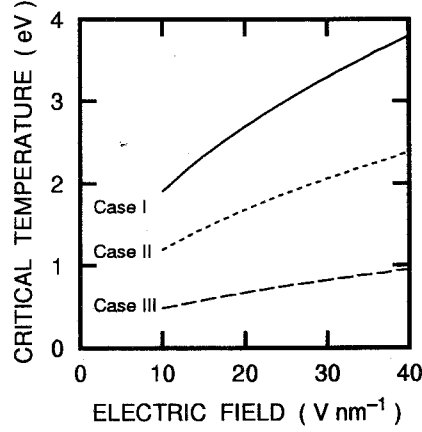
Figure 3.4: Relation between T and $F_{\rm P}$ for different cases.

$\Delta X = 1.27, Y_I = 100$, and $\Delta X = 0.88, Y_{I.} = 40$. Anyway, these strong relations between I_Ω and $F_{\rm P}$ agree with the result of numerical solution made in Chapter 2. The numerical simulation made in Chapter 2 corresponds to this case and $F_{\rm P}$ indeed increases [8].

3.3.4 Temperature necessary to give lower dependence of current density on electric field

In order to have the weak dependence of J on $F_{\rm P}$, it is necessary to assume that the temperature is high, as the author mentioned at the beginning of this chapter. The relation between J and $F_{\rm P}$ is

$$\frac{\mathrm{d}J}{J} = \frac{s_1}{2k_{\rm B}T_{\rm a}}F_{\rm P}^{1/2}\frac{\mathrm{d}F_{\rm P}}{F_{\rm P}}. \tag{3.31}$$

If we obtain the critical relation, $T_{\rm cr}$ necessary to satisfy the critical relation can be calculated with the following equation.

$$k_{\rm B}T_{\rm cr} = \frac{1}{2\delta_{\rm cr}}\left[\frac{e^3 F_{\rm P}}{4\pi\varepsilon_0}\right]^{1/2}, \tag{3.32}$$

where $\delta_{\rm cr}$ is the power of critical relation for the cases I, II and III. From eq.(3.32), it is known that the critical temperature $T_{\rm cr}$ is dependent on F. Figure 3.4 shows the relation between $T_{\rm cr}$ and $F_{\rm P}$ for these cases. It is shown that approximately 0.5 – 3 eV is necessary for $F_{\rm P}$ between 10 – 30 V nm^{-1}. And these values agree with those already shown in Fig. 3.2. For this $k_{\rm B}T_{\rm cr}$, $F_{\rm P}$ may be reduced to 10 V nm^{-1}. In such a condition, the left hand side of the FD equation is of the order of 10^8 N m^{-2}. $S_{\rm T}$ can be in balance with this stress with $r_{\rm a}$ of 5 nm. K of the liquid at 10 μA emission through an area of which radius is
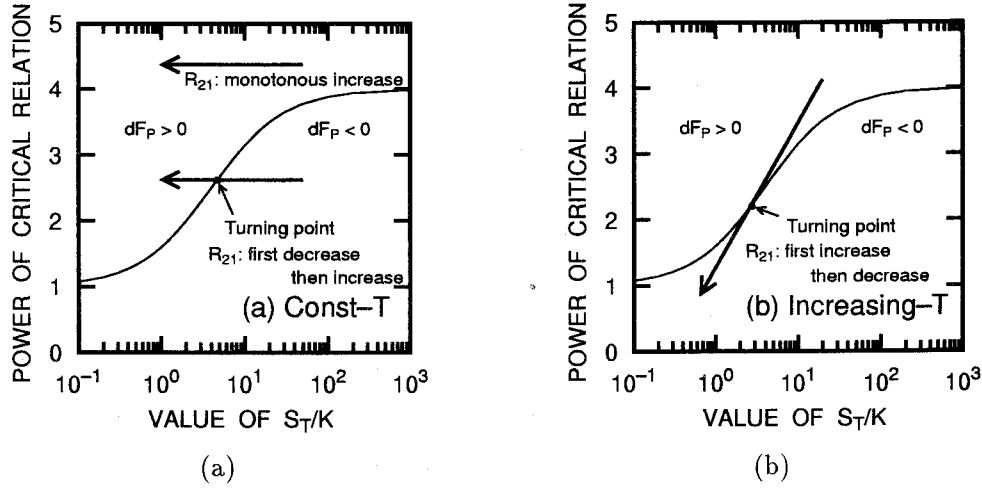
Figure 3.5: Power of critical relation for decrease of F_P due to increase of V.

5 nm, is 10^7 N m^{-2}. This corresponds to the case III rather than case I or II. But these values are sensitive to r_a, thus the case I or II may be plausible depending on the situation.

3.4 On the increase of R_{21} at low current regime

3.4.1 Consideration of variation in temperature

As for the increase of R_{21}, the conventional model may be acceptable. The Au and Cu ion sources showed the decrease of R_{21} at the higher current, but R_{21} increased at the lower current regime. Also Sn source exhibited a tiny peak of R_{21} at the extremely low current [33]. From the argument made above, the change is monotonically, so something should be changed for this behavior. For eq.(3.19), the magnitude of each term in this equation would change in accordance with I_s. At the very low current regime, K is small, and thus the case III is plausible. As I_s increases, the balance would become the case II or the case I. If the dependence of J on F_P does not change throughout the range in consideration, F_P decreases at first then increases. Figure 3.5 shows a rough sketch of the criterion for the increase or decrease of F_P with an increase in I_s. The abscissa is taken for the ratio of S_T/K and the ordinate is the critical power relation between J and F_P. The solid curve shows the critical relation between J and F_P which is $Y_{J,cr}$ in eq.(3.25). The left side of the curve indicates the increase of F_P and the right side indicates the decrease of F_P, with respect to the increase in I_Ω. If J depends only on F_P, the working point moves from the right to the left, as shown in Fig. 3.5(a). At the point where the working point crosses

the critical relation, the tendency of R_{21} changes. However, this case, R_{21} first decreases and then increases. The model which has different dependence of J on F_{P} is required.

One of the solutions is introducing the increase of T_{a}. For this, we should start at the low temperature where the dependence of J on F_{P} is strong, as is the case with LTFE. The change in J is expressed in the following manner, if J of the singly charged ion dominates.

$$\frac{\mathrm{d}J}{J} = \frac{s_1'}{2k_{\mathrm{B}}T}\frac{\mathrm{d}F_{\mathrm{P}}}{F_{\mathrm{P}}^{1/2}} + \frac{H + V_1 - \phi - s_1'F_{\mathrm{P}}^{1/2}}{k_{\mathrm{B}}T}\frac{\mathrm{d}k_{\mathrm{B}}T}{k_{\mathrm{B}}T}, \tag{3.33}$$

where s_1' is the coefficient of field dependent term (in this model, $s_1' = \sqrt{e^3/4\pi\varepsilon_0}$). If the T_{a} increases with an increase in I_Ω, the operational points moves along the arrow in Fig. 3.5(b). Such a motion explains the behavior of R_{21} throughout the observed current region.

The changes of J and R_{21} with the changes in $k_{\mathrm{B}}T$ and F_{P} are

$$\begin{cases} \dfrac{\mathrm{d}J}{J} = \dfrac{1}{k_{\mathrm{B}}T}\left[\dfrac{s_1'}{2}F_{\mathrm{P}}^{1/2}\dfrac{\mathrm{d}F_{\mathrm{P}}}{F_{\mathrm{P}}} + (Q_1 - s_1'F_{\mathrm{P}}^{1/2})\dfrac{\mathrm{d}(k_{\mathrm{B}}T)}{k_{\mathrm{B}}T}\right], \\[4mm] \dfrac{\mathrm{d}R_{21}}{R_{21}} = \dfrac{1}{k_{\mathrm{B}}T}\left[\dfrac{s_{21}'}{2}F_{\mathrm{P}}^{1/2}\dfrac{\mathrm{d}F_{\mathrm{P}}}{F_{\mathrm{P}}} + (V_2 - \phi - s_{21}'F_{\mathrm{P}}^{1/2})\dfrac{\mathrm{d}(k_{\mathrm{B}}T)}{k_{\mathrm{B}}T}\right]. \end{cases} \tag{3.34}$$

The above equations imply that the effects of increase both in temperature and in field result in the increase of R_{21} or J, because $Q_1 - s_1'F_{\mathrm{P}}^{1/2}$ and $V_2 - \phi - s_{21}'F_{\mathrm{P}}^{1/2}$ are both positive for Au and Cu. Assuming the material is Au, in which the operational field would be about 52 V nm^{-1} and the operational temperature of about 1400 K (0.12 eV), these equations can be written as

$$\begin{cases} \dfrac{\mathrm{d}J}{J} = 0.69\mathrm{d}F_{\mathrm{P}} + 2.8\mathrm{d}k_{\mathrm{B}}T, \\[4mm] \dfrac{\mathrm{d}R_{21}}{R_{21}} = 1.3\mathrm{d}F_{\mathrm{P}} + 32\mathrm{d}k_{\mathrm{B}}T, \end{cases} \tag{3.35}$$

where F_{P} and $k_{\mathrm{B}}T$ are in V nm^{-1} and eV. The physical parameters of Au are taken from Tsong's paper [34]. The increase in $k_{\mathrm{B}}T$ will cause the decrease of F_{P}. If the deformation of the liquid due to change in the operational parameters, maintains so as to have the same current density, that is, $\mathrm{d}J = 0$, $\mathrm{d}F_{\mathrm{P}} = -0.41\mathrm{d}k_{\mathrm{B}}T$. In such a case $\mathrm{d}R_{21}/R_{21}$ becomes $29\mathrm{d}k_{\mathrm{B}}T$. This means R_{21} can increase with less significant increase in J. It is also possible that J decreases with an increase in $k_{\mathrm{B}}T$, so far as

$$|\mathrm{d}F_{\mathrm{P}}| > 0.41\mathrm{d}k_{\mathrm{B}}T, \tag{3.36}$$

holds.

3.4.2 R_{21} as a function of I_s

Since the present model assumes the lower temperature at the low current regime, F_P is almost constant. In such a case, $Q_{21}(F_P)$ becomes a constant value of Q_{21}. The variation of r_a with respect to I_Ω is not clear, but if we obey the argument made by Kingham and Swanson [1] and assume $I_i \propto I_\Omega$, r_a is proportional to $I_\Omega^{1/2}$, and in our case r_a is proportional to $I_\Omega^{2/3}$. If the heating of the apex is achieved by the bombardment of the electrons backstreaming from the counter electrode to the apex, those contributing this effect is restricted to the small solid angle close to the beam axis. Consequently, the input power is proportional to I_Ω rather than I_s. Considering this, we can write as $W = V_{ext}\gamma_{ie}I_\Omega$, where γ_{ie} is the secondary electron emission coefficient. Substituting eq.(3.6) together with the above relations to eq.(3.10), we obtain

$$\ln R_{21} \propto -\frac{\kappa Q_{21}}{k_B \gamma_{ie} V_{ext}} I_\Omega^{-1/2} = -\frac{\kappa Q_{21}}{k_B \gamma_{ie} V_{ext}} I_s^{-\zeta_1/2}, \tag{3.37}$$

where ζ_1 is the power of the angular current of singly charged ions as defined in Chapter 2. Note that at the low current regime, the relation between I_Ω and r_a should be such that $r_a \propto I_\Omega^{1/2}$, as Kingham and Swanson derived. Since almost all experimental results except Sn at very low current has the value of $R_{21} < 1$, then $Q_{21}(F_P)$ is positive. The curve will be upward convex. This equation suggests that the metal with lower κ shows the higher R_{21} and the increase of R_{21} with respect to the increase in I_s is slower for those with a lower ζ_1. This agrees with the results shown in Fig. 2.13. Especially, the author emphasizes here the raise up of R_{21} at the low current regime is similar for Au and Cu, if the abscissa is taken for I_Ω. Figure 3.6 shows the comparison of the rate of increase of R_{21} for Au and Cu ion sources. This figure is a redraft of Fig. 2.13, but the intensity of R_{21} for Cu is multiplied by 5 for better comparison. As is clearly seen in this figure, The slope of the initial increase of R_{21} for Cu overlaps with that for Au.

3.5   Consistency of high temperature field evaporation model

3.5.1   Acceptable apex radius and current density

As discussed above, the HTFE model explains the discrepancy that has not been explained by the conventional LTFE model. However, it is necessary to show the consistency of HTFE model with the other experimental evidences, such as energy distribution, and change in the liquid shape.

As described previously, J derived from the theory of Kingham and Swanson is too large. In the present model, we can also estimate the rate of ion formation. If we accept
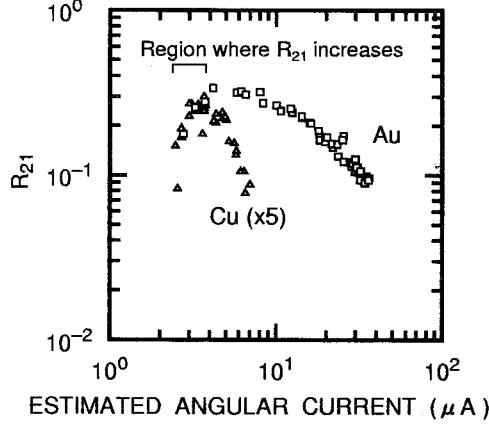
Figure 3.6: Comparison of the rate of increase of R_{21} for Au and Cu ion sources. The magnitude of R_{21} for Cu is multiplied by 5 for better comparison.
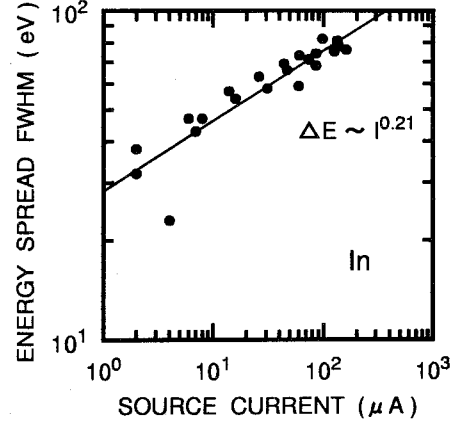
Figure 3.7: Dependence of energy spread as a function of source current. Redraft of Fig. 2.10 in Chapter 2.

the assumption made in Chapter 2, r_a at 40 μAsr^{-1} is approximately 4.3 nm for Au, where 720 atoms are arranged. In such a situation, J becomes 2×10^{12} Am^{-2}, which is equal to the ejection frequency of 350 GHz. The possibility for evaporation from the liquid surface per an atom is lower than 1×10^{12} Hz, as shown in Table 3.3. Similar calculation is possible for the other metals and the ejection frequencies are all less than 10^{12} Hz. This frequency is lower than that of atomic vibration at the surface, and thus the present model can be treated as a quasi-static model. At the same time, the above value satisfies the lowest value of J which was derived in Chapter 2.

The jet-structure observed in transmission electron microscope is less than 10 nm in r_a [35]. r_a obtained in the present model agrees with the experimentally observed value.

3.5.2 Energy distribution

As shown in Chapter 2, energy spread increased with an increase in I_s. The wide energy spread is believed to be due to Börsch effect and Knauer derived the following relationship [36].

$$\Delta E = 5.8\pi \frac{e}{4\pi\varepsilon_0} \left(\frac{m_I}{V_0}\right)^{1/3} r_a J^{2/3}. \tag{3.38}$$

Knauer showed agreement of this relation with experimental results showing that $\Delta E \propto I_s^{2/3}$. However, as is shown in the above equation, ΔE also depends upon r_a. Assuming the relationship between I_s and r_a as derived in Chapter 2, the above relation becomes

$$\Delta E \propto I_s^{0.3}. \tag{3.39}$$

Table 3.3: Ejection frequency of surface atoms for various metals calculated by the HTFE model.

Metal	Cu	Au
r_a at 40 μAsr^{-1} (nm)	2.47	4.3
ν_{ejec} (THz)	0.86	0.35

The relation obtained in Chapter 2 is redrafted in Fig. 3.7 in order to show the dependence of ΔE upon I_s. The experiments show that the relation should be

$$\Delta E \propto I_s^{0.2}, \qquad (3.40)$$

which does not disagree with eq.(3.39).

3.5.3   Effect of jet-like protrusion

The author has argued the change of the liquid shape in the simplified model. However, the change of the liquid shape is complicated, and thus the model should explain the change including the jet-like protrusion. At the current under 10~ 30 μA, the jet-like protrusion is not long enough [23]: the shape is almost "Taylor cone". Above 30 μA, the jet-like protrusion is formed and the length becomes larger with an increase in I_s. The formation of the jet-like protrusion is generally believed to be necessary to maintain high field under significant space charge shielding [31]. If so, ion emission occurs not only from the apex but also from the side face of the liquid jet. This cannot be accepted because the current density at the apex is large enough, and consequently, escape of the atoms toward the radial direction is not possible. Considering this, the effect of the jet-like protrusion does not alter the above arguments.

3.6   Modeling of the ionization point

3.6.1   Changes in physical parameters during evolution of liquid cone

Since the approximate F_P and r_a values have been determined, we can now discuss the modeling of the LMIS. Here in this section, the author draws a brief sketch of the operation

of the LMIS. As shown in Chapter 2, an LMIS has a threshold voltage V_{th} but once cone is formed, it can be operated at a voltage lower than V_{th}. We should explain now the balance between S_T and S_F, which was once broken at the initial stage, and again achieved at the operation. At the initial stage, liquid has a curvature of r_0 on the base needle. At the apex, the electric field F, which is roughly expressed by V/kr_0, is applied. The field causes the electric stress of $S_F = (1/2)\varepsilon_0 F^2 = (1/2)\varepsilon_0 V^2/(kr_0)^2$ and the liquid would maintain its curvature owing to the surface tension stress $S_T = 2\gamma/r_0$. The liquid will be pulled to be deformed when V exceeds the threshold V_{th},

$$V_{th} = 2k\sqrt{\gamma r_0/\varepsilon_0}, \tag{3.41}$$

This process was already suggested [37], and the threshold is confirmed by many researchers [38].

As for the physics after breaking the initial balance, little argument has been made so far [39]. We can calculate the physical parameters with three essential equations which were already expressed.

$$\begin{cases} \dfrac{1}{2}\varepsilon_0 F_P^2 = \dfrac{1}{2}\varepsilon_0 \left(\dfrac{V}{kr_a}\right)^2 - \dfrac{c_3}{2}J\sqrt{V}, \\ \dfrac{1}{2}\varepsilon_0 F_P^2 = \dfrac{1}{2}\rho_m \left(\dfrac{J}{eN_v}\right)^2 + \dfrac{2\gamma}{r_a}, \\ J = \overline{k}e\nu N_s \exp\left[-\dfrac{Q(F_P)}{k_B T_a}\right], \end{cases} \tag{3.42}$$

which are the equations of the SCLC, FD, and field evaporation (FE). These are equivalent to eqs.(3.13), (2.32), and (3.1), respectively, but the equation of SCLC was slightly modified to meet the explanation in the following. The term at the left-hand side of the modified SCLC equation has now the dimension of stress, the author here newly defines the terms in the right hand side as $S_{F(L)}$ and S_{SC}, respectively.

These equations are unified to:

$$V^2 - \dfrac{c_3}{\varepsilon_0}k^2 J r_a^2 \sqrt{V} - \left(\dfrac{k^2 \rho_m}{\varepsilon_0 e^2 N_v^2}J^2 r_a^2 + \dfrac{4k^2\gamma r_a}{\varepsilon_0}\right) = 0. \tag{3.43}$$

This equation is complicated because we should take T_a which does not have explicit relation with the other parameters, into consideration. If the FD equation does not contain the inertia term (K), the above equation is quite similar to that of an electron source [32]. In the case of the electron source, we have two solutions for the equations of the balance between S_F and S_T. One is the balance without space charge and the other is the balance with space charge. The author has demonstrated the explanation graphically for this specific electron source [32], and here in this dissertation also, he tries to explain the operation of the LMIS in a similar manner.
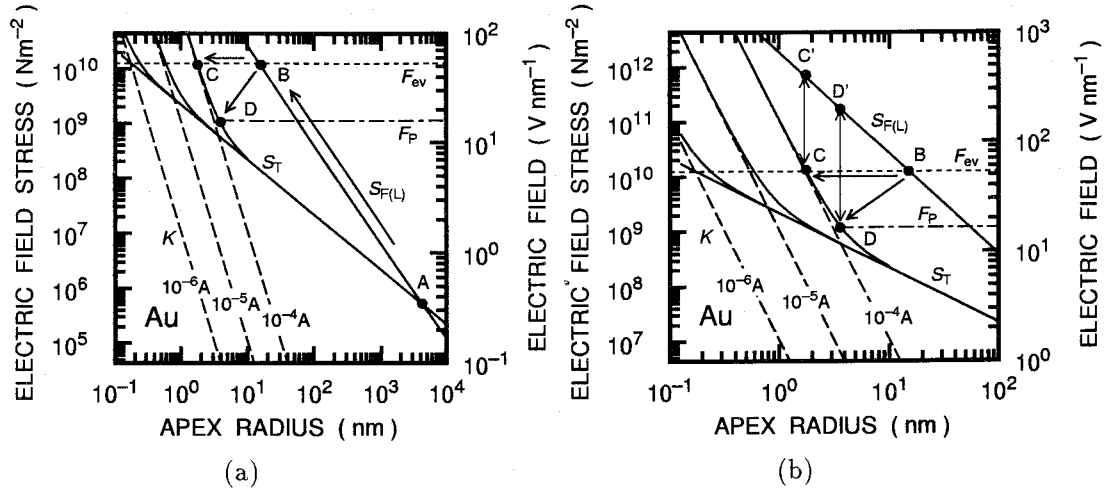
Figure 3.8: Changes in the parameters during the evolution of liquid cone.
(a) from initiation to termination of cone formation, and (b) magnified
figure of (a) around operating point.

In the following, the author explains the changes in the physical parameters under the evolution of liquid cone with Fig. 3.8, taking eq.(3.42) into consideration. Figure 3.8(a) shows the relation between r_a and S_T or K. Figure 3.8(b) is a magnified figure of Fig. 3.8(a). The abscissa of Fig. 3.8 is r_a and the ordinate at the left-hand side is S_F, and that at the right hand side is F_P corresponding to the left-hand side. The solid line with F_L shows the change in the Laplace field. This line has the slope of -2 with the scale of the left-hand side. Also S_T is given by a solid line in this figure, and it has the slope of -1 with the scale of the left-hand side. K values corresponding to $1 \sim 100 \, \mu A$ are also shown by broken lines.

The initial point, where the cone formation starts, is expressed by the point A. This case r_0 is almost 4 μm and the physical parameters chosen are for Au. After the break of the balance, r_a becomes smaller maintaining V. Thus, the operating point moves from the point A toward the upper left along the line of F_L. The balance will be never achieved again without the presence of the space charge that shields the electric field. At the first stage, the "evaporation field" may be achieved. F becomes higher and finally ion emission occurs at $F = F_{ev}$, which is shown as the point B in Fig. 3.8. According to the conventional LTFE model, the operating point moves to the point C, whereas it moves to the point D, if the new HTFE model is assumed.

First, the author explains how the conventional LTFE model works in this diagram, especially with Fig. 3.8(b). At the point B, sudden appearance of the ion flux causes a

large space charge, a higher $F_{\rm L}$ is necessary to satisfy the SCLC equation. Due to this, of course, the jet-like protrusion may be produced to realize a high field. As the further reduction of $r_{\rm a}$, $F_{\rm L}$ becomes larger but $F_{\rm P}$ remains at $F_{\rm ev}$. The operating point is stabilized at the point C. At the point C, $S_{\rm F(L)}$ can be shown by the point C'. The difference between C and C' corresponds to the $S_{\rm SC}$ value:

$$S_{\rm F(L)} = S_{\rm SC} + K. \tag{3.44}$$

The way to determine the exact position of the point C should be owing to the numerical calculation. In the present case, $I_{\rm i}$ is 100 μA, and K dominates the operation.

In the author's new model, however, some optimization of the emission point is made. During the evolution of the cone (and probably the jet), we allow the temperature increase. Due to this, the operating $F_{\rm P}$ will become lower. Because of the increase in $F_{\rm L}$ and decrease in $F_{\rm P}$, the operating point is stabilized at the point D, where $r_{\rm a}$ is larger than the conventional model. This point D assumes that K and $S_{\rm T}$ are comparable each other, as assumed in Chapter 2 (the case II in this chapter). In this case also, the difference of the points between D and D' gives $S_{\rm SC}$.

The above two cases are not easily compared because of uncertainty of the temperature, but one can easily understand that the latter model gives lower $F_{\rm P}$ and larger $r_{\rm a}$.

3.6.2 Changes in physical parameters with varying voltage

When V changes, $I_{\rm i}$ changes. Figure 3.9 shows the changes of the physical parameters with the change in V. $S_{\rm SC}$ is dominated mostly by J, this term should increase when V is reduced. In the figure, E shows possible operating point. The difference between E and E' corresponds to $S_{\rm SC}$ and it can be larger as compared with difference between D and D'. At a certain point, $S_{\rm SC}$ should decrease because R_{21} had maximum. So far as considering the reduction of $r_{\rm a}$, it may not be possible.

As the lowering of V, the operating point moves toward left along the thick solid line and finally approaches the $F_{\rm ev}$ line. Here the current is small, and thus no temperature elevation is necessary. Indeed, the lower current reduces the input power at the apex. Thus after the point comes to F, it moves toward G along the $F_{\rm ev}$ line. After the point reaching the $F_{\rm ev}$ line, the field is extremely high and further increase of J is not expected. Nevertheless, balancing condition requires higher $S_{\rm SC}$ value. At the point where this $S_{\rm SC}$ can not maintain, the cone collapses and ion emission stops. This motion of the operating point satisfies the argument that the author made. At the very low current regime, the operation is somewhat similar to the LTFE, and through the temperature increase, the operating point moves to the HTFE model. The above model gives monotonous decrease of J, which may be related to the reduction of the brightness of the LMIS with $I_{\rm s}$.
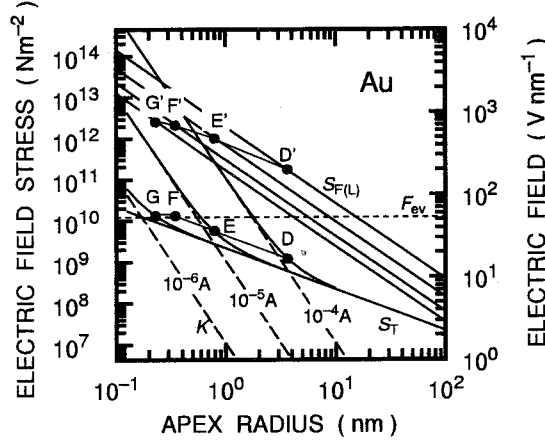
Figure 3.9: Changes in the parameters during the operation.

The above explanation includes all the phenomena described in the present dissertation.

3.6.3 Prediction of source characteristics

Since we have drawn a sketch of the LMIS, now we can predict the characteristics of an ion source with a given source material.

The apex is stabilized by the ion emission, and so F_P at the apex is almost determined by F_{ev}. If the material has a lower F_{ev}, ion emission starts, of course, at the lower F_P. However, there is the important parameter of temperature. The temperature raise significantly reduces F_P at the high current regime. It should be noted that the temperature elevation is material dependent. If the material has a lower κ, T_a would increase rapidly, and thus the operating field is somewhat lower than F_{ev}. On the contrary, if the material has a higher κ, T_a would not increase easily. Of course, even in the latter case, increase of T_a is necessary because the reduction in F_P is required to avoid an excess ionization rate at the apex. Consequently, F_P is mostly determined by κ and F_{ev} at the low current regime.

At the high current regime, the situation becomes different. At the higher current regime, the jet-like structure may be terminated where K is in balance with S_T. This may be true considering the fact that the change in a mass spectrum due to the change in I_s seems to be dominated by γ. In this regime, F_P may depend upon γ. And if we obey the above assumption, F_P can be expressed by eq.(2.40),

$$F_P = \sqrt{\frac{8\gamma}{\varepsilon_0}} \left[(\bar{k}eN_v)^2 \frac{4\gamma}{\rho_m} \right]^{1/6} I_i^{-1/3}. \tag{3.45}$$

Table 3.4: Comparison of F_{P} derived by the author's assumption and the F_{ev}. F_{P} is normalized by that of Au.

Metal	Cu	Au	Ge	Sn
F_{P} (arb.units)	1.6	1.0	0.75	0.59
F_{ev}^{1} (V nm^{-1})	30	53	35	26
F_{ev}^{2} (V nm^{-1})	43	54	29	23
γ (N m^{-1})	1.3	1.1	0.6	0.5

Table 3.4 summarizes the comparison of F_{P} derived by the above equation and the field evaporation theory. Ishitani *et al.*'s such a claim that F_{P} is dominated by γ [40] is explained in terms with the above argument.

F_{ev} and γ are both important parameters in the LMIS operation. It could not be said that only γ is the dominant factor. Whether the above field can be achieved or not is dependent on the local temperature at the apex.

3.7 Conclusion

As shown above, the HTFE model successfully explained the experimentally observed tendency. Starting with the three essential equations, the author derived the necessary condition for the decrease in F_{P}. The author assumed the high temperature and explained the increase and decrease in R_{21}, the molecular ion formation mechanism, and so on. The model gave an approximate rate of ion formation and agreed with the other ion beam characteristics such as energy spread. The present model is based on the assumption that the shape of the liquid does not change significantly. It is, of course, necessary to consider the effect of the jet-like structure for more detailed investigation. For this analysis, the numerical method will play an important role. However, the present approach gave an analytical solution for the present issue. Further detailed investigation on this issue is expected to clarify the quantitative relation among r_{a}, F_{P} and the other structural parameters. In the next chapter, the author deals with the alloy ion sources. The model proposed in this chapter is extended to the alloy ion sources, and the validity will be shown.

References in Chapter 3

[1] D. R. Kingham and L. W. Swanson: Appl. Phys. A **34** (1984) 123.

[2] G. L. R. Mair: J. Phys. D **17** (1984) 2323.

[3] G. L. R. Mair and R. G. Forbes: Surf. Sci. **266** (1992) 180.

[4] N. K. Kang and L. W. Swanson: Appl. Phys. A **30** (1983) 95.

[5] M. S. Chung, N. M. Miskovsky, P. H. Cutler, T. E. Feuchtwang and E. Kazes: J. Vac. Sci. Technol. B **5** (1987) 1268.

[6] C. Zheng and T. Linsu: J. Vac. Sci. Technol. B **6** (1988) 2104.

[7] G.-S. Cho, Y. Seo, S.-O. Kang: J. Appl. Phys. **72** (1992) 5892.

[8] Y. Gotoh, T. Kashiwagi, H. Tsuji, J. Ishikawa: Appl. Phys. A **64** (1997) 527.

[9] L. W. Swanson and A. E. Bell, *Liquid Metal Ion Sources*, in *Physics and Technology of Ion Sources*, ed. I. G. Brown (John-Wiley and Sons, New York, 1989) Chapter 12, p.313.

[10] D. R. Kingham and L. W. Swanson: Appl. Phys. A **41** (1986) 157.

[11] R. J. Culbertson, G. H. Robertson and T. Sakurai: J. Vac. Sci. Technol. **16** (1979) 1868.

[12] L. W. Swanson: Nucl. Instrum. Meth. **218** (1983) 3417.

[13] R. Hornsey and T. Ishitani: Jpn. J. Appl. Phys. **29** (1990) L1107.

[14] R. Hornsey and T. Ishitani: Jpn. J. Appl. Phys. **29** (1990) 2116.

[15] H. Börsch: Z. Phys. **139** (1954) 115 [in German].

[16] E. W. Müller: Phys. Rev. **102** (1956) 618.

[17] T. T. Tsong: *Atom-Probe Field Ion Microscopy*, (Cambridge University Press, Cambridge, 1990).

[18] S. Nagakura, H. Iguchi, H. Ezawa, S. Iwamura, F. Sato and R. Kubo eds. *Rikagaku Jiten dai 5 han* (Iwanami Encyclopedia of Science and Chemistry, 5th Edition) (Iwanami, Tokyo, 1998) [in Japanese].

[19] D. R. Kingham: Surf. Sci. **116** (1982) 273.

[20] C. Kittel: *Introduction to Solid State Physics, 5th edition*, (John Wiley and Sons, New York, 1976).

[21] P. D. Prewett, G. L. R. Mair and S. P. Thompson: J. Phys. D **15** (1982) 1339.

[22] G. L. R. Mair and K. L. Aitken: J. Phys. D **17** (1984) L13.

[23] H. Gaubi, P. Sudraud, M. Tencé and Van de Walle: *Proc. of 29th Field Emission Symposium*, Göteberg, Sweden eds. H. O. Audren and H. Norden (Stockholm, Almqvist and Wiksell, 1982) p.357.

[24] G. Benassayag, P. Sudraud and B. Jouffrey: Ultramicroscopy **16** (1985) 1.

[25] Y. Gotoh, M. Matsubara, K. Inoue, H. Tsuji, J. Ishikawa, Tech. Report of IEICE ED95-138 (1995) 15 [in Japanese].

[26] L. Vályi: *Atom and Ion Sources* (John Wiley & Sons, London, 1977) Table 11, p.385.

[27] T. E. Stern, B. S. Gossling, and R. H. Fowler: Proc. Roy. Soc. (London) A **124** (1929) 699.

[28] S. Masuda and T. Kohno translated: *Denkai Keisan Hou* (H. Printz: *Hochspannungsfelder*) (Asakura-shoten, Tokyo, 1974) [in Japanese].

[29] I. Langmuir and K. B. Blodgett: Phys. Rev. **24** (1924) 49.

[30] Y. Gotoh: unpublished data.

[31] R. G. Forbes: Appl. Surf. Sci. **67** (1993) 9.

[32] Y. Gotoh, H. Tsuji and J. Ishikawa: Appl. Surf. Sci. **146** (1999) 377.

[33] Y. Gotoh: *Analysis of Liquid-Metal Ion Sources and Transport of Intense Ion Beam*, M. E. Thesis, Kyoto University 1987 [in Japanese].

[34] T. T. Tsong: Surf. Sci. **70** (1978) 211.

[35] G. L. R. Mair: J. Phys. D **21** (1988) 1654.

[36] N. Knauer: Optik **59** (1981) 335.

[37] A. Wagner and T. M. Hall: J. Vac. Sci. Technol. **16** (1979) 1871.

[38] J. Ishikawa and T. Takagi: J. Appl. Phys. **56** (1984) 3050.

[39] S. P. Thompson and P. D. Prewett: J. Phys. D **17** (1984) 2305.

[40] T. Ishitani, K. Umemura and Y. Kawanami: J. Appl. Phys. **61** (1987) 748.

Chapter 4
Modeling of alloy ion sources

The previous chapter dealt with the modeling of an element LMIS. However, only limited elements are available as an element state, because many elements have either high vapor pressure, high reactivity, or high melting point. Use of alloys is one of the most probable way to obtain various kinds of ions. For example, antimony is one of the important elements in semiconductor fabrication, but it is not available in its element form due to the high vapor pressure. Observation of the ion emission property of alloy ion sources is important not only for the development of reliable ion source but also for the understanding the operation of the LMIS. This is because the incorporation of heterogeneous atoms causes the change in properties of source material, and make it possible to investigate the mechanism of ion formation. In the present chapter, the model which was proposed in the previous chapter is examined whether it could work also for alloy ion sources or not.

4.1   Significance of modeling of alloy ion sources

In view of wide application of the LMIS, it is expected to produce the ions of almost all elements in the periodic table. However, the source materials of the LMIS's are restricted within those have appropriate chemical property, as shown below.

- The source materials should show good wettability to the base needle material but should not react with it,

- The vapor pressure at the melting point is low enough not to be vaporized during the source operation,

- The material should melt at the temperature as low as 1000°C to reduce the heat problems.

From the beginning of the development of the FIB machines, these problems are serious because the elements in group III or V, which are essential element as a dopant of semiconductor devices, have a high melting point, react with the base material, and have a high vapor pressure. Besides these, transition metals generally react with the base tungsten [1,2]. In order to ionize these materials, various kinds of alloys have been examined so
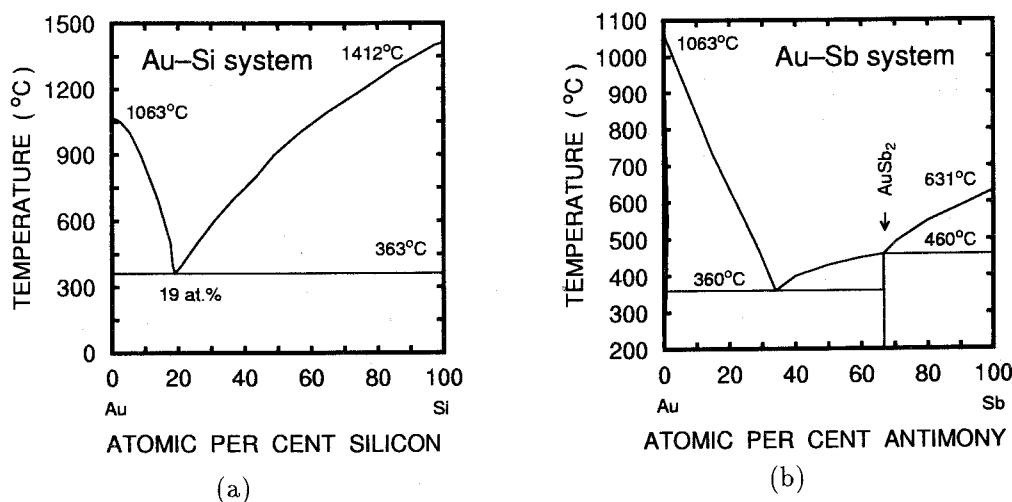
Figure 4.1: Equilibrium phase diagram of (a) gold silicon and (b) gold antimony system.

far [3-15], because some kinds of alloys show lower melting points and also alloying reduces the reactivity with the base material.

Not only from the application point of view, but also from the characterizing point of view, an investigation of the alloy ion source is important. Incorporated impurity element can be used as "a probe" for the analysis of the ionization point. From the above point of view, the author developed new alloy ion sources and examined the validity of the HTFE model with the developed ion sources.

4.2 Experimental procedure

4.2.1 Selection and synthesis of source material

Here the author selected two different kinds of metals. One is silicon (Si) that is not volatile, and the other is antimony (Sb) that is volatile. Si has high reactivity with the base tungsten (W) and many researchers have fabricated Au-Si ion sources so far [3]. Sb, as well as the other elements in the group V, has a high vapor pressure at its melting point. This high vapor pressure prevents us from ionizing these elements with an element metal. As for Sb, no superior ion source has been developed before the author's development of Au-Sb ion sources [4].

Figures 4.1(a) and 4.1(b) indicate the equilibrium phase diagrams of Au-Si [16] and Au-Sb systems [17]. The Au-Si system exhibits simple eutectic reaction at the temperature of

approximately 360°C with the Si atomic composition of 18 – 19 % [16]. The Au-Sb system has an intermetallic phase at $AuSb_2$ and shows eutectic reaction between Au and $AuSb_2$ at $Au_{66}Sb_{34}$ [17]. Presence of an intermetallic phase implies that the atomic bonding is not simple metallic bonding but contains some sort of ionic bonding [18]. From this point of view, Au and Sb atoms have a large binding energy.

The source materials of Au-Si and Au-Sb alloys were produced in a vacuum furnace from element Au, Si, and Sb with a nominal purity of 99.99 %, 99.999 %, and 99.9 %, respectively. Since the inner diameter of the reservoir of the IELMIS is almost 1 mm, it is necessary to synthesize the source material with a diameter less than 1 mm. The starting materials, 0.5 mm-diameter Au wire and Si or Sb chunk, were put into an alumina (Al_2O_3) pipe with an inner diameter of 1 mm and the tube was encapsulated by boron nitride (BN). Two or three tubes were held in a larger tube made of BN, which acted as a heater with a W filament. The nominal compositions were $Au_{82}Si_{18}$, $Au_{66}Sb_{34}$ and $AuSb_2$, but no quantitative analysis of the produced alloys was performed.

4.2.2 Measurement of mass spectrum

The measurement of mass spectrum was performed with the identical sector magnet as described in Chapter 2, but the author refined its mass resolution of $M/\Delta M$ to about 60. It is because the Au-Sb ion sources emitted many kinds of ion species, it was required to separate these ions to identify the mass peaks. The peaks of two isotopes of Sb^{2+} with mass-to-charge ratios of 60.5 and 61.5 could be narrowly distinguished. For the Au-Sb ion sources, the ion currents are represented by the peak current except for the ions of Sb^{2+}. The current of Sb^{2+} was represented by that of $^{121}Sb^{2+}$. As for the Au-Si ion source, Au has no stable isotope and Si has only small amount of minor isotopes. No care was taken for mass analysis of the Au-Si ion source.

Investigations on mass spectra were performed under a fixed I_s with varying T_s, and also under a fixed T_s with varying I_s. This is necessary because volatile atoms may escape from the alloy, and thus interpretation of mass analysis is quite difficult with a single mass spectrum measurement at a fixed condition. Here T_s was defined by the temperature at the reservoir of the source, and was monitored with a thermocouple at below 900 °C, and with a pyrometer at above 900 °C. The calibration of the temperature was performed by melting point of the alloy. At the temperature lower than the melting point, ion emission disappeared.
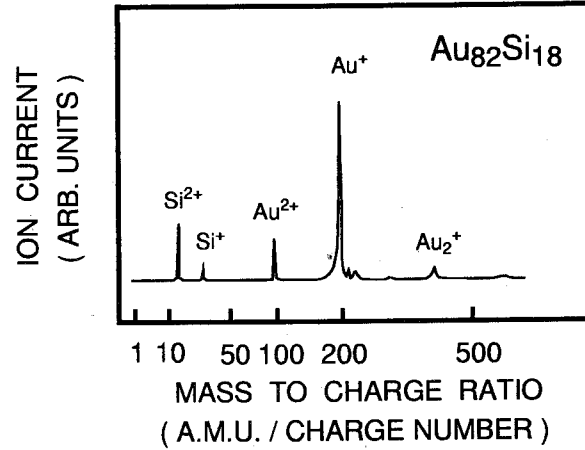
Figure 4.2: Typical mass spectrum of $Au_{82}Si_{18}$ ion source.

4.3 $Au_{82}Si_{18}$ ion source

4.3.1   Mass spectrum

Figure 4.2 shows the typical mass spectrum of $Au_{82}Si_{18}$ alloy ion source. The ion species identified from this spectrum are shown in Table 4.1. The $Au_{82}Si_{82}$ ion source emitted both doubly charged and singly charged ions of Si and Au. Together with these ions, small amount of molecular ions, which were also doubly charged and singly charged, were observed. The mass spectrum observed in the present study well agreed with those seen in the literature [3]. The atom flux ratio of Si Φ_{Si} was defined as the ratio of $N_{Si}/(N_{Si} + N_{Au})$ where the numbers of Si and Au atoms, N_{Si} and N_{Au} were obtained summing the number of atoms contained in the ions listed in Table 4.1. Φ_{Si} did not reach the original alloy composition of 18 at.% of Si, especially at the low current.

4.3.2   Variation of mass spectrum with source temperature

Figures 4.3(a) and 4.3(b) show the variations of the relative ion currents for $Au_{82}Si_{18}$ ion source with varying T_s. Figs. 4.3(a) and 4.3(b) show the ion currents for Au and Au-Si ions, and for Si ions, respectively. I_s was set to 100 μA. During the measurement, V_{ext} required to maintain I_s to be 100 μA did not change significantly. Little difference among the mass spectra at different T_s would be seen. This suggests that there is no significant selective evaporation of constituent elements for this ion source.

Table 4.1: Ion species observed for Au-Si ion source. Relative currents are for I_s of 100μA.

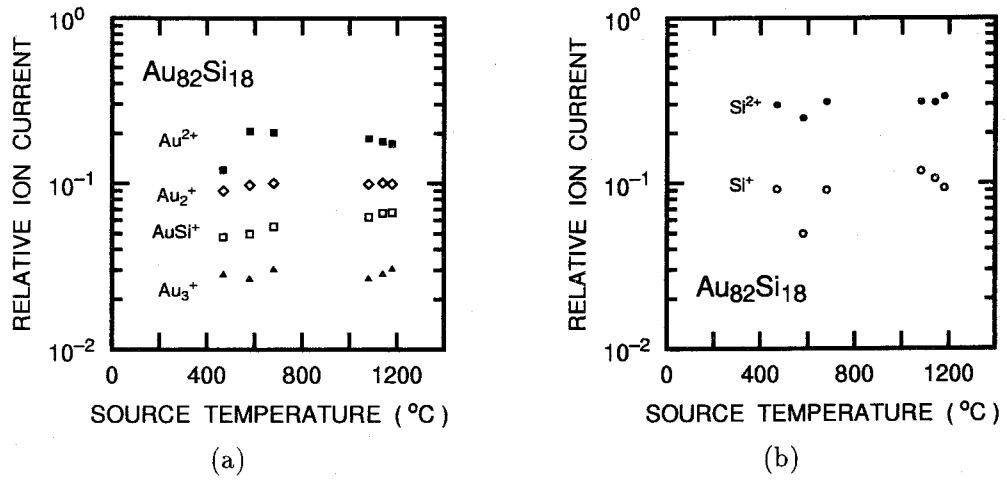| Ion species	Mass-to-charge ratio	Relative ion current
Si^{2+}	14	0.29
Si$^+$	28	0.091
Au^{2+}	98.5	0.21
Au$^+$	197	1.0
Au$_2$Si^{2+}	211	0.066
AuSi$^+$	225	0.061
Au$_3^{2+}$	295.5	0.015
Au$_2^+$	394	0.10

Figure 4.3: Variation of mass spectrum of Au$_{82}$Si$_{18}$ ion source with source temperature. (a) Au and Au-Si ions, and (b) Si ions.
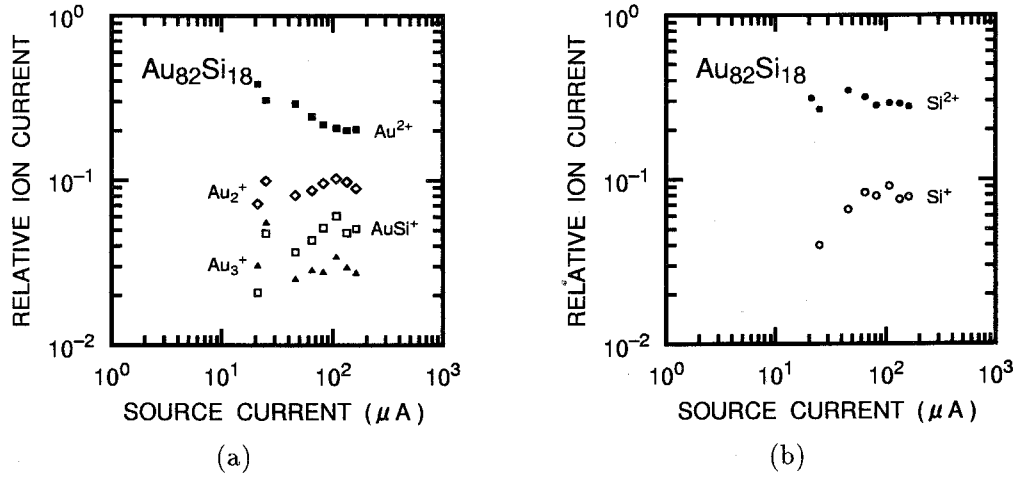
Figure 4.4: Variation of mass spectrum of $Au_{82}Si_{18}$ ion source with source current. (a) Au and Au-Si ions, and (b) Si ions.

4.3.3   Variation of mass spectrum with source current

Figures 4.4(a) and 4.4(b) show the variations of the relative ion currents for $Au_{82}Si_{18}$ ion source with varying I_s. Figs. 4.4(a) and 4.4(b) show the ion currents for Au and Au-Si ions, and for Si ions, respectively. One of the prominent changes is the increase of the relative ion current of Si^+, especially at the low currents. The relative ion currents of molecular ions of Au_2^+ and Au_3^+ slightly increased with an increase in I_s. But the increase of $AuSi^+$ is much larger than the increase of the above homogeneous molecules.

   The author will discuss the details of the above characteristics together with those of Au-Sb ion sources later.

4.4 $Au_{66}Sb_{34}$ ion source

4.4.1   Mass spectrum

The typical mass spectrum of the $Au_{66}Sb_{34}$ ion source is shown in Fig.4.5. The ion source emitted a wide variety of ion species, as shown in Table 4.2. In this table, those observed for the $AuSb_2$ ion source are also listed. Although the detailed investigation with very precise mass resolution performed by Umemura *et al.* revealed that Au-Sb ion sources emitted Sb_2^{2+} ions [19], here in this table, doubly charged dimer ions were not distinguished from singly charged atomic ions. Besides Sb_2^{2+}, there were many doubly charged dimer, trimer, and larger ions that were composed of Au and Sb atoms ($Au_mSb_n^{2+}$). Presence
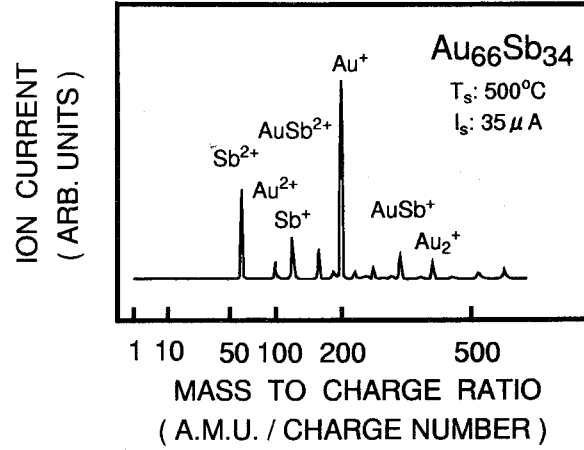
Figure 4.5: Typical example of the mass spectrum of the $Au_{66}Sb_{34}$ ion source.

of multiply charged molecular ions is surprising. Confirmation of the ion species with the mass-to-charge ratio of about 160 [20] will be performed by the analysis of an ion-implanted sample through Rutherford backscattering spectrometry and particle induced x-ray emission measurements, as shown in Chapter 5.

4.4.2 Variation of mass spectrum with source temperature

The mass spectra were investigated at a constant I_s of 35 μA with varying T_s. As T_s increased, V_{ext} to obtain a constant current of 35 μA increased. The variation of the spectra when T_s was varied is shown in Figs. 4.6(a) and 4.6(b). Figure 4.6(a) shows the current fractions of Au^+, Au^{2+}, Sb^+ and Sb^{2+}, as a function of T_s. In Fig. 4.6(b), the Sb atom flux ratio Φ_{Sb} is shown together with the vapor pressure of pure Sb. When the ion source was operated below 750 °C, Φ_{Sb} was constant at about the composition of the original alloy. At the elevated T_s, Φ_{Sb} and the current fractions of the Sb-containing ions decreased, while those of Au ions without Sb atoms increased. Even at the temperature of 1000 °C, at which the vapor pressure of pure Sb is about 10^3 Pa, Φ_{Sb} of 20 % was observed. As the temperature increased, it was necessary to increase V_{ext}.

4.4.3 Variation of mass spectrum with current

The variation of the mass spectra with varying I_s was investigated at two different T_s's: (a) 500 °C, where the evaporation rate of Sb is low, and (b) 850 °C, where the evaporation of Sb atoms becomes significant, as shown in Fig. 4.6. Figures 4.7(a) and 4.7(b) show the

Table 4.2: Ion species and their current fractions for the $Au_{66}Sb_{34}$ source and for the $AuSb_2$ source at T_s of 500 °C.

Ion species	$M/k^{a)}$	Current fraction (%)		Ratio of ion current		Exp./Cal.
		$Au_{66}Sb_{34}$	$AuSb_2$	Measured	Calculated	
		(A)	(B)	(C)=(B)/(A)	(D)	(C)/(D)
Sb^{2+}	61.0	20.3	16.7	0.83	1.6	0.52
Au^{2+}	98.5	4.2	0.7	0.17	0.68	0.25
Sb^{+} [b)]	122.0	8.8	14.1	1.6	1.6	1.0
$AuSb^{2+}$	159.5	6.5	7.4	1.1	1.1	1.0
Sb_3^{2+}	183.0	0.8	4.2	5.3	4.3	1.2
Au^{+}	197.0	41.4	23.2	0.56	0.68	0.82
$AuSb_2^{2+}$	220.5	1.5	4.3	2.9	1.8	1.6
Sb_2^{+}	244.0	0.8	3.7	4.6	2.5	1.8
Au_2Sb^{2+}	258.0	2.3	2.7	1.2	0.73	1.6
$AuSb_3^{2+}$	281.5	0.4	1.7	4.3	2.9	1.5
Au_3^{2+}	295.5	0.4	0.2	0.5	0.31	1.6

Continues to the next page

Table 4.2: *Continued*

Ion species	$M/k^{a)}$	Current fraction (%)		Ratio of ion current		Exp./Cal.
		$Au_{66}Sb_{34}$	$AuSb_2$	Measured	Calculated	
		(A)	(B)	(C)=(B)/(A)	(D)	(C)/(D)
$AuSb^+$	319.0	5.4	9.7	1.8	1.1	1.6
$AuSb_4^{2+}$	342.5	–	0.7	–	4.7	–
Au_3Sb^{2+}	356.5	0.4	1.0	2.5	0.51	4.9
Sb_3^+	366.0	–	1.3	–	4.4	–
Au_2^+	394.0	3.1	2.0	0.6	0.45	1.3
$AuSb_2^+$	441.0	0.8	2.4	3.0	1.8	1.7
$Au_3Sb_3^{2+}$	478.5	–	0.1	–	1.5	–
Sb_4^+	488.0	–	0.3	–	7.0	–
Au_2Sb^+	516.0	1.5	2.7	1.8	0.74	2.4
$AuSb_3^+$	563.0	–	0.1	–	2.9	–
Au_3^+	591.0	1.5	1.0	0.7	0.3	2.3

a) Sb has two isotopes with the masses of 121 and 123. In this table, calculation

is performed assuming the mass of an Sb atom to be 122.

b) Au-Sb ion source emits Sb_2^{2+} as indicated by Umemura *et al.* [19]. In this

table, Sb_2^{2+} is not distinguished from Sb^+ owing to low mass resolution of our
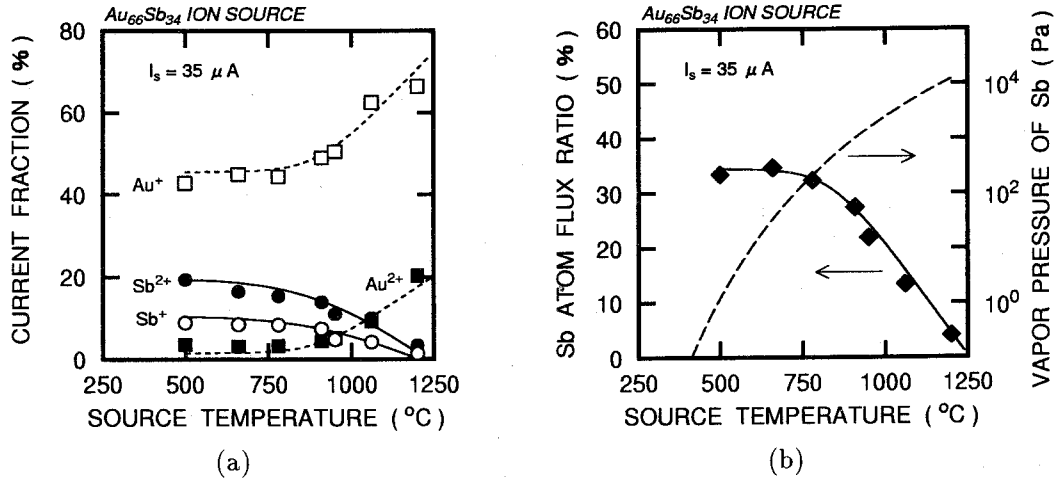
analyzer.

Figure 4.6: (a) Current fractions of Sb^{2+}, Sb^+, Au^{2+}, Au^+ and (b) Sb atom flux ratio, as a function of T_s under the fixed I_s for $Au_{66}Sb_{34}$ alloy ion source.

results of these experiments. At the lower T_s, the current fractions of the dominant ion species and Φ_{Sb} were constant. The results indicated that I_s did not seriously affect the spectrum of the emitted ions. This is surprising because the current fraction of the doubly charged ions generally tends to decrease with I_s, as shown in Chapter 2. The author will discuss on this issue later. On the other hand, at the higher T_s, the current fraction of Sb^+ and Φ_{Sb} increased with an increase in I_s. The increase in Φ_{Sb} was mainly due to the increase in Sb^+. At the higher current, the peak of Sb^+ showed a tail at lower energy which would be attributed to the field ionized ions. The quantity of the tail is small, and thus major ionization process for this ion source is considered to be primarily field evaporation.

Figure 4.8 shows the angular currents of dominant ion species as a function of I_s at T_s of 500°C. The increase in the angular currents is slower than that of the element metal ion sources [21]. The author will argue R_{21} of this ion source later in Section 4.6.

4.5   AuSb$_2$ ion source

4.5.1   Mass spectrum

The typical mass spectrum of the AuSb$_2$ ion source is shown in Fig. 4.9. The current fractions of the ions emitted from the AuSb$_2$ ion source are already shown in Table 4.2. One of the differences between the spectrum of the $Au_{66}Sb_{34}$ ion source and that of the AuSb$_2$ ion source is the higher fraction of Sb^+ for the latter ion source. Also, molecular ions
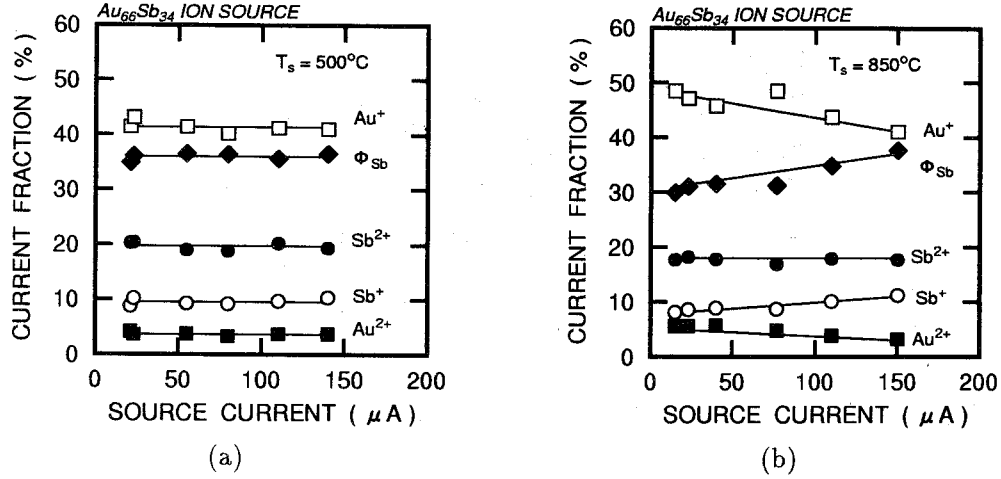
Figure 4.7: Current fractions of Sb^{2+}, Sb^+, Au^{2+}, Au^+ and Sb atom flux ratio as a function of I_s under the fixed T_s's of (a) 500°C and (b) 850°C for $Au_{66}Sb_{34}$ alloy ion source.
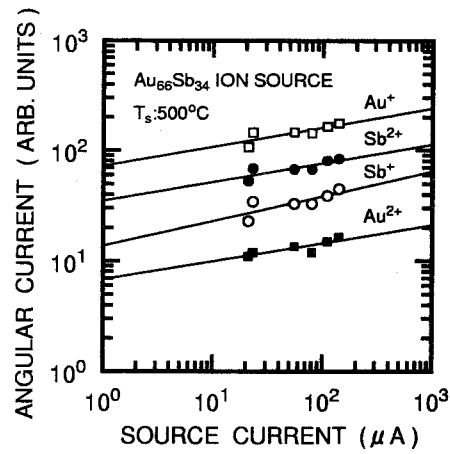
Figure 4.8: Angular currents of Au^+, Au^{2+}, Sb^+, and Sb^{2+} of $Au_{66}Sb_{34}$ ion source under T_s of 500°C
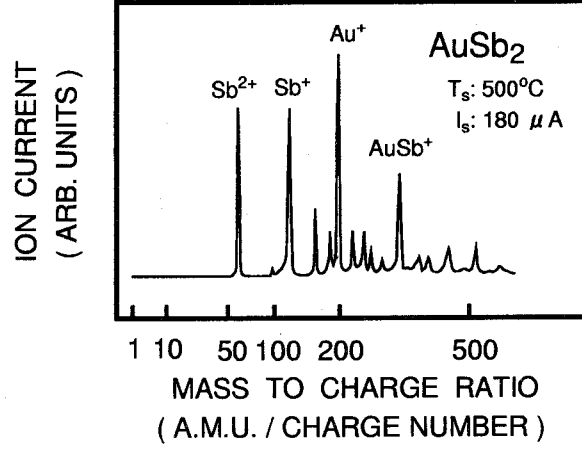
Figure 4.9: Typical mass spectrum of AuSb$_2$ ion source.

were seen with higher magnitudes. In Table 4.2, the relative currents of each ion species is also shown. Here in this table, the measured ratios are the ratios of the ions for the AuSb$_2$ ion source to those for the Au$_{66}$Sb$_{34}$ ion source. The calculated ratios (D) are obtained from the probabilities of formation of these ions according to the composition of the alloys, without consideration of ionization process. For example, the relative current of Au$_m$Sb$_n$ ions from Au$_x$Sb$_{1-x}$, $I_{m,n}(x)$, is assumed to be expressed by

$$I_{m,n}(x) \quad \propto \quad {}_{m+n}C_m x^m \cdot (1-x)^n = \frac{(m+n)!}{m!n!} \cdot x^m \cdot (1-x)^n. \tag{4.1}$$

The composition of AuSb$_2$ is assumed to be Au$_{45}$Sb$_{55}$ from the experimental results, as shown later in Fig. 4.10. Although the measured ratios for the ions of Au$_m$Sb^{k+} ($m = 2, 3$) are larger than calculated ones, increases of the relative magnitude of the molecular ion current are well explained within a factor of two, by the present simple model. This implies that the formation of molecular ions was mainly governed by the composition of the alloy at the ionization point.

4.5.2   Variation of mass spectrum with source temperature

The variation of the spectrum was investigated in a manner similar to that for the Au$_{66}$Sb$_{34}$ ion source. Figures 4.10(a) and 4.10(b) show the current fractions of the dominant ion species and Φ_{Sb} as a function of T_s. In this experiment, I_s was kept at 100 μA. The current fractions of Sb-containing ions decreased rapidly with T_s. Φ_{Sb} at the temperature of 800 °C was comparable to that of the Au$_{66}$Sb$_{34}$ ion source at the same T_s. This implies
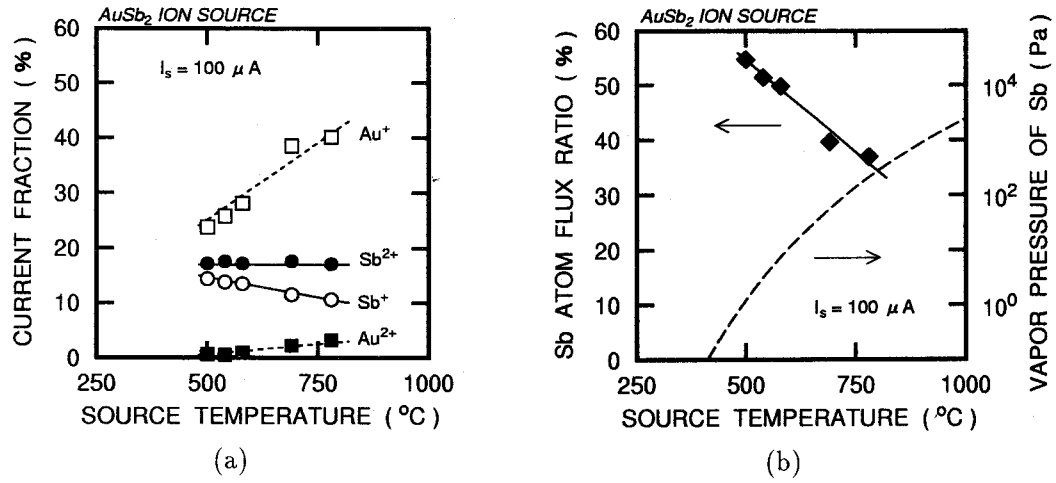
Figure 4.10: (a) Current fractions of Sb^{2+}, Sb^+, Au^{2+}, Au^+ and (b) Sb atom flux ratio, as a function of T_s under the fixed I_s for $AuSb_2$ alloy ion source.

that the suppression of Sb evaporation is less effective than that of an $Au_{66}Sb_{34}$ ion source. The reduction of Φ_{Sb} was mainly dominated by the decrease of Sb^+.

4.5.3   Variation of mass spectrum with source current

The variation of mass spectrum with I_s was measured at T_s of 500°C. Figure 4.11 shows the current fraction of the dominant ion species as a function of I_s. The tendency was quite similar to that in the case of the $Au_{66}Sb_{34}$ ion source operated at 850°C. Slight increase of the Sb^+ current fraction with I_s was observed. However, Φ_{Sb} was slightly lower than the nominal composition of the liquid and estimated to be 0.55.

4.6   Modeling of alloy ion sources

4.6.1   Liquid flow and evaporation of volatile atoms

The spectrum varied with I_s for the $Au_{66}Sb_{34}$ ion source at 850 °C and also for the $AuSb_2$ ion source at 500 °C. While the spectrum did not vary significantly with I_s for the $Au_{66}Sb_{34}$ ion source at 500 °C. These variations could be interpreted to be the result of selective evaporation of the Sb atoms during the transport of the liquid from the reservoir to the ionization point. In order to confirm that the obtained results can be explained by selective evaporation, the author discusses the following model of liquid transport from the reservoir
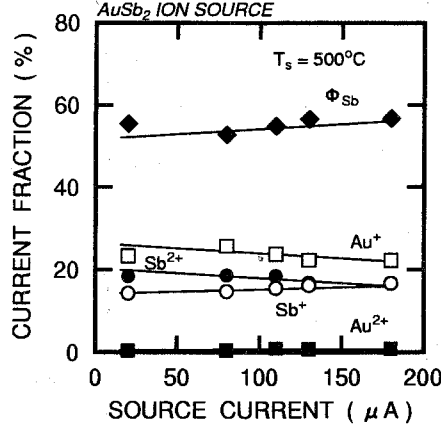
Figure 4.11: Relative ion intensities of Sb^{2+}, Sb^+, Au^{2+}, Au^+ and atom flux ratio as a function of I_s under the fixed T_s for $AuSb_2$ alloy ion source.

to the ionization point.

Figure 4.12 shows the schematic drawing of the system in which the liquid flow was analyzed. Although the liquid metal is supplied to the ionization point mostly through the inner part of the porous region of the ion source, a portion of the volatile atoms will escape from the liquid surface to vacuum. Neglecting the evaporation of Au atoms, we can roughly estimate the Sb concentration of the alloys at the ionization point c_{Sb} in a following manner. Here we take the z—axis along the axis of the symmetry, which is the opposite direction of liquid flow. The porous region is expressed as a cone with a height of z_r, and the cone half-angle of θ. Let the liquid flows of Sb and Au at the reservoir be $q_{Sb}(z_r)$ and $q_{Au}(z_r)$, and the liquid flows at the ionization point be $q_{Sb}(0)$ and $q_{Au}(0)$. If the evaporation of Au atoms is neglected, the following equation holds at $0 < z < z_r$:

$$\begin{cases} dq_{Sb}(z) & = 2\pi z \dfrac{\tan\theta_r}{\cos\theta_r} f_{eff}[p_1(z)]dz, \\ dq_{Au}(z) & = 0, \end{cases} \qquad (4.2)$$

where $f_{eff}[p_1(z)]$ is the effective atom evaporation rate of Sb from the liquid with the Sb concentration of p_1, at the position of z. Solving the above equation is fairly difficult due to the presence of f_{eff}. Here we assume that the atom evaporation rate does not change with respect to slight change of the composition. In such a situation, we can express the atom evaporation rate f_{eff} as

$$f_{eff} = f_{Sb}\eta, \qquad (4.3)$$

where f_{Sb} is the atom evaporation rate of pure Sb, and η the suppression factor of evapo-
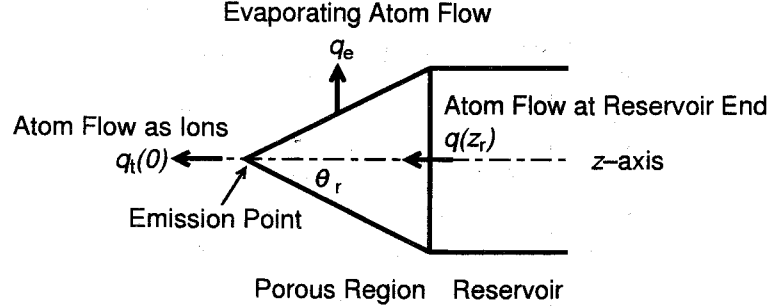
Figure 4.12: Coordinates for analysis of transport of volatile element in alloy source.

ration due to alloying. Then the differential equation is easily solved and we obtain

$$\begin{cases} q_{\mathrm{Sb}}(z_{\mathrm{r}}) = q_{\mathrm{Sb}}(0) + f_{\mathrm{eff}}S, \\ q_{\mathrm{Au}}(z_{\mathrm{r}}) = q_{\mathrm{Au}}(0), \end{cases} \tag{4.4}$$

where S is the evaporation area described by the following equation.

$$S = \pi z_{\mathrm{r}}^2 \frac{\tan\theta_{\mathrm{r}}}{\cos\theta_{\mathrm{r}}}. \tag{4.5}$$

The total flow at the ionization point q_{t} is expressed by

$$q_{\mathrm{t}} = q_{\mathrm{Sb}}(0) + q_{\mathrm{Au}}(0). \tag{4.6}$$

By reducing the equation,

$$c_{\mathrm{Sb}} = p_1 - p_2 S f_{\mathrm{eff}}/q_{\mathrm{t}} = p_1 - p_2 q_{\mathrm{e}}/q_{\mathrm{t}}, \tag{4.7}$$

where p_1 and p_2 the initial compositions of Sb and Au, and q_{e} the evaporating atom flow to the vacuum. If we assume that the evaporation rate does not significantly depend on the initial alloy composition, q_{e} can be treated as a function of only T_{s}, $q_{\mathrm{e}}(T_{\mathrm{s}})$. While q_{t} can be treated as a function of I_{s}, $q_{\mathrm{t}}(I_{\mathrm{s}})$. This equation is helpful to understand how the volatile atom in liquid is transported to the emitter apex: composition at the ionization point varies at the temperature where $q_{\mathrm{e}}(T_{\mathrm{s}}) > q_{\mathrm{t}}(I_{\mathrm{s}})$. Under a fixed I_{s}, since the denominator of the second term on the right-hand side is constant, the composition at the apex decreases at higher T_{s} where $q_{\mathrm{e}}(T_{\mathrm{s}}) > q_{\mathrm{t}}(I_{\mathrm{s}})$. Under a fixed T_{s}, the numerator of the same term is constant, and composition at the apex increases with I_{s} when evaporation is significant. We assume that the composition c_{Sb} corresponds to Φ_{Sb}.
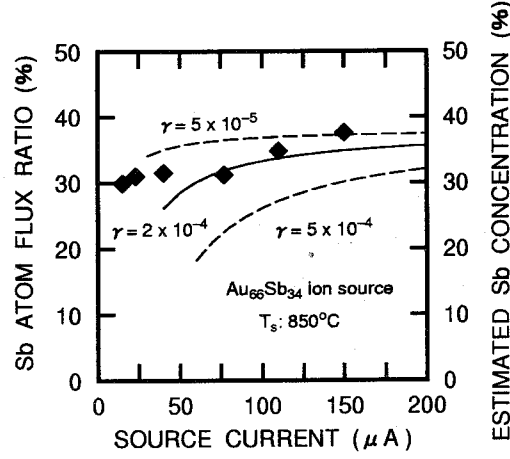
Figure 4.13: Comparison of calculated Sb atom flux ratio with the experimental value.

Here we compare the calculated results with the experimental results. The $Au_{66}Sb_{34}$ ion source operated at 500 °C exhibited no significant change in Φ_{Sb} with I_s. This means that $q_e(500°C)$ for the $Au_{66}Sb_{34}$ ion source is sufficiently low as compared with $q_t(35~\mu A)$. The $Au_{66}Sb_{34}$ ion source operated at 850 °C exhibited a variation in Φ_{Sb}, which means that $q_e(850°C)$ is as large as $q_t(35~\mu A)$. We can obtain the quantitative relation, substituting the values of the present ion source geometry, and assuming the Sb evaporation rate f_{Sb} to be 3×10^{19} atoms·cm^{-2}s^{-1} [22]. Assuming that f_{eff} is reduced by a suppression factor η of 2×10^{-4}, the variation of c_{Sb} as a function of I_s could be calculated and is shown by solid line in Fig. 4.13. The calculated values with η's of 5×10^{-5} and 5×10^{-4} are also illustrated by broken lines. The calculated c_{Sb} almost agrees with Φ_{Sb}. Discrepancy at the low current is attributed to the assumption that the evaporation rate does not depend on the alloy composition. For the $AuSb_2$ ion source, the evaporation was significant at T_s of 500 °C, where the evaporation rate of pure Sb is lower than that at 850 °C by four orders of magnitude, which means little suppression of evaporation. The presence of Sb atoms at the ionization point is due entirely to the lowering of T_s.

4.6.2   Magnitude of the current for multiply charged atomic ions

Here we investigate F_P at the apex of the liquid by comparing R_{21} further in detail. As described above, the relative ion currents of the doubly charged ions are strongly dependent on c_{Sb}. Figure 4.14 shows the relationship between the estimated Sb concentration c_{Sb},
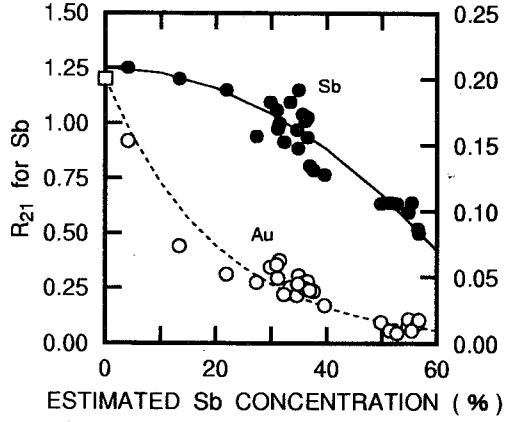
Figure 4.14: R_{21} of Au and Sb ions as a function of estimated Sb concentration at the apex.
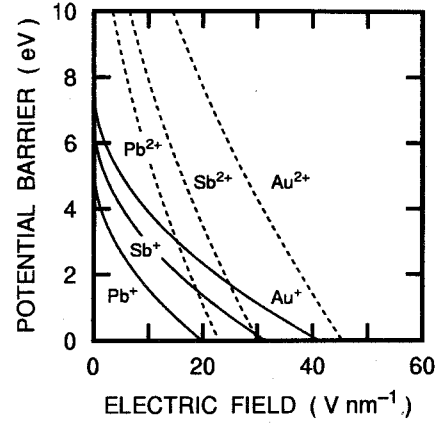
Figure 4.15: Potential barrier for element Pb, Au, and Sb. Image hump model was used to calculate the barrier.

which is identical to Φ_{Sb}, and R_{21}'s. All the data shown in Figs.4.6, 4.7, 4.10, and 4.11 are plotted in this figure. It is clear that the ratios are dominated by c_{Sb}, irrespective of I_s and T_s. The reason for the decrease in R_{21} would be the lower F_{ev} for Sb ions or the lower γ for Sb.

Figure 4.15 shows the potential barriers as a function of F_P for Au, Pb, and Sb ions. If there are ions which escape the liquid surface at a lower F_P, the cone apex will not be sharp enough to produce the ions which require higher F_{ev}, since the liquid cone is terminated where the ion emission rate becomes large. The results agree with those obtained by Gamo et al. for Pb-Au-Sb alloys: Pb has lower F_{ev}, and thus the obtained mass spectrum showed lower current of Sb^{2+} as compared with that of Sb^+. As described in Chapter 3, also γ is the important parameter for the determination of the field. In the next subsection, the author argues the field at the ionization point further in detail.

4.6.3 Increase of extraction voltage at higher temperature for Au$_{66}$Sb$_{34}$ ion source

As described above, at the higher T_s, the composition at the apex changed due to selective evaporation of the Sb atoms during transport of the source material to the apex. As a result, V_{ext} required to maintain I_s became higher, which is equivalent to the fact that I_s decreased under the same V_{ext}. As stated in eq.(3.43), the equations of the SCLC and FD are unified to

$$V^2 = \left[\frac{c_3}{\varepsilon_0} k^2 I_i^2 \sqrt{V} + \frac{k^2 \rho_m}{\varepsilon_0 e^2 N_v^2} \frac{I_i^2}{r_a^2} \right] + \frac{4 k^2 \gamma r_a}{\varepsilon_0}. \tag{4.8}$$

In the above equation, the term in the left hand side is almost in balance with the first term in the right hand side, and the second term in the right hand side is almost in balance with the last term. The experimental results showed that the first term of the right hand side becomes smaller as the temperature raise, and it is necessary that the balance between the second and the last terms should be achieved at the higher values.

If the evaporation of Sb atoms becomes significant, the terms in the block parentheses of the above equation reduces, because the field is not sufficiently high to produce sufficient amount of Au ions. In such a situation, r_a can become larger or smaller from this equation. It is natural to consider that r_a becomes smaller, because larger S_F pull the liquid cone to have smaller r_a. First, the author argues this situation. If r_a becomes smaller, the last term in the right hand side of eq.(4.8) becomes smaller, if the other parameters are not changed. As the loss of Sb from the alloy, γ will become larger. The reduction of r_a should be smaller than the increase of γ, for the increase of the last term. As for the second term, the magnitude will become as follows. If we assume that N_v and ρ_m is in proportion to the alloy composition, ρ_m/N_v^2 slightly decreases, in the present case. Since I_i decreases, r_a should decrease. Rapider decrease in r_a than that in I_i will realize increase of the second term. The balance between the second term and the last term can be realized.

If r_a becomes larger, the last term becomes larger. However, in this case, the second term becomes smaller due to enlargement of r_a. The above arguments show the latter is not the case.

Although the detailed investigation which takes the elongation of the jet-like protrusion into consideration is necessary, the present results show that the operation of the LMIS at the higher current regime seems to be dominated by γ.

4.6.4   Rate of decrease in R_{21}

Figures 4.16(a) and 4.16(b) show the relation between R_{21} and I_s and that between R_{21} and I_Ω. The slopes ξ_Ω's shown in Fig. 4.16 become more gentle than those shown in Fig. 2.13. For Au of $Au_{66}Sb_{34}$ ion source, the slope includes a large ratio of error because the increase in I_Ω is very small.

If the argument in Chapter 2 holds, the rate of decrease in R_{21} is

$$\xi_{ana} = \frac{s_{21}}{3} \left[(\overline{k}eN_v)^2 \frac{\gamma^4}{2\epsilon_0^3\rho_m} \right]^{1/12}, \tag{4.9}$$

which is the same with eq.(2.45). Since the atomic density N_v is almost proportional to the surface tension γ, the above equation can be very roughly expressed as

$$\xi_{ana} \propto \gamma^{1/2}. \tag{4.10}$$
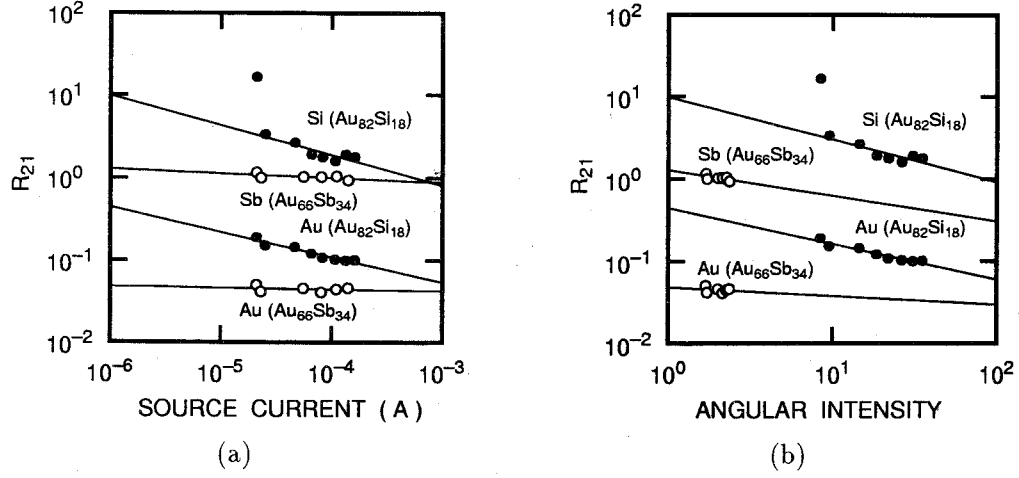
Figure 4.16: R_{21} values of $Au_{66}Sb_{34}$ ion source at constant temperature of 500°C: (a) as a function of I_s, and (b) as a function of I_Ω.

γ of the Au-Si system was investigated by Naidich *et al.* [23] and found to be about 0.95 N·m^{-1} at the Si composition of 18 at.% at the temperature of 1450°C. Generally, γ gradually decreases with an increase in the temperature, but here we use this value because the decrease would not be large. γ of the Au-Sb system is not known and we assume it here to be 0.7 N·m^{-1}, but it may have a value between 0.4 (γ of Sb) and 0.86 N·m^{-1} which is calculated assuming linear relation between γ and the alloy composition. Figure 4.17 shows the relation between ξ_Ω and γ for the alloys together with the element metals already investigated [21]. Open circles indicate ξ_Ω's of some element metal ion sources, shown in Chapter 2. A solid circle, a solid square, and a solid rhombus indicate the Au, Si, and Sb ions from the alloy ion sources. Uncertainty of γ for the $Au_{66}Sb_{34}$ alloy is shown by an error bar. The dotted line is drawn for a guide of view. As shown in the figure, ions emitted from lower γ exhibited lower ξ_Ω. The present results indicates qualitatively the same tendency with the element metal ion sources, although the relation between γ and ξ_Ω is strong:

$$\xi_\Omega \propto \gamma^2. \tag{4.11}$$

The results are summarized in Table 4.3. In Table 4.3, the data from the pure Au ion source [21] is also listed.

In order to obtain ξ_{ana} for each alloy, N_v and ρ_m should be known. As for N_v and ρ_m, the values were determined in accordance with the composition. Putting physical parameters into eq.(4.9), we obtain ξ_{ana}. Comparing ξ_{ana} with experimentally obtained ξ_Ω, we can estimate s_{21} or the local temperature at the apex T_a. The calculated results are also shown

Table 4.3: Rate of decrease of R_{21} of various liquid metal ion sources.

Ion species	Au	Au	Au	Si	Sb
Source material	pure Au [21]	$Au_{82}Si_{18}$	$Au_{66}Sb_{34}$	$Au_{82}Si_{18}$	$Au_{66}Sb_{34}$
ξ_s	0.64	0.31	0.019	0.36	0.054
ξ_Ω	0.81	0.44	0.11	0.51	0.31
γ (Nm^{-1})	1.1	0.95	0.7	0.95	0.7
ρ_m $(10^4 kgm^{-3})$	1.94	1.63	1.50	1.63	1.50
N_v $(10^{28} m^{-3})$	5.89	5.73	4.99	5.73	4.99
$\bar{k}$	1.3	1.2	1.1		
ξ_{ana} (10^3)	$3.9 s_{21}$	$3.8 s_{21}$	$3.3 s_{21}$	$3.8 s_{21}$	$3.3 s_{21}$
s_{21} estimated from ξ_s $(10^{-4} m^{1/2} V^{-1/2})$	1.6	0.82	0.058	0.92	0.16
s_{21} estimated from ξ_Ω $(10^{-4} m^{1/2} V^{-1/2})$	2.1	1.2	0.33	1.4	0.94
T_s estimated from ξ_s (eV)	0.43	0.84	12.0	0.75	4.3
T_s estimated from ξ_Ω (eV)	0.33	0.59	2.2	0.50	0.73
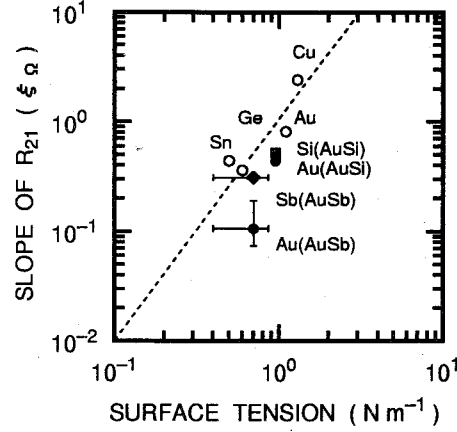
Figure 4.17: Rate of decrease of Au-Sb and Au-Si alloy ion sources together with those of the element metal ion sources.

in Table 4.3. In most cases, s_{21} is approximately 10^{-4} $m^{1/2}V^{-1/2}$ but for Au in the $Au_{66}Sb_{34}$ source s_{21} is about 3.3×10^{-5} $m^{1/2}V^{-1/2}$. The theoretical value of s_{21} for T_s of 450 °C is 1.1×10^{-3} $m^{1/2}V^{-1/2}$. This means that T_a is as high as 0.5 eV (5,800 K). This temperature is in good agreement with those for the element Cu, Au, Sn and Ge ion sources shown in Chapter 2. The extremely high temperature of 2 eV (23,000 K) for Au may be attributable to errors included in ξ_{ana}. However, the error limits correspond to a temperature range between 1.2 and 3 eV (14,000 and 35,000 K), which is still higher than the other ions in Table 4.3. This is a consequence of the very small ξ_Ω value.

R_{21} for Si ions exhibited a rapid decrease at very low current regime in contrast to the element Au and Cu ion sources. This would be attributed to the increase of T_a. In the case of Si, F_{ev} is lower for the doubly charged ions. As described before, R_{21} can be expressed by

$$R_{21} = \exp\left[-\frac{V_2 - \phi - s'_{21}F_P^{1/2}}{k_B T}\right]. \tag{4.12}$$

As is clearly shown by this equation, if the material has low V_2, the activation energy for ion formation is lower for the doubly charged ions. At the working F_P, the term in the parenthesis may become positive, and for this case, R_{21} exceeds unity. With an increase in T_a, R_{21} will decrease, unlike the case for the element metals observed in Chapter 2. More clearly, the difference is explained in Fig. 4.18. In this figure, the solid curve shows $R_{21} = \exp[(V_2 - \phi - s'_{21}F_P^{1/2})/k_B T_a]$ as a function of $(V_2 - \phi - s'_{21}F_P^{1/2})/k_B T$. The arrows show the change in R_{21} with an increase in T_a. If the value in the block parentheses is
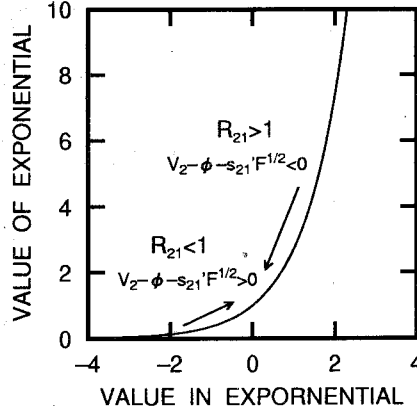
Figure 4.18: Difference in the behavior of R_{21} with an increase in T_a between the elements which have lower and higher F_{ev}^2 as compared with F_{ev}^1.

negative, R_{21} becomes larger with an increase in T_a, as shown by the lower arrow. While the value in the block parentheses is positive, R_{21} becomes smaller with an increase in T_a, as shown by the upper arrow. The former is the case for Cu and Au, and the latter is the case for Si. The temperature raise causes a rapid reduction of F_P and rapid decrease of Si^{2+} is reasonable. This result also holds the HTFE model.

4.6.5 Formation of molecular ions

As described in the previous section, the relative magnitudes for the molecular ions were almost proportional to the formation probabilities of the molecules in the liquid: intensities of molecular ions formed were determined by the alloy composition. This means that F_{ev} for molecular ions is similar to or lower than that of atomic ions. According to the HTFE model, F_{ev} for $Au_m Sb_n^{k+}$ ions $F_k(m,n)$ can be written as

$$F_k(m,n) = \frac{4\pi\epsilon_0}{e^3 k^3} \left[m H_{Au} + n H_{Sb} - E_b(m,n) + \sum_{i=1}^{k} V_i - k\phi \right]^2, \qquad (4.13)$$

where H_{Au} and H_{Sb} are the sublimation energies for Au and Sb, respectively, and $E_b(m,n)$ is the total binding energy for $Au_m Sb_n$ molecules. Although we have no exact values for $E_b(m,n)$, V_i, and ϕ in eq.(4.13) for alloys, we can roughly estimate $F_k(m,n)$ in the following manner. ϕ, V_1, and V_2 have values similar to those for Au and Sb (no significant differences exist between these elements). The binding energies of Au-Au and Sb-Sb are 2.30 and

Table 4.4: Evaporation field strength for dimer ions calculated using HTFE model. Values in parentheses are those normalized by $I_{m,n}(x)$.

Ion Species	Au_2^+		$AuSb^+$		Sb_2^+	
Evaporation field (V·nm^{-1})	73		43		47	
Observed current fraction for $Au_{66}Sb_{34}$ (%)	3.1	(7.1)	5.4	(12.0)	0.8	(6.9)
Observed current fraction for $AuSb_2$ (%)	2.0	(9.9)	9.7	(19.6)	3.7	(12.2)

3.09 eV, respectively [24]. One of the difficulties is that the absolute value of H_{Sb} [25] in the literature is smaller than the binding energy of Sb, E_b(Sb–Sb). If $|H_{Sb}| < |E_b$(Sb–Sb)$|$, F_{ev} of the molecular Sb ions with a larger size would decrease. In order to avoid this, we here assume H_{Sb} to be 3.2 eV. Table 4.4 shows the evaporation fields for dimer ions, together with the observed ion current fractions. The values in parentheses are those normalized by $I_{m,n}(x)$. The values of ϕ and V_1 used are those for Au atoms, and the binding energy of Au-Sb $|E_b$(Au–Sb)$|$ is assumed to be 4 eV. It is shown that $F_1(1,1)$ $(AuSb^+)$ is lower as compared with $F_1(2,0)$ or $F_1(0,2)$. With a lower binding energy of 2 or 3 eV, such a relation was not obtained. The present model also explains the formation of Sb_2^{2+} ions: if H_{Sb} is close to E_b(Sb-Sb), no significant difference between F_{ev}'s of atomic ions and doubly charged atomic ions exist. If the molecular ions are formed by field ionization of thermally evaporated molecules from the liquid shank [26,27], Sb_2^+ and Sb_4^+ should be intense, because these Sb molecule has a higher vapor pressure than atoms [28].

4.7 Design of the source material

Owing to the HTFE model, we can expect some ways of designing the LMIS. If we want to obtain doubly charged ions, which is preferred for ion implanter with lower voltage power supplies, alloying with the material that owns high γ is effective. However, it should be noted that there is an optimum composition to obtain the highest ion current for doubly charged ions, because F_P would decrease by incorporation of the element with lower γ. Also the material which has low F_{ev} may not enhance F_P. While we want to obtain singly charged ions, which is preferred for low energy application such as ion beam deposition, alloying with the material that owns lower γ is effective. These selection of the material

significantly reduces the size, weight, and cost to realize the desired ion beam systems.

4.8   Conclusion

In the present chapter, the author analyzed the characteristics of the ion sources of which source material was either Au-Si or Au-Sb alloy. The mass spectra were investigated for the $Au_{82}Si_{18}$, $Au_{66}Sb_{34}$ and the $AuSb_2$ ion sources as a function of I_s and also as a function of T_s. The Sb atom flux ratio exhibited appreciable variations with respect to change either in T_s or in I_s at a high temperature. While $Au_{82}Si_{18}$ ion source did not show significant change in mass spectrum when T_s was elevated. These variations of Au-Sb ion source with the temperature were explained by solving a differential equation with respect to the liquid flow and the evaporating atom flow in the present source geometry, and were found to be due to the selective evaporation of the Sb atoms. It was also found that F_P of Au-Sb ion sources is reduced because of the presence of Sb, of which γ are lower than those of Au. The rate of decrease in R_{21} can be also explained by the lower γ of the Sb containing liquid. The experimental results suggested that the dominant factor for F_P determination is γ. Rapid decrease of R_{21} for Au-Si ion source at the low current regime is also explained by the rapid temperature elevation. The experimental results for the alloy ion sources have been well explained in terms with the HTFE model. The HTFE model is considered to be one of the possible models of the LMIS, and the author gave the way to design the source material.

References in Chapter 4

[1] A. Bondi: Chem. Rev. **52** (1953) 417.

[2] K. Sugiyama: *Ion Beam Characteristics of Impregnated-Electrode-Type Liquid-Metal Ion Source with a Volatile Element*, B. E. Thesis, Kyoto University, 1984 [in Japanese].

[3] V. Wang, J. W. Ward and R. L. Seliger: J. Vac. Sci. & Technol. **19** (1981) 1158.

[4] K. Gamo, T. Ukegawa, Y. Inomoto, Y. Ochiai and S. Namba: J. Vac. Sci. Technol. **19** (1981) 1182.

[5] E. Miyauchi, H. Hashimoto and T. Utsumi: Jpn. J. Appl. Phys. **22** (1983) L225.

[6] T. Ishitani, K. Umemura and H. Tamura: Jpn. J. Appl. Phys. **23**, (1984) L330.

[7] T. Ishitani, K. Umemura, S. Hosoki, S. Takayama and H. Tamura: J. Vac. Sci. Technol. A **2** (1984) 1365.

[8] H. Arimoto, A. Takamori, E. Miyauchi and H. Hashimoto: Jpn. J. Appl. Phys. **23** (1984) L165.

[9] G.-M. Chen, Y. Gotoh, H. Tsuji, J. Ishikawa and T. Takagi: *Proc. 9th Symp. on Ion Sources and Ion-Assisted Technology ISIAT'85*, Tokyo (The Research Group of Ion Engineering, Kyoto, 1985) p.81.

[10] Y. Gotoh, T. Kashiwagi, H. Tsuji, J. Ishikawa and T. Takagi: *Proc. 10th Symp. on Ion Sources and Ion-Assisted Technology ISIAT'86*, Tokyo (The Research Group of Ion Engineering, Kyoto, 1986) p.19.

[11] J. Ishikawa, Y. Gotoh, H. Tsuji and T. Takagi: Nucl.Instrum. Methods B **21** (1987) 186.

[12] H. Arimoto, E. Miyauchi and H. Hashimoto: Jpn. J. Appl. Phys. **26** (1987) L253.

[13] W. M. Clark, Jr., R. L. Seliger, M. W. Utlaut, A. E. Bell, L. W. Swanson, G. A. Schwind and J. B. Jergenson: J. Vac. Sci. Technol. B **5** (1987) 197.

[14] S. Nagamachi, Y. Yamakage, H. Maruno, M. Ueda, S. Sugimoto, M. Asari and J. Ishikawa: Appl. Phys. Lett. **62** (1993) 2143.

[15] S. Nagamachi, Y. Yamakage, M. Ueda, H. Maruno, K. Shinada, Y. Fujiyama, M. Asari and J. Ishikawa: Appl. Phys. Lett. **65** (1994) 3278.

[16] W. G. Moffatt: *The Handbook of Binary Phase Diagrams* (General Electric Company, New York, 1978).

[17] M. Hansen: *Constitution of Binary Alloys* (MacGraw-Hill, New York, 1958).

[18] A. H. Cottrell: *An Introduction to Metallurgy* (Edward Arnold, London, 1967).

[19] K. Umemura, Y. Kawanami and T. Ishitani: Jpn. J. Appl. Phys. **27** (1988) L2392.

[20] Y. Gotoh, H. Tsuji and J. Ishikawa: Rev. Sci. Instrum. **71** (2000) 780.

[21] Y. Gotoh, T. Kashiwagi, H. Tsuji and J. Ishikawa: Appl. Phys. A **64** (1997) 527.

[22] R. G. Wilson and G. R. Brewer: *Ion Beams with Application to Ion Implantation* (John Wiley & Sons, New York, 1973).

[23] Yu. V. Naidich, V. M. Perevertailo and L. P. Obushchak: Sov. Powder Metall. & Metal Ceram. **14** (1975) 403.

[24] K. P. Huber and G. Herzberg: *Molecular Spectra and Molecular Structure IV. Constants of Diatomic Molecules* (Van Nostrand Reinhold, New York, 1979).

[25] T. T. Tsong: Surf. Sci. **70** (1978) 211.

[26] R. J. Culbertson, G. H. Robertson and T. Sakurai: J. Vac. Sci. Technol. **16** (1979) 1868.

[27] L. W. Swanson: Nucl. Instrum. Meth. **218** (1983) 3417.

[28] O. Kubashewski and C. B. Alcock: *Metallurgical Thermochemistry, 5th Edition* (Pergamon, Oxford, 1979).

Part II

Development of systems
for single point source

Chapter 5

Development of lens system for divergent ion beams

This chapter together with the following chapter deals with the development of novel ion beam systems for single point LMIS's. For utilization of the ion beams extracted from an LMIS, it is necessary to converge the divergent beam. It is difficult to converge the beams from an LMIS, because of a relatively wide energy spread and a large divergence angle, which yield significant effects on the aberrations of the lens. The author developed a physically asymmetric lens system and evaluated its performance by computer simulation and experiments. The experiments of the beam transport were performed with the Ga and In ion sources. This is because that the beam is consisted mostly of the singly charged atomic ions, which is convenient for the evaluation of the transmittance. After confirming the property of the lens, the author designed an ion implanter equipped with a sector magnet. The transmittance of the beam was also evaluated by computer simulation and experiments. Finally, the author demonstrated a novel technique of molecular ion implantation into silicon substrate.

5.1 Design of lens system

5.1.1 Concept of effective focusing of divergent beam

As described in Chapter 2, the ion beam extracted from an LMIS has a large divergence up to $30°$ as also reported by many researchers [1] together with a wide energy spread [2,3]. Both of these cause serious problems when we want to transport the ion beam. It is because an ion-optical element has higher order aberrations such as spherical and chromatic aberrations. The former is directly affected by the large divergence and the latter by the large energy spread.

For the plasma-type ion sources, adjustment of the extraction geometry greatly improve the ion trajectory [4], and thus focusing of the ion beam is relatively easy. However, in the case of the LMIS, the ion extraction surface is always protruding outwards, irrespective of the extraction geometry or operational conditions. As a result, the ion beam is essentially divergent. In designing the lens for a divergent beam, the author took the following issues

into consideration.

One of the most important issues is that the divergent beam should be converged before the diameter of the beam becomes significantly large. It is necessary to give the inward electric field just after the extraction. A cylinder lens requires a large working distance, a thin but strong lens, which is different from the cylinder lens, is necessary. One of the suitable lens is an aperture lens.

From the application point of view, a three-electrode system is preferred. This is because optimum focusing property can be determined for a given beam energy by adjusting the potential of the center electrode. In the case of a two-electrode system, focal length is determined by the ratio of the acceleration voltage. There are two modes of three-electrode lens system: accel-type and decel-type. The former gives the negative (accelerating) potential to the center electrode and the latter gives the positive (decelerating) potential to the center electrode. Generally, the latter lens requires lower voltage. In the present study, the decel-type lens system is adopted. The three-electrode system consists of two gaps where lens effect occurs. The trajectory of charged particles is dominated by the electric field where the velocity of the charged particles is slow. In the case of the decel-type three-electrode lens, the electric field near the second gap will play an important role. In order to realize a strong convergent field, the electric field at the second gap should be inward.

Another important feature of an electrostatic lens is such that both converging and diverging region exist within a lens, unlike the light optics. The paraxial ray equation [5] in a rotationally symmetrical coordinates is given by

$$\frac{d^2 r}{dz^2} + \frac{U'(z)}{2U(z)}\frac{dr}{dz} + \frac{U''(z)}{4U(z)}r = 0, \tag{5.1}$$

where $U(z)$ is the electrical potential on the axis. From the arithmetical manipulation [6], the focal length f_i can be calculated as [6]

$$\frac{1}{f_i} = \frac{1}{4\sqrt{U(z_{\text{out}})}} \int_{z_{\text{in}}}^{z_{\text{out}}} \frac{1}{\sqrt{U(z)}} \frac{d^2 U(z)}{dz^2} dz, \tag{5.2}$$

where z_{in} and z_{out} are the positions where lens effect occurs. To make a strong lens, *i.e.*, shorter f_i, the right hand side should be large. The second differential of the potential has both positive and negative region along the integration range of eq.(5.2). For an acceleration lens, these two regions correspond to converging and diverging fields, respectively. If the lens is in good symmetry, the magnitude of this positive and negative area is the same, but owing to the presence of the denominator $\sqrt{U(z)}$, the lens has a finite focal length. To give an effective convergence, enlargement of this positive region is necessary. In order to achieve this, the lens system should have asymmetry.

Taking above factors into consideration, the author designed the physically asymmetric lens system with three electrodes. Figure 5.1 shows one of the examples of the lenses

Extractor Decelerating lens electrode   Grounded electrode
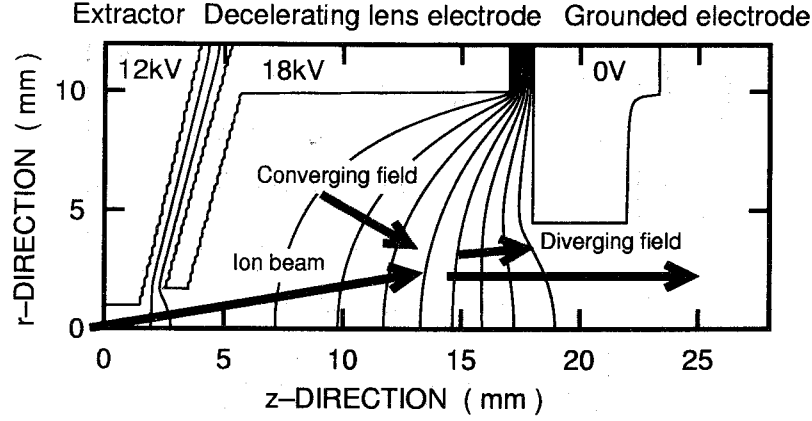
Figure 5.1: Proposed lens system with strong converging effect for divergent ion beam.

which would be appropriate for the present system. The first electrode is equivalent to the extractor, and then decelerator and grounded electrode are placed. The first gap is similar to an aperture lens. The extracted beam is once decelerated just after the extraction, and here slightly converged. The closely located second electrode may affect the electric field around the extraction region, thus an aspect ratio of the extractor aperture was set a low value of 2/3. After the deceleration, the ions are accelerated with strong converging effect. The most important part of the lens is the small aperture of the third electrode. This grounded third electrode forms the electric field between the second and the third electrodes much higher than the usual cylinder type configuration.

5.1.2 Evaluation of lens performance by computer simulation

The computer simulation was performed to confirm the capability of focusing of the divergent beams. The simulation code was developed in the present study. To solve a Laplace potential, finite difference method [7] was adopted. The entire space of 12 mm by 28 mm was divided by 120 × 280 meshes. The mesh size was consequently 0.1 mm. In order to obtain the electric field between the meshes precisely, the potential was represented by the second order Lagrange interpolation [8]. This interpolation largely improved the calculating precision which was confirmed by the trajectory calculation of the FIB system [9]. Integration of the equation of motion was solved by Euler method [8]. The potential distribution of extraction region should be necessary, but simulation from a point source involves some difficult issues. In the present simulation, the ion optics at the extraction region was

Figure 5.2: The integrand function.

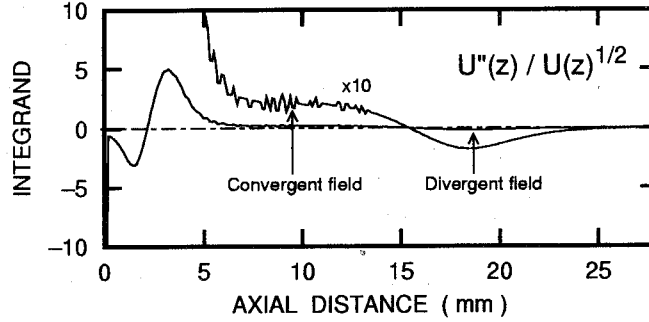neglected and it was assumed that the beam entered the lens system straightly from the source point. The ion beam was divided to beamlets with different radial velocities. The number of the beamlets were more than 14, depending upon the extraction geometry. Since the space charge is less effective due to enlargement of the beam size after extraction, the space charge effect was neglected here in the present trajectory calculation.

Figure 5.2 shows the distribution of $U''(z)/\sqrt{U(z)}$ in eq.(5.2). The positive region continues from the first aperture lens to the second gap. The total area of the positive region is larger than that of the negative region, and thus converging lens is formed. The largest value of $U''(z)/\sqrt{U(z)}$ appears at the first gap, because the electric field is stronger here due to short distance between the electrodes.

Figures 5.3(a)–5.3(d) show the focusing properties at the different lens voltages V_{pre} of 17.5, 18.0, 18.5, and 19.0 kV, respectively. The object position is −0.6 mm, which is the same as the typical experimental condition. As the lens voltage increases, the beam tend to be converged and becomes a parallel beam. It should be noted that at the beam envelop, where the beamlet experiences the stronger lens effect, the enhanced focusing effect is seen. At V_{pre} of 18 kV, the beam is almost parallel at the exit of the lens and higher V_{pre} yields the aberration for the beamlets at the envelope.

In order to evaluate the direction of each beamlet, distribution of the beamlet was drawn in a two-dimensional phase space of which abscissa and ordinate are the radial position and the tangent of the beamlet with respect to the beam axis. This is an emittance diagram, but the emittance of the beam extracted from an LMIS is small enough. Owing to this, the distribution should be drawn by a line with a negligible width. However, distortion due to aberration makes the line warped, and the effective emittance becomes finite. Figures 5.4(a)–5.4(d) indicate the distributions of beamlets in two dimensional phase space at the exit of the lens. V_{pre}'s are the same as those shown in Fig. 5.3, for V_{pre} of 17.5, 18.0, 18.5, and
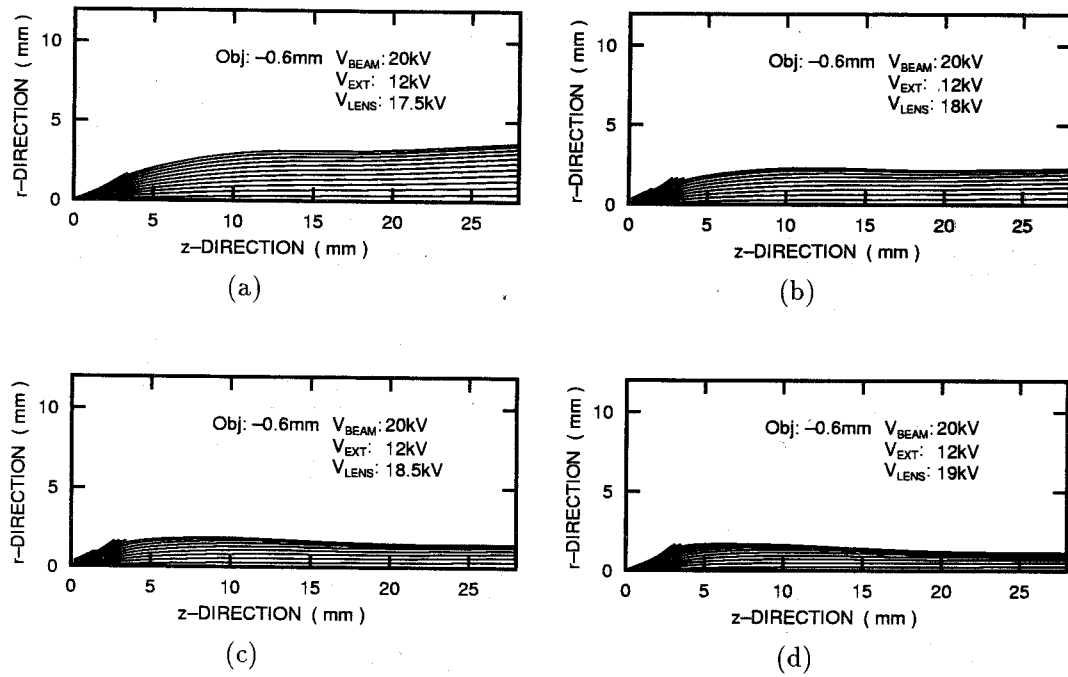
Figure 5.3: Results of computer simulation of ion trajectories at different lens voltages. (a) V_{pre}=17.5 kV, (b) V_{pre}=18.0 kV, (c) V_{pre}=18.5 kV, and (d) V_{pre}=19.0 kV.
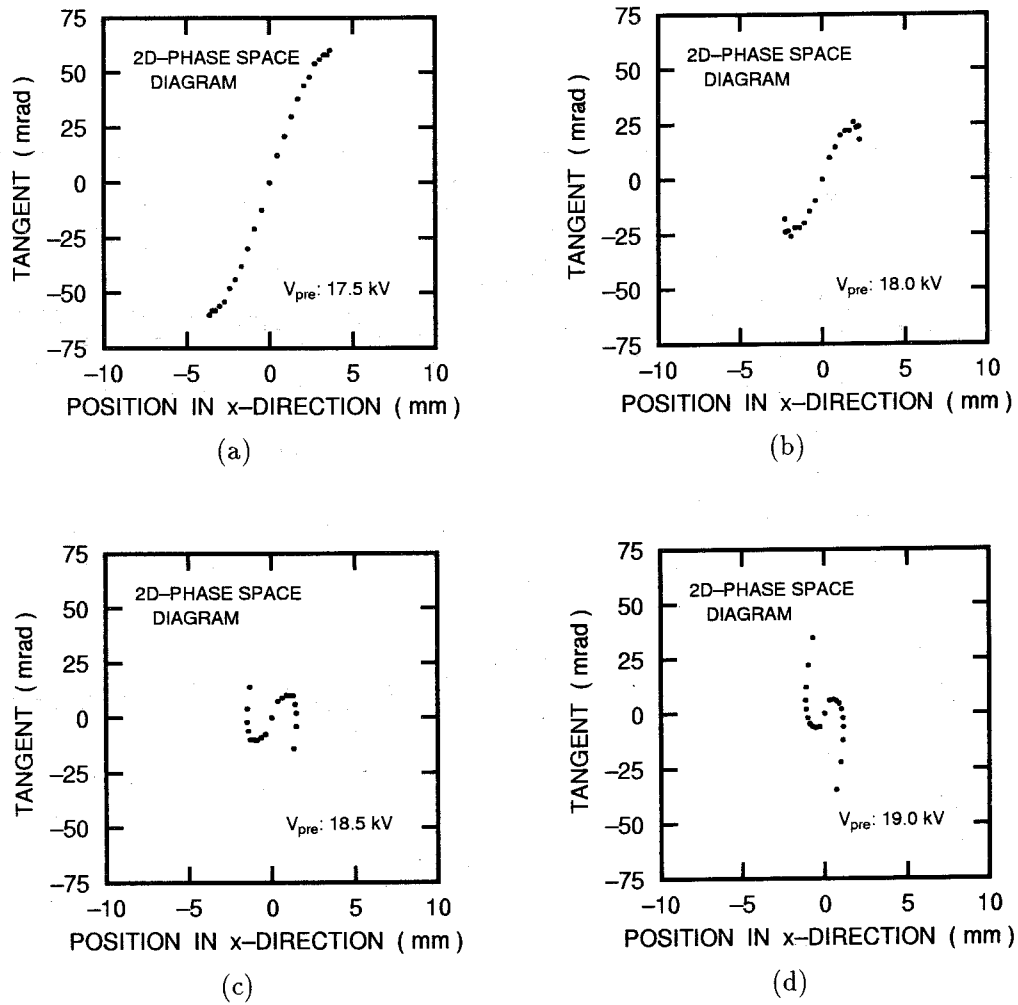
Figure 5.4: Distribution of beamlets in 2-dimensional phase space. (a)
V_{pre}=17.5 kV, (b) V_{pre}=18.0 kV, (c) V_{pre}=18.5 kV, and (d) V_{pre}=19.0 kV.
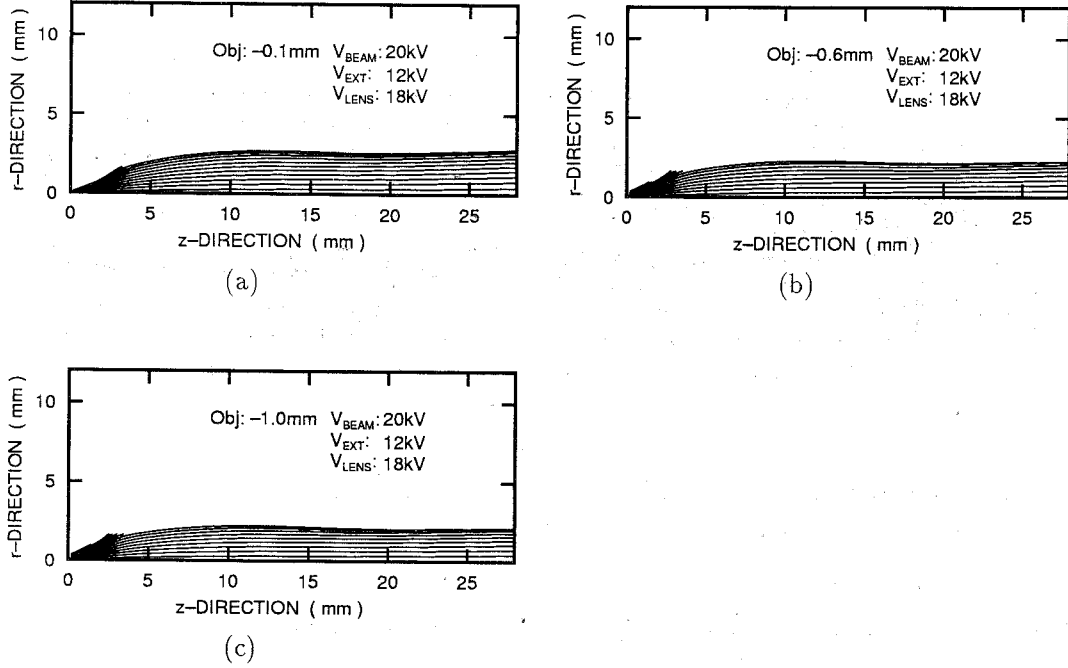
Figure 5.5: Results of computer simulation of ion trajectories at different extraction gaps. (a) 0.1 mm, (b) 0.6 mm, and (c) 1.0 mm.

19.0 kV, respectively. In Fig. 5.4(a), the distribution of the beamlets is deviated slightly from the linear line. In the case of Fig. 5.4(c), distortion becomes significant. It is clearly seen from Fig. 5.4, the strong lens effect converges the ion beam but with significant non-linear effect, *i.e.*, aberration. For Fig. 5.4(d), the effective emittance became approximately 35π mm mrad.

Figures 5.5(a)–5.5(c) show the dependence of the lens property on the extraction gap lengths of 0.1, 0.6, and 1.0 mm, respectively. The number of the beamlets that can pass through the lens decreased from 12 to 10, resulting in the decrease of the current of 45 to 36 μA. As the extraction gap is reduced, the beam tend to pass through the extractor, resulting in a high current transmittance.

5.1.3   Addition of post-stage lens

When considering the transportation of the ion beam for a long distance, it is necessary to adjust the focal length, which is the position of the image. For this purpose, addition of a post-stage lens is one of the ways to solve the above problem. Here the author demonstrates the effect of addition of post-stage lens just after the present lens system (pre-stage lens). It
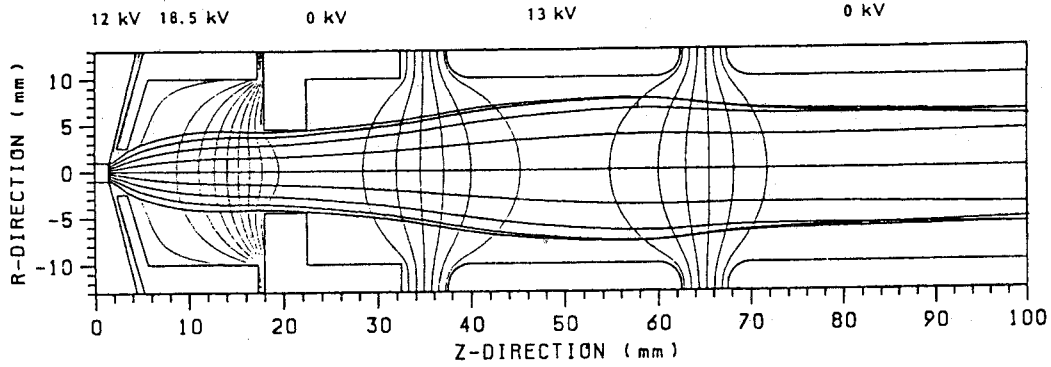
Figure 5.6: Example of the computer simulation of trajectories of beam-
lets with an additional post-stage lens.

is not necessary to use a special lens for this purpose, because the beam is almost parallel.
A conventional cylinder einzel lens is, for example, available.

Figure 5.6 shows the example of the computer simulation of the trajectories of the beam-
lets with a small post-stage lens. The beam at the exit of the pre-stage lens still has a radial
component, but acting the post-stage lens, the beam becomes almost parallel. Figure 5.7
shows the experimental results of the effect of the pre-stage and post-stage lens systems.
The experiments were performed with a Faraday cup settled at 50 cm below the ion source.
The limiter of the Faraday cup has an aperture with a diameter of 20 mm. A Ga ion source
was used to check the property. This is because the Ga ion source has similar property
with the In ion source, of which beam profile was measured. The dot-dashed line indicates
the current of I_i, estimated from I_s. Use of both lenses works well as compared with the
operation with either lens.

5.2   Design of ion implanter

5.2.1   Specification of ion implanter

As described in the previous section, the author could converge the divergent beam suc-
cessfully. Here the author applies the LMIS to an ion implantation system. Generally,
ion implantation requires precise determination of depth distribution of implanted atoms,
and thus ion species and ion energy should be precisely determined. In order to achieve
this, use of a mass separator is inevitable. As a mass separator, a sector magnet is widely
used. Although E × B type Wien filter is easy to analyze, because the ion path is straight,
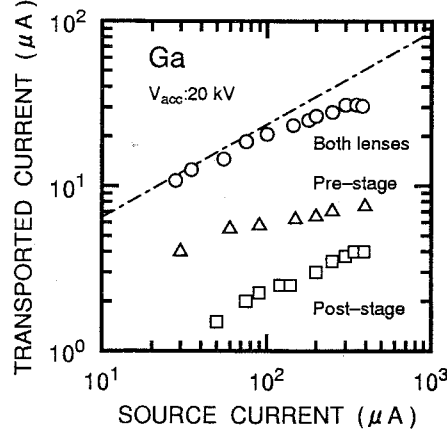
Figure 5.7: Experimental results on the beam transportation with the above lens.

neutral droplets may pass through it.

The purpose of the present design and development of the ion implanter is to demonstrate feasibility of the lens system developed in the previous section. The entire system was not optimized and transport in a given vacuum system was assumed. The first step of the design of the implanter is to obtain high transmittance of the ion beams. Here in this section, the author argues the way to transport the ion beam through a mass separator. It was assumed that the ion implantation is performed at the exit of the mass separator.

5.2.2 Ion trajectory analysis program smpltraj

It is surely possible to calculate the beam trajectories from the ion source to the target in numerical way, but it consumes too much time and requires too much memories for computations. Especially at the first stage of the development of an ion beam machine, rough estimate of the beam optics is adequate. If such an assumption that the beam can be represented by the paraxial beam, transport of the ion beam can be expressed by a matrix method [4]. The motion of the ions incident on an ion-optical element can be expressed with the transport matrix M and the vector x_{in} of which components are the position and the tangent of the ion velocity.

$$x_{out} = M x_{in} \tag{5.3}$$

where the subscripts out and in imply that the vectors are at the incident and outgoing of the optical system M. In more detail, eq.(5.3) can be expressed as,

$$\begin{bmatrix} x_{\text{out}} \\ \Delta x_{\text{out}} \end{bmatrix} = \begin{bmatrix} m_{11} & m_{12} \\ m_{21} & m_{22} \end{bmatrix} \begin{bmatrix} x_{\text{in}} \\ \Delta x_{\text{in}} \end{bmatrix}, \tag{5.4}$$

where x_{in} and Δx_{in} are the radial position of the beam and the tangent of the ion velocity at the entrance of the system, and x_{out} and Δx_{out} are those at the exit of the system. m_{11} and m_{22} are dimensionless parameters, m_{12} has the dimension of length and m_{21} has the dimension of reciprocal length. Quite similarly, the same notation for y direction is possible. Combining both x and y directions, we obtain

$$\begin{bmatrix} x_{\text{out}} \\ \Delta x_{\text{out}} \\ y_{\text{out}} \\ \Delta y_{\text{out}} \end{bmatrix} = \begin{bmatrix} m_{11} & m_{12} & m_{13} & m_{14} \\ m_{21} & m_{22} & m_{23} & m_{24} \\ m_{31} & m_{32} & m_{33} & m_{34} \\ m_{41} & m_{42} & m_{43} & m_{44} \end{bmatrix} \begin{bmatrix} x_{\text{in}} \\ \Delta x_{\text{in}} \\ y_{\text{in}} \\ \Delta y_{\text{in}} \end{bmatrix} \tag{5.5}$$

The matrix components of m_{13} and m_{14} are necessary if the tangent of the ion velocity or the position in x direction affects motion in y direction. Presence of an axial magnetic field is the case. In the present case, the author uses only a sector magnet and no axial magnetic field was applied. In such a case, the components of m_{13}, m_{14} etc. are equal to zero.

In the present study, ion beam trajectory analysis program based on the present matrix method was developed. The code is called SMPLTRAJ, written in FORTRAN77 and has the following features.

- Multiple beamlets can be analyzed:
  radial positions, energy distributions, emittance can be taken into consideration.

- All optical units are prepared as a subroutine, the designer chooses some subroutines arranged in the order of the optical elements in the system.

- Subroutines has parameters easily understood.

- Beam transport without azimuthal rotation is assumed.

- Output of cross section of beam profile and two-dimensional phase space diagram, providing the beam cross-section and focusing state.

The program can be used in various kinds of analysis of ion beams such as those with a large energy spread relative to the ion energy [10] or with a large emittance. In this case, the beamlets with the different radial positions and radial component of the velocity were calculated. This is because the ion beam focused by the pre-stage lens developed in the previous section was largely distorted, thus, virtual source position differs among the beamlets, as shown in Fig. 5.8.
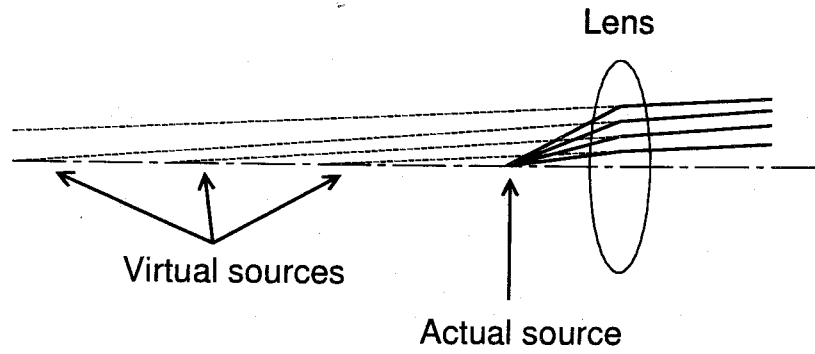
Figure 5.8: Virtual source position of the ion beam focused by pre-stage lens system.
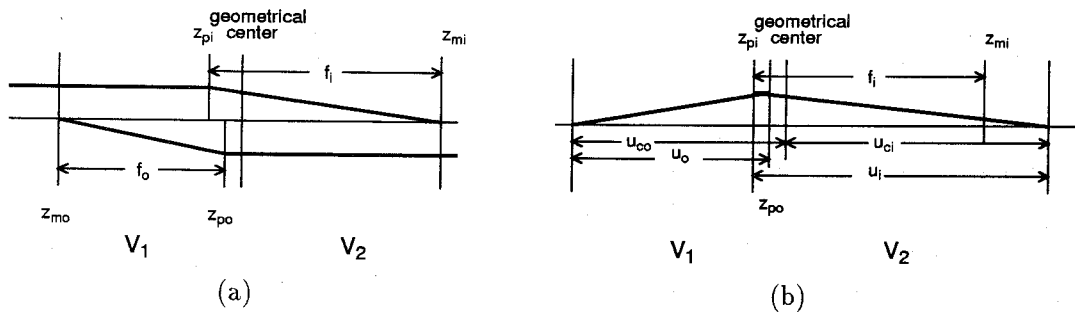

Figure 5.9: Principal planes of electrostatic immersion lens.

Drift space

The transport matrix of the drift space with a length of L is given by the following formula.

$$\begin{bmatrix} x_{\text{out}} \\ \Delta x_{\text{out}} \end{bmatrix} = \begin{bmatrix} 1 & L \\ 0 & 1 \end{bmatrix} \begin{bmatrix} x_{\text{in}} \\ \Delta x_{\text{in}} \end{bmatrix}. \tag{5.6}$$

Einzel lens

The second lens should be unipotential lens, thus conventional cylinder type einzel lens is adopted. If the diameter of the lens is large enough as compared with the beam diameter, the optical property can be well expressed within the first-order approximation. For an electrostatic lens, the assumption of the linear relation described in eq.(5.4) does not hold. This is simply because the cardinal points of geometrical optics does not coincide the geometrical center of the lens. Nevertheless, the radial position and the tangent of the ion velocity at the exit is a function of those at the entrance.

Before describing the einzel lens, first the author deals with the immersion lens consisting of two cylinders. In the case of an electrostatic lens, a principal plane does not coincide with the geometrical center of the lens. Figures 5.9(a) and (b) show the characteristic points of the lens system. The focal point in the image space u_{ci} with the object at the distance from the lens of u_{co}, can be expressed by the following formula, with the positions of the principal planes of z_{po} and z_{pi} [5],

$$\frac{n_{\text{o}}}{u_{\text{co}}} + \frac{n_{\text{i}}}{u_{\text{ci}}} = \frac{n_{\text{o}}}{z_{\text{co}} - z_{\text{po}}} + \frac{n_{\text{i}}}{z_{\text{ci}} - z_{\text{pi}}} = \frac{n_{\text{o}}}{f_{\text{o}}} = \frac{n_{\text{i}}}{f_{\text{i}}}, \tag{5.7}$$

where f_{o} and f_{i} are the focal lengths in the object space and that in the image space, and n_{o} and n_{i} are the refractive indices of the object space and that of the image space, respectively. Generally, reflective index of the space is square root of the beam voltage. That is,

$$n_{\text{o}} = \sqrt{V_1} \qquad \text{and} \qquad n_{\text{i}} = \sqrt{V_2}, \tag{5.8}$$

where V_1 and V_2 are the voltages that correspond to the beam energy in the corresponding space and not the electrode potential. These parameters for typical lens are available in tabulated form [5]. However, the book does not provide the values for a unipotential lens. To realize the properties of an einzel lens, the author combined the parameters of two lens systems, the same but symmetric in voltage.

$$\begin{cases} u_{\text{i1}} &= \left[\dfrac{1}{f_{\text{o1}}} - \dfrac{1}{u_{\text{o1}}} \right]^{-1} \dfrac{n_{\text{i1}}}{n_{\text{o1}}} \\ z_{\text{i1}} &= u_{\text{i1}} + z_{\text{pi1}} \\ u_{\text{o2}} &= -z_{\text{i1}} + d_{\text{sep}} + z_{\text{po2}} \\ u_{\text{i2}} &= \left[\dfrac{1}{f_{\text{o2}}} - \dfrac{1}{u_{\text{o2}}} \right]^{-1} \dfrac{n_{\text{i2}}}{n_{\text{o2}}} \end{cases} \tag{5.9}$$
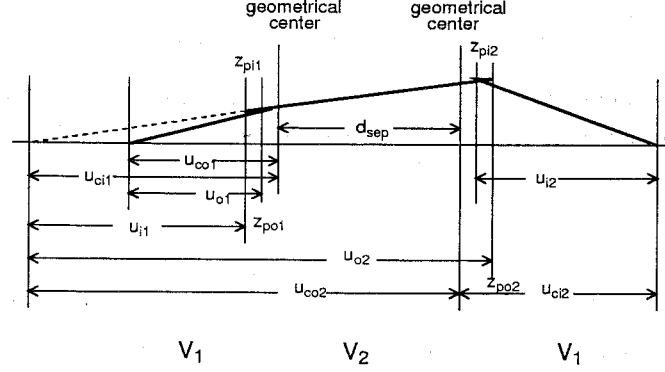
Figure 5.10: Coordination for analysis of einzel lens.

where d_{sep} is the separation of two cylinders of the einzel lens, and subscripts 1 and 2 indicate the first and second lens properties. In the case of an einzel lens, the following relations hold.

$$n_{o1} = n_{i2} = \sqrt{V_1}, \qquad \text{and} \qquad n_{i1} = n_{o2} = \sqrt{V_2}. \qquad (5.10)$$

Details of the above notations are drawn in Fig. 5.10. The calculation of the source point (u_{o1}) requires calculation of $x_{in}/\Delta x_{in}$. This is the reason why the transfer matrix does not give a linear relation. Nevertheless, the ion trajectory can be described with x_{in} and Δx_{in}.

Mass separator

The transport matrix of the mass separator [4] with the radius of curvature of R and deflection angle Ψ is

$$\begin{bmatrix} x_{out} \\ \Delta x_{out} \\ y_{out} \\ \Delta y_{out} \end{bmatrix} = \begin{bmatrix} \cos\Psi & R\cos\Psi \\ -\dfrac{1}{R}\sin\Psi & \cos\Psi \\ 1 & R\Psi \\ 0 & 1 \end{bmatrix} \begin{bmatrix} x_{in} \\ \Delta x_{in} \\ y_{in} \\ \Delta y_{in} \end{bmatrix} + \frac{\Delta(m_I v)}{m_I v} \begin{bmatrix} R(1-\cos\Psi) \\ \sin\Psi \\ 0 \\ 0 \end{bmatrix}. \qquad (5.11)$$

Beam transport without azimuthal rotation

Since the optical system of this implanter is three dimensional, because of the mass separator. The positions of the beamlets along x and y directions are to be calculated. Since the exact calculation of each beamlets takes much time, "beam transport without azimuthal rotation" was assumed. The position vector $\boldsymbol{p} = (p_y, p_y)$ of the each beamlet along the

azimuthal direction can be described by,

$$p_x = x \cos \psi, \quad \text{and} \quad p_y = y \sin \psi, \tag{5.12}$$

since axial magnetic field which rotates the beamlet along the rotational direction does not exist. This case, only the calculation of the vectors x and y is necessary.

Beam limiting element

Finite acceptance of an aperture or a slit is realized by limiting the current of the beamlets to zero, when the beamlet was incident on these elements. Summing the currents over the transported beamlets gives the total transmittance of the system.

5.2.3 Analysis of beam transmittance

Figure 5.11 shows the designed ion implantation system. Due to the fact that it is easy to operate an LMIS in vertical mode, the present ion implantation system stands upright. The total transporting distance was approximately 0.5 m before entering the mass separator, because the pumping system required fairly long space. The design was based on the general specification of an ion implanter so that the acceleration voltage of injector is 30 kV.

Testing of the beam transmittance of the implanter was performed assuming the current density profile of In ion source measured in Chapter 2. The present implanter can be expressed as

$$x_{\text{out}} = M_{\text{MS}} M_{\text{DS2}} M_{\text{EL}} M_{\text{DS1}} x_{\text{exit}}. \tag{5.13}$$

where subscript MS means mass separator, DS means drift space, EL means einzel lens, and x_{exit} is the vector of a beamlet at the exit of the pre-stage lens. Since the position and tangent with respect to the beam axis can be obtained from the results of the computer simulation, x_{exit} can be known.

Figures 5.12(a)–(d) show the beam spot cross sections for various points: (a) position-1: just after the pre-stage lens, (b) position-2: before entering the einzel lens, (c) position-3: just after the einzel lens, and (d) position-4: after the mass separator. The voltage of the post-stage lens V_{post} was 14 kV. The calculation was performed with V_{pre} of 18.0 kV, and V_{ext} of 8 kV, and V_{acc} of 20 kV. The object position (extraction gap) was 0.6 mm. Figures 5.13(a)–(d) show the phase space distributions for $x-$direction at the same condition as Fig. 5.12. In the present condition, all the beamlets could be transported through the mass separator. The ion current of 36 μA could be transported from the calculated results. However, lens voltages of 13 kV and 15 kV do not allow all the beamlets transported, and the currents were reduced to 30 μA.

Actually, the ion beam has a wide energy spread up to 100 eV, as shown in Chapter 2. This surely affects the transmittance of the beam. The author calculated the transmittance
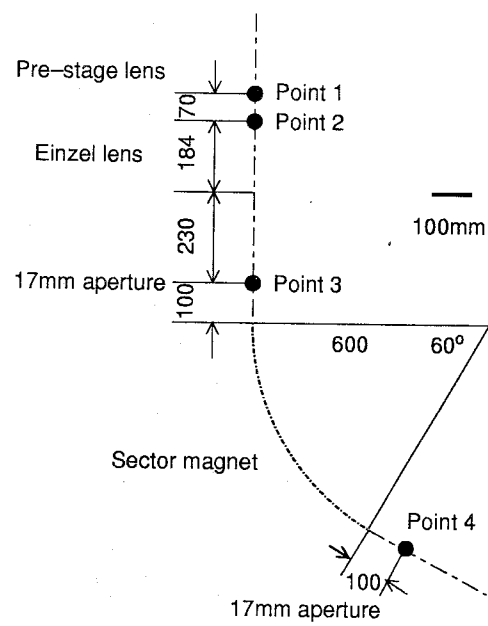
Figure 5.11: Schematic diagram of the ion implantation system.
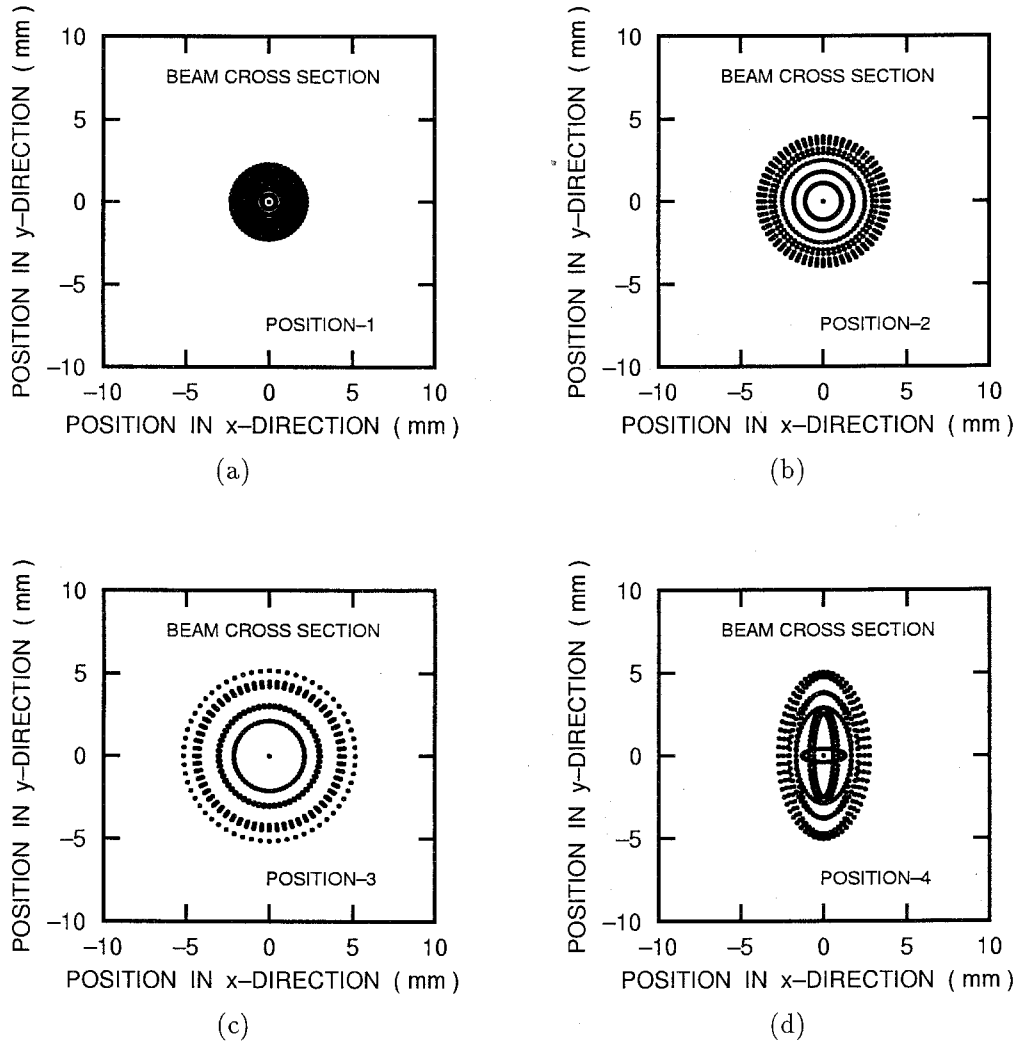
Figure 5.12: Calculated beam cross section. $V_{\mathrm{pre}}{=}18$ kV and $V_{\mathrm{post}}{=}14$ kV. (a) at the exit of pre-stage lens, (b) at the entrance of the post-stage lens, (c) at the exit of the post-stage lens, and (d) at the exit of the sector magnet.
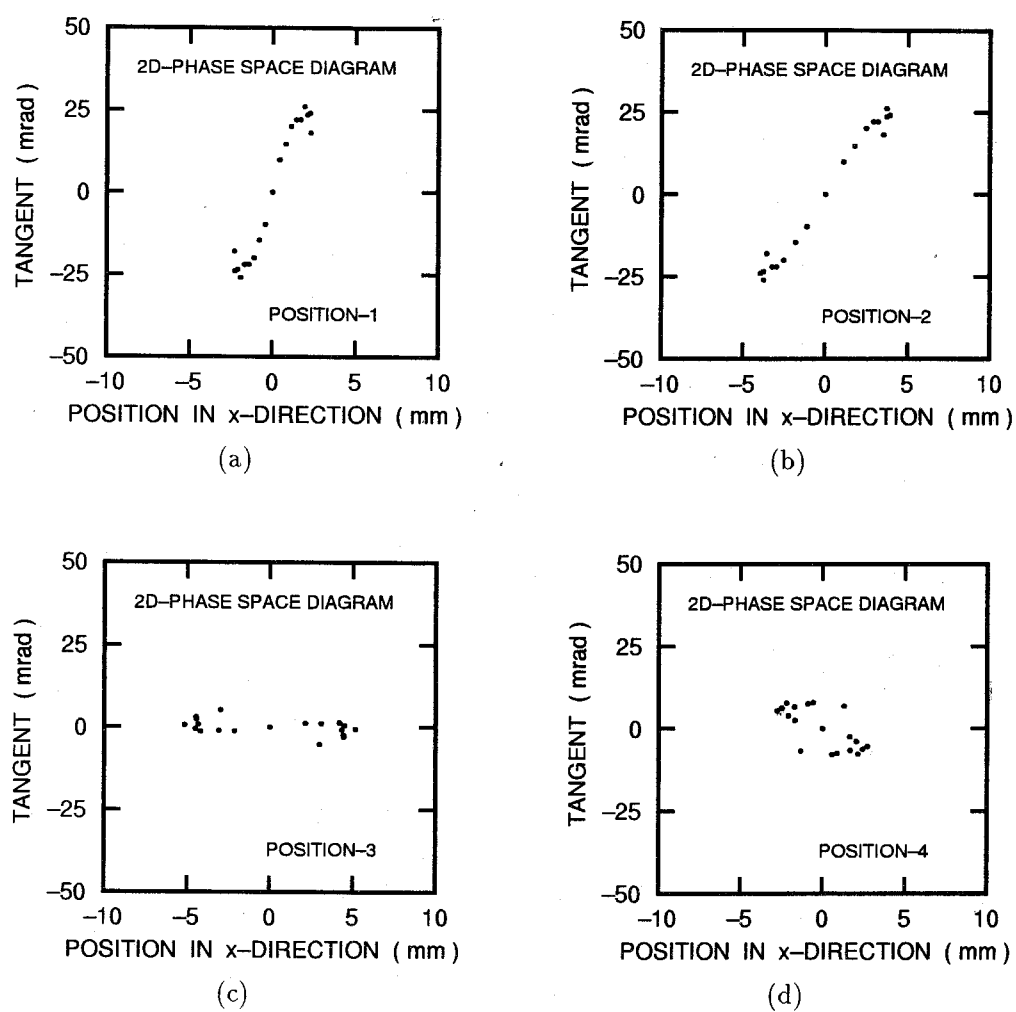
Figure 5.13: Distribution of beamlets in 2-dimensional phase space at various points of ion transportation system. V_{pre}=18 kV and V_{post} = 14 kV.

also for the ion beam with multiple ion energies. The energy spread was assumed to be ±100eV. Figures 5.14(a)–(d) shows the calculated beam spots for this multiple-energy beam, at the positions shown in Fig. 5.11. As is clearly shown in Fig. 5.14(d), the beam cross section was distorted due to transverse magnetic field which acts differently for the ions with the different energies. Figures 5.15(a)–(d) show the calculated distribution in two-dimensional phase space in x−direction for the multiple-energy beam.

Dependence of transported current on source current

Since we have the data of the beam profiles at various I_s values, we can predict the transported current through the mass separator as a function of I_s. Since almost all ions could be transported, the available current at the target would be that pass through the extraction electrode. The acceptance angle of the present lens system under the extraction gap of 0.6 mm is 25°. Figure 5.16 shows the dependence of the current accepted in the present aperture I_a as a function of I_s. At the higher current region, the dependence is

$$I_a \propto I_s^{0.56}, \tag{5.14}$$

which is similar to the relation between I_i and I_s.

5.3   Performance of ion implanter

5.3.1   Beam analyzing system

Since the author has demonstrated successful transport of the divergent beam by computer simulation, here the effectiveness is confirmed by the experiments. In Fig. 5.17, the beam analyzing system for the designed implanter is given. Feeding voltages to the pre-stage lens was made at the ion source base flange, and feeding voltages to the post-stage lens was made at the transportation chamber. The ion source chamber can move along x− and y−directions, in order to align the ion source to the mass separator. The performance of the designed ion implanter was evaluated by Faraday cups settled at just in front of, and at just after the mass separator. The diameter of the beam-limiting aperture of Faraday cup 1 was 20 mm, and that of the beam-limiting aperture of Faraday cup 2 was 17 mm. A Ga ion source was used to check the performance. As denoted previously, Ga ion source yields large amount of Ga^+ and the magnitudes of the currents for the other ion species are little. Furthermore, the Ga ion beam has proven to have a similar profile as In has [11], in spite of the difference in the mass to charge ratio. Thus it is possible to examine the lens performance with the Ga ion source.
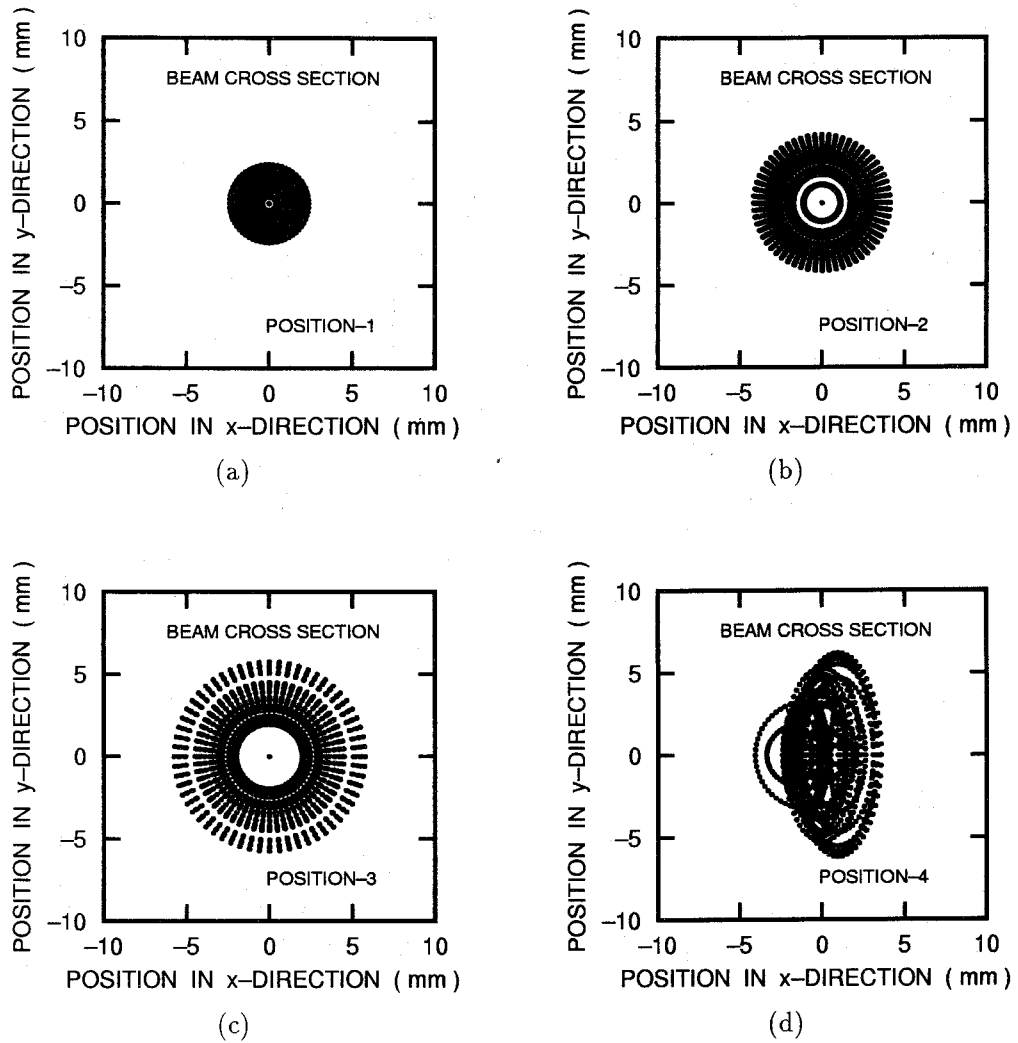
Figure 5.14: Calculated cross-section of the beam with energy spread of ±100 eV. V_{pre}=18 kV, and V_{post}=14 kV.
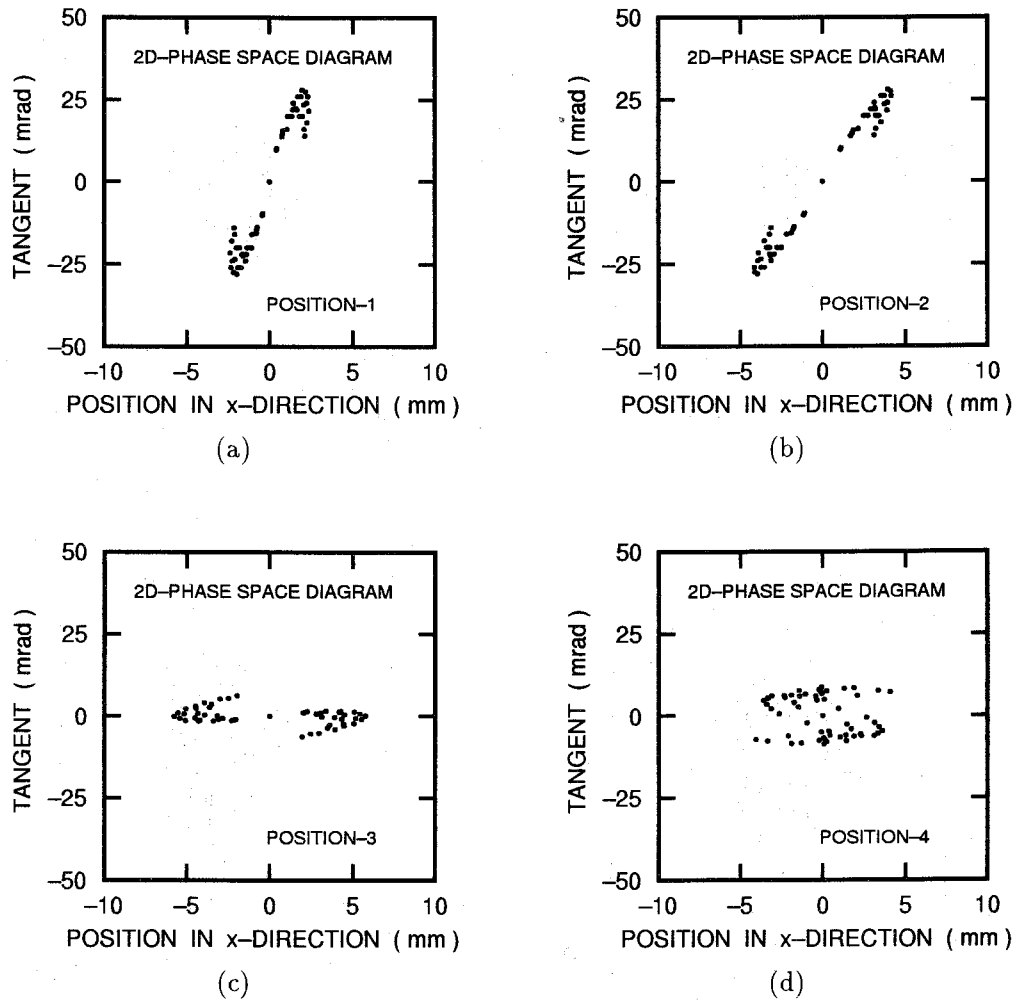
Figure 5.15: Calculated distribution of beamlets in 2-dimensional phase space. V_{pre}=18 kV and V_{post}=14 kV. The effect of energy spread is also taken into consideration.
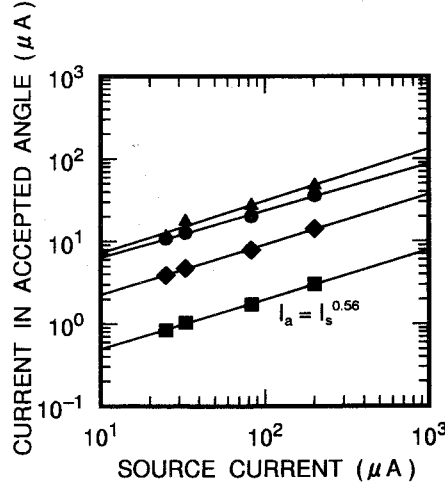
Figure 5.16: Relation between I_a and I_s.

5.3.2 Transportation in drift space

The transported current just before the mass separator was measured by the Faraday cup 1. Figure 5.18 shows the typical example of the transported current as a function of I_s. The solid circles show the experimental results and the open circles show the predicted value. The transported current I_{tr} has the relation of

$$I_{tr} \propto I_s^{0.47},$$ (5.15)

and this relation is close to the relation between I_a and I_s.

$$I_a \propto I_s^{0.5\sim0.6}.$$ (5.16)

This means almost all extracted ions are transported to the Faraday cup 1. In fact, I_{tr} reached 50 μA at I_s of 200 μA. This value was larger than I_a. This is probably due to the fact that the difference in the extraction geometry affected the yield of the secondary electrons at the extractor.

5.3.3 Mass separated ion current

Figure 5.19 shows a result of the experiments for the transportation through the mass separator. In the present experiment, extraction gap was set to be 0.5 mm. Up to I_s of 0.2 mA, the mass-separated current I_{ms} did not depend upon the beam energy. I_{ms} was
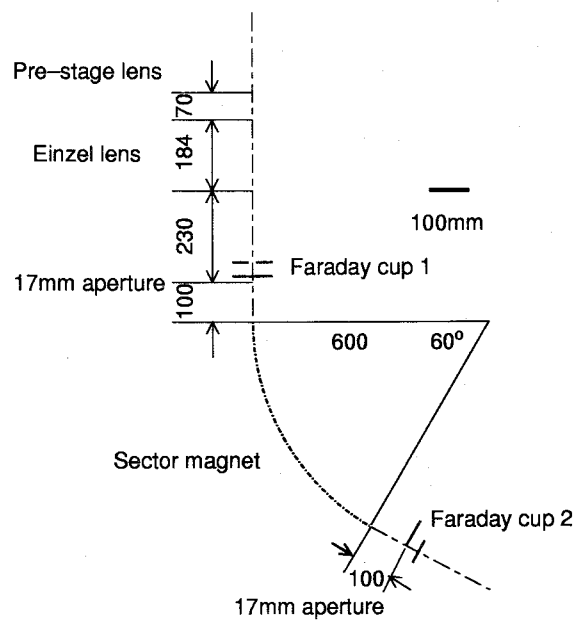
Figure 5.17: Beam analyzing system.
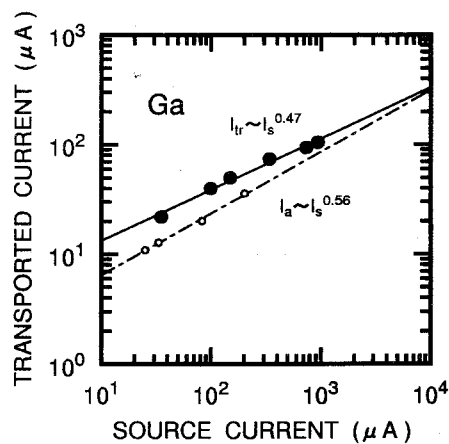
Figure 5.18: Transported current just before the mass separator.
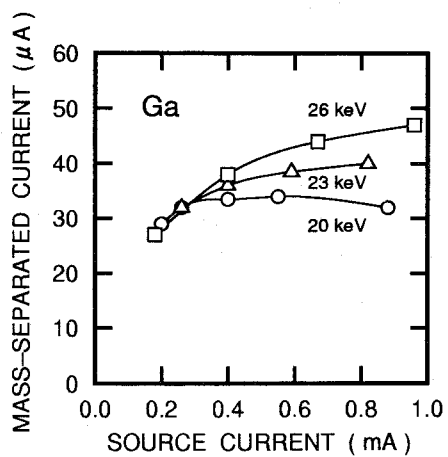
Figure 5.19: Mass separated ion current as a function of I_s.
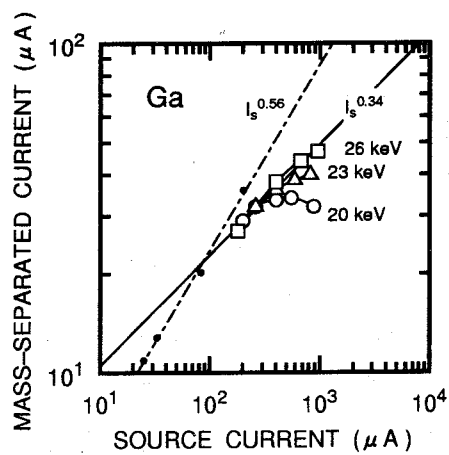
Figure 5.20: Mass separated ion current as a function of I_s in logarithm plot.

about 30 μA at I_s of 200 μA, which is equivalent to I_a of 36 μA. At the acceleration voltage of 20 kV, I_{ms} saturated and decreased at the higher current regime. As the acceleration voltage was increased to 26 kV, the saturation tended to cease. At the 26 kV acceleration, with I_s of approximately 1 mA, I_{tr} was almost 50 μA.

Figure 5.20 shows the relation between I_{ms} and I_s. The slope of the curve at 26 kV is almost 0.34, so the relation between I_{ms} and I_s becomes

$$I_{ms} = I_s^{0.34}. \tag{5.17}$$

The present experiments showed that the lens could transport about 50 μA of Ga$^+$, which enables us various kinds of application. Also it can be said that saturation at the higher current lowers the total efficiency of the system.

5.3.4   Discussion

The reason for the lower transmittance at the higher current regime is not clear. Since the mass-separation selects ions with different mass-to-charge ratios, reduction of the efficiency is inevitable. However, for the case of Ga, it emits only minor amount of molecular ions, as shown in Chapter 2. Thus, this is not the reason of the reduction in transport efficiency. There seems to be some candidates. One is an emittance growth at the extraction region. The growth of the emittance was shown by Alton and Read [12]. They measured the emittance growth for two different types of extractors and compared the results. Their results suggested the emittance came to approximately 30π – 70π mm mrad at 6 kV extraction. This emittance growth is comparable to that grown with the present asymmetric lens, which means the relatively large effect for the reduction of the transmittance can be considered. Their results could not be fully utilized in the estimation of the present transmittance, because the value was measured at far from the source.

Together with the emittance growth, the large energy spread is also one of the candidates. The author calculated the lens performance with the energy spread of ±100 eV. However, operation at a high source current often showed a large width of the mass spectrum [13], which means the larger energy spread than 100 eV. As was shown in the previous section in the present Chapter, the ions with different energy have difficulties in transportation through a mass separator. At the measured current range, the energy spread would be estimated to approximately 120 eV from Fig. 3.7. Considering that the energy spread was determined by the FWHM of the energy distribution, some portion of the beam may become out of the range of $\pm$ 100 eV.

Also the experimental set up may create the low-efficiency, in this case. One is the increase of ripple in the output voltage of the acceleration power supply. As the wave form of the output voltage was not observed, it is not known how the wave shape at the ion source

operation was. If the ripple of the output voltage is proportional to the output current, namely I_s, an apparent energy broadening occurs with $\Delta V \propto I_s$. The mass-separation property is roughly dependent on $\Delta V/2V$, and thus the property is improved for smaller $\Delta V/2V$. That is to say, it is improved for higher V_{acc} at the same I_s. Kashiwagi *et al.* obtained I_s of 72 μA with a Li ion source and the equivalent lens system [14,15]. Li^+ is a light ion, the condition for passing through the mass separator allows large ΔV.

5.4 Example of ion implantation

5.4.1 Molecular ion implantation

Since the author constructed a unique ion implanter with an LMIS, application of this system is expected to be also unique. As described in Chapter 4, the alloy ion sources, of which source material has large binding energy between the constituents, yielded molecular ions with a relatively high magnitude. Here the author demonstrates the result of the molecular ion implantation of $AuSb^{2+}$ to a silicon substrate. Molecular ion implantation is currently of great importance as reported by many researchers. So far, molecular implantation was performed with homogeneous molecules such as N_2 and O_2, or hydrides of boron, phosphor and arsenic [16]. Also decaborane [17] implantation attracted much interest for formation of a shallower $p - n$ junction.

Here the author demonstrates molecular ion implantation with heterogeneous molecules [18]. Simultaneous implantation of heterogeneous atoms into solid may show significant effect on the alteration of the implanted layer. In fact, implantation of diborane reduced the annealing temperature necessary to recover the crystallinity. Also in a low energy regime, diatomic carbon ion deposition showed superior property of the films [19] as well as ionized cluster beam deposition developed by Takagi *et al.* [20]. As for the heterogeneous molecular deposition, a carbon nitride ion is used to deposit CN films [21].

If the molecular ions consisted of atom A and atom B are accelerated by a voltage of V_{acc}, the energies provided to atoms A and B, E_A and E_B are

$$\begin{cases} E_A &= \dfrac{m_A}{m_A + m_B}eV_{acc}, \\[2mm] E_B &= \dfrac{m_B}{m_A + m_B}eV_{acc}, \end{cases} \tag{5.18}$$

where m_A and m_B are the masses of atoms A and B, respectively. The velocities of the atoms A and B are of course the same value. When the ion is incident on the solid target, the ion penetrates into the solid, suffering from the energy loss due to nuclear stopping power $S_n(E)$ [22]. The electronic stopping power $S_e(E)$ in this energy range (<30 keV) is small enough to be eliminated from the argument. $S_n(E)$ is almost proportional to the

square root of the ion energy in the energy range of some tens keV, which means that S_n is almost proportional to the ion velocity. Since the ion range R_p is roughly estimated by

$$R_{\mathrm{p}} = \int_{E_0}^{0} \frac{1}{\mathrm{d}E/\mathrm{d}z} \mathrm{d}E = \int_{E_0}^{0} \frac{1}{N_{\mathrm{v}} S_{\mathrm{n}}(E)} \mathrm{d}E, \qquad (5.19)$$

where E_0 is the incident energy, and N_v is the atomic density of the solid. The ions that experience a similar nuclear stopping rest at the similar depth. Owing to this, the implantation of molecular ions gives a similar projected range, and the implantation of heterogeneous atoms at the same time can be achieved.

Although the concept of the molecular ion implantation is proposed, no ion sources that can produce heterogeneous molecular ions exist. As described previously, LMIS provides molecular ions unlike the plasma type ion sources, especially when an alloy system with a large binding energy, heterogeneous molecular ions could be easily obtained with a high intensity. Here in this section, the author argues the implantation of $AuSb^{2+}$, which was observed in Chapter 4. Figures 5.21(a) and 5.21(b) show $S_n(E)$ and $S_n(V_{acc})$ for the present case. In the calculation, the screening function used was the "universal screening function", proposed by Ziegler [22]. Incidentally, S_n's for Au and Sb are similar, so the two curves are almost similar in Fig. 5.21(a). If the molecule of AuSb is accelerated and is implanted into the solid, the relation between the acceleration voltage and S_n's become like those in Fig. 5.21(b). From this figure, it is noted that the stopping powers are similar each other, and the ion range would be similar in the solid. Much more precisely, if we select the ion energy and the combination of the molecules, we can fabricate the very shallow junction which is metallized might be produced.

5.4.2   Sample preparation

Molecular ion implantation was performed with the $AuSb_2$ ion source developed in Chapter 4 and also with the high current transportation system developed in this chapter. Table 5.1 shows the implantation condition. The average ion current during implantation was 0.6 μA. Taking the fraction of $AuSb^{2+}$ ions in the total beam current (7.4 %), transported total current was calculated to be 8.1 μA, which was due to the low acceleration voltage of 12 kV. The conventional LSS theory [24] predicts the projected range of 8.3 nm and 10.6 nm for Sb and Au atoms. From this, it is known that the projected ranges are similar for Sb and Au. Also the standard deviations are predicted to be 2.8 nm and 3.0 nm, respectively. The peak concentrations are calculated to be 9.6×10^{21} and 8.9×10^{21} atoms cm^{-3}, respectively.
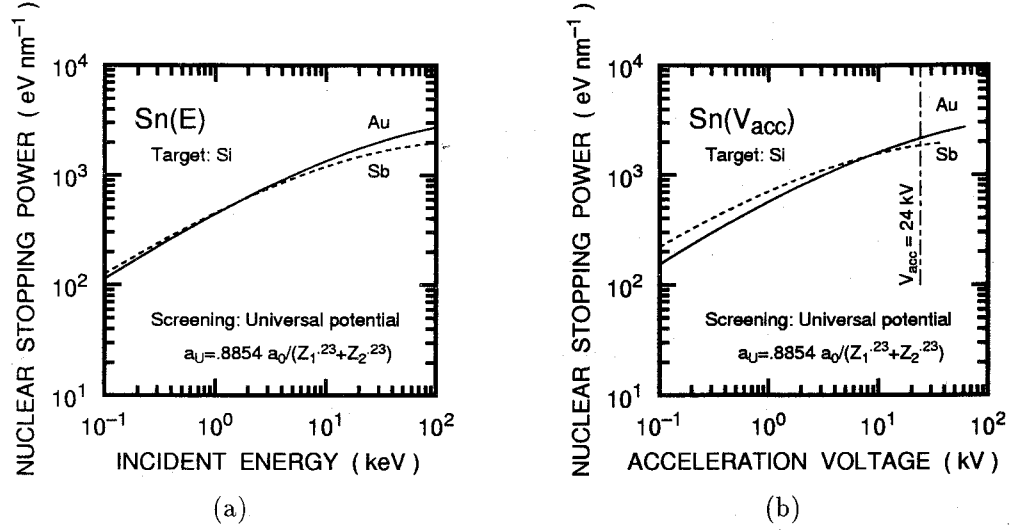
Figure 5.21: Nuclear stopping power for Au and Sb atoms in Si. (a) as a function of energy, and (b) as a function of acceleration voltage of heterogeneous molecular ion of AuSb.

Table 5.1: Condition of molecular ion implantation.

Terms	Conditions
Ion species	$AuSb^{2+}$
Ion energy	24 keV
Ion current	0.6 μA, equivalent to 0.2 μA cm^{-2}
Ion dose	6.7×10^{15} ions cm^{-2}
Substrate	n-Si(100)
Ion incident angle	7° off with respect to substrate normal
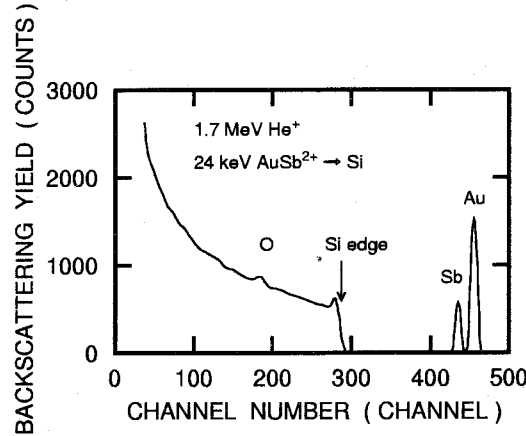
Figure 5.22: RBS spectrum from implanted sample.

5.4.3   Analysis of implanted sample

In order to confirm the implanted ion species, characterization of implanted sample was performed. Figures 5.22 and 5.23 indicate the spectra of RBS and Particle Induced X-ray Emission (PIXE) measurements, respectively. These experiments were performed by the 1.7 MeV van de Graff accelerator, Quantum Science and Engineering Center, Kyoto University. The probe beam was 1.7 MeV He^+ and scattering angle of 135°. From the RBS spectrum, two peaks due to heavy atoms can be seen. The positions of these peaks well agree with those for Au and Sb. Due to poor depth resolution of RBS, the distribution of these elements toward the interior of the substrate could not be determined. The peak area ratio of Sb/Au was 0.40 that showed a good agreement with the theoretical value of 0.42 [25]. The absolute implanted dose could not be confirmed because RBS spectrum shows channeling effect of substrate Si, but considered to be within an error of 20 %. Further confirmation of the implanted elements was performed by PIXE. Figure 5.23(a) shows the raw data obtained from implanted and virgin samples. Only slight difference could be seen, and subtracting the virgin signal from the implanted signal emphasized the difference. The difference was normalized by the virgin signal. This result is shown in Fig. 5.23(b). The peak at the lower energy corresponds to Au $M\alpha$ (2.12 keV), and that at the higher energy corresponds to Sb $L\alpha$ (3.60 keV) [26,27]. From these measurements, it was shown that the implanted ions were composed of Sb and Au.
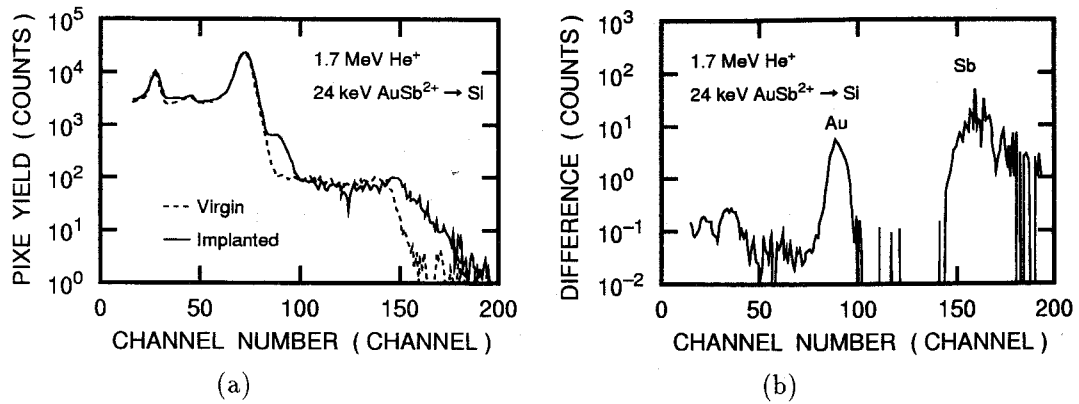
Figure 5.23: PIXE spectrum of molecular ion implanted sample. (a) signals from implanted sample and virgin substrate and (b) difference of two signals.

5.5 Conclusion

An electrostatic lens system that owns an adequate capability of converging the divergent ion beam was developed and the ion implanter was designed with the new lens system. It was found that the almost all of the ions could be transported to the 1 m distant target through a mass separator at the lower current regime. At the higher current regime, probably due to the increase of the apparent energy spread, the efficiency decreased. However, 40 μA of the Ga ion was transported to the target at the acceleration voltage of 26 kV. As a demonstration of the ion implanter, a novel ion implantation of "molecular ion implantation" was performed. As demonstrated in the present chapter, the ion implanter with a LMIS will provide a novel ion beam processing for the materials science.

References in Chapter 5

[1] P. D. Prewett, D. K. Jeffereies and T. D. Cockhill: Rev. Sci. Instrum. **52** (1981) 562.

[2] L. W. Swanson, G. A. Schwind and A. E. Bell: J. Appl. Phys. **51** (1980) 3453.

[3] T. Ishitani, K. Umemura, S. Hosoki, S. Takayama and H. Tamura: J. Vac. Sci. Technol. A **2** (1984) 1365.

[4] R. G. Wilson and G. R. Brewer: *Ion Beams with Application to Ion Implantation* (John Wiley & Sons, New York, 1973).

[5] A. B. El-Kareh and J. C. J. El-Kareh: *Electron Beams, Lenses and Optics* (Academic Press, Orlando, 1970).

[6] Y. Shibata, *Shinku Denshi Kogaku, (Vacuum Electronics)* (Corona, Tokyo, 1985) [in Japanese].

[7] E. Sugata ed. *Denshi-Ion Biimu Hando Bukku Dai 2 Han* (Handbook of Electron and Ion Beams, 2nd Edition) (Nikkan Kogyo Shinbun, Tokyo, 1986) Chapter 2, p.29 [in Japanese].

[8] H. Sunomoto: *Suchi Keisan (Numerical Analysis)* (Saiensu, Tokyo, 1978) [in Japanese].

[9] Y. Gotoh: *Analysis of Liquid-Metal Ion Sources and Transport of Intense Ion Beams,* M. E. Thesis, Kyoto University, 1987 [in Japanese].

[10] Y. Gotoh, H. Kubo, H. Tsuji and J. Ishikawa: Rev. Sci. Instrum. **71** (2000) 1160.

[11] Y. Gotoh: *Ion Beam Characteristics of Impregnated-Electrode-Type Liquid-Metal Ion Source*, B. E. Thesis, Kyoto University (1985) [in Japanese].

[12] G. D. Alton and P. M. Read: J. Phys. D **22** (1989) 1029.

[13] Y. Gotoh, unpublished data, 1986.

[14] T. Kashiwagi: *Intensification of Impregnated-Electrode-Type Liquid-Metal Ion Sources* M. E. Thesis, Kyoto Unviersity, 1988 [in Japanese].

[15] J. Ishikawa, H. Tsuji, T. Kashiwagi and T. Takagi: Nucl. Instrum. Meth. **B37/38** (1989) 155.

[16] A. Yoshida, M. Kitagawa and T. Hirao: Jpn. J. Appl. Phys. **32** (1993) 2151.

[17] D. Takeuchi, N. Shimada, J. Matsuo, I. Yamada: Nucl. Instrum. Meth. B **121** (1997) 345.

[18] J. Ishikawa, H. Tsuji, M. Mimura and Y. Gotoh: *Proc. of the 11th International Conference on Ion Implantation Technology, IIT'96*, Austin, June 17–21, 1996 (1996) p.776.

[19] J. Ishikawa, Y. Takeiri, K. Ogawa and T. Takgai: J. Appl. Phys. **61** (1987) 2509.

[20] T. Takagi: *Ionized Cluster Beam Deposition and Epitaxy* (Noyes Publications, Park Ridge, 1988).

[21] H. Tsuji, S. Nakamura, Y. Gotoh, J. Ishikawa: Thin Solid Films **343/344** (1999) 17.

[22] J. F. Ziegler: *The Stopping and Range of Ions in Solids*, in J. F. Ziegler ed. *Ion Implantation Science and Technology*, 2nd edition (Academic Press, San Diego, 1988).

[23] Y. Gotoh, H. Tsuji and J. Ishikawa: Jpn. J. Appl. Phys. **33** (1996) 3670.

[24] B. Smith: *Ion Implantation Range Data for Silicon and Germanium Device Technologies* (Learned Information (Europe), Oxford, 1977).

[25] W.-K. Chu, J. W. Mayer and N.-A. Nicolet: *Rutherford Backscattering Spectrometry* (Academic Press, Orlando, 1978).

[26] S. A. E. Johanson and J. L. Campbell: *PIXE A Novel Technique to Elemental Analysis* (John Wiley and Sons, Chichester, 1988).

[27] J. W. Mayer and E. Rimini: *Ion Beam Handbook for Material Analysis* (Academic Press, Inc., New York, 1977).

Chapter 6

Development of metal ion beam self-sputter deposition system

The author demonstrates the application of intense metal ion beam to materials science in this chapter. The author proposes a novel thin film processing, "metal ion beam self-sputter deposition". In this technique, a noble gas ion source in an ion beam sputtering system, is replaced by an LMIS. Since the sputtered neutrals experiences no gaseous medium, they do not lose their kinetic energy which is suitable for film formation. Furthermore, due to absence of noble gas ions, the film is free from incorporation of noble gas atoms, which is seen in the conventional ion beam sputtering. The author describes the development of the metal ion beam self-sputter deposition system and demonstrates the possibility of thin film formation with this technique.

6.1 Concept of metal ion beam self-sputter deposition

It has been well known that the kinetic energy of the depositing particles significantly affects the resulting film properties such as crystallinity, orientation, surface morphology, internal stress and so on [1]. The depositing particles should have an appropriate kinetic energy to migrate on the film surface, which is generally several to a few tens electron volts. There are many deposition techniques which are characterized by the presence of energetic particles: sputter deposition [1–5], ion beam deposition (IBD) [6–12], ion beam assisted deposition (IBAD) [13–19], ion plating [20–22] and ion beam sputter deposition (IBSD) [23].

Generally, production and transportation of the ion beam with the energy of a few tens electron volts is quite difficult, owing to the huge space charge effect. For this reason, IBD and even IBAD may have difficulties in producing an atom flux with the appropriate energy for film formation. Sputtering is one of the processes that produce neutral atom fluxes with the above energy, which does not have space charge problem. However, in diode sputtering or in magnetron sputtering, sputtered particles are thermalized by the collision with the carrier gas atoms to have lower energies [24]. The film property is often dominated by the bombardment of carrier gas ions or by the reflected ions, rather than by the kinetic energy of the sputtered particles themselves [3,4]. Incorporation of gas ions

Table 6.1: Sputtering yield of copper against the incidence of various ions.

Metal	Projectile	500 eV	1 keV	5 keV	10 keV	20 keV
Cu	Ar	2	3	5	6	7
	Cu	2.4	3.6	7	9	10
	Kr	2.2	3.6	7	9	10
	Xe	2	3.7	9	11	16

results in the increase of the electrical resistivity for metallic films [25, 26]. Even in the IBSD, where deposition is performed in high vacuum, ions reflected at the target impinge on the growing film and affect the film properties [23] or are incorporated in the films. These bothersome problems are attributed to the fact that sputtering takes place by noble gas ions. Besides the problems of the incorporation of noble gas atoms, gas inlet often create difficulties such as leakage or introduction of unexpected gases into the chamber. Especially for semiconductor fabrication, ultra clean environment is necessary [27] to avoid residual gas molecules from the pipes for gas introduction. Sputtering without gas introduction is desired for thin film processing.

In order to overcome these problems, the author proposes a new technique, in which the target is sputtered by the metal ions of the same element as the target (self-sputtering). So far, self-sputtering was achieved by post-magnetron sputtering and also planer magnetron sputtering [28, 29]. In these attempts, however, gas should be introduced to ignite the plasma. Furthermore, the material is restricted to have a high sputtering yield so that the discharge continues. If the metal ion is provided externally, there would be no limitation of the material. In addition to this, self-sputtering yield is generally higher than Ar ion sputtering, as shown in Table 6.1 [30]. The sputtering yield of Cu due to an Ar ion bombardment is approximately 6 to 7, and that due to a Cu ion bombardment is almost 10 [30,31]. This higher sputtering yield is also one of the advantages of the present method.

The LMIS is suitable for this purpose, because it requires no carrier gas, and can be operated in UHV as was emphasized in Chapter 1. Mass separation is not necessary, if element metal is used as a source material. This is because the LMIS emits only the same
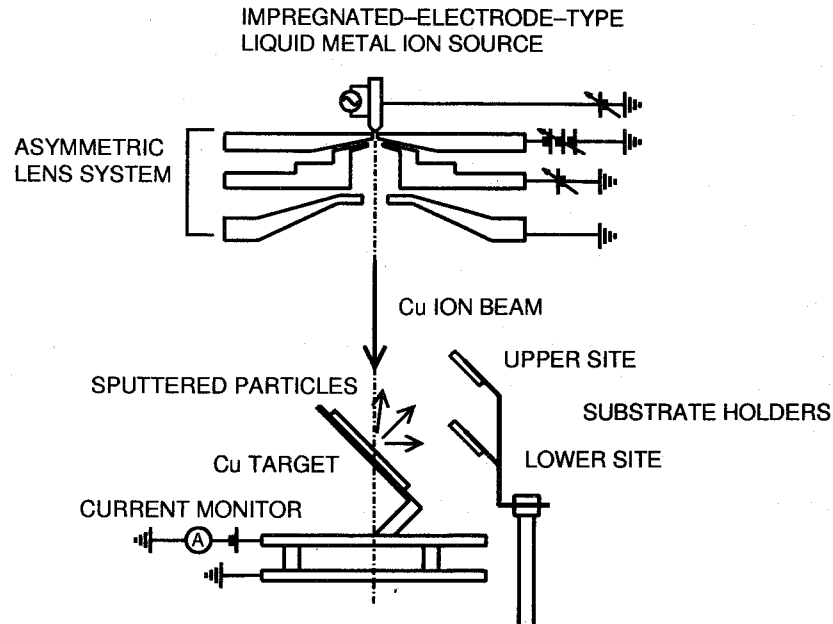
Figure 6.1: Schematic illustration of metal ion beam self-sputter deposition system.

species of ions, although doubly charged ions, molecular ions, and droplets as well as singly charged atomic ions are involved as shown in Chapter 2. The system is simple and bakable, the deposition chamber can be maintained in UHV. Since the sputtered particles experience no gaseous medium, they do not lose their energy until sticking to the substrate. In the present study, the author demonstrates the formation of Cu thin films, which is expected to be the material for interconnects of the large scale integrated circuits [32].

6.2 Metal ion beam self-sputter deposition system

Figure 6.1 shows the schematic diagram of the deposition system. The system is composed of the IELMIS, an electrostatic lens system, a target, and substrate holders. Here in this study, an ion emission tip with a 5 mm-wide reservoir, which was already shown in Chapter 2 was used, in order to mount sufficient amount of Cu. The emission cusp was machined to have only one emission point. The holding system of the IELMIS was modified so as to be similar to those reported by Nagamachi et al. [33].

In order to focus the divergent ion beam extracted from the LMIS, the physically asym-

metric lens system developed in Chapter 5 was employed. No post-stage lens was used because we can set the target at the position close to the ion source.

A 50-mm-diameter Cu target was used as a sputtering source, which is located about 13 cm below the ion source. Nominal purity of the target was 99.99%. The ion incident angle was 45° off from the target normal, to increase the sputtering yield. The target was positively biased (+90V) to measure the primary ion current exactly.

Substrate holders were placed at the distance of 60 mm (upper site) and 40 mm (lower site) from the target center. The upper site was almost at the opposite of the target, and the lower site located about 45° off with respect to the target normal. For the upper site, the incident angle of the depositing particles to the substrate was almost normal and for the lower site, almost 45° off with respect to the substrate normal. The substrate holder could be turned behind to prevent the sputtered particles from sticking to the substrate during pre-sputtering. The entire system was pumped by a turbo molecular pump with the pumping speed of 0.5 m^3s^{-1} through an angle valve. The chamber was evacuated to lower than 10^{-5} Pa.

6.3 Performance of deposition

6.3.1 Deposition conditions

Depositions were performed under the condition denoted in Table 6.2. The residual gas pressure was typically 6×10^{-6} Pa, and increased to 1×10^{-5} Pa during deposition, due to heating up of the ion source. The energy and the current of the primary beam were varied, in order to investigate the effect of the deposition rate and also the effect of the reflected fast ions on the resulting film properties. Five to seven depositions were performed for each ion energy, with the ion currents between $100 - 200$ μA. Prior to the deposition, Si substrates were degreased ultrasonically in acetone and in trichrolethylene, followed by the elimination of the oxide layer with a hydrofluoric acid etch. Pre-sputtering of the target before deposition was performed about 10 min to eliminate the tarnished layer of the target surface.

6.3.2 Deposition performance

Figure 6.2(a) indicates the primary ion current at the target as a function of the primary ion energy. The ion current of more than 300 μA was obtained at maximum. The ion beam was stable at the target current up to 200 μA. Figure 6.2(b) indicates the deposition rates as a function of the primary ion current with the primary ion acceleration of 12 kV.

The deposition rate was defined by the weight thickness of the film measured by RBS. The RBS measurements were performed by the "Experimental System for Ion Beam Analysis",

Table 6.2: Deposition condition of copper thin films by metal ion beam self-sputter deposition.

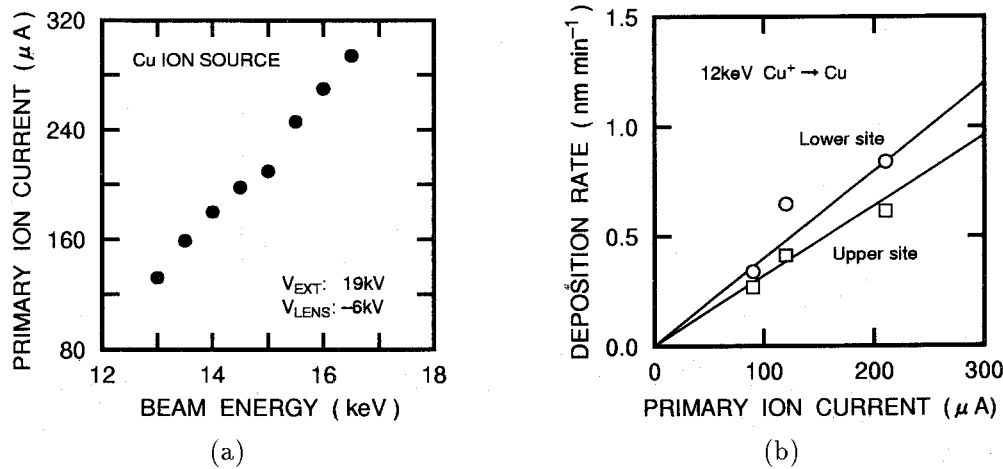| Terms	Conditions
Background pressure	6.5×10^{-6}Pa
Gas pressure during deposition	1.2×10^{-5}Pa
Primary ion species	Cu^+ (no mass separation)
Acceleration voltage of primary ion beam	12, 14, 15, 17 kV
Primary ion current	$\sim 300 \ \mu A$
Target material	Cu (99.99%)
Substrates	Si(100) and Si(111)
Substrate temperature	RT ($< 80°C$)

Figure 6.2: Deposition performance of metal ion beam self-sputter deposition system. (a) Primary ion current as a function of beam energy, and (b) deposition rate as a function of primary ion current.

Quantum Science and Engineering Center, Kyoto University. The weight thickness was calculated using the energy loss data [34]. The calculation was made by fitting the RBS spectrum with a simulation soft RBS80 which had been developed by the author. The thickness had a distribution of about $\pm 20\%$ within the substrate of 17 mm $\times$ 10 mm. The deposition rate was approximately proportional to the primary ion current, and 0.4 nm $\min^{-1}$ per 100 μA for the lower site and 0.32 nm $\min^{-1}$ per 100 μA for the upper site. Similar relation was observed for higher primary ion energies, but the deposition rate fluctuated from run to run, probably due to the difference of the focusing conditions. The film properties were arranged in accordance with the deposition rate, not with the primary ion current. The maximum deposition rate of 2.5 nm $\min^{-1}$ was obtained at the lower site. The deposited film thickness ranged between 40 nm and 120 nm.

In the present energy regime, angular distribution of the sputtered particles will become over cosine with its axis approximately normal to the target surface [35]. Kay *et al.* observed an angular distribution which is proportional to $\cos^4 \theta$ [23]. We can roughly estimate the deposition rate, assuming the sputtering yield is from 10 to 20, and the primary ion beam is focused to a spot. The deposition rate at the lower site can be calculated to be about 1$\sim$2 nm $\min^{-1}$ per 100μA. The practical deposition rate was between one fifth and a half of the calculated value. One of the reasons for this discrepancy is that the primary beam was not focused to a spot, but had a diameter of more than 20mm. The power efficiency is calculated to be 1 nm $\min^{-1}$ W^{-1} for 1$\sim$2 nm $\min^{-1}$ per 100 μA at 17 keV without consideration of heating power of the LMIS.
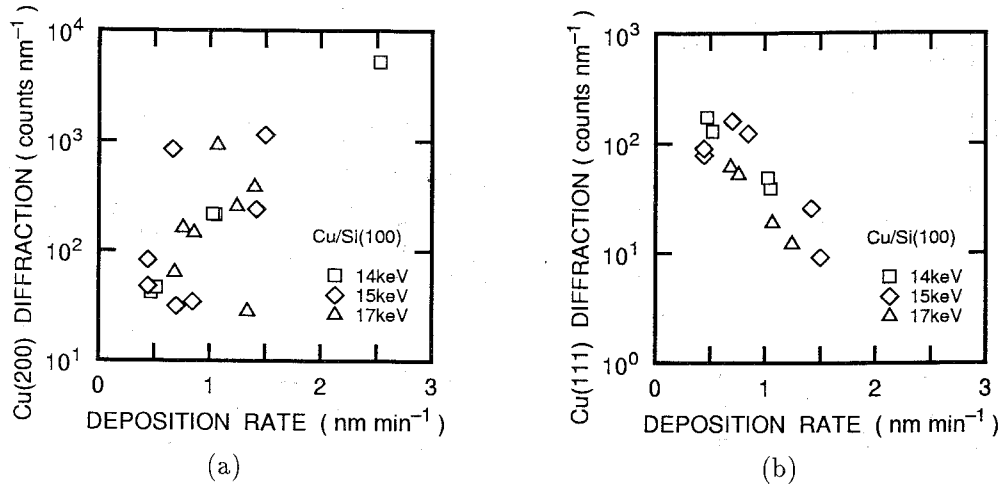
Figure 6.3: Crystallinity of the deposited films. (a) Cu(200) diffraction intensity as a function of deposition rate, and (b) Cu(111) diffraction intensity as a function of deposition rate. The intensities are integrated value and normalized by the film thickness.

6.4 Properties of deposited films

6.4.1 Crystallinity

The characteristics of the deposited thin films are shown in the present section. The data argued in this section are those of the films deposited at the lower site. Crystallinity was evaluated by x-ray diffraction (XRD). Figures 6.3(a) and (b) show the Cu(200) and Cu(111) diffraction intensities for the films deposited on Si(100) substrate as a function of the deposition rate, respectively. For the films on Si(100) substrates, Cu(200) diffraction peak rapidly increased with an increase in the deposition rate, while Cu(111) diffraction peak decreased. The grain size and internal stress of the film was calculated from the x-ray diffraction peak shift with the Scherrer equation [36]. The size of (100) oriented grains also increased from 13 to 25 nm with an increase in the deposition rate. For the films on Si(111) substrates, Cu(200) diffraction peak was not observed and Cu(111) diffraction peak also decreased with an increase in the deposition rate, in a similar way as shown in Fig.6.3(b). No significant dependence on the primary ion energy could be observed, which would be one of the evidences that the crystallinity was not determined by the reflected ions. The strong Cu(200) diffraction would be attributed to the fact that Cu film can be epitaxially grown on Si(100) substrate for azimuthal orientation of Cu(011)||Si(100) [37]. The internal stress observed was found to be tensile for all films. Figure 6.4 shows the
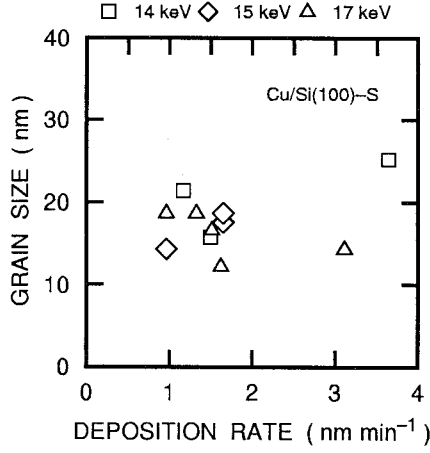
Figure 6.4: Grain size as a function of deposition rate.
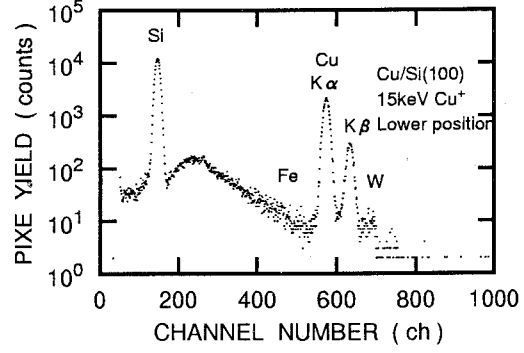
Figure 6.5: PIXE spectrum of deposited sample.

relation between the grain size and the deposition rate. No significant change in vertical grain size was observed.

Thompson [38] derived the energy distribution of the sputtered particle toward the ejection angle ψ_{eje} as

$$
\begin{cases}
dN(E) = N_0 \cos \psi_{eje} \dfrac{1 - \sqrt{(E_b + E)/\Lambda E_1}}{E^2 (1 + E_b/E)^3} dE, \\[3mm]
\Lambda = \dfrac{4 m_1 m_2}{(m_1 + m_2)^2},
\end{cases}
\tag{6.1}
$$

where E_b is the surface binding energy, Λ is the energy conversion factor, and E_1 is the primary ion energy. N_0 is a constant which is uniquely defined for a given ion-target combination. In this equation, $\sqrt{(E_b + E)/\Lambda E_1}$ is much smaller than unity, and the equation can be reduced to:

$$
dN(E) = N_0 \cos \psi_{eje} \frac{E}{(E + E_b)^3} dE,
\tag{6.2}
$$

which is independent of the incident ion energy E_1. This theory is based on a rough estimation of sputtering phenomenon, but is a good modeling [5]. In the present deposition process, only the effect of kinetic energy of the sputtered Cu atoms is reflected, and no dependence of the primary beam energy could be observed.

6.4.2 Impurity incorporation

Impurity incorporation in the films was estimated by RBS and PIXE measurements. The "Experimental System for Ion Beam Analysis" was used to perform RBS [39] and PIXE
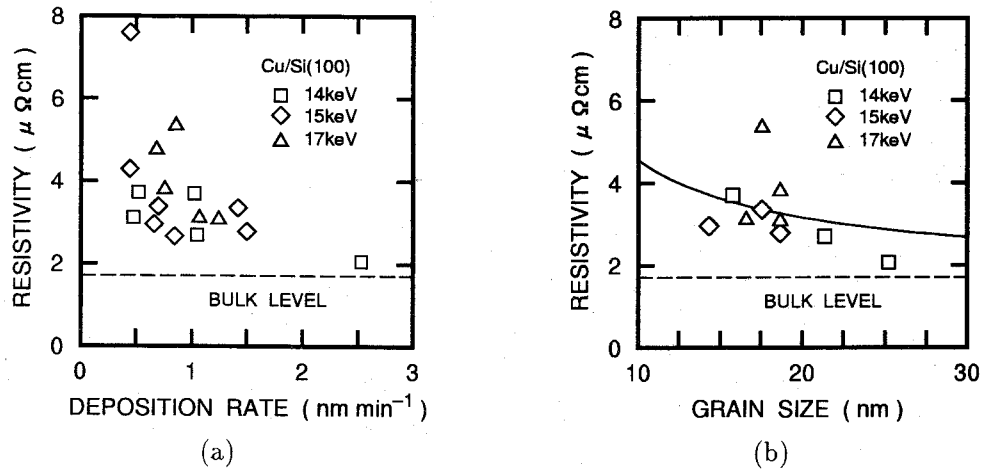
Figure 6.6: Electrical resistivity of the deposited films (a) as a function of deposition rate, and (b) as a function of grain size.

[40, 41] measurements. Figure 6.5 shows a typical example of the PIXE spectrum for the deposited film. Tungsten (W) may be detected by RBS, if reaction between the ion emission tip and copper occurs, but it was not detected. This means no serious reaction of W and Cu occurred at the ionization point. Some of the samples deposited on Si(100) contained oxygen. These oxygen atoms would be incorporated from the residual gas, since the deposition rate was fairly low. Slight amount of iron, nickel were narrowly detected from PIXE signal for some of the films. The detection limit of the PIXE may be dependent on the inner shell excitation cross section, but it is estimated to be approximately 10^{12} atoms cm^{-3}. This can be known from the fact that one monolayer heavy metal on the 200 nm-thick metal substrate can be detected by PIXE [42]. These impurity would come from the electrodes which is made of stainless steel, which will be eliminated by coating the system with the same material as the target.

6.4.3 Electrical resistivity

Electrical resistivity was measured by a four point probe at room temperature. The electrical resistivity was almost inversely proportional to the deposition rate, as shown in Fig. 6.6(a), and no significant dependence on the primary ion energy could be observed. The lowest resistivity obtained in the present study was as low as 2.1 $\mu\Omega$ cm. This value is very close to the bulk resistivity of 1.70 $\mu\Omega$ cm [43]. The electrical resistivity decreased with an increase in the grain size obtained by an XRD analysis, as shown in Fig. 6.6(b). In case of thin films, the excess electrical resistivity is dominated by the grain boundary

scattering. Mayadas and Shatzkes [44] have derived the effect of grain boundary scattering in the increase of the electrical resistivity.

$$
\begin{cases}
\rho_0/\rho_g &= 3\left\{\dfrac{1}{3} - \dfrac{1}{2}\alpha + \alpha^2 - \alpha^3\ln(1+1/\alpha)\right\}, \\[2ex]
\alpha &= \dfrac{\ell_0}{d_g}\dfrac{\Gamma}{1-\Gamma},
\end{cases}
\tag{6.3}
$$

where ρ_0 and ρ_g are the resistivity of bulk and the resistivity with a small grain size, respectively, ℓ_0 is the mean free path of electrons within a Cu lattice, d_g is the grain size, Γ is the reflective coefficient. In the case of Cu, Γ was determined to be 0.24 [44]. Mean free path ℓ_0 assumed in Ref. 44 is 38.8 nm, because they estimated $\rho_0\ell_0 = 6.6 \times 10^{-12}$ Ω cm^2. The value of ℓ_0 can be obtained with the value of bulk resistivity $\rho_0 = 1.70$ $\mu\Omega$ cm [43]. In Fig. 6.6(b), the theoretical curve is also illustrated by a solid line. The relation approximately agrees with the theoretical curve, but some samples showed lower electrical resistivity. It may be related to the fact that the grain size measured by XRD represents the vertical grain size. If the grain is not isotropic, a lower resistivity means a larger lateral grain size as compared with a vertical grain size [26]. Under the significant ion bombardment (IBAD), it was suggested that the film structure became columnar, and the present case does not agree with the IBAD results. From this point also, it was suggested that the film formation is not affected by the high energy particle bombardment.

6.4.4   Endurance against oxidation

The deposited films have been left in atmospheric environment for more than 7 years, but some of the films deposited on Si(111) substrate showed almost similar appearance as deposited. It is reported that the oxidation of metals is largely suppressed if the film contains very little amount of impurity atoms such as sulfur. Actually, the Fe films deposited onto Si substrate by mass-separated ion beam deposition showed high resistance against oxidation [12]. Detailed investigation on this issue is necessary.

6.5   Conclusion

The author demonstrated the novel ion beam processing of metal ion beam self-sputter deposition with the lens system developed in Chapter 5. The deposition rate of 0.4 nm min^{-1} per 100 μA was achieved. This value is lower than that of plasma sputter-type deposition. Considering that the input beam power was 17 kV $\times$ 0.1 mA = 1.7 W, the deposition rate per a unit input power becomes 0.2 nm min^{-1} W^{-1}. Conventional magnetron sputtering system provides the deposition rate of 40 nm min^{-1} at 100 W under the condition

of target-substrate separation of 30mm [45], This implies 0.4 nm min^{-1} W^{-1}. The present deposition rate is almost half of the above value but is approximately the same. If we have the metal ion source which provides much higher current, this processing may achieve the deposition rate as high as the conventional magnetron sputtering. Further intensification of the ion source with a single tip is difficult, and we should develop a high current ion source with multiple tips. In the next chapter, the author develops high current ion sources with multiple ion emission tips.

References in Chapter 6

[1] J. L. Vosson and W. Kern ed., *Thin Film Processes* (Academic Press, San Diego, 1978).

[2] J. A. Thornton, J. Tabok and D. W. Hoffman: Thin Solid Films **64** (1979) 111.

[3] J. A. Thornton and D. W. Hoffman: Thin Solid Films **171** (1989) 5.

[4] Y. Gotoh and Y. Taga: J. Appl. Phys. **67** (1990) 1030.

[5] Y. Taga and Y. Gotoh: Thin Solid Films **193/194** (1990) 164.

[6] J. Amano, P. Bryce and R. P. W. Lawson: J. Vac. Sci. Technol. **13** (1976) 591.

[7] K. Yagi, S. Tamura and T. Tokuyama: Jpn. J. Appl. Phys. **16** (1977) 245.

[8] T. Miyazawa, S. Misawa, S. Yoshida and S. Gonda: J. Appl. Phys. **55** (1984) 188.

[9] J. Ishikawa, Y. Takeiri, K. Ogawa and T. Takagi: J. Appl. Phys. **61** (1987) 2509.

[10] S. Shimizu, O. Tsukakoshi, S. Komiya and Y. Makita: Jpn. J. Appl. Phys. **24** (1985) 1130.

[11] T. E. Haynes, R. A. Zuhr, S. J. Pennycook and B. R. Appleton: Appl. Phys. Lett. **54** (1989) 1439.

[12] K. Miyake and T. Ohashi: Jpn. J. Appl. Phys. **32** (1993) L120.

[13] R. A. Roy, J. J. Cuomo and D. S. Yee: J. Vac. Sci. Technol. A **6** (1988) 1621.

[14] J. M. E. Harper, J. J. Cuomo, R. J. Gambino and H. R. Kaufman: in *Ion Bombardment Modification of Surfaces: Fundamentals and Applications*, ed. by O. Auciello and R. Kelly (Elsevier, Amsterdam, 1984).

[15] S. M. Rossnagel and J. J. Cuomo: Thin Solid Films **171** (1989) 143.

[16] P. J. Martin, R. P. Netterfield, W. G. Sainty, G. J. Clark, W. A. Lanford and S. H. Sie: Appl. Phys. Lett. **43** (1983) 771.

[17] H. Takaoka, J. Ishikawa and T. Takagi: Thin Solid Films **157** (1988) 143.

[18] H. Kitamura and Y. Masaki: *Proc. 3rd Symp. on Beam Engineering of Advanced Material Synthesis, BEAMS1992* (The Beam Engineering Research Society of Japan, 1992) p.375 [in Japanese].

[19] Y. Gotoh, M. Nagao, T. Ura, H. Tsuji and J. Ishikawa: Nucl. Instrum. Meth. B **148** (1999) 525.

[20] D. M. Mattox: J. Vac. Sci. Technol. **10** (1973) 47.

[21] T. Takagi: *Ionized Cluster Beam Deposition and Epitaxy* (Noyes Publications, Park Ridge, 1988).

[22] R. Srinvasan, S. P. Murarka and T.-M. Lu: J. Appl. Phys. **65** (1989) 1198.

[23] E. Kay, F. Permigiani and W. Parrish: J. Vac. Sci. Technol. A **5** (1987) 44.

[24] T. Motohiro: J. Vac. Sci. Technol. A **4** (1986) 189.

[25] V. Stambouli, O. Burat, D. Bouchier, F. Meyer, J.-P. Gilles and G. Gautherin: Thin Solid Films **193/194** (1990) 181.

[26] Y. Gotoh, H. Yoshii, T. Amioka, K. Kameyama, H. Tsuji and J. Ishikawa: Thin Solid Films **288** (1996) 300.

[27] Typical example is the super clean room in Tohoku Univerisy, Sendai, Japan.

[28] T. Asamaki, R. Mori and A. Takagi: Jpn. J. Appl. Phys. **33** (1994) 2500.

[29] W. M. Posadowski and Z. I. Radzimski: J. Vac. Sci. Technol. A **11** (1993) 2980.

[30] N. Matsunami, Y. Yamamura, Y. Itikawa, N. Itoh, Y. Kazumata, S. Miyagawa, K. Morita, R. Shimizu and H. Tawara: *Energy Dependence of the Yields of Ion-Induced Sputtering of Monatomic Solids"*, (Institute of Plasma Physics, Nagoya University, 1983).

[31] Y. Yamamura, N. Matsunami and N. Itoh: Rad. Eff. **71** (1983) 65.

[32] Jian Li, S. Hong, S. Russell, and J. W. Mayer: *Copper-based metallization*, in *Crucial Issues in Semiconductor Materials and Processing Technologies* (Kluwer Academic Publishers, 1992) p.305.

[33] S. Nagamachi, Y. Yamakage, H. Maruno, M. Ueda, S. Sugimoto, M. Asari and J. Ishikawa: Appl. Phys. Lett. **62** (1993) 2143.

[34] W.-K. Chu, J. W. Mayer and N.-A. Nicolet: *Rutherford Backscattering Spectrometry* (Academic Press, Orlando, 1978).

[35] H. Oechsner: Appl. Phys. **8** (1975) 185.

[36] B. D. Curity: *Ekkususen Kaisetsu (Elements of X-ray Diffraction)*, 2nd Edition, Translated by G. Matsumura (Agune, Tokyo, 1980) [in Japanese].

[37] Y. Gotoh, H. Yoshii, H. Tsuji and J. Ishikawa: *Proc. of the 14th Symp. on Ion Sources and Ion-Assisted Technologies, ISIAT'91* (Ion Engineering Society of Japan, Tokyo, 1991) p.317.

[38] M. W. Thompson: Phil. Mag. **18** (1968) 377.

[39] W.-K. Chu, J. W. Mayer, M.-A. Nicolet, *Backscattering Spectrometry* (Academic Press, Orlando, 1978).

[40] S. A. E. Johanson and J. L. Campbell: *PIXE A Novel Technique to Elemental Analysis* (John Wiley and Sons, Chichester, 1988).

[41] J. W. Mayer and E. Rimini: *Ion Beam Handbook for Material Analysis* (Academic Press, New York, 1977).

[42] Y. Gotoh and N. Kiwa: unpublished results, 2001.

[43] C. Kittel: *Kotai Butsurigaku Nyumon (Introduction to Solid State Physics)*, 5th Edition Translated by Y. Uno, N. Tsuya, A. Morita and J. Yamashita (Maruzen, Tokyo, 1978) [in Japanese].

[44] A. F. Mayadas and M. Shatzkes: Phys. Rev. B **1** (1970) 1382.

[45] Y. Gotoh: unpublished results, 2001.

Part III

Intensification of ion source
by multipoint emission

Chapter 7
Development of high current ion sources

In the previous chapters, the author demonstrated the feasibility of the metal ion beam extracted from the LMIS. For use of LMIS's to various kinds of applications, especially surface modification, the ion current should be as large as several tens milliamperes. In order to achieve this, the ion emission points should be multiplied because the ion emission from a single point has a maximum of approximately 0.5 mA. In order to construct a metal ion source which can be operated at about 1000° C, technologies related to heating-up a large ion source are necessary. Also, the uniform field formation at each ion emission points is required. The present chapter deals with the development of linear array ion sources and formation of a metal sheet beam by a rectangular lens system.

7.1   Requirement of high current ion source

High current LMIS's are expected to play an important role in the materials science and industry, because of their many advantages such as pure metal ion beam formation with simple structure, low power consumption, and especially being operative in high vacuum as the author emphasized in Chapter 1. Now, the subject left is the increase of the ion current. As shown in Chapter 2, the IELMIS can provide an ion current of almost half milliamps from a single point, but this ion current is not sufficient as yet. For further intensification, multiplying the number of the ion emission tip is necessary. This is also because even at relatively low currents, for example, I_s of several hundreds of microamperes, multiplication is important from the viewpoint of the efficiency. Figure 7.1 shows the efficiency of the liquid Au ion source [1]. The efficiency is defined as the ratio of the ions to atoms which were lost during operation. The loss of atoms was calculated from the difference of the weights before and after operation. From the figure, it is seen that the efficiency is almost inversely proportional to I_s. Taking the fact that the available current is not proportional to I_s, but is proportional to $I_s^{0.7}$, the net efficiency is further lower. This would be attributed to the droplet emission at high emission currents [2], or evaporation due to raise in T_s.

Ion emission from the array ion sources has already been reported by Clampitt [3] and Bartoli *et al.* [4]. In these reports, however, the source material was cesium which requires no intentional heating of the ion source. However, the present study is directed towards the
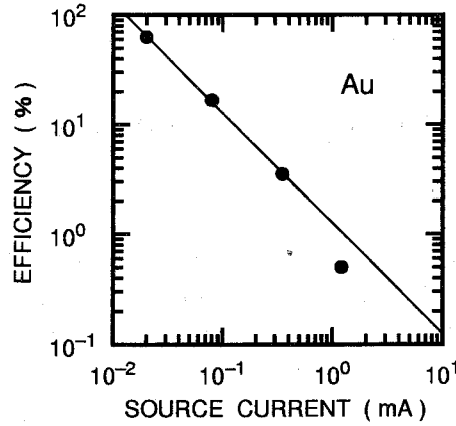
Figure 7.1: Efficiency of the emission current and loss of the source materials of Au ion source[1].

application to materials science, and most of the materials in this field require more than several hundreds degrees centigrade to be melted. In order to achieve the high temperature, there are some problems such as low impedance of TAR's. A new structure which realizes the simultaneous operation of multiple TAR's under the same temperature and the electric field should be introduced to obtain a larger ion current.

7.2 Technological difficulties in developing high temperature linear array source

7.2.1 Fabrication of wedge-shaped tip-and-reservoir for multipoint emission

As described above, multiplication of ion emission points is one of the most appropriate way to increase the ion current. Here the author develops a linear array source. It is not of use to arrange some cylindrical TAR's like the conventional ion thrusters because of difficulties in holding system. The ion source used here in the present dissertation is IELMIS of which tip is made of porous W and machinable. If the TAR is elongated to one direction, it is expected to have multiple cusps for ion emission, of which schematic drawing is already shown in Fig. 2.1(b). It may be possible to produce a wide TAR, for example, 50 mm in width. However, a wide TAR involves the following shortcomings.

1. Low mechanical strength: since the heating current flows to the reservoir, the reser-

Tip–and–reservoir

Heating current

Separated TAR

(a)

Tip–and–reservoir

Heating current

Separated TAR

(b)
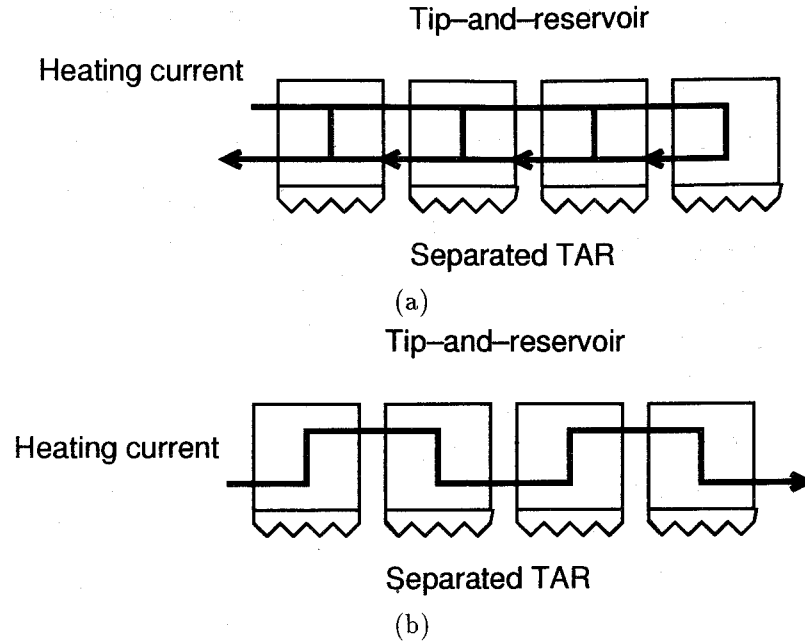
Figure 7.2: Connection of TAR's: (a) parallel load system and (b) series load system.

voir is subjected to the strong stress from current feeding electrode due to thermal expansion. If the width of TAR is elongated, the wall of the reservoir should be thicker.

2. Difficulties in sintering process: the porous region has been pre-sintered in hydrogen furnace but it does not have sufficient strength. In usual case, the TAR is operated after re-sintering process up to 2600°C. Electron bombardment is used for heating the porous region, it becomes difficult to bombard all the region of the wide TAR.

From the above point of view, TAR should be separated to some parts.

7.2.2 Simultaneous heating of multiple tip-and-reservoirs

If we have multiple TAR's which should be operated at the same time, problems associated with the simultaneous operation of these TAR's. The major problem is how to heat the TAR's arise. Figures 7.2(a) and 7.2(b) show the method for heating the multiple TAR's. Figure 7.2(a) shows a parallel load system and Fig. 7.2(b) shows a series load system. Since the electrical resistivity of each TAR is fairly low (typically 0.01Ω), as will be shown

later, connection of TAR's to make a series load is preferred. However, in multiplying the source, parallel load system is easily realized because we only multiply the conventional system.

7.2.3 Formation of uniform electric field at each tip apex

For the simultaneous operation of multiple tips, the threshold voltage for each ion emission tip should be similar. This implies that the electric field should be uniform along the emitter array. It is necessary to form the porous cusps with the same radius of the curvature. Since it is difficult to fabricate the tips at the process of pre-sintering of the porous region, porous region should be wedge-shaped. After the pre-sintering, the porous region was divided to almost 10 cusps per 10 mm width TAR. The machining of the tips was made manually through the observation with a microscope.

Also presence of the edge tips causes a significant reduction of threshold voltage for these tips. The threshold voltage V_{th} is expressed for the isolated tip with an assumption that the electrode configuration is well approximated by spherical coordinates [5],

$$V_{th} = 2 \left(\frac{\gamma}{\epsilon_0} \right)^{1/2} r_0^{3/2} \left(\frac{1}{r} - \frac{1}{d} \right) \sim 2 \left(\frac{\gamma r_0}{\epsilon_0} \right)^{1/2}. \tag{7.1}$$

V_{th}' for the tips inside the array can be derived using cylindrical coordinates [5].

$$V_{th}' = \sqrt{2} \left(\frac{\gamma r_0}{\epsilon_0} \right)^{1/2} \ln(d/r_0). \tag{7.2}$$

To equate these two thresholds, a curved extractor (different d values at each position) was proposed [6], but this method is not suitable if we use a wider TAR. Thus, in the present dissertation, the author adopted such an extraction electrodes that has same gap with each tip throughout the array. Instead of the curved extractor, the author put auxiliary electrodes at the both ends of the TAR array to form a uniform electric field.

7.3 Preliminary versions of high current source

7.3.1 Versions of the test sources

It is necessary to examine the issues described in the previous section and here the author developed some versions of ion sources for preliminary experiments. Table 7.1 denotes all the ion sources developed in the present dissertation. The version I is equivalent to the cylindrical reservoir type TAR source. The versions IIa, IIb and IIc are based on the conventional TAR holder, but the width of the reservoir was enlarged. The versions IIa and IIb have widths of 5 mm and 10 mm, respectively and the version IIc is the source

Table 7.1: Versions of high current ion sources.

Source version	Number of TAR's	Emission points	TAR width	TAR holder	Exam. issue	Source material
I	1	1–3	2 mm$^{\#}$	Conv.†	Possibility of MPE*	Ga
IIa	1	1–5	5 mm	Conv.†	MPE*	Au, Ge
IIb	1	1–10	10 mm	Conv.†	MPE*	Ge
IIc	2	28	10 mm	Conv.†	Two-column, 13+15	Ge
III	1–2	2–20	10 mm	Modified	Heating up of TAR's	Ge
IV	2, 4, 6	2–60	10 mm	New	Heating up of TAR's	Au, In

$^{\#}$: cylindrical reservoir

†: conventional TAR holder

*: Multi-Point Emission

for two-column source. The version III is a modified version of the conventional source to equip two TAR's, which are connected electrically in parallel. The version IV, the last version, was newly re-designed high current source with a series connection of TAR's. Up to six, but even number of TAR's are equipped in this source.

The source material used in the version I ion source was Ga, which is easy to be operated, because the purpose was to show the possibility of the multi-point emission. The version II ion sources were tested to examine the heating property. For this purpose, metals with higher T_m of approximately 1000°C should be used. In this study, Au and Ge of which T_m are 1063°C and 960°C, respectively, were selected. Since the purpose of the examination of the version III ion source was similar to that of the version II, Ge was used as a source material for the version III ion source. The version IV ion source should show both appropriate heating characteristics and the ion beam extraction from many tips. For the former issue, Au was used because of its high T_m. For the latter issue, In was used, because In is relatively easy to be operated, but requires the temperature as high as 700°C
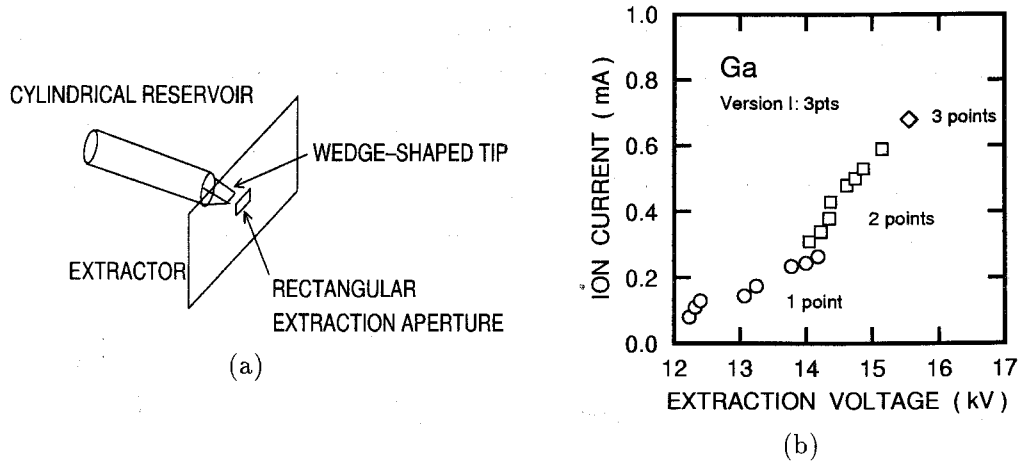
Figure 7.3: The version I ion source: (a) Schematic drawing, and (b) $I_i - V_{ext}$ characteristics.

for wetting the base W, in spite of T_m. In this section, the author briefly explains the sources up to version III, and details of version IV will be given later.

7.3.2 Wedge-shaped tip with cylindrical reservoir

The version I ion source is a wedge-shaped tip with a cylindrical reservoir. This source was fabricated to confirm multipoint emission from a porous tip. The ion emission tip was machined to be wedge-shaped. The extractor has a rectangular hole. Figures 7.3(a) and 7.3(b) show the schematic drawing of the version I source and its current-voltage $(I_i - V_{ext})$ characteristics with Ga as a source material, respectively. First, the ion emission occurred at an end, and increasing the voltage, the ion emission from the opposite side began at 14.2 kV. Finally at 15.6 kV, ion emission from the center was observed. The obtained I_i reached approximately 0.8 mA. The result showed that multipoint emission is possible but also there were some problems. A significant backstreaming of the electrons produced at the extractor raised the tip temperature.

7.3.3 Wedge-shaped tip and reservoir

The ion sources of versions IIa and IIb own a wedge-shaped TAR with the width of 5 mm and 10 mm, respectively. The height of the reservoir is 20 mm and that of the porous tip is 3 mm. Although arrangement of many cusps in a restricted area would result in a higher current, there is a upper limit. It is because the presence of the neighboring cusp standing
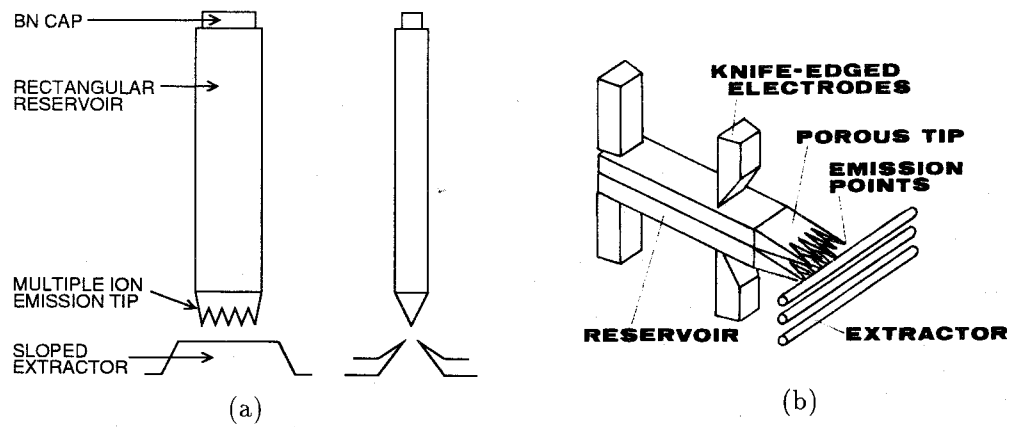
Figure 7.4: Schematic figures of the ion sources: (a) version IIa or IIb and (b) version IIc.

aside, lowers the electric field at the cusp apex. The author has numerically calculated the apex field for some geometries, and found that it is necessary to maintain the unity aspect ratio of cusp height and separation [7]. Taking it into consideration that the machining is made by hands through microscope, resolution less than 1 mm is not obtained in general. Thus 1 mm separation is most appropriate to create the ion emission cusps with good reproducibility. A schematic figures of the version IIa or version IIb ion sources are drawn in Fig. 7.4(a). The holding system of the TAR was the conventional one. The version IIc source is equipped with a similar TAR but two TAR's are arranged in parallel to be two-column array. The extraction system becomes complicated for these arrays, and one of the possible extractor is a rod made of refractory metal, as shown in Fig. 7.4(b). The author examined the two-column array source with W rods as an extractor.

The author examined $I_i - V_{ext}$ characteristics of the ion sources with multiple emission points with Au or Ge as a source material. Details of $I_i - V_{ext}$ characteristics are shown elsewhere [8] and here the maximum currents are argued. Table 7.2 summarizes the results obtained with the version II ion sources together with the version I ion sources. Here the effective point number is defined as the ratio of the maximum ion current with multipoint source to that with a single-point ion source. The effective point number agrees well with the number of the cusps. The results indicate that the ion current of multipoint emission is proportional to the number of cusps. From the present results, multipoint emission proved to be a potential method for developing a high-current ion sources.

The current was lower for type IIc ion source than that expected from the number of the tip, but this is attributed to the fact that arranging the tips in two-column significantly

Table 7.2: Summary of version II ion sources. Effective point number is calculated by dividing the total current by the total current of single point source for each material. Average current per tip is the value that was obtained by dividing the total current by the number of the manufactured tips.

Source material	Au			Ge				
Version	I	IIa	IIa	I	IIa	IIa	IIb	IIc
Number of cusps	1	3	5	1	3	5	8	28 (13+15)
Maximum current (mA)	0.30	0.85	1.3	0.50	1.3	1.8	4.2	5.2
Effective point number	1	2.8	4.2	1	2.6	3.6	8.4	10.4
Average current per point (mA)	0.30	0.28	0.26	0.50	0.43	0.36	0.53	0.18

lower the electric field by shielding effect. Furthermore, the extractor rods were heated up to about more than 700°C, due to the ion bombardment. The temperature raise was enhanced because the rod has a small cross section, accumulated heat could not disperse away. It was not possible to apply higher V_{ext}. One-column array is generally adequate for applications, because the work that should be processed is moving toward perpendicular direction to the array [9]. Also the one-column array is preferred when mass separation is necessary to maintain mass resolution.

7.3.4   Linear array source with parallel heating

The version III source equips multiple TAR's that are connected electrically in parallel. The configuration is shown in Fig. 7.5. Figure 7.6 shows the typical current-voltage characteristics of the ion source with Ge as a source material. The ion current of approximately 4.6 mA was obtained at maximum. The average current was 0.27 mA which is similar to those of the single TAR sources as listed in Table 7.2. The parallel operation was confirmed to be effective to increase the emission current. The parallel heating will cause a serious problem in heating the TAR as shown in Fig. 7.7. Since the heating current is inversely proportional to the width of the TAR, the heater current of 300 A is expected for the 40
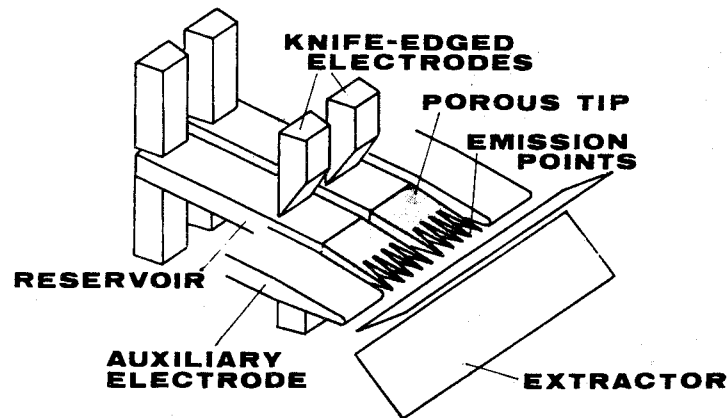
Figure 7.5: Schematic drawing of the version III ion source.

mm-wide TAR. If we use Au instead of Ge, the heater current would become higher due to lower electrical conductivity. From this result, it can be found necessary to connect TAR's electrically in series.

7.4 Configuration of intense liquid-metal ion source

7.4.1 General design

Since it was shown that the simultaneous operation of multiple TAR's is possible, the author designed a high current LMIS with a series heating system. Figure 7.8 shows a schematic drawing of the developed ion source that can be equipped with six TAR's at maximum, as well as two auxiliary electrodes that realize a uniform electric field among the apices of the ion emission cusps. One TAR possesses ten ion emission cusps. Each TAR is fixed with knife-edged electrodes made of Ta at the lower end of the reservoir and with flat electrodes made of Mo at the upper end of the reservoir. The use of the flat electrode at the upper end is to fix the TAR firmly to the Cu-block, and the use of the knife-edged electrode at the lower end is not to transfer the heat from TAR to the Cu block. As is shown later, the use of Ta electrodes exhibited a superior heating property as compared with the use of Mo electrodes which had been used in the conventional IELMIS.
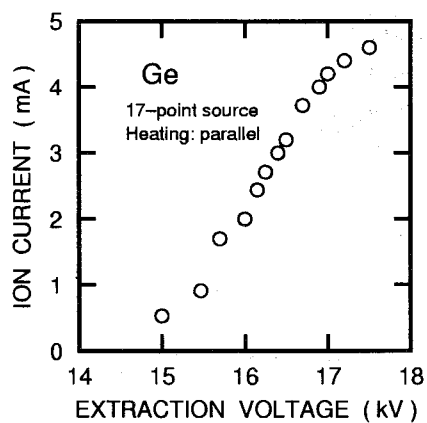
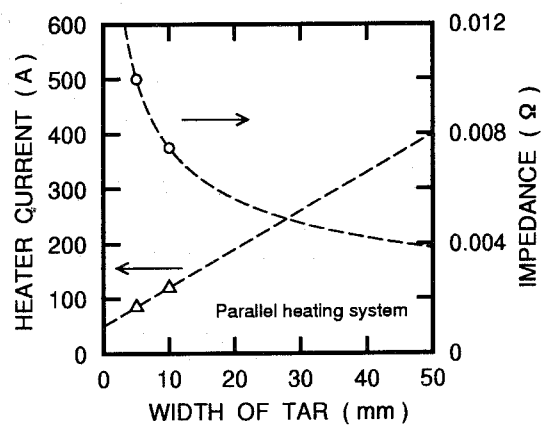Figure 7.6: $I_i - V_{ext}$ characteristics of 17-point ion source with Ge as a source material.

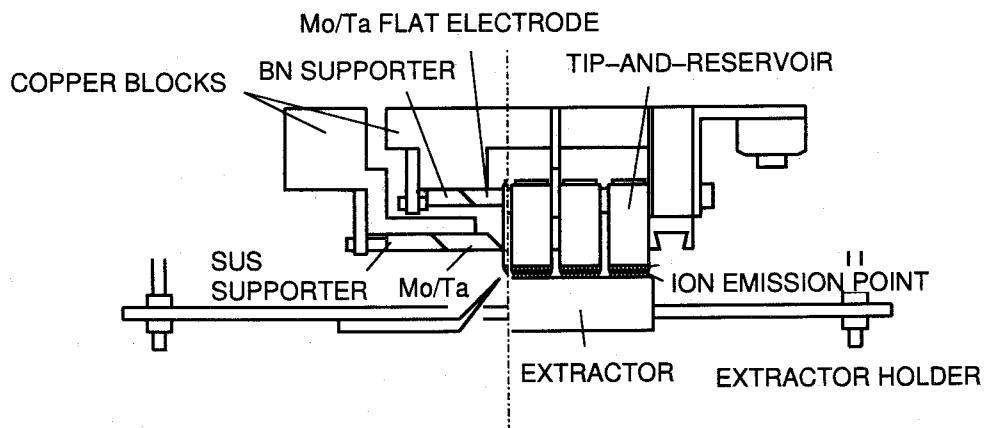Figure 7.7: Heating characteristics of ion source with parallel heating.

Figure 7.8: Configuration of the ion source.

7.4.2 Heating system

The heating unit was designed to connect the TAR's electrically in series. The knife-edged electrode (lower electrode) of the first TAR and that of the second TAR are fixed at a common Cu block, and the flat electrode (upper electrode) of the second TAR and that of the third TAR are fixed at a common Cu block. The entire unit is fixed to the base flange through the insulators. Since the heating current passes through the upper electrode of the first TAR, the first TAR itself, lower knife-edged electrode of the first TAR and then the lower knife-edged electrode of the second TAR, and so on. The present method can suppress the increase of the heating current due to the multiplication of the TAR's.

In order to avoid the excess thermal expansion of the TAR's which often breaks the reservoir, the opposite end of the Mo or Ta electrodes were cut obliquely. This structure disperses the force due to thermal expansion of the TAR toward the horizontal and the vertical directions, which results in the tight connection between the Cu block and the electrodes. The temperature of the electrodes that hold the TAR would become lower.

7.4.3 Extraction system

In order to reduce the secondary electron current, which is an extra load for the ion-extraction power supply, the extraction electrode used in the present study was a sloped-type which is described elsewhere [8]. This sloped extractor has smaller cross section, when viewing from the ion emission point. Furthermore, generation of direct electron backstreaming to the tip increase the tip temperature so high that the control of the liquid flow to the ionization point becomes difficult. In the present structure, the source can be equipped with even number of TAR's; two, four, or six TAR's can be operated simultaneously.

7.4.4 Cooling system

Water-cooling is possible but forced air-cooling showed sufficient effect for 4-TAR operation. A fan was settled outside the chamber and cooled the feed through. No coolant such as fluorocarbon is required. Elimination of liquid coolant is one of the solutions for the pure processing.

7.5 Operational performances

7.5.1 Heating characteristics

The heating characteristics were measured with a pyrometer through a view port. Figure 7.9(a) and 7.9(b) show the typical examples of the relation between the total input power

Au ION SOURCE
2-TAR SERIES
Mo ELECTRODES

Au ION SOURCE
2-TAR SERIES
Ta ELECTRODES
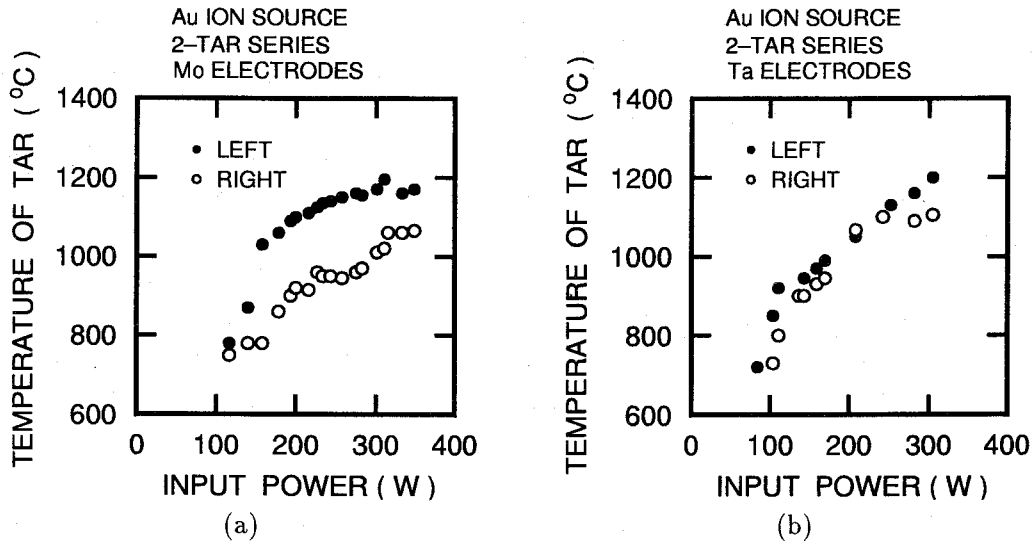
Figure 7.9: Heating characteristics of the source.

and the temperature of the TAR's. Au was selected as the source material to confirm the raise up to 1100°C. Figure 7.9(a) is with Mo knife-edged electrodes and figure 7.9(b) is with Ta knife-edged electrodes. Although the temperature difference between the left and the right TAR's with Mo electrodes is more than 100 °C, that with Ta electrodes is less than 100 °C. These figures clearly show the superior property of the Ta electrodes. The input power at 1000 °C was almost 200 W.

The reason why the Ta electrode exhibited a superior property is presently unknown. However, as denoted in Table 7.3 [10], Ta has lower κ together with lower electrical conduc-

Table 7.3: Thermal and electrical properties of Mo and Ta.

Material	ρ ($\mu\Omega$cm at 900 K)	Thermal expansion coefficient (10^{-6}K^{-1})	κ (W m^{-1} K^{-1})
Mo	20	5.1	138
Ta	40	6.5	54

Figure 7.10: Current-voltage characteristics of the 19-emission point ion source with In as a source material.

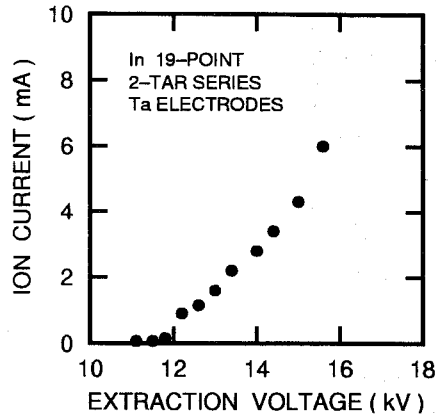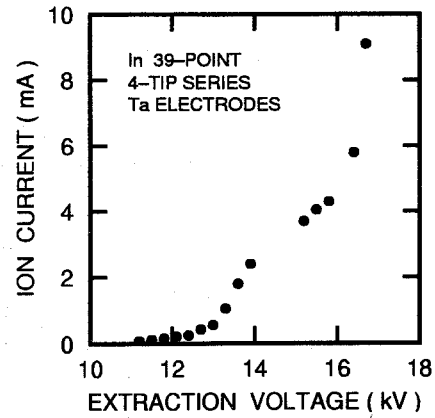Figure 7.11: Current-voltage characteristics of the 39-emission point ion source with In as a source material.

tivity. These may keep the temperature high even when the heating of the holding TAR decreased.

7.5.2 Current-voltage characteristics

$I_i - V_{ext}$ characteristics were measured using a Faraday cup located at 5 cm distant from the ion emission points. The ion current gathered within the area of 60 mm × 130 mm was measured with the suppressor voltage of −3 kV, which was high enough to suppress the secondary electrons. In was used as a source material.

Figure 7.10 shows $I_i - V_{ext}$ characteristics of the developed ion source. In this case, two TAR's were used. The maximum I_i of 6 mA was obtained from the 19 emission points. The average ion current from one emission point was almost 0.3 mA. Figure 7.11 shows $I_i - V_{ext}$ characteristics of the ion source with four TAR's. I_i of 9.1 mA at maximum was obtained. Abrupt change from 6 mA to 9.1 mA implies that at this V_{ext}, ion emission began to occur from all emission cusps. The ion emission at the 9.1 mA was stable and only the reason why the source could not supply further ion current is the limit of the capacity of the extraction power supply. The ion emission from at least 39 points was confirmed by observing plasma balls at the apex of the 39 cusps. I_i per an emission point was 0.23 mA and slightly lower than the previous values.

Since it has become clear that we can obtain the ion emission from almost all ion emission cusps, and the maximum I_i obtained in the two TAR's source was proportional to the number of ion emission points. We can estimate the maximum I_i that should be obtained in the four-TAR ion source is about 12 mA. This current is comparable value with the result obtained with Cs as a source material [4, 11], and also with the Freeman-type ion
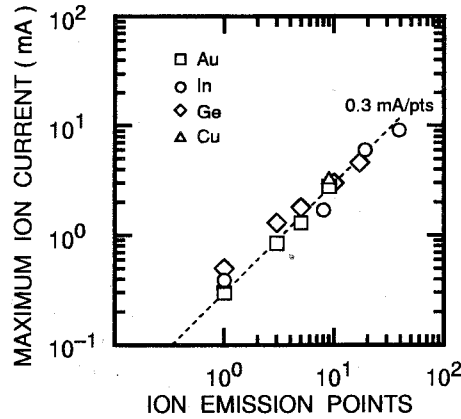
Figure 7.12: Relation between the number of emission points and the obtained maximum ion current.

source [12]. The developed ion source demonstrated that even the metals with a high T_m can be used.

Figure 7.12 indicates the summary of the maximum I_i's obtained in a series of the studies. The dashed line indicates the line proportional to 0.3 mA per an emission point. It is clearly seen that I_i was approximately proportional to the number of the emission points.

7.5.3 Heating power consumption per ion current

The total current of approximately 10 mA was obtained with In as a source material. Power consumption per ion current is about 20 – 30 W/1 mA for heating (In). For Au, power consumption would be 40 – 60 W/1 mA. This value would be fairly low as compared with the plasma type metal ion sources.

7.6 Characterization of extracted ion beams

7.6.1 Profiles of linear array ion beam

Since the intense metal ion beam has been obtained, the left subject is to form a metal sheet beam. To design the lens system, it is necessary to obtain the beam profile. Figure 7.13 shows a schematic diagram of the ion source and beam divergence measurement system used in the present study. The cusps were arranged in a line and distance between the cusps was about 1 mm. Slit-type electrodes, such as the sloped type as shown in Fig.7.13 and the flat type were used for ion extraction. The spacing of the slit was 2.5 mm and
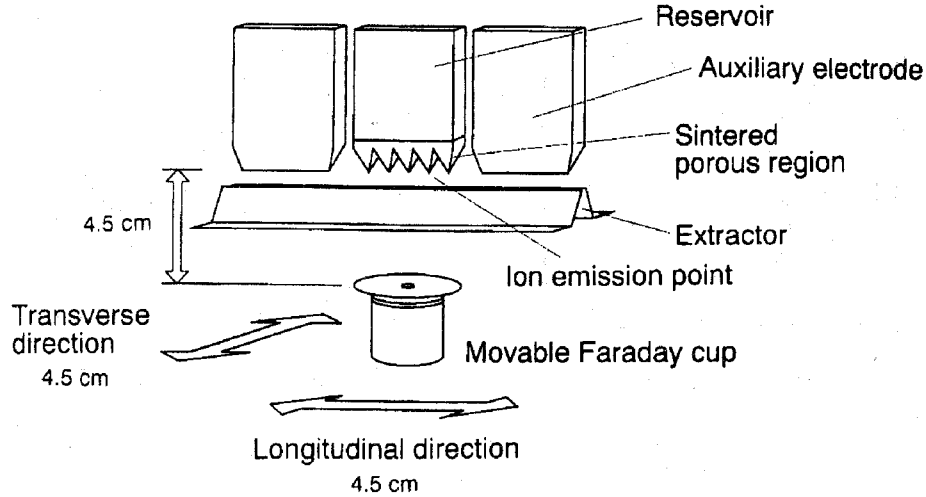
Figure 7.13: Schematic diagram of the ion source and beam profile measurement system.

ion-emission points were set to be 0.5 mm above the slit. Since the extraction system allows large transmittance of the ion beam, more than 50 % of the current can pass through the extraction electrode.

In order to obtain beam profiles, a movable Faraday cup with an aperture of 1 mm in diameter was placed at 4.5 cm below the ion emission point. The profile measurement area that was be covered by the Faraday cup was within a circle with a radius of 4.5 cm; ions emitted 45° off-axis can be detected. Here the author defines the longitudinal direction as the direction along the ion-emission array, and the transverse direction as the direction perpendicular to the array, as shown in Fig.7.13. The Au ion source was used.

Figure 7.14 shows a typical example of the ion current density distribution in the longitudinal and transverse directions of the ion beam extracted from the five emission points at V_{ext} of 16 kV and I_s of 1 mA. It is clearly seen that the beam has larger divergence in the transverse direction than that in the longitudinal direction. The ion current density was about 50 μA cm^{-2} at the center of the beam. The distribution in the transverse direction was cut at the right and left edges ($x = +3.5$cm and $x = -4.0$cm) due to presence of the extractor. The FWHM of the beam spreads for the longitudinal and transverse directions are 4.1 cm and 5.1 cm, respectively. These values correspond to the divergence angle of 24.5° and 29.5°. Figure 7.15 indicates the equi-current density lines at the beam cross-section. It is noted that although the equi-current density line is almost a circle near
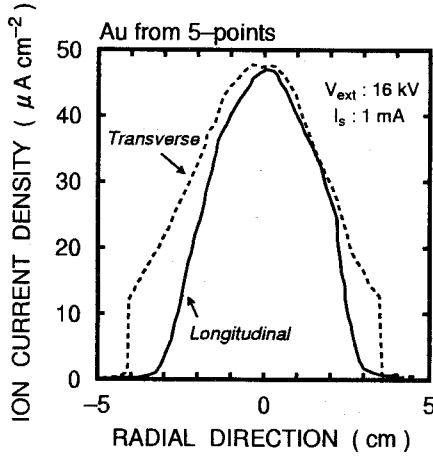
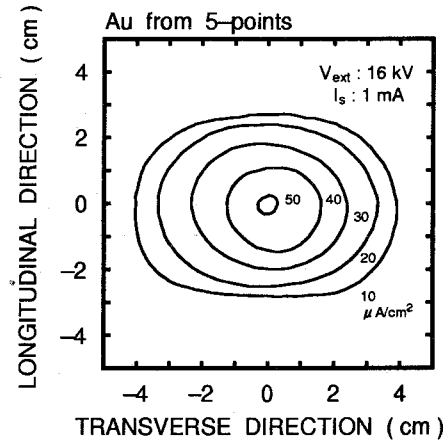Figure 7.14: Ion current density distributions of the 5-point source with Au.

Figure 7.15: Equi-current density lines of the 5-point source with Au.

the axis, it becomes elliptic at the beam envelope. The result implies that the ion beam extracted from this ion source has anisotropy in its current density. Similar distribution was obtained for the ion source with eight emission points.

7.6.2 Analysis of beam profile

As described above, the profiles of the ion beams extracted from the source with a linear array show an asymmetry. This asymmetry should be attributed to the asymmetry of the geometry of the tip-and-reservoir. In order to analyze the above current density distribution, fundamental experiments with single emission point sources were performed. Figure 7.16 shows a schematic diagram of an ion source pair; (a) the original single point source as described in Chapter 2, and (b) the single emission source with auxiliary electrodes. The auxiliary electrodes simulate the neighboring cusps of the array source. In this experiment, a sloped-type extractor was used.

Figures 7.17(a) and 7.17(b) show the typical equi-current density (equi-J)lines of the ion beam extracted from the single point source without and with the auxiliary electrodes, respectively. The results shown in Fig. 7.17(a) is in good agreement with the distribution that was previously reported in single point sources by Prewett et al. [13] and also by the author shown in Chapter 2. Since the configuration of the ion-emission tip has rotational symmetry, the beam profile has fairly good symmetry, even the extraction was performed with the sloped slit-type extractor that has an asymmetry in shape. In the case of the ion source with the auxiliary electrodes, as shown in Fig. 7.17(b), the beam profile became elliptic with the major axis along the transverse direction. The difference is clearly shown
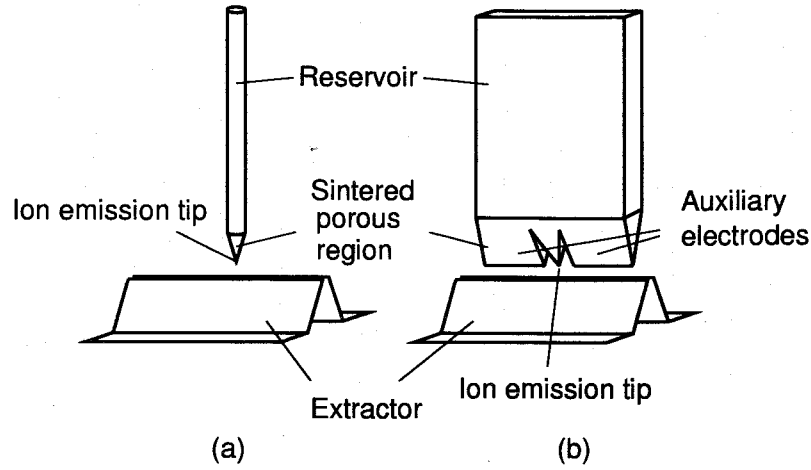
Figure 7.16: Schematic diagram of the sources with a single ion emission point: (a) without auxiliary electrodes, and (b) with an auxiliary electrodes.

in these figures. The profiles with auxiliary electrodes are narrower and have shoulders; beam full spread is confined to 30°. J at the center of the beam is increased by the presence of the auxiliary electrodes.

Since the envelope of the ion beam contains a large amount of ion current due to large area, even if the density is low, it is important to know the relation between the radial distance from the beam axis and the ion current distribution, as described in Chapter 2. Figure 7.18 shows the radial ion current distribution, in which the rotational symmetry of the profiles indicated in Figs.7.17(a) and (b) is assumed. Data under the similar I_s of about 0.3 mA were chosen. From the figure, the convergent effect in the longitudinal direction is clearly seen; most of the ion current is concentrated within 3 cm for the ion source with auxiliary electrodes but spread over 5 cm for the ion source without auxiliary electrodes. The difference is obviously attributed to the presence of the auxiliary electrodes. Similar optics might be formed in the extraction region of the array source.

Using the data obtained by the single-point ion source, a beam profile of a five-point tip array is synthesized. Figure 7.19 shows the synthesized profile. The broken line and the dotted lines indicate the synthesized distributions using the data with and without auxiliary electrodes, respectively. In the figure, the measured distribution in the longitudinal direction of the ion beam extracted from a practical five-point ion source as is already shown in Fig. 7.14, is also indicated. The synthesis were performed with the profiles obtained under I_s of about 0.2 mA, because the average current per point of the measured

(a)   (b)
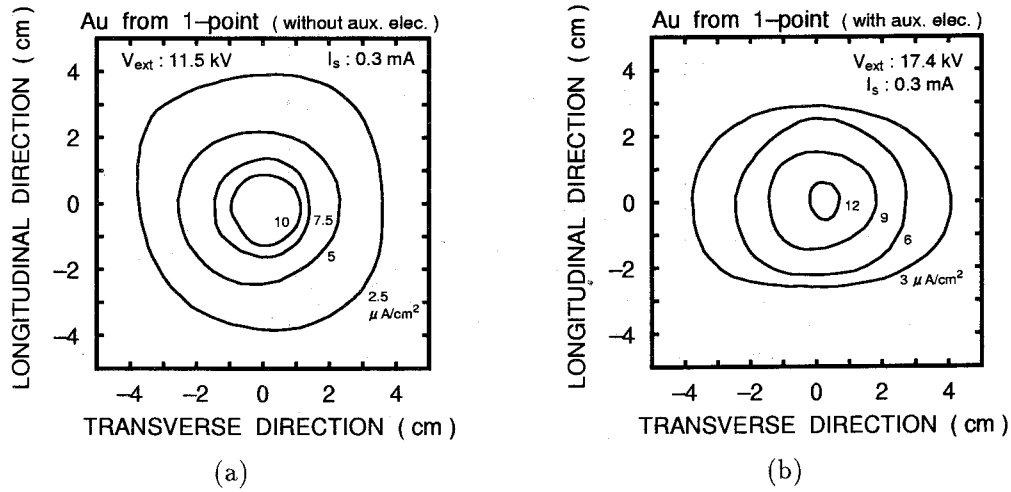
Figure 7.17: Equi-current density lines for the ion beams extracted from the single emission point sources at the source current of 0.3 mA. (a) without auxiliary electrode, and (b) with auxiliary electrode.
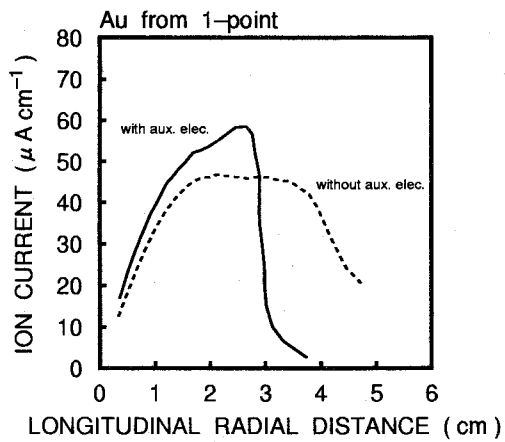
Figure 7.18: Estimated radial ion current distributions of the single emission point sources with and without auxiliary electrodes.
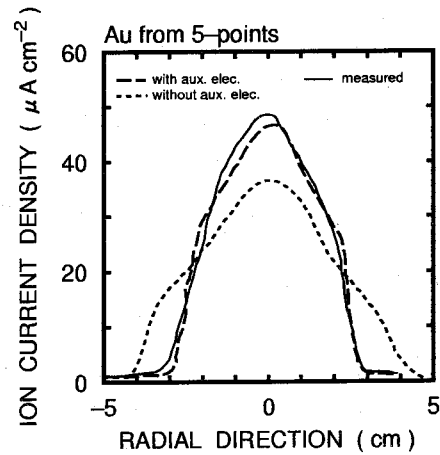
Figure 7.19: The synthesized profiles of the ion current distributions: the broken line indicates the synthesized distribution by using the data with the auxiliary electrodes, and the dotted line indicates that without auxiliary electrode. The solid line shows the measured distribution in the longitudinal direction of the ion beam extracted from the 5-point source.

five-point ion source corresponds to 0.2 mA.

The shape of the synthesized profile is almost the same as the measured one when the data with auxiliary electrodes are used, while a large discrepancy is seen for the data without auxiliary electrodes. The profile of the beams extracted from a single emission point with auxiliary electrodes represents the profile of each beamlet for the multiple emission-point ion source, so that the synthesis of the beam profile is possible.

7.6.3 Discussion

The beam extracted from the ion source with a linear array of emission-points had smaller divergence in the longitudinal direction than in the transverse direction. This result should be attributed to the presence of the neighboring ion-emission cusps; the neighboring cusps suppress the electric field along the longitudinal direction near the apices, that is, the spherical electric field. This effect works strongly when the distance between the pyramidal cusps is nearly equal to or shorter than the ion-extraction gap. The optics is similar to that in the extraction region of the high perveance electron gun with Whenelt electrodes. It is considered that the space-charge interaction between beamlets from different emission points is of less importance in the present experiment. This self-convergence extraction is suitable for an application such as an ion implanter with a mass separator.

7.7   Sheet beam formation with linear array source

7.7.1   Rectangular lens system for linear array source

As described above, the profile of the beamlets is distorted from the complete circle with the presence of the neighboring emission cusps. This self-convergent effect is suitable for the formation of a sheet beam. Whilst along the transverse direction with respect to the array, a lens system that can converge the beamlets is required. In Chapter 5, the author indicated that a physically asymmetric lens was suitable for the convergence of divergent beams [15]. In the present case, however, we should modify the lens system. The shape of the lens was changed to a rectangular shape with the longer side along the longitudinal direction. This modification was performed so that the cross section of the new lens is similar to the previous lens. The ends were terminated by a metal plate. Figure 7.20 shows the schematic diagram of the lens system used in the present study.

The effectiveness of the lens was confirmed by a two-dimensional computer simulation [14]. Since the results were quite similar to those described in Chapter 5, the author does not duplicate the results here.
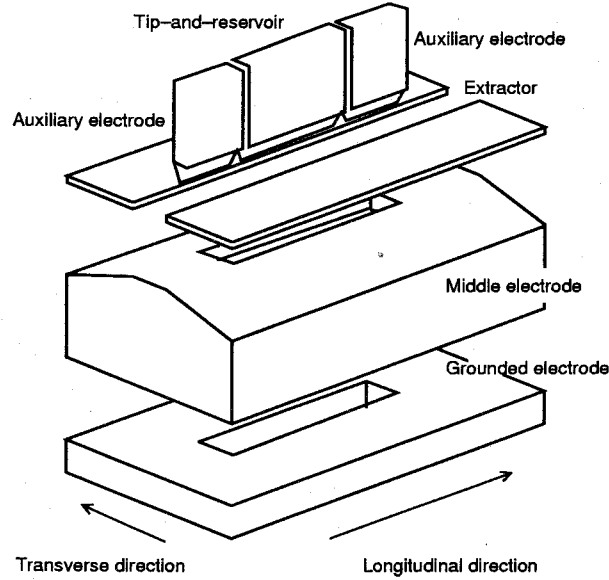
Figure 7.20: Schematic drawing of lens system designed for array source.

7.7.2   Performance of rectangular lens

Beam profiles of the converged ion beams were measured with the same system for the beam profile measurement in the previous section. Only the difference was that the profiles were measured at 120 mm below the ion source. Figure 7.21 shows the birds' eye view of the typical profile of the converged ion beam from a five-point ion source with I_s of about 1 mA.

As can be seen from the figure, the ion current distribution has a narrow width along the transverse direction, and a wide width along the longitudinal direction. Figures 7.22(a) and 7.22(b) show the current distribution along the transverse direction and that along the longitudinal direction. The beam was 2 mm in thickness and 50 mm in width. It is clearly seen that the converged ion beam is sheet-shaped. Formation of sheet beam suggests possible processes for large area processing [9].

7.8   Conclusion

In this chapter, the author has constructed a ten-mA class LMIS which can be heated up to approximately 1000°C. This implies that most of the source materials developed so far can be used. The obtained ion currents were almost proportional to the number of the
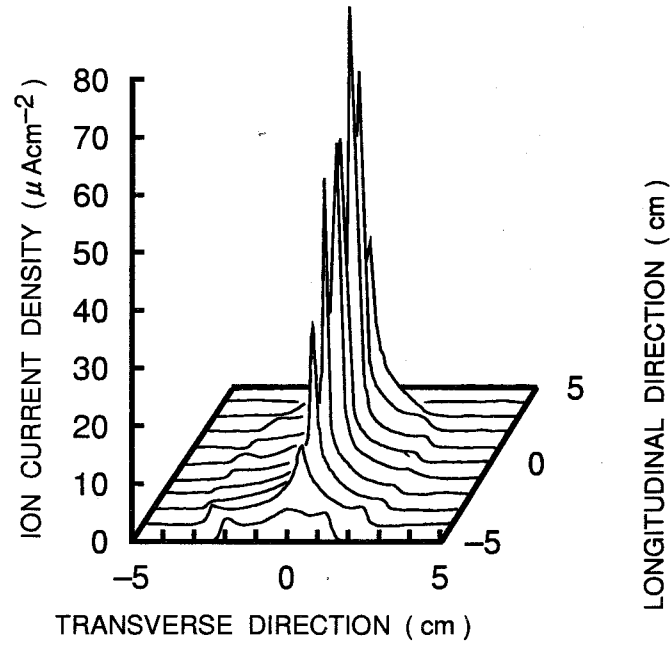
Figure 7.21: Typical beam profiles of the converged ion beam extracted from the five emission-point source.

(a)   (b)
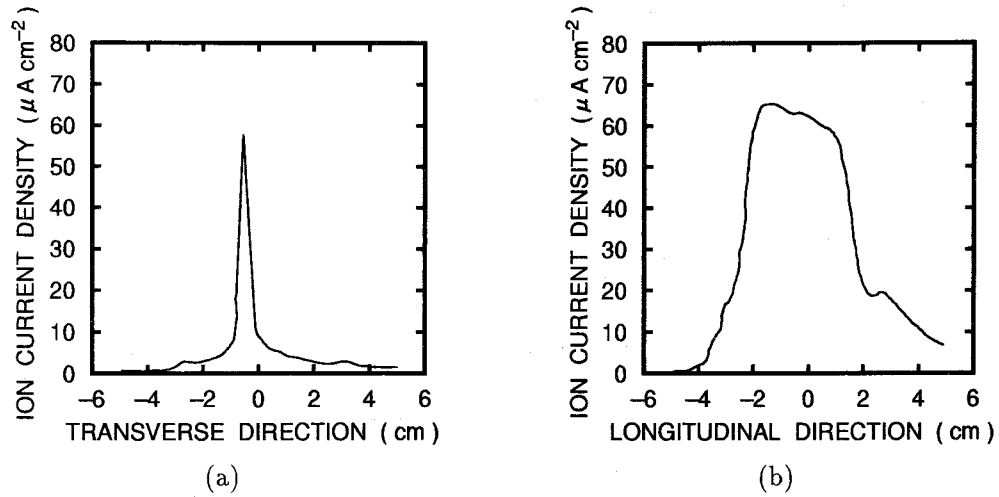
Figure 7.22: Ion current distributions: (a) along the transverse direction, and (b) along the longitudinal direction.

ion emission points, and further intensification of the ion source by multiplication of the number of the emission points is expected.

A rectangular lens system that forms a metal sheet-beam was also developed. The structure is similar to that of the single-point ion source developed in Chapter 5. In this lens, the author took advantage of the self-convergence along the longitudinal direction. Formation of sheet-beam was confirmed by measuring the beam profile. Since the ion beam extracted from the array source can be well controlled, application will be now possible to ion beam sputtering system [16] or ion implanter [17] which is compatible to UHV systems.

References in Chapter 7

[1] T. Kashiwagi: *Intensification of Impregnated-Electrode-Type Liquid-Metal Ion Sources*, M. E. Thesis, Kyoto University, 1988 [in Japanese].

[2] A. Wagner, T. Vankatesan, P. M. Petroff, and D. Barr: J. Vac. Sci. Technol. **19** (1981) 1186.

[3] R. Clampitt: Nucl. Instrum. Meth. **189** (1981) 111.

[4] C. Bartoli, H. H. von Rohden and S. P. Thompson: *Proceedings of the 29th International Field Emisison Symposium*, Göteborg, Sweden, 1982 (Almqvist and Wiksell International, Stockholm, 1982) p.363.

[5] Y. Gotoh, *Analysis of Liquid-Metal Ion Sources and Transport of Intense Ion Beam* M. E. Thesis, Kyoto University, 1987, Appendix D [in Japanese].

[6] J. Ishikawa, H. Tsuji, Y. Aoyama and T. Takagi: Rev. Sci. Instrum. **61** (1990) 592.

[7] Y. Gotoh: unpublished results, 1991.

[8] J. Ishikawa, H. Tsuji and Y. Gotoh: Nucl. Insturm. Meth. B **55** (1991) 343.

[9] T. Motohiro, H. Yamadera and Y. Taga: Rev. Sci. Instrum. **60** (1989) 2657.

[10] J. Ishikawa: *Iongen Kogaku (Ion Source Engineering)* (Aionikusu, Tokyo, 1986) Chapter 8, Table 8-1.

[11] R. Clampitt and J. K. Jefferies: *Molten Metal Field Ion Sources*, in *Inst. Phys. Conf. Ser. No.38* (1978, IOP, Bistrol) p.12.

[12] J. H. Freeman: Nucl. Instrum. Meth. **22** (1963) 306.

[13] P. D. Prewett, D. K. Jefferies and T. D. Cockhill: Rev. Sci. Instrum. **52** (1981) 562.

[14] Y. Gotoh, J. Ishikawa, H. Tsuji, N. Fukayama, Y. Ogata: Nucl. Instrum. Meth. B **74** (1993) 35.

[15] J. Ishikawa, Y. Gotoh, H. Tsuji and T. Takagi: Nucl. Instrum. Meth. B **21** (1987) 186.

[16] Y. Gotoh, T. Amioka, H. Tsuji and J. Ishikawa: Rev. Sci. Instrum. **67** (1996) 1996.

[17] Y. Gotoh, H. Tsuji, J. Ishikawa: Rev. Sci. Instrum. **71** (2000) 780.

Chapter 8

Conclusion

8.1 Progress made in the present research

The present dissertation dealt with the development of novel ion beam systems with an LMIS that has various features to match the ion source for "pure processing". The author first argued the features of the LMIS, and showed that the LMIS is a promising candidate for a metal ion source of novel ion beam systems. At the same time, the author investigated the reason why LMIS's have not been utilized in materials science except the FIB technologies: 1) undetermined ionization mechanism, 2) difficulties in converging divergent beam, and 3) insufficient total ion current. The author examined the development of lens system for divergent ion beam and also development of high current ion source, as well as elucidation of the ionization mechanism. These subjects were treated in three major parts in the present dissertation.

The elucidation of ionization mechanism was dealt in Part I. First, the ion beam characteristics of LMIS's with some element metals were measured in Chapter 2. It was found that the ion flux ratio of doubly charged ions to singly charged ions decreased with an increase in the source current at the high current regime. This behavior could not be well explained by the conventional field evaporation model. Giving a restriction to the term in the fluid dynamics equation, the author derived the formula that explains the decrease of this ion flux ratio. In this argument, the author suggested that the liquid jet is terminated at the point where the kinetic energy per unit volume of the liquid is comparable to the surface tension stress. This formula requires weak dependence of the current density on the electric field. The results of the estimation of the electric field by image hump model, suggested that the temperature at the apex is significantly high.

As a consequence of the above results, the author proposed the high temperature field evaporation model that also includes the ionization mechanism of molecular ions in Chapter 3. The local temperature at the ion emission site is assumed to be elevated up to a non-equilibrium temperature of 1–2 eV. In this chapter, the author argued the ionization mechanism in an analytical way. To show the validity of this model, first the author derived the criterion for the decrease of electric field with the source current. High temperature field evaporation model can clear this criterion with the source temperature of 1–2 eV,

which agrees with the value estimated in Chapter 2.

In Chapter 4, alloy ion sources were also investigated to show the model proposed in Chapter 3 is valid for these ion sources. The variations in mass spectra of Au-Sb and Au-Si ion sources were argued. The alloy that is composed of volatile element (Sb) suffered from evaporation of these atoms during the transportation of liquid to the apex. Also rate of decrease in ion flux ratio of doubly charged ions to singly charged ions was argued and the similar results with the element ion sources were shown. Lastly, the author gave the way of designing the source material for the user's request.

Following the above fundamentals, the author developed the novel ion beam systems in Chapters 5 and 6, which were unified to be Part II. The first one is the lens system that can converge the divergent beam, in Chapter 5. A physically asymmetric lens was developed and the property was evaluated both by computer simulation and by experiments. High transmittance of divergent ion beam with a large energy spread was shown. As an example of this lens system, the author designed an ion implanter. The ion implantation was demonstrated with a heterogeneous molecular ion of $AuSb^{2+}$.

With the lens system, the author proposed a novel ion beam processing of metal ion beam self-sputter deposition which replaced the noble gas ions with the metal ions, in Chapter 6. This is one good example of applications of the metal ion beam provided by the LMIS in a UHV chamber. Cu thin films with low resistivity were obtained.

In Part III, the author approaches final goal of the present study, development of intense metal ion sources with LMIS. The author designed an intense metal ion source, through developments of preliminary test sources with solving the problems of uniform heating and uniform fabrication of the ion emission tips. The author obtained the metal ion current of 9 mA just below the ion source with 39 ion emission points. The ion beam characteristics of the ion source were evaluated and self-convergence along the longitudinal direction was observed. With this result, the author modified the asymmetric lens developed for cylindrical source in Chapter 5 to a rectangular lens and demonstrated the formation of sheet beam. Since the present dissertation demonstrated the possibility of a metal sheet beam formation and, for example, metal ion beam self-sputter deposition, simple combination of these technologies yields novel ion beam processes.

8.2 Future prospect

Not only for the metal materials dealt in the present dissertation, various kinds of materials including transition metals are now possible [1,2] and surface acoustic wave device or super conducting devices are attempted. The applications of the LMIS not only to semiconductor device fabrication but also to various kinds of device fabrication, has become active. These

attempts are for the focused beams, but hereafter it may become active with high current ion sources. In designing the source material, the established model will play an important role.

Use of the ion beam extracted from the LMIS with the focusing lens system treated in the present dissertation was followed by some researchers [3] who constructed accel-decel type lens system. As the author demonstrated, use of metal ions with high current is now possible, various kinds of applications to machining, implantation, and deposition with LMIS's will be realized as new technologies without exhaustion of harmful gases.

The example of use of self-sputtering demonstrated in Chapter 6, can be extended to FIB applications to form a protruding gate electrode of vacuum microelectronics device [4]. Self-sputtering is an interesting method, and a combination with a FIB technique, etching and sputter deposition can be performed simultaneously. This focused ion beam sputter etching and deposition (FIBSED) is a three-dimensional machining and will become a new technique. The application is not restricted within the area of high current application but also FIB application, which may salvage FIB technologies in a different field.

8.3   Subjects left in the future

The author would like to point out the subject left in the future. As for the establishment for the high temperature field evaporation theory, a detailed investigation, for example, brightness change or energy distribution, for Au and Cu is necessary. Unfortunately, no detailed measurement for these elements, covering the high current regime, is seen in the literature. Especially, Cu is an interesting material because it has relatively lower evaporation field and relatively higher surface tension.

The subject of the high current ion source is: how to storage sufficient amount of source material to the ion source. The developed high current ion source still has the disadvantage of the short lifetime due to small volume of the reservoir, even for the version II. It is necessary to enlarge the reservoir or to develop effective mounting system of the source material. For the previous LMIS's which are applied to ion thrusters, the source materials were liquid. In such a case, feeding of the material is relatively easy. However, the present case treats a metal that is solid at room temperature. The simplest way is to make a larger reservoir. For this reservoir, the conventional resistive heating may not be useful, thus the other heating method such as inductive heating [5] is expected.

References in Chapter 8

[1] J. Ishikawa, H. Tsuji, Y. Aoyama and T. Takagi: Rev. Sci. Instrum. **61** (1990) 592.

[2] S. Nagamachi, Y. Yamakage, M. Ueda, H. Maruno, K. Shinada, Y. Fujiyama, M. Asari and J. Ishikawa: Appl. Phys. Lett. **65** (1994) 3278.

[3] Y. Mori, H. Wang, K. Endo, K. Yamauchi and T. Ide: Rev. Sci. Instrum. **61** (1990) 1874.

[4] Y. Gotoh, N. Fujita, H. Tsuji, J. Ishikawa, S. Nagamachi and M. Ueda: J. Micromech. Microeng. **9** (1999) 364.

[5] T. Kawai: *Examination of Inductive Heating for Simultaneous Operation of Multiple Tip-and-Reservoirs of Impregnated Electrode Type Liquid Metal Ion Source*, B. E. Thesis, Kyoto University, 1993 [in Japanese].

List of publications

Publications in scientific journals and reports at international conferences related to the contents of this dissertation are listed below.

Regular journals

1. J. Ishikawa, Y. Gotoh, H. Tsuji and T. Takagi: "Impregnated-electrode-type liquid metal ion source", Nuclear Instruments and Methods in Physics Research B Vol.21 (1987) pp.186-189 [Chapters 2, 4, and 5].

2. Y. Gotoh, T. Kashiwagi, H. Tsuji and J. Ishikawa: "Empirical relation between electric field at the ionization point and emission current of liquid copper, gold, germanium, and tin ion sources", Applied Physics A: Materials Science and Processing Vol.64 (1997) pp.527-532 [Chapter 2].

3. Y. Gotoh, H. Tsuji and J. Ishikawa: "Criterion for decrease of electric field at ionization point of liquid-metal ion sources", Review of Scientific Instruments Vol. 71, No. 2 (2000) pp.725-727 [Chapter 3].

4. Y. Gotoh, H. Tsuji and J. Ishikawa: "On the increase of intensity ratio of doubly charged ions to singly charged ions for liquid gold and copper ion sources", Ultramicroscopy Vol.89, No.1-3 (2001) pp.69-74 [Chapter 3].

5. Y. Gotoh, H. Tsuji, and J. Ishikawa: "Theoretical approach to liquid-metal field-emission electron sources", Applied Surface Science Vol. 146 (1999) pp.377-381 [Chapter 3].

6. Y. Gotoh, H. Tsuji and J. Ishikawa: "Liquid gold-antimony ion sources", Japanese Journal of Applied Physics Vol.35, No.6A (1996) pp.3670-3676 [Chapter 4].

7. Y.Gotoh, H.Tsuji and J. Ishikawa: "Rate of decrease in the intensity ratio of doubly charged ions to singly charged ions in liquid metal ion source with gold-based alloy", Ultramicroscopy Vol.73 (1998) pp.83-87 [Chapter 4].

8. Y. Gotoh, H. Tsuji and J. Ishikawa: "Molecular ion implanter equipped with liquid-metal alloy ion source", Review of Scientific Instruments Vol.71, No.2 (2000) pp.780-782 [Chapter 5].

9. <u>Y. Gotoh</u>, T. Amioka, H. Tsuji and J. Ishikawa: "Metal ion beam self-sputter deposition system", Review of Scientific Instruments Vol.67, No.5 (1996) pp.1996-1999 [Chapter 6].

10. J. Ishikawa, H. Tsuji and <u>Y. Gotoh</u>: "Milliampere metal-ion-beam formation using multipoint emission by an impregnated-electrode type liquid-metal ion source", Nuclear Instruments and Methods in Physics Research B Vol.55 (1991) pp.343-347 [Chapter 7].

11. <u>Y. Gotoh</u>, N. Fukayama, H. Tsuji and J. Ishikawa: "Intensification of an impregnated-electrode-type liquid-metal ion source by multiplying the number of tip-and-reservoirs", Review of Scientific Instruments Vol.63, No.4 (1992) pp.2438-2440 [Chapter 7].

12. <u>Y. Gotoh</u>, K. Yoshida, T. Kawai, N. Fukayama, Y. Ogata, H. Tsuji and J. Ishikawa: "Operational charactersitics of the impregnated-electrode-type liquid metal ion source with multiple tip and reservoirs", Review of Scientific Instruments Vol.65, No.4 (1994) pp.1351-1353 [Chapter 7].

13. J. Ishikawa, <u>Y. Gotoh</u>, N. Fukayama, Y. Ogata, K. Yoshida and H. Tsuji: "Profiles of metal ion beams extracted from impregnated-electrode-type liquid-metal ion source with linear array emission points", Vacuum Vol.44, No.3/4 (1993) pp.357-360 [Chapter 7].

14. <u>Y. Gotoh</u>, J. Ishikawa, H. Tsuji, N. Fukayama and Y. Ogata: "Metal-sheet-beam formation using impregnated-electrode-type liquid-metal ion source with linear array of emission points", Nuclear Instruments and Methods in Physics Research B Vol.74 (1993) pp.35-38 [Chapter 7].

Contribution to international conferences

1. J. Ishikawa, <u>Y. Gotoh</u>, H. Tsuji and T. Takagi: "Impregnated-electrode-type liquid metal ion source", presented at the 6th International Conference on Ion Implantation Technology IIT'86, July 28 – August 1, 1986, Berkeley, U.S.A. [Chapters 2, 4, and 5].

2. <u>Y. Gotoh</u>, H. Tsuji and J. Ishikawa: "Criterion for decrease of electric field at ionization point of liquid-metal ion sources", presented at the 8th International Conference on Ion Sources ICIS'99, September 6 – 10, 1999, Kyoto, Japan [Chapter 3].

3. <u>Y. Gotoh</u>, H. Tsuji and J. Ishikawa: "On the increase of intensity ratio of doubly charged ions to singly charged ions for liquid gold and copper ion sources", presented

at the 46th International Field Emission Symposium, July 23 – 27, 2000, Pittsburgh, U.S.A. [Chapter 3].

4. Y. Gotoh, H. Tsuji, and J. Ishikawa: "Theoretical approach of liquid-metal field electron sources", presented at the 2nd International Vacuum Electron Sources Conference, July 7 – 10, 1998, Tsukuba, Japan [Chapter 3].

5. Y. Gotoh, H. Tsuji and J. Ishikawa: "Rate of decrease in the intensity ratio of doubly charged ions to singly charged ions in liquid metal ion source with gold-based alloy", presented at the 44th International Field Emission Symposium, July 7 – 11, 1997, Tsukuba, Japan [Chapter 4].

6. Y. Gotoh, H. Tsuji and J. Ishikawa: "Molecular ion implanter equipped with liquid-metal alloy ion source", presented at the 8th International Conference on Ion Sources ICIS'99, September 6 – 10, 1999, Kyoto, Japan [Chapter 5].

7. J. Ishikawa, H. Tsuji and Y. Gotoh: "Milliampere metal-ion-beam formation using multipoint emission by an impregnated-electrode type liquid-metal ion source", presented at the 8th International Conference on Ion Implantation Technology IIT'90, July 30 – August 3, 1990, Surrey, U.K. [Chapter 7].

8. Y. Gotoh, J. Ishikawa, H. Tsuji and N. Fukayama: "Intensification of an impregnated-electrode-type liquid-metal ion source by multiplying the number of tip-and-reservoirs", presented at the 3rd International Conference on Ion Sources, September 30 – October 4, 1991, Bensheim, Germany [Chapter 7].

9. Y. Gotoh, J. Ishikawa, H. Tsuji, N. Fukayama and Y. Ogata: "Metal-sheet-beam formation using impregnated-electrode-type liquid-metal ion source with linear array of emission points", presented at the International Conference on Ion Implantation Technology IIT'92, September 20 – September 24, 1992, Gainesville, U.S.A. [Chapter 7].

10. J. Ishikawa, Y. Gotoh, N. Fukayama, Y. Ogata, K. Yoshida and H. Tsuji: "Profiles of metal ion beams extracted from impregnated-electrode-type liquid-metal ion source with linear array emission points", presented at Technology and Applications of Ion Beams, April 4 – 7, 1992, Loughborough, U.K. [Chapter 7].

11. Y. Gotoh, K. Yoshida, T. Kawai, N. Fukayama, Y. Ogata, H. Tsuji and J. Ishikawa: "Operational charactersitics of the impregnated-electrode-type liquid metal ion source with multiple tip and reservoirs", presented at the 5th International Conference on Ion Sources, August 31 – September 4, 1993, Beijing, People's Republic of China, [Chapter 7].

Other publications on liqiud-metal ion sources and their applications

1. Y. Gotoh, K. Inoue, T. Ohtake, H. Ueda, Y. Hishida, H. Tsuji and J. Ishikawa: "Application of focused ion beam techniques to the fabrication of lateral-type thin-film edge field emitters", Japanese Journal of Applied Physics Vol. 33, No.1 (1994) pp.L63-L66.

2. Y. Gotoh, T. Ohtake, N. Fujita, K. Inoue, H. Tsuji and J. Ishikawa: "Fabrication of lateral-type thin-film edge field emitters by focused ion beam technique", Journal of Vacuum Science and Technology B Vol.13, No.2 (1995) pp.456-459.

3. J. Ishikawa, T. Ohtake, Y. Gotoh, H. Tsuji, N. Fukayama, K. Inoue, S. Nagamachi, Y. Yamakage, M. Ueda, H. Maruno and M. Asari: "Application of the focused ion beam technique to the direct fabrication of vertical-type field emitters", Journal of Vacuum Science and Technology B Vol. 13, No.2 (1995) pp.452-455.

4. J. Ishikawa, H. Tsuji, K. Kameyama, S. Shimada and Y. Gotoh: "Development of ion irradiation system for in situ observation of ion irradiated semiconductor surface by ultrahigh vacuum scanning tunneling microscope", Applied Surface Science Vol. 100/101 (1996) pp.342-346.

5. Y. Gotoh, N. Fujita, H. Tsuji, J. Ishikawa, S. Nagamachi and M.Ueda: "Self-aligned formation of a vertical-type micro field emitter with volcano-shaped gate protruding towards the cathode by focused ion beam sputter etching and deposition", Journal of Micromechanics and Microengineering Vol. 9, No. 4 (1999) pp.364-368.

Appendix A
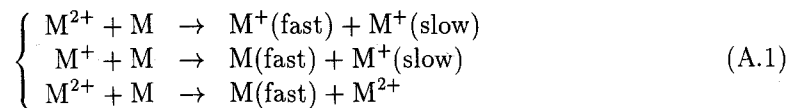# Estimation of factors affecting the final charge state distribution

Difference in space charge effect for doubly charged ions and singly charged ions

Since near the ionization point, the current density is so high that significant space charge effect may distort the initial charge state distribution of the ion beam. One of the possible candidates is difference in space charge effect for doubly charged ions and singly charged ions. If these ions have the same initial energy per charge, an electronic field can not separate the ions with different mass to charge ratio, as described in the textbook. The initial energy is closely related to the energy deficit of the ions. The energy deficit should be a function of the external field. In the conventional theory, the energy deficit should become larger because the electric field should increase as the current increases. However, the energy distribution measurement gave lower energy deficit for the In ion beams, as well as the other ion sources. This means that the energy of the ions are strongly affected by the space charge at the ionization region. The space charge effect is not dependent on the mass to charge ratio, thus the effect of this effect should be the same for the doubly charged ions and the singly charged ions.

Possibility of loss of ions during extraction

If the ions do not collapse until they come into the collector, R_{21} represents the electric field at the apex. However, if there is a collapse of ions, such as charge exchange between the doubly charged ions and singly charged ions, R_{21} does not represents the original charge state distribution. Charge exchange between doubly charged ions and singly charged ions should hardly occurs, due to Coulomb repulsion within the present energy regime. The author discusses the possible processes that prevent us from estimating the electric field at the apex from R_{21} value and showed the validity for estimation of the electric field from R_{21} in Appendix A.

The charge exchange processes related to the present argument are mostly with neutrals:

$$
\begin{cases}
M^{2+} + M & \rightarrow & M^+(\text{fast}) + M^+(\text{slow}) \\
M^+ + M & \rightarrow & M(\text{fast}) + M^+(\text{slow}) \\
M^{2+} + M & \rightarrow & M(\text{fast}) + M^{2+}
\end{cases}
\tag{A.1}
$$

First two processes are singly electron transfer (capture) and the last process is double electron transfer (capture). We should be careful of the charge exchange process of single electron transfer for a doubly charged ion. The number of ions which escape this charge exchange process I at distance z from the source can be written as

$$I = I_0 \exp\left[-N\sigma_{21}z\right], \tag{A.2}$$

where I_0 is the initial quantity of the ions, N is the density of neutral atoms and σ_{21} is the single electron-transfer cross section for a doubly charged ion. If we expect the reduction of ion yield due to collapse by this process, the term in the above parenthesis should be almost of the magnitude of unity. Here we estimate the quantity of $N\sigma z$. N is unknown, but assume $2.7 \times 10^{25}\mathrm{m}^{-3}$ (atmospheric pressure). The exact values of σ_{21} for the heavy ions are not known either, but it would be generally of the order of $10^{-19}\mathrm{m}^{-2}$ [1]. z should be as short as several nanometers, because potential drop of this range gives energy deficit of several tens electronvolts. Assuming z of 10 nm, we obtain $N\sigma_{21}z$=0.027. This gives the change in the current 2.7 %.

Next, we should argue the probability of single electron transfer to neutral atoms for singly charged ions. The final ion current can be estimated from the same equation with replacing σ_{21} with σ_{10}. In this estimation, z should be the distance between the ion emitter and the ion collector. Thus, product of Nz determines the significance of this process. If the cross section is as large as $10^{-19}\mathrm{m}^2$, the product Nz should be lower than 10^{19} m^{-2}. z of the interest is approximately $10^{-3}\mathrm{m}$, which is the ion extraction region. Consequently, N should be smaller than 10^{22} m^{-3}. This corresponds to the pressure of several hundreds Pa. It is not plausible that the average pressure within the extraction region maintains this pressure. Thus, it is not necessary that the single electron transfer for a singly charged ion is taken into consideration.

The last interaction, double electron transfer is further unlikely to occur due to strong repulsion between ions. Thus, the obtained charge state distribution represents primarily the charge state at the ionization point. The observation of the plasma ball was performed [2]. Although the ionization mechanism for Ga includes field ionization, that for Au source is field evaporation.

References in Appendix A

[1] S. C. Brown: *Basic Data of Plasma Physics, 1966, Second Edition, Revised* (MIT press, Cambridge, 1967).

[2] T. Venkatesan, A. Wagner, and D. Barr: J. Appl. Phys. **53** (1982) 787.